Mechanistic Modelling of Blocking Formation and Decay.

Andrew John Holland

Doctor of Philosophy

University of Edinburgh

1998

"Everybody talks about the weather but nobody does anything about it."

- Remembered Yesterdays, Robert Johnson (Mark Twain)

In the atmospheric mid-latitudes, upper-level jets exists which transport storms, generated through baroclinic instability, eastward across the oceans to the continental land masses.

Under atmospheric blocking conditions, the normal passage of storms is interrupted by a region of high-pressure which remains lodged at the end of the storm tracks for periods of a week or more, causing the jet to split and the storms forced to pass around to the north and south, causing anomalous weather conditions over this high-pressure region.

Being able to predict when these events occur, how long they will persist, and their eventual decay would be of value to improve weather prediction. This work looks at a simplified idealisation of this situation, with a view to improve understanding of any precursors to such events occurring, and their subsequent behaviour.

A 2-layer, β-plane, quasi-geostrophic channel model is used to examine the interactions between an upper-layer jet and high-frequency eddies supplied from a wavemaker in the lower layer. For certain initial jets, a dipole similar to an atmospheric block is formed, which remains stable to large-amplitude. By adding a shear to the upper-layer jet, a low-frequency vacillation cycle is induced, whereby the high-frequencies excite a split in the jet, which breaks down due to instability. This instability is demonstrated using a local instability analysis technique, and is also reflected in energy diagnostics. The role of the high-frequency eddies through the various phases of the cycle is also examined.

A spherical-geometry model is also used with an aim to help bridge the gap between this highly-simplified model and the real atmosphere.

These results suggest that the meridional shear in the upper-level atmospheric jetstream may determine whether blocking would develop, persist or breakdown. The structure of the upper-level jet could be controlled by seasonal variations or large-scale teleconnection patterns.

To Eric and Ernie, for the sunshine .....

I'd like to thank my supervisor Keith Haines for his boundless enthusiasm throughout my period of research, whose contribution to this work cannot be underestimated. Also I'd like to thank Mike Robinson and Brian Cameron for maintaining the computing facilities essential for this work. Dr. Chris Thorncroft of Reading University also provided discussion and help during the early part of my research, and Dr. Karl Helfrich also helped with difficulties. A big thank you should go to anyone who has helped me through the difficult times. The included those who've lived with me during this time (especially the lads at 34), friends, second mothers and therapists. Thanks must go also to my brother Steve, not least for four great holidays as much-needed breaks from work. Last, but not least, I'd like to thank my Mum and Dad for their continual support, guidance and love, despite all I've put them through.

Contents

Chapter 1

Introduction

Over the past century, great advances have been made in the field of weather prediction, especially with the advent of powerful supercomputers. However, due to the highly complex and chaotic nature of weather systems, there is still room for substantial improvement, although 100% accuracy will never be acheived. Medium-range weather forecasts, in the range of 5 to 10 days in advance, are being improved continually. However, one of the main causes for error in these forecasts arises from quasi-stationary anomalous events such as "blocking", which often develop fairly rapidly and have a dramatic effect on local weather conditions, often for timescales greater than a week, in severe cases several months. It is obviously of great importance to be able to predict as accurately as possible when these events will occur, how long they will persist, and how they will eventually breakdown.

In a period of blocking, a high-pressure anticyclone weather system, often accompanied by a southern low-pressure region, remains lodged at the eastern end of the stormtracks. This splits the jetstream, preventing the usual synoptic-scale eddies from following their usual path since their direction of travel is largely controlled by the strong upper-level winds. These blocking periods therefore have major implications for the local weather conditions, which are usually quite different from the seasonal normal for the particular time of year. For example, over the British Isles during the wintertime, a block can cause periods of cold weather by advecting arctic air from the North which can bring the country to a standstill in extreme conditions. Conversely, in the summertime a prolonged period of blocking can lead to drought conditions, which was the case in the record-breaking summers of 1976 and 1995.

Obviously, being forewarned of these conditions would prove very useful to all kinds of people, from farmers, the emergency services, water companies etc.

Despite improvements in forecasting accuracy, the conditions necessary for the onset and decay of blocking are still not thoroughly understood, which is the main aim of this thesis to investigate.

The main hypothesis to be tested is that the structure of the incoming upper-level jet stream can act as a pre-cursor to blocking events. In other words, the occurrence or persistence of blocking anticyclones may be more or less favoured depending on the state of the background flow. There are several reasons why this might be a valid proposition. For instance, blocking activity is not constant throughout the year, with a peak in activity over the Atlantic during the spring months (see Chapter 2 for a more detailed discussion). This might suggest that the typical planetary wave structure of this time of year might be conducive for the development and persistence of such blocking anomaly patterns.

This work has tried to capture the fundamentals of the jet stream and wave-interaction in two simple models, with a hope of gaining insights into the more complex behaviour of the real atmosphere. Although direct inferences to the atmosphere are limited by the simplifications of the models, the experiments demonstrate that even the simplest of models can display a wide range of behaviour patterns which are similar to those seen in the atmosphere.

In this study, a 2-layer, β-plane, quasi-geostrophic channel model is used to examine the interactions between an upper-layer jet and high-frequency eddies supplied from a wavemaker in the lower-layer.

With no flow in the lower-layer, different velocity flows with no horizontal shear are applied in the upper-layer as the simplest scenario which can be analysed theoretically. The contributions of various terms in the time-mean eddy equations are shown and the major balances high-lighted. It is demonstrated that a splitting of the jet stream similar to that found in the real atmosphere under blocking can be obtained for certain upper-layer velocities, which can remain stable even at large amplitudes. This type of flow configuration would be considered favourable to the excitation and maintenance of blocking patterns.

Horizontal shear is then added to the upper-layer flow. This reduces the stability of the growing split and causes the flow to oscillate in a vacillation cycle or growth and decay. This flow configuration would be less favourable to supporting long-lived blocking flows. This vacillation cycle is examined using a stability analysis and energy diagnostics to investigate the importance of the high-frequency eddies at different parts of the cycle.

A spherical-geometry model (the UGAMP SGCM) is utilised as a step towards a

more realistic representation of the atmosphere. Due to the further complications introduced by such a model, a regular vacillation cycle is not expected to be generated. However, using a baroclinically-stable jet with a low-level wavemaker, in a similar set-up as the channel model, periods of splitting behaviour are observed. Obviously much more work could be done with such a model than is presented here.

The thesis will be laid out as follows. Chapter 2 will provide a background to the work to be studied, including a brief summary of some previous works which have provided a further understanding in this and related fields of study. Chapter 3 provides a description of the model to be used in the subsequent two chapters. The first of these, Chapter 4, examines flows with only baroclinic shears, and their response to various forcings. Chapter 5 incorporates flows with both vertical and horizontal shear, which provides very different behaviour, which is then further examined including stability analyses. The work in Chapter 6 extends this to use a spherical geometry model, albeit very briefly. Chapter 7 concludes with a final summary and discussion, with suggestions for further work.

Chapter 2

Review of Previous Theory

2.1 Introduction

This chapter will give a brief description of the general atmospheric circulation, with an emphasis placed on anomalous low-frequency events which occur, especially blocking. The rest of the chapter will describe the work of other researchers in trying to provide a better understanding of these observed events.

2.2 General Circulation of the Atmosphere

2.2.1 Sources of energy

The main source of energy for the atmosphere comes in the form of heat input from the Sun. There is a positive net input of radiation near the equator and positive net output towards the polar regions with the result that the atmosphere and oceans must provide a poleward transport of heat. This provides a continual energy source for atmospheric motions. This heat input will also vary according to season, where the angle of incidence of the sun to the Earth varies dramatically, and to a lesser extent, the distance between the Sun and the Earth. Also, the daily variation due to the Earth's rotation provides changes in solar input which are evident predominantly over land regions near the surface. The low-specific heat capacity means that daily temperature fluctuations are much greater than over water, which acts as a heat reservoir preventing rapid changes in temperature.

The intensity of the sun's input is known to vary on longer time-scales than a day. Increased sun-spot activity on its surface provides another frequency of variability. As well as this heat input difference, there are other features which provide a forcing on the atmospheric flow. The spinning of the Earth maintains a rotation of the atmosphere provided through surface friction. As the Earth's

rotation rate is approximately constant ($\omega = 2\pi/(1 \text{ day}) = 7.27 \times 10^{-5} \text{ rad s}^{-1}$) , there must be closely zero net transfer of angular momentum between the two, the Earth providing a forcing when surface winds are less westerly than the Earth's rotation rate, and the atmosphere forcing the Earth when the winds are more westerly than the rotation rate of the Earth. The surface orography also provides mechanisms for forcing with pressure differences across mountains. Large variations in surface height can generate a standing-wave response (the Himalayas and Andes mountains have a large influence, due to their extreme height), and surface material contrasts, especially between the oceans, with their high-specific heat capacity, and the land can provide energy sources, often reversing with the seasons (the monsoon circulation for instance).

2.2.2 Tropical Regions

Associated with heating in the tropical regions is convection. The air rises up and must diverge at upper-levels, where it moves poleward. Therefore, at lower-levels, there must be an in-flux of air from continuity considerations. Away from the tropics, the meridional circulation will be completed by a downward movement of air. This form of circulation is known as a Hadley circulation. Associated with these meridional movements are zonal movements, caused by the effect of the Coriolis 'force' (which arises from using rotating co-ordinates fixed to the Earth's surface). This provides an apparent 'force' directed to the right of any horizontal motion. Therefore, at lower-levels where there is flow towards the equator, this results in eastward forcing, leading to north-easterly winds in the northern hemisphere, and south-easterlies in the southern hemisphere. Conversely, at upper-levels where the flow is polewards, these wind directions are reversed. This model of circulation provides an explanation of the observed equatorial trade winds, which were used for propulsion in the days of sailing ships.

2.2.3 Mid-Latitudes

It might be expected that this Hadley cell would extend all the way to the pole, providing a complete hemispheric circulation. In fact, the cells only continue to latitudes of approximately 30^o. At middle latitudes, a westerly jet is formed, with a maximum at upper-levels which is most intense over oceanic regions, especially the eastern sides of continents (see Hoskins and Valdes (1990) for discussion). This jet, increasing with height, is consistent with the thermal wind equation, derived from the geostrophic and hydrostatic approximations, which states that:

$$\frac{\partial \mathbf{V}_g}{\partial \ln p} = -\frac{R}{f}\mathbf{k} \times \nabla_p T \tag{2.1}$$

where $\mathbf{V}_g$ is the horizontal component of geostrophic velocity, p is the pressure (used as a vertical coordinate), R is the gas constant for dry air, f is the Coriolis parameter and $\nabla_p T$ is the horizontal gradient of temperature on a constant pressure surface. In words, this states that the geostrophic velocity will increase with height in a direction perpendicular to the horizontal temperature gradient.

Figure 2.1 shows the zonal-mean winds for both northern-hemisphere winter and summer periods from Holton (1992), taken from analyses from the European Centre for Medium-Range Weather Forecasts (ECMWF) from between 1980-1987. The mid-latitude jet structures are the dominant features of these plots, being stronger and more equatorward in the winter hemisphere than during the summer.

Figure 2.2 shows the mean 500-mb height contours in the Northern hemisphere for January (winter) and July (summer) taken from Palmén and Newton (1969). Immediately apparent is the difference in the number of contours between the plots, showing that the winds are much stronger in the winter-time circulation. From this plot we can see the zonal asymmetries in the flow, which must arise from features on the Earth's surface, especially height variations and land-sea temperature contrasts. The tightest contour gradients (and hence strongest velocities) occur at the Eastern edge of the two main continental masses, America and Europe/Asia. The differences between these and the equivalent southern hemisphere plots are that there is much less land-sea contrast in the southern hemisphere, and so there are less zonal variations and weaker planetary wave patterns in the southern hemisphere.

Because of the nature of the incoming-outgoing radiation excess in the tropics, heat must be transported across this jet region. This is done by means of baroclinic instability, which gains its energy from the low-level horizontal thermal gradients. These gradients are tightest over the eastern edges of continental masses, where the land-sea differences provide the greatest temperature variations. This instability generates eddies, which are transported eastward in the westerly current over the ocean, developing into the cyclonic storm patterns with a system of fronts, regions of sharp temperature gradients associated with strong winds and clouds. These cyclone waves then pass over Europe and the west coast of America with a usual frequency of 2-3 days, bringing a variety of weather with them.

An action of these eddies is to reduce the thermal gradients and remove the available potential energy from the jet, thereby providing a northward flux of

a

b

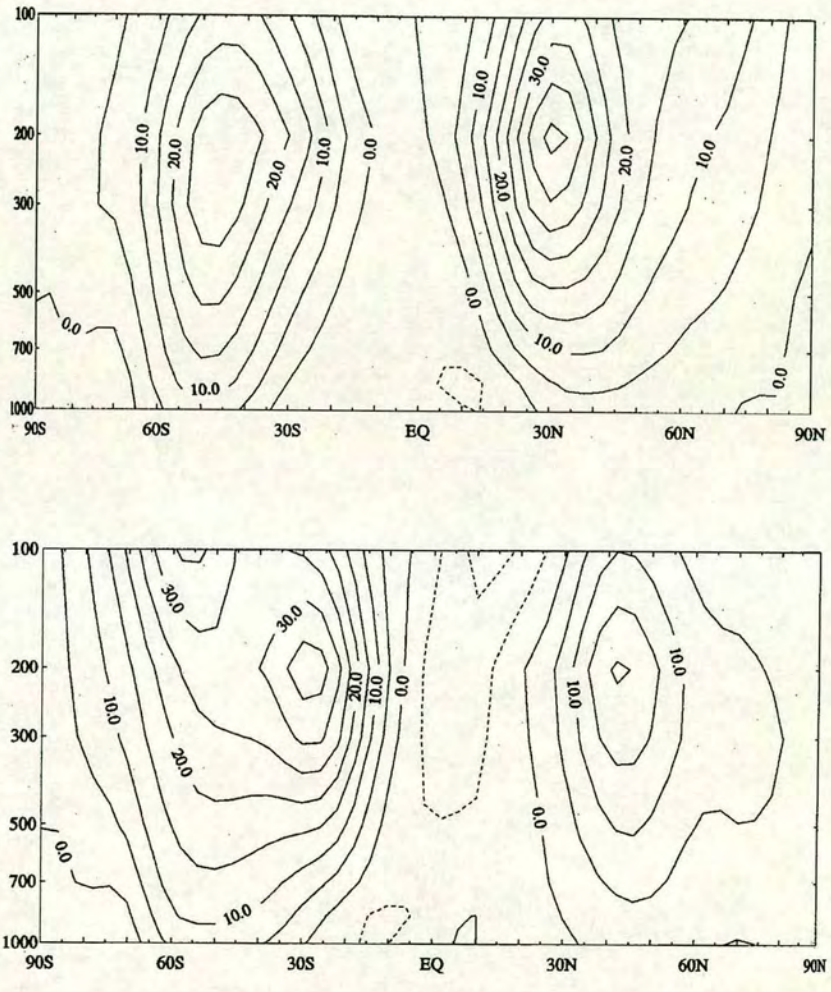

Figure 2.1: Zonal-mean winds for northern hemisphere winter (December January February) DJF (figure a) and summer (June July August) JJA (figure b), averaged for years 1980 - 1987 from ECMWF analyses. Units ms^{-1}. From Holton (1992).

a

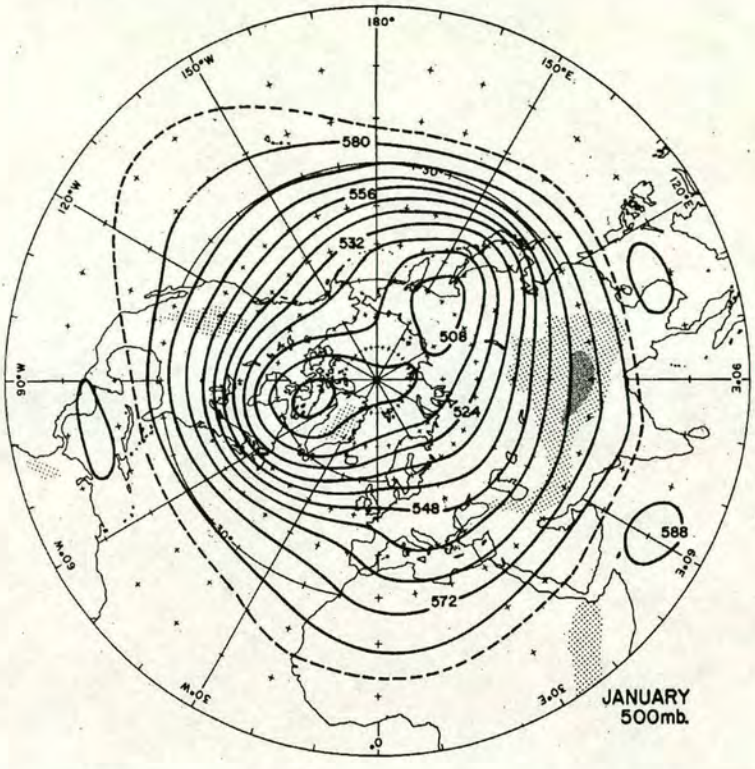

b

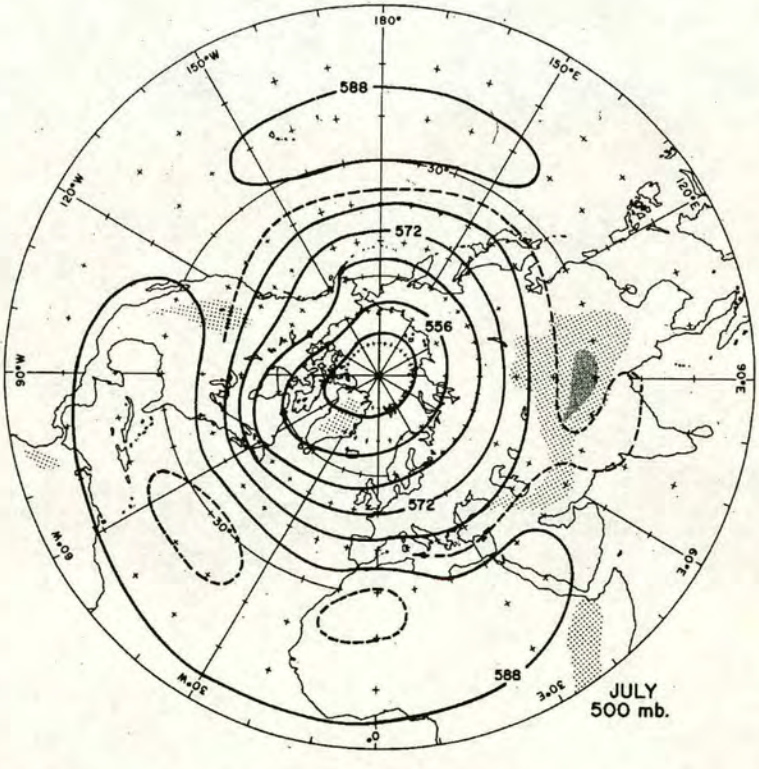

Figure 2.2: Northern-hemispheric mean 500mb contours for January (figure a) and July (figure b). Stippling shows regions where topography is over 1.5km (light shading) and 5km (heavier shading). Contour spacing 80m. From Palmén and Newton (1969).

heat. The passage of eddies in the jet current gives rise to features referred to as "storm tracks", which are characterised by elongated regions of increased high-frequency variability (Hoskins and Valdes (1990)).

2.3 Atmospheric Variability

We have seen in the previous section how baroclinic instability generates disturbances on timescale of several days in the form of synoptic-scale waves. The solar input varies on several time-scales, from the daily variation, to seasonal variation, and beyond to more-irregular cycles highlighted by sun-spot activity changes, which has the form of a quasi-11-year cycle.

Atmospheric and oceanic motions also occur on many different timescales. The following sections will describe some of the main causes of low-frequency variability in the troposphere and oceans.

2.3.1 El Niño - Southern Oscillation (ENSO)

An oscillatory pattern with a time-scale greater than 1 year is that of the El Niño - Southern Oscillation (ENSO). Because of sea surface temperature (SST) contrasts in equatorial regions caused by wind-driven ocean currents, zonally-asymmetric circulation cells are formed, the largest and strongest of these being over the Pacific, known as the Walker Circulation. Normally this pattern will consist of low surface atmospheric pressure in the western Pacific of the east coast of Asia and high surface pressure in the eastern Pacific off the west coast of America. This pressure distribution drives surface easterlies over the equatorial Pacific, which in turn affect ocean currents. However, this east-west pressure difference varies with an inter-annual oscillation with a period of between 2-5 years, known as the Southern Oscillation. This oscillation affects wind, temperature, precipitation and oceanic circulation and SST patterns. The SST changes, and in particular a warming of the sea off the west coast of America is known as El Niño, however this term can be used to describe a more general SST variation of this kind. The effect of these large SST anomalies on atmospheric circulations in extra-tropical regions, via the excitation of Rossby Waves, is considerable (see Hoskins and Sardesmukh (1975)).

2.3.2 Teleconnection Patterns

Surface differences, either from El Niño type SST anomalies, orography or thermal contrasts (mainly differences between land, sea and ice cover), can produce large-scale anomaly patterns in the atmospheric circulation, often global in scale. By plotting correlations between the variations of 500mb streamfunction compared to the variation at a single point, Wallace and Gutzler (1981) constructed maps to show these large-scale teleconnection patterns. A summary of such maps for the strongest correlations is shown in figure 2.3, taken from Wallace and Blackmon (1983). The five patterns are PNA - the Pacific/North American pattern; WA - the West Atlantic Pattern; EA - the East Atlantic pattern; EU the Eurasian pattern; and WP - the West Pacific Pattern. The positive and negative signs indicate the sense of correlation within each pattern. These patterns are much more clearly defined at 500mb than at the surface, and have an equivalent-barotropic structure with amplitude increasing with height. The nodes and anti-nodes of the pattern remain fixed geographically, but wave activity passes along the line of centres causing variations in the amplitude of the anomalies. Hoskins and Karoly (1981) have shown how Rossby wave activity propagates roughly along paths of great circles (circles having a common centre and radius as that of the Earth), provided there are no other wave-guide effects (e.g. jet streams), which might explain these patterns as atmospheric responses to a localised region of forcing.

2.4 Blocking

Another more localised form of low-frequency variability is that of atmospheric blocking, of which much of this thesis is concerned. The early pioneering studies of Berggren *et al.* (1949), Rex (1950a) and Rex (1950b) provided the first detailed analyses of blocking events.

2.4.1 Definition

Blocking involves the development of an equivalent-barotropic anti-cyclonic region of high-pressure at higher latitudes ($> 40°$) than normal, which persists for a period from a week to several months. This is often accompanied by an associated region of low pressure to the south, forming a dipolar pair. They form toward the eastern end of the storm tracks, where the time-mean wave pattern forms a ridge i.e. a localised poleward extension of contours (James 1994). The effect of this is to split the time-mean upper-level jet, forcing it to pass in two branches around

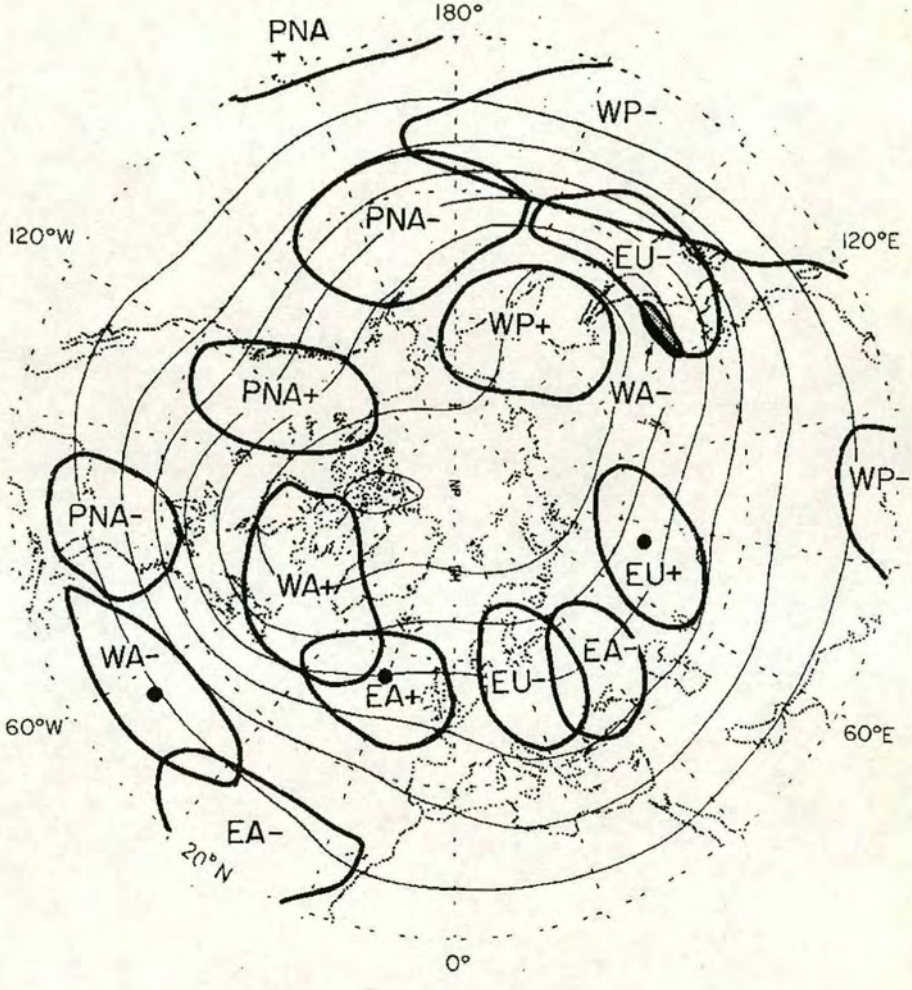

Figure 2.3: Main teleconnection patterns in the atmosphere from 500mb monthly mean height data. The five patterns are PNA - the Pacific/North American pattern; WA - the West Atlantic Pattern; EA - the East Atlantic pattern; EU the Eurasian pattern; and WP - the West Pacific Pattern. The positive and negative signs indicate the sense of correlation within each pattern. From Wallace and Blackmon (1983).

the high-pressure region. A picture of a typical European blocking event is shown in figures 2.4 and 2.5.

Figure 2.4 shows contours of geopotential height of the 200hPa (200 mb) pressure surface (figure a) and the 500hPa pressure surface (figure b) on Saturday the 19th of August 1995 for the Northern Hemisphere over Europe. Figure 2.5 shows the surface pressure field analysis taken at the same time. This date was chosen, partly because it occurred during the research period of this thesis, and because August 1995 was very hot, dry and sunny in the United Kingdom, due to a prolonged period of blocking. Averaged over the whole country, it was the hottest and sunniest month on record, and one of the driest, with sunshine totals being 60% above normal values, and the national rainfall was 15% of its normal monthly value. The 200hPa chart (figure 2.4a) shows a region of high contour height located over northern Europe, with a region of low pressure to its south. The branches of the jetstream are shown to split around this dipole anomaly, with the northern branch being the stronger of the pair. The equivalent barotropic nature of the block can be seen by comparing this figure with that of the 500hPa chart (figure 2.4b), which shows a similar high-pressure anticyclone and low-pressure cyclone system at the same location as on the higher-level pressure surface. At the 500hPa pressure level, very little of the jet appears to branch to the south of the block, the northern branch being predominant. The surface pressure chart of figure 2.5 shows the block less clearly. It shows a small high-pressure region over northern Europe, but the more noticeable region of high pressure, located to the north of the British Isles, corresponds to the ridge seen at upper levels in figures 2.4(a,b).

2.4.2 Implications for Local Weather

The effect of this high-pressure region on local weather conditions is often very dramatic and is dependent on the season. Under normal un-blocked conditions, the weather at the end of the storm tracks will be characterised by the incoming synoptic eddies with periods of 2-3 days, which will bring periods of strong winds and precipitation. However, under blocked conditions, the jet no longer passes over this region, and so these eddies are transported to the north and south around the block. This constant high pressure is associated with clear skies and therefore fine weather, which will cause very different conditions during summer and winter. During January, February and part of March 1963, a region of high-pressure remained over the British Isles. Normally during the winter, the synoptic

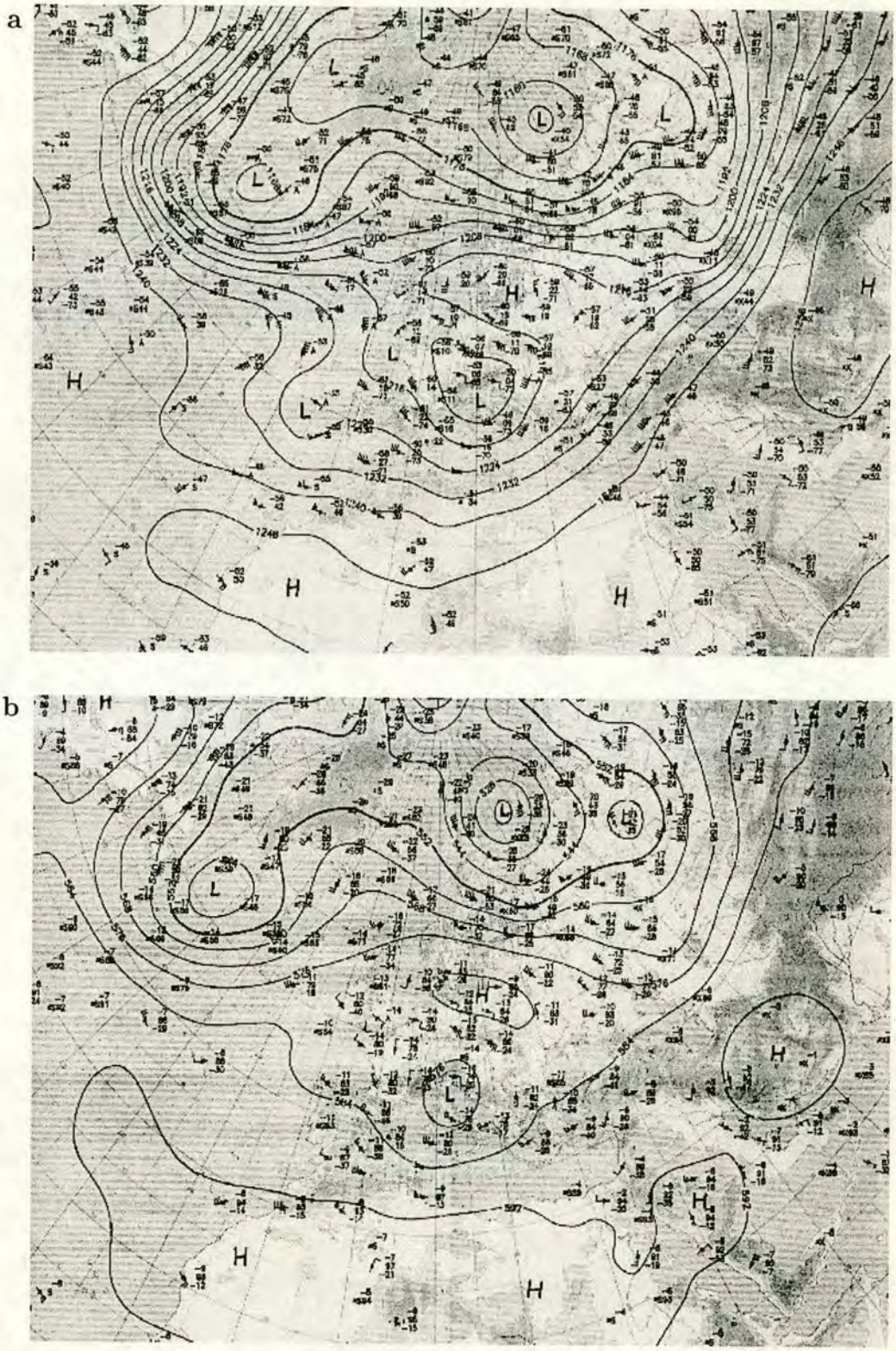

Figure 2.4: 200hPa (figure a) and 500hPa (figure b) charts for the Northern Hemisphere over Europe on Saturday 19th August 1995 during a blocking event.

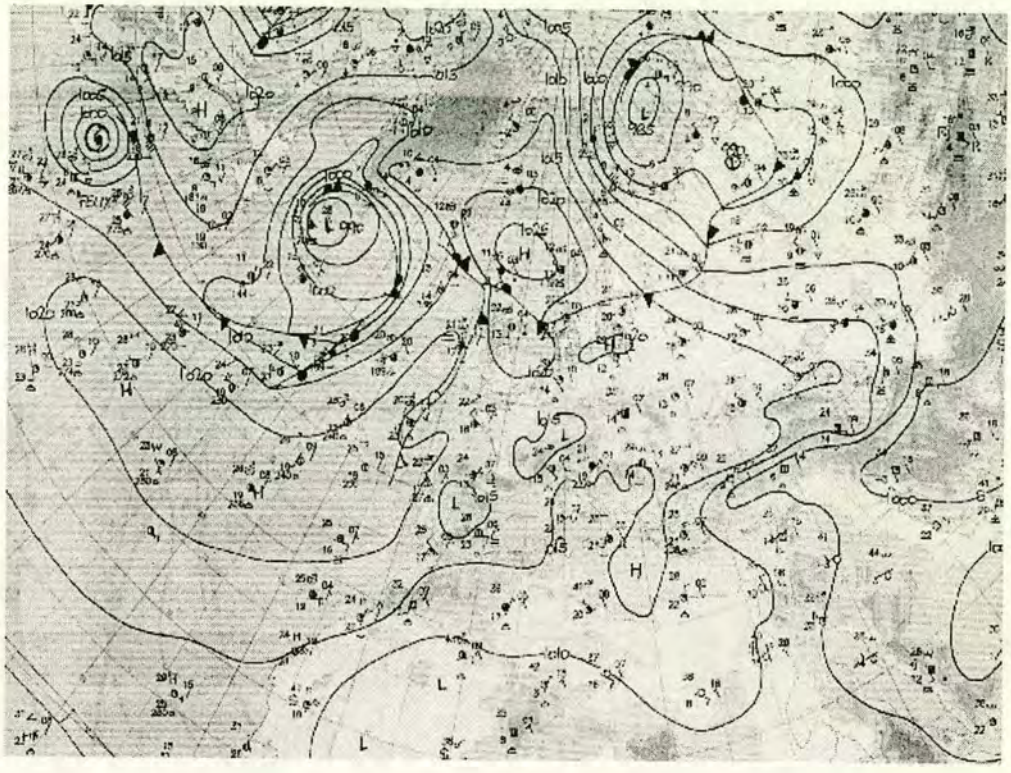

Figure 2.5: Surface pressure chart for the Northern Hemisphere over Europe from 12pm, Saturday 19th August 1995 during a blocking event.

eddies bring in air which is relatively warm due to passing over the oceans which act as a heat reservoir due to their large specific heat capacity. However, because of the anti-cyclonic circulation, the mean winds entering the British Isles was from Europe, which was much colder due to their lack of heating from any oceanic heat source. Also, there was no longer the thick cloud cover over the British Isles which normally helps retain heat by limiting cooling during the long winter nights. A combination of these three facts meant that monthly mean temperatures during this period were reduced by 4° (McIlveen 1992). This prolonged period of cold weather caused major disruption to transport and industry and affected wildlife and plants which were unused to such low temperatures. Also during winter-time blocks, a low-level subsidence inversion can occur, trapping any smoke and pollution near the ground, increasing low-level concentrations of these harmful substances. During a summer blocking episode, different characteristics emerge. Rather than extreme low temperatures, due to the lack of cloud, precipitation and influx of relatively cool air from over the oceans, extremely hot and dry conditions occur. A good example of this is the major drought of July and August 1976, with a slightly less-severe case during the summer of 1995. During the year prior

to the 1976 extended block, there had been a larger than normal incidence of blocking events, resulting in reduced precipitation which was unable to maintain reservoir levels. During the summer, with much evaporation from high daytime temperatures and a low relative humidity and no precipitation, the U.K. had a severe drought.

Conversely, regions to the north and south of these blocks will receive the incoming synoptic eddies which would not normally travel to their latitudes. This can bring very cold and snowy weather at low latitudes (Carlson 1992) and increased precipitation at higher latitudes (Rex 1950b).

Because of these large differences in weather patterns for blocked and un-blocked states, the ability to predict blocks is very important to weather forecasters.

2.4.3 Occurrence Characteristics

Figures 2.6(a-d), taken from Rex (1950b), show various characteristics of blocking location and season.

Figure 2.6a shows the relationship between blocking occurrence and longitude in the northern hemisphere, compiled from data from 1933-1940 and 1945-1949 inclusive. We see there are two main regions, centred between 5° and 15° W longitude, which corresponds to the end of the Atlantic storm track, and one centred between 145° and 155° W, the end of the Pacific storm tracks. If we compare this with the time-mean contours of figure 2.2, we see that these correspond to regions of jet diffluence where ridges are formed.

Blocks also occur in the southern hemisphere, but these tend to be less long-lived (James 1994). Carlson (1992) reports that blocks are favoured to occur when the 500mb ridge is close to 55°E (south-east of Africa), 175°E (near New Zealand) and 65°W (near South America).

Figure 2.6b shows the seasonal trend in the mean longitude of block initiation compared with the seasonal longitudinal movement of the mean Atlantic low-pressure centre (figure 2.2 shows the time-mean winter position of such a low-pressure region). This shows a seasonal dependence for the longitude of initiation, and a loose correlation between this and the position of the low, the main difference in August comes at the time of the minimum number of cases.

Figure 2.6c shows the relationship between blocking frequency and season for both Pacific and Atlantic cases. This shows a clear bias toward the spring months for both Atlantic and Pacific cases. There is a distinct difference in that incidences of Pacific blocking fall to zero during Autumn, whereas the Atlantic case never

falls below 15%. The preference for spring months must be related to the structure of the mean circulation of stationary waves at this time, excited by a particular arrangement of SST anomalies and other heating and orography contrasts.

Figure 2.6d shows how the longitude of the block changes during its lifetime, with the three plots showing histograms at the initial stage, 7 days after initiation and 14 days after initiation. Although hard to draw any firm conclusions, it is noticeable that the spread increases with time, and that the position of the median and mode appear to move westward then eastward during the lifecycle.

Using a general circulation model (GCM), Carlson (1992) indicates that numerical simulations with realistic surface boundaries and topography place the high-pressure ridge at the correct longitude, confirming the dependence of blocking position on the structure of the Earth's surface.

2.5 Atmospheric Flow Regimes

This picture of blocking as an intermittent yet persistent phenomenon leads to the idea of the atmosphere having several quasi-stationary states which act as attractors for the flow, a zonal state and a blocked state may be considered as two such states.

2.5.1 Multiple Equilibria

One of the simplest demonstrations of atmospheric-type wave phenomena comes from the laboratory annulus experiment (see Hide (1966) for a review of this and other laboratory experiments). Fluid (usually water) is contained between two-coaxial cylinders with different radii. The wall of the inner cylinder is held at a lower temperature than that of the outer one, maintaining a temperature gradient across the channel. The cylinders are then rotated, and the evolution of the flow observed. Depending on the different combinations of rotation rate and temperature gradient, different flow patterns are seen, many of which are similar to those seen in the atmosphere despite the lack of a planetary vorticity gradient. For a weak temperature difference, the motion is similar to a Hadley circulation, as found in the tropics. As the temperature difference across the channel is increased, the mean thermal wind must increase, until the the flow becomes baroclinically unstable. At this point a wave regime occurs, where regular wave patterns can be seen in the flow, similar to those found in atmospheric mid-latitudes. In some cases these are steady, but for certain combinations of heating and rotation, reg-

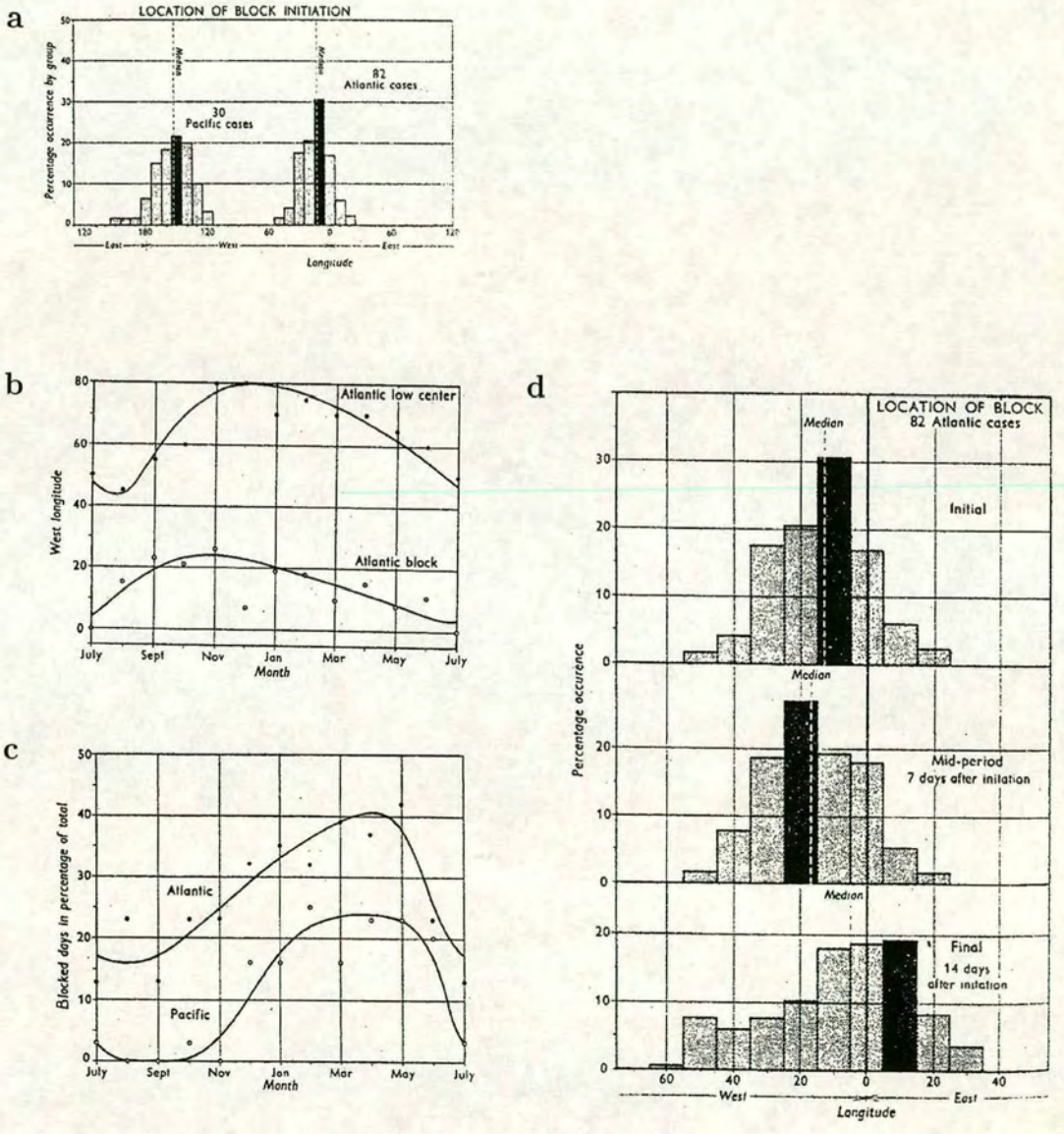

Figure 2.6: Plots showing dependence of blocking on longitude, month and changes in longitude during event. From Rex (1950b).

ular periodic vacillation cycles can occur, analogous to low-frequency variability observed in the atmosphere. More recently, annulus experiments of Früh (1996) and Früh and Read (1997) have been used to examine the interactions between different wavenumbers, and competitions between instabilities of different wavelengths.

Lorenz (1963) presented the famous Lorenz chaotic model, with severely truncated equations involving three variables in a non-linear dissipative dynamical system. The evolution of this system involved circuits around one of two "attractor" points, with transitions at unpredictably-irregular intervals from one circuit to the other. The analogy to the atmosphere was that the two "nodes" around which the system trajectory would circulate were unstable steady states which the atmospheric flow could reside near but never actually attain, with a chaotic crossover between these two such states which would be highly unpredictable. Palmer (1993) linked this chaotic model with that of ensemble forecasting. Because of the high-level of unpredictability in the atmosphere and the inexactness of the initial conditions from which to initialise a model, several forecast models are run with slightly varying initial conditions. If the trajectories of these models are found to be similar after integration, the confidence in the forecast will be much higher than if the forecast trajectories are highly different. Palmer (1993) demonstrated that the predictability confidence of the Lorenz model depended highly on the initial start position, even for this simplest of equation sets.

Charney and DeVore (1979) used a highly truncated spectral barotropic channel model with an orographic forcing term. They discovered that for the same prescribed forcing, more than one stable state solution to the equations could be found, the idea of multiple equilibria. One of their states had a strong zonal flow with weak waves (high index state), and the other had a weak zonal flow with large amplitude waves (low index state). These would be analogous to a zonal and blocked state of the mid-latitudinal atmospheric flow. They suggested that transient eddies could be the mechanism responsible for shifting the flow between the two regimes. However, Tung and Rosenthal (1985) found that the parameter range for which they obtained multiple equilibria were not consistent with the real atmosphere, and that for realistic parameter values, no multiple equilibria could be shown. However, the model of Charney and DeVore (1979) was highly truncated, and even with the correct parameters would be hardly representative of the real atmosphere.

Reinhold and Pierrehumbert (1982) again used a highly-truncated model, but unlike Charney and DeVore (1979), it had two layers, and incorporated a baroclinically unstable synoptic-scale wave, which can interact with the large-scale wave. They again found multiple equilibria solutions, but due to the net forcing from the transients, the regimes were not coincident with those of the pure stationary equilibria of the model. They argued that the variability of the synoptic eddy forcing would account for the indefinite persistence of the regimes. Cehelsky and Tung (1987) claimed that these regimes were unrealistic due to the truncation, and that true steady states would be needed for an attractor.

Anderson (1995) showed that integrations of a forced barotropic model under certain parameter settings would exhibit regime behaviour, one zonal and one blocked. This was similar to the work of Reinhold and Pierrehumbert (1982), except using a much less truncated model. He argued that the regimes seen were related to nearly steady states (NSSs) of the barotropic vorticity equation (BVE) acting as flow attractors, with strong barotropic short waves pushing the flow between the two regimes.

Haines and Hannachi (1995) have searched for weather regimes in output from a long GCM run using Empirical Orthogonal Function (EOF) Analysis and found certain patterns which may be acting as attractors.

Molteni (1996a) used a more complicated 3-level global quasi-geostrophic model, and examined the behaviour using generalised neutral vectors. For example, if the model has two steady states of roughly equal population, the neutral vectors would be similar to the anomaly fields. His results agreed with those of Reinhold and Pierrehumbert (1982), in that the high-frequency interactions could shift the regime centre away from the position of the steady state.

Hoskins (1983a) stated the importance of using a range of numerical models, rather than just very simple and very complicated ones, which should provide a more continuous link between theory and observations. With this in mind, Molteni (1996b) used a simpler model than previously, and claimed that the regimes of Reinhold and Pierrehumbert (1982) were not artifacts of truncations, as Cehelsky and Tung (1987) had claimed earlier.

2.5.2 Flow Regimes in Atmospheric Data Sets

Wallace and Gutzler (1981) looked for recurrent large-scale spatial patterns (teleconnection patterns) in atmospheric data sets. They recovered the now familiar Pacific North-American pattern (PNA) and a North-Atlantic Oscillation (NAO),

which accounted for many of the fluctuations in strength and position of the jet over the Atlantic. As shown later on, the structure of the jet is thought to greatly influence the likelihood of a blocking event occurring.

Three linked studies (Dole and Gordon (1983), Dole (1986) and Dole (1989)) examined the Northern Hemisphere wintertime circulation identifying persistent anomalies. Three key regions (North-East Atlantic, North-East Pacific and Arctic Ocean and Northern Russia) for persistence were found. Over each of these regions, the majority of persistent cases were of a single anomaly pattern, either positive or negative in amplitude. These opposite amplitude anomalies were often associated with either a blocking or an intense-jet flow. By then looking at the evolution of these anomalies in time it was shown that precursors to these events include anomaly patterns to the southwest of the key region, indicating a change in the structure of the westerly jet.

Hansen and Sutera (1986) searched for evidence of multiple equilibria in observational data sets. They defined a wave amplitude index (WAI) as a measure of the longer wavelengths (wavenumbers 2-4) over a latitudinal belt, and found a bimodal distribution of the probability density function (PDF) for their WAI. Nitsche *et al.* (1994) cast doubt on the statistical significance of the above work, saying that 150 years worth of data would be required to distinguish this from samples drawn from a Gaussian distribution.

Vautard (1990) looked for regimes in the atmosphere where the large scale flow was quasi-stationary. He found 4 main regimes; a zonal jet (ZO) and a blocked (BL) regime, as discussed previously, and also one with an anti-cyclone over Greenland (GA) and another with a ridge (tongue of high pressure) over the Atlantic (AR). Figure 2.7 shows these 4 states. He also examined the transitions between these different regimes, and discovered that some were preferred and others were unlikely e.g. ZO $\rightarrow$ BL $\rightarrow$ GA and ZO $\rightarrow$ AR were preferred transitions, indicating that the state of the atmospheric jet could be crucial in determining the likelihood of a blocking event ensuing.

These results have since been confirmed by a later study using a different technique, Multi-channel Singular Spectrum Analysis (M-SSA) by Plaut and Vautard (1994). This technique recovers patterns in space and time, and discovered that blocking occurrence was often linked to the phase of a 30-35 day Atlantic oscillation, but that the phase of this oscillation was not sufficient to produce blocking.

Wallace and Cheng (1991) looked for evidence of regime behaviour in winter datasets and found no evidence of bimodality in the frequency distributions.

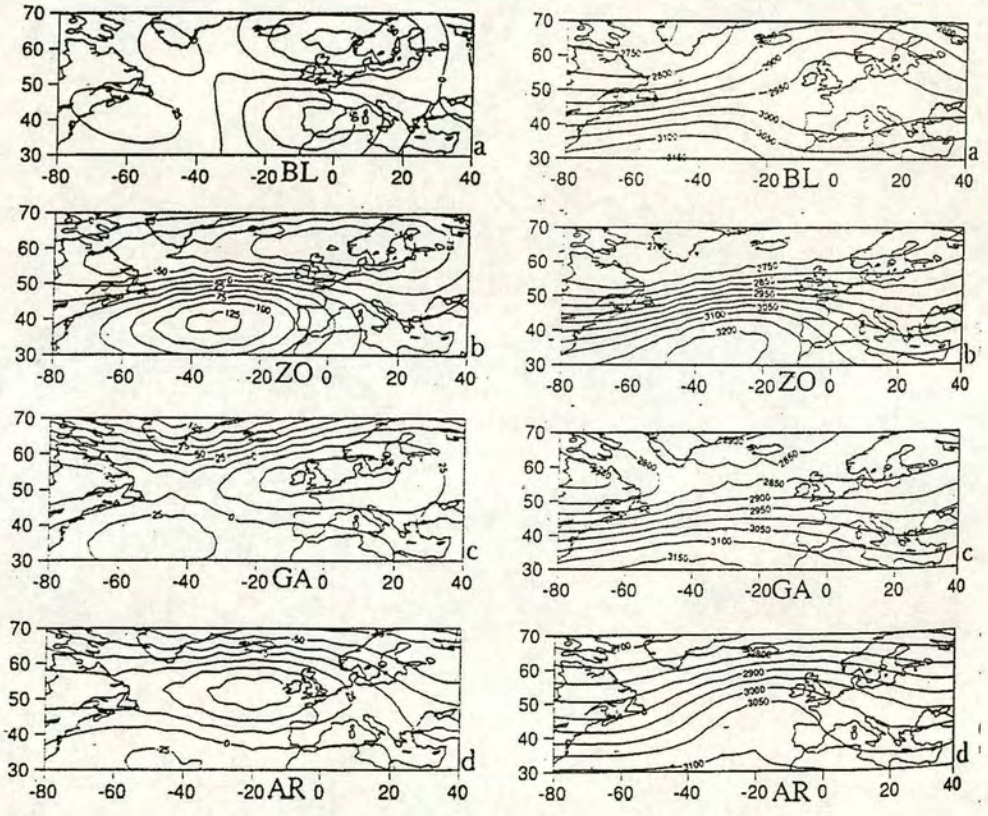

Figure 2.7: Four regimes identified, left-hand column shows the anomalies, right-hand column with climatology superimposed. From Vautard (1990).

Kaas and Branstator (1993) show that the zonal mean state influences blocking activity. By forcing two model runs towards climatologies of statistically enhanced and reduced blocking activity, they showed that the enhanced case run had more blocking events than the reduced case run.

2.6 Studies of Blocking in Atmospheric Data Sets

As previously mentioned, the studies by Berggren *et al.* (1949), Rex (1950a) and Rex (1950b) provided detailed accounts of blocking events. Interest was renewed after the 1976 summer drought of prolonged blocking activity, which was first studied by Green (1977).

Colucci *et al.* (1981) analysed the spectral evolution of a blocking episode. The initial stages were associated with increases in energy of zonal wavenumbers 1 and 2 and meridional wavenumber 1. During the blocking phase, it was the wave with zonal wavenumber 3 and meridional wavenumber 2 which was dominant. They suggested that non-linear resonant triad wave interaction theory could help to explain these observed energy transitions.

Hansen and Chen (1982) examined the spectral energetics of two blocking episodes, one over the Atlantic and one over the Pacific. The Atlantic block was forced by the nonlinear interaction of intense synoptic-scale waves with barotropic planetary waves, the Pacific case developed from the baroclinic amplification of planetary-scale waves. In both cases, the growth of the blocking ridge was preceded by intense upstream cyclogenesis.

Colucci (1985) looked at two observed cases of explosive surface cyclogenesis, one of which preceded the retrogression of a blocking high, the other formed an upstream cut-off low, with no downstream high. He discovered that the response was dependent on the relative position of the synoptic-scale eddies and the planetary wave structure, with an anticyclone more likely to be produced if the cyclogenesis occurred just downstream of a trough region.

Hansen (1986) looked at analyses of 4 winter's data, using a global measure of wave amplitude, rather than the usual local measure of blocking. He found a bimodality of the flow, with one regime being fairly zonal (mode 1), the other having an enhanced ridge (mode 2), what would be termed an amplified wave pattern. It was found that the local high-north-of-low blocking patterns, as defined by Rex (1950a), were not in this latter category, but were classified as mode 1 types. He declared that there were two different classes of large-scale persistent phenomena,

which were distinguished by their global or more local characteristics.

Schilling (1986) looked at many incidences of blocking, and tried to define blocking criteria based on circumpolar energetics, rather than the more conventional local deviations.

Kaas and Bränstator (1993) tried to establish whether zonally averaged conditions can influence blocking activity. They found that weak zonal mean winds between 50° and 60° N, and strong zonal winds around 30° N, tend to influence periods of increased blocking activity over the north-east Pacific and north Atlantic. They also showed a link between prominent planetary wave amplitude anomalies and blocking. This link could be partially caused by anomalous planetary-wave highs in the blocking region, which would enable a blocking criterion to be satisfied more easily.

Liu (1994) looked at the distinction between when a positive geopotential anomaly could be regarded as a block, rather than an extension of the tropical region of high pressure. He concluded that the amplitude and latitude were necessary for a reliable definition. He also stated that blocking and intensification anomalies (similar anomaly patterns but with opposing signs, as studied by Dole (1986)) had similar durations. The blocking phase may appear more persistent due to the reduced high-frequency variability near the blocking centre, but the strong zonal flow was found to be equally persistent.

Ek and Swaters (1994) studied a block which developed into an omega shape, then became dipolar and finally broke down. This type of omega blocking is more common over Pacific regions. They showed that increased synoptic wave activity seemed to change the phase of the large scale flow and that the omega shape block was more stable than the dipole one, which was supported by the fact that the omega block persisted for a longer period of time than the subsequent dipolar one.

Hansen and Sutera (1995) examined the events of January 1963 and searched for other similar events over winters from 1946 to 1988. They suggested that the spatial evolution of the initial rapid development resembled that of a standing wave, with the decay being associated with translation in space.

2.7 High-frequency eddies

2.7.1 Wave Interaction

This section covers the hypothesis that the interactions between waves with different frequencies and spatial scales can influence the development and maintenance

of anomalous atmospheric circulations.

Fjortoft (1953) examined the flow of energy between triad interactions of waves with different spatial scales, using the conservation of kinetic energy and total vorticity squared in two-dimensional, non-divergent flow. He showed that the energy would flow predominantly to the larger scales.

Egger (1978) proposed that blocking highs could result from the non-linear interaction between forced standing waves and slowly moving free waves. From his experiments, he claimed that "a geographically fixed forcing was an almost necessary condition for the onset of blocking". He only used simple models retaining only waves with longer wavelengths, so made no claims for a role for high-frequency transients.

Cai and Mak (1990) described a "symbiotic relation" between the planetary and synoptic-scale waves, which is more commonly used for describing two biological species which critically depend on each other in order to survive. The planetary waves would receive energy from the synoptic scales through an up-scale cascade. The planetary waves would then organise themselves to create a locally unstable region, which provides a mechanism for the generation of synoptic-scale eddies.

Malguzzi (1993) performed an analytical study of the feedback between large-scale stationary Rossby waves and small-scale high-frequency eddies and found a quadrupolar forcing structure, consistent with that seen in the observational study of Illari (1984).

2.7.2 Transient eddy feedback on the mean flow

Green (1977) studied the events of the long-lived block of the summer of 1976. He first suggested that the synoptic eddies were having a positive feedback on the time-mean large-scale blocked flow i.e. the eddies were maintaining the flow against dissipation. Later studies have provided evidence to support this.

Shutts (1983) used a barotropic channel model with an artificial 'wavemaker' to simulate the baroclinic eddies. Provided that the zonal velocity was weak enough to allow a stationary dipolar Rossby wave to be a free-mode solution of the channel, he found that the wavemaker excited a split in the jet downstream of the wavemaker reminiscent of a block. Over the block region there were down-gradient eddy pv-fluxes, in agreement with the observations of Illari and Marshall (1983). Figure 2.8 shows a diagram of the splitting in his model, with a jet speed of $U = 7.5\text{m s}^{-1}$, with the eddy feedback superimposed. The dispersion relation for a stationary Rossby wave in the channel would be given by:

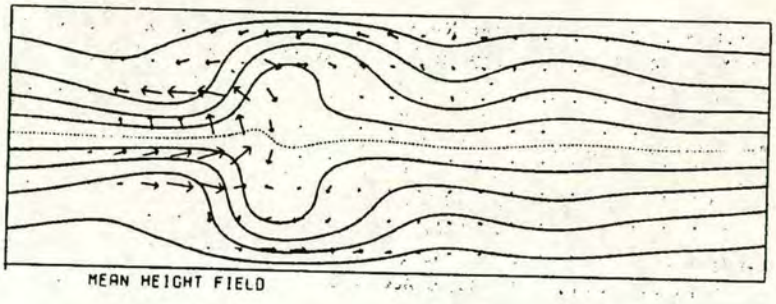

Figure 2.8: Diagram showing splitting by wavemaker forcing, $U = 7.5\text{m s}^{-1}$. Arrows show residual eddy flux. From Shutts (1983).

$$0 = c = U - \frac{\beta}{k^2 + l^2} \tag{2.2}$$

His channel had a width of 6000 km and length of 18000 km, with $\beta = 1.64 \times 10^{-11}\text{m}^{-1}\text{ s}^{-1}$. For meridional dipolar Rossby waves, $l = \frac{2\pi}{6\times10^6}\text{m}^{-1}$. With $U = 7.5\text{m s}^{-1}$, equation 2.2 gives a value for k of $1.044 \times 10^{-6}\text{m}^{-1}$, which gives a wavelength of approximately 6000 km, allowing three complete waves in the zonal direction. Figure 2.8 reflects this, with the largest anomaly magnitude coming from over the wavemaker region. If the flow is increased to $U = 15\text{m s}^{-1}$, this gives a value for the total wavenumber $\frac{\beta}{U}$ of $1.09 \times 10^{-12}\text{m}^{-2}$, which means that now a meridionally-dipolar wave is not a solution of the channel. When the same experiment is run in this case, no block is formed, only an intensification, highlighting the need for a stationary Rossby wave solution in order for a block to form through resonant excitation.

His Eddy Straining Hypothesis, whereby the eddies propagating into a split were sheared meridionally, which by energy and enstrophy conservation laws caused them to give up their energy to the larger scale flow, was his explanation for how the eddies maintained the large scale flow. In his model he found either persistent blocking or a persistent zonal jet, no oscillation of any kind. He also tried to separate the divergent component of the eddy flux by assuming that the flow was close to a free mode, i.e that pv contours and streamlines were parallel (this flux was originally derived in Marshall and Shutts (1981)), allowing a rotational component to be removed. This was termed the residual flux. However, Haines (1994) showed that the primary balance in the enstrophy equation involved the external forcing from the wavemaker, in which case the residual flux was not a good indicator of the divergent flux as originally intended.

Illari and Marshall (1983) observed northward eddy heat fluxes and southward eddy fluxes of potential vorticity over the blocked region, which indicated a reduction in the zonal eastward momentum i.e. a slowing down and splitting of the jet. Illari (1984) presented a case study of a warm block, showing a balance between time mean and 'eddy' ('eddy' being deviation from the time mean) potential vorticity advection i.e. $\overline{\mathbf{v}}.\nabla\overline{q} \simeq -\overline{\mathbf{v}'.\nabla q'}$, which prevented the structure from being 'blown' downstream. Shutts (1986) showed how a meridionally extended trough (tongue of low pressure) upstream of the block enabled the eddies to sweep tropical air with associated low-potential vorticity northwards and deposit it in the blocking anticyclone, reinforcing it against decay. Colucci *et al.* (1981) examined the 500mb heights using a Fourier analysis technique, showing the dominant wave components at the various phases of the blocking episode.

Mullen (1987) examined the forcing of blocks by transients in both observed and GCM data. He found that an anti-cyclonic forcing was one quarter wavelength upstream of the blocking region, and that the temperature tendency from the transients was out of phase with the block's temperature perturbations. This upstream vorticity forcing would tend to make the block retrogress (move upstream), which would be offset by the advection by the large-scale flow.

The two papers by Vautard *et al.* (1988) and Vautard and Legras (1988) used a two-level baroclinic channel model but forced a jet at one end to be baroclinically unstable to produce eddies. They found several 'regimes' or patterns where the flow tended to remain, the two main ones being a zonal and a blocked state (similar to the high and low index states of Charney and DeVore (1979), which were close to the free-modes of the channel. They indicated that these free modes (ones in which $q = G(\psi)$) could act as attractors for the flow, supporting the hypothesis of Charney and DeVore (1979). Figure 2.9 shows the zonal and blocked states from their work.

Higgins and Schubert (1994) used a kinetic energy budget analysis to examine the role of synoptic scale eddies. They found that barotropic processes dominated during the growth phases of blocking, and that baroclinic conversions were associated with the decay (Plumb (1983) discusses the dangers of using energy diagnostics). They claimed that the transient-eddy maintenance of large-scale anomalies was "rather selective", and depends on the structure of the large-scale flow anomaly.

Robinson (1994) looked at the transient eddy feedback on low-frequency variability. By forcing the flow at different frequencies, he found that for very low-

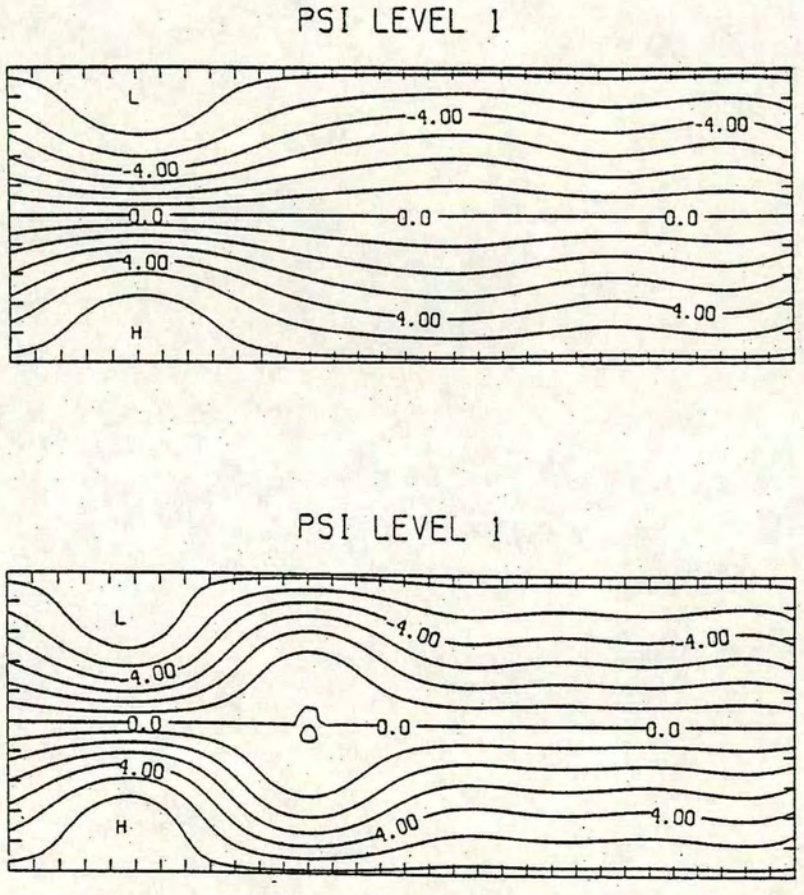

Figure 2.9: Zonal (upper plot) and Block (lower plot) composites from Vautard *et al.* (1988).

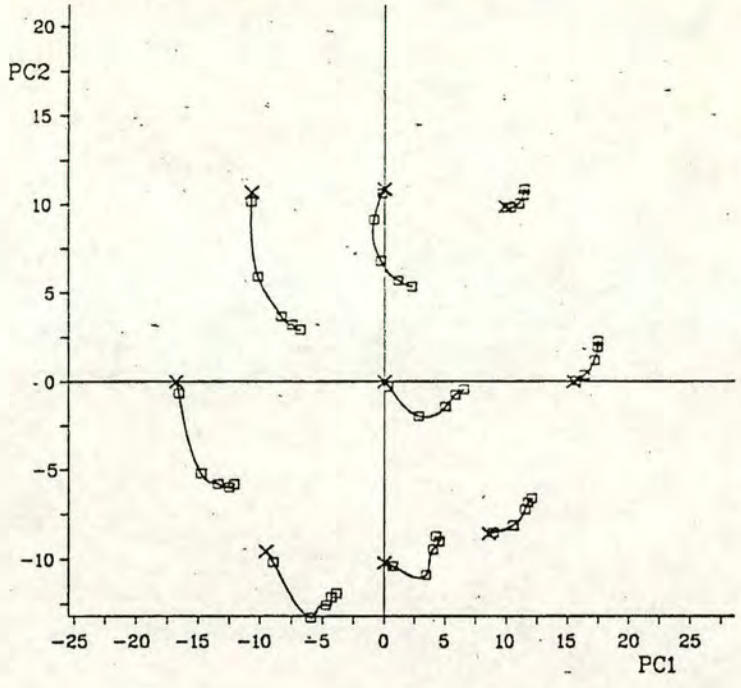

Figure 2.10: Phase-space representation of oscillation with non-linear mode progression at various points superimposed. From James *et al.* (1994).

frequency forcing, the high-frequency eddy feedback was positive, but when the forcing applied had a period less than a month, the feedback from the high-frequency eddies was negative.

James *et al.* (1994) showed that the effects of successive baroclinic-wave lifecycles could provide a feedback onto the zonal flow, producing an ultra-low-frequency circulation (in his model, the UGAMP SGCM, a cycle with a period of 150 days was produced). They tried to demonstrate that normal-mode lifecycles could be used to explain this "pushing" around the phase-space circuit. Figure 2.10 shows a diagram from their paper for the phase-space evolution of normal modes at different phases of the oscillation cycle. There is a general tendency for these lifecycles to push the flow anti-clockwise around the circuit in phase space, but they are unable to push the flow out of the upper-right quadrant.

Branstator (1995) showed, using a GCM, that the momentum fluxes by the transients were not random, but that storm-track activity is modified by the presence of large-scale circulation anomalies. This means that some anomalies would produce a positive feedback from the high-frequency eddies, giving them an advantage to persist over those in which the organisation of the large-scale flow

did not lead to a positive transient-eddy feedback.

Molteni (1996a) showed the importance of high-frequency eddies in affecting the position in phase-space of weather regimes, as Reinhold and Pierrehumbert (1982) had done for a highly truncated model. He also re-confirmed the balances of the eddy feedback, that at upper-levels it was balanced by advection, and at lower-levels it was balanced by dissipation.

2.7.3 Eliassen-Palm Fluxes

Eliassen-Palm fluxes (EP) provide a measure of the influence of eddy motions on zonal flows. Andrews and McIntyre (1976) introduced the zonal equations in a transformed Eulerian mean. The conventional zonal mean quasi-geostrophic equations for zonal momentum and thermodynamic energy equations on a mid-latitude β plane can be written as (from Holton (1992)):

$$\frac{\partial \overline{u}}{\partial t} + f_0 \overline{v} = -\frac{\partial \overline{u'v'}}{\partial y} + \overline{X} \tag{2.3}$$

$$\frac{\partial \overline{T}}{\partial t} + \frac{N^2 H}{R} \overline{w} = -\frac{\partial \overline{v'T'}}{\partial y} + \frac{\overline{J}}{c_p} \tag{2.4}$$

where an overbar indicates zonal average and $'$ a deviation from this, u is zonal velocity, f_0 is Coriolis parameter, $\overline{X}$ is zonal drag owing to small scale eddies, T is temperature, N is the buoyancy frequency, H is a scale height, R is the gas constant for dry air, w is vertical velocity, J is heating rate and c_p is the specific heat capacity at a constant pressure. In equation 2.4, there tends to be a large cancellation between the eddy heat flux convergence and adiabatic cooling, with the heating term being a small residual. Air will only rise in the mean through changing its potential temperature by diabatic heating, and so we wish to highlight this term in the equations, which is done by moving to a new co-ordinate system for y and z, the transformed Eulerian mean. We define a residual circulation as:

$$\overline{v}^* = \overline{v} - \frac{R}{\rho_0 H} \frac{\partial}{\partial z} \left(\frac{\rho_0 \overline{v'T'}}{N^2} \right) \tag{2.5}$$

$$\overline{w}^* = \overline{w} - \frac{R}{H} \frac{\partial}{\partial y} \left(\frac{\overline{v'T'}}{N^2} \right) \tag{2.6}$$

which is the component which the eddy heat flux does not cancel with.

Written in this new co-ordinate system, equation 2.3 becomes:

$$\frac{\partial \overline{u}}{\partial t} + f_0 \overline{v}^* = -\frac{1}{\rho_0} \nabla . \mathbf{F} + \overline{X} \tag{2.7}$$

where:

$$\mathbf{F} = (F_y, F_z) = \left(-\rho_0 \overline{u'v'}, \frac{\rho_0 f_0 R \overline{v'T'}}{N^2 H} \right) \tag{2.8}$$

where ρ_0 is the density (constant). Equation 2.7 shows that the divergence of this vector field represents an eddy flux of zonal momentum, the direction indicating the principal fluxes of heat and momentum by the eddies. It can also be shown (Edmon *et al.* (1980), Holton (1992)) this this divergence is equivalent to a northward flux of quasi-geostrophic potential vorticity. Edmon *et al.* (1980) show cross-section plots of this flux and its divergence for observed and modelled baroclinic waves. Figure 2.11 shows these cross-sections from their paper for 0, 5 and 8 days after the start of integration (figures 2.11 a, b and c) and the time-mean average (figure 2.11 d). During the early linear stages of a modelled life-cycle of baroclinic instability, these vectors tend to be directed vertically with a low level convergence of $\overline{v'T'}$ at $800hPa$. It is the release of potential energy from near the surface by baroclinic instability which provides the energy for the wave to grow. This region of convergence then moves vertically upwards then equatorwards during the non-linear stages of the eddy lifecycle. Due to the reduced air density at upper levels, this propagation can then cause wave-breaking events to occur. They stated that the upward propagation of planetary waves seemed to be the most important factor in this non-linear phase, and these similar patterns would emerge however the initial low-level disturbance was generated, in this case by baroclinic instability.

By adding a barotropic shear component to the basic state, Thorncroft *et al.* (1993) generated an anomalous lifecycle, LC2, which has increased cyclonic wrap-up which has less equatorward motion. Palmer (1980) and Palmer (1981) used these fluxes to examine upward wave propagation into the stratosphere during a sudden warming event. Pfeffer (1992) indicates that vertical convergences are associated with a poleward eddy heat flux in the source region for baroclinic eddies, and these drive the residual circulation. The horizontal divergences are associated with the meridional eddy momentum flux and equatorward propagation of waves away from the source region, and these generate fluctuations in the zonal wind.

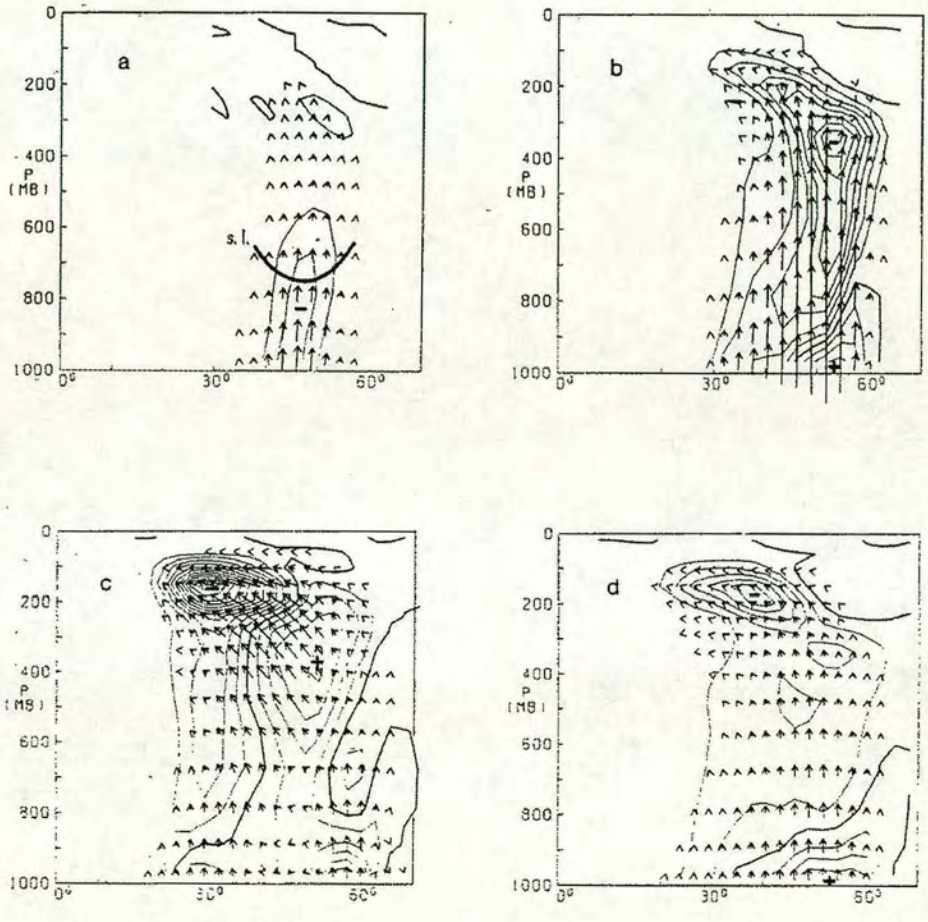

Figure 2.11: Cross sections showing EP fluxes and divergence for a growing baroclinically unstable wave on a realistic mean state. Figures a,b,c show the fields after 0, 5 and 8 days after start of integration respectively, and figure d is the time-average for the life-cycle. From Edmon *et al.* (1980).

2.7.4 Refractive Index

Matsuno (1970) first described the refractive index of the background flow which can provide an indication of the characteristics of wave propagation. In its simplest form for a zonal flow, the refractive index n^2 can be defined as:

$$n^2 = -\frac{\partial q}{\partial \psi} = -\frac{\partial q}{\partial y}\frac{\partial y}{\partial \psi} = \frac{\frac{\partial q}{\partial y}}{u} \tag{2.9}$$

where q is the quasi-geostrophic potential vorticity, ψ is the streamfunction and u is the velocity in the zonal direction. It is equivalent to the total wavenumber. In the case of a purely zonal flow with no shear, it reduces to be the stationary resonant wavenumber ($K^2 = \frac{\beta}{u}$). In a similar way to optics, propagating waves are refracted toward regions of larger refractive index. Matsuno (1970) showed that weak potential vorticity gradients, which would reduce the refractive index if the velocity did not similarly reduce, could act as a barrier to wave propagation. This can also help to understand the propagation phase of EP fluxes, as they tend to be focussed towards a region of high refractive index. This linear theory becomes invalid near critical lines, where $u = 0$, and there are various theories concerning the properties of critical lines, such as whether they absorb or reflect wave activity. The refractive index diagnostic has been used by, amongst others Butchart *et al.* (1982) and Karoly and Hoskins (1982), to look at propagation of wave activity vertically upwards into the stratosphere, in particular with respect to sudden warmings. In these cases, the stratosphere can rapidly increase in temperature, and it is thought to be caused by increased wave propagation from below. Branstator (1983) looked at the horizontal propagation of energy away from steady sources in a barotropic model with a variety of background states, showing how relatively small changes in the background flow can have a great effect on energy propagation. The refractive index structure of a jet is also crucial in soliton theory, and determines which type of solution the jet can support (see section 2.8.2 for a discussion of solitary waves and their relevance to blocking).

2.7.5 E Vectors

E vectors were introduced by Hoskins *et al.* (1983) to help interpret the feedback of large-scale eddies on the mean flow. Rather than a zonal diagnostic as the E-P flux, these vectors are plotted on a pressure surface. The vector is equivalent to a negative eddy flux of zonal momentum. Section 4.5 contains a derivation of these vectors from the momentum equations. Where there is a convergence, this

indicates a slowing-down of the westerly flow by the eddies. They showed that for high-pass eddies which were meridionally elongated, this vector would point eastward, and a convergence at the end of the storm tracks, indicating a slowing down of the westerly flow by the synoptic eddies. During periods of blocking, this convergence is often strong, highlighting their role in maintaining the anomalous circulation. The vector would be westward pointing for low-pass zonally-elongated eddies.

Plumb (1986) defined similar sort of extended EP Flux vector, which provided a measure of the flux of eddy activity parallel to the group velocity. He discusses the relation between this flux and the E vector.

2.7.6 Effect of background flow on eddy development

2.7.6.1 Effect on Baroclinic Wave Lifecycles

Simmons and Hoskins (1977) looked at the non-linear effects of baroclinic waves growing in a simplified GCM. The initial linear growth from the baroclinic instability was primarily at low levels, and during the later phases of the lifecycle, this low-level energy would propagate vertically into the upper troposphere. Because the density is much less at higher altitudes, the wave amplitudes become larger, and can often "break", causing an enstrophy cascade to smaller scales which would be dissipated by friction. Simmons and Hoskins (1980) continued this work by altering the initial jet by adding barotropic shear. They found an anomalous case, in which the eddy kinetic energy evolution of the life-cycle differed by having a delayed maximum and longer time to decay. These two kinds of lifecycles, labelled LC1 and LC2 respectively, were studied by Thorncroft *et al.* (1993). Figure 2.12 shows the non-linear stages of such lifecycles by plotting theta on a PV surface showing the flow near the tropopause. In the LC1 case, there has been much cross-jet potential vorticity exchange, which would be necessary for the case of atmospheric blocking. In the anomalous LC2 case, there is a cut-off cyclone of PV, and very little cross-jet transport. They speculated that LC2-type synoptic eddies would be less able to support blocking anomalies. Since the differences in lifecycle came from a difference in the barotropic component of the basic-state jet (therefore unchanging the initial eddy growth). The results add to the argument for the dependence of blocking on the background flow.

Marcus (1990) showed how vortices in sheared flow would be either strained into long filaments or be wrapped up, depending on whether the sign of the rotation of the vortex was the same or opposite to that of the background flow.

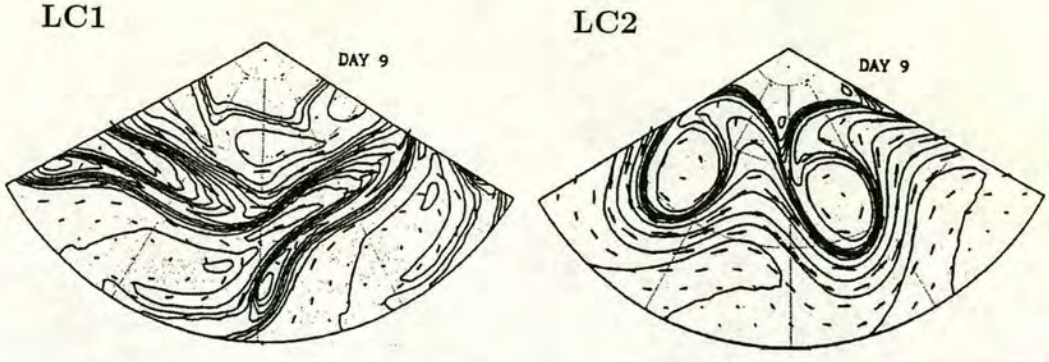

Figure 2.12: Later stages (day 9) in the two lifecycles from Thorncroft *et al.* (1993). LC1 has cross-jet pv transport, and so is conducive to blocking, whereas LC2 does not, with its increased cyclonic wrap-up, and so is unlikely to support blocking.

In a series of papers (Tung and Lindzen (1979a), Tung and Lindzen (1979b) and Tung (1979)), the authors speculated that blocking was caused by the resonant amplification of large-scale planetary waves, which were forced by topography and surface heating. This resonance would be caused by the effect of the jet structure permitting wave trapping (see section 2.7.4 on refractive index). Under certain conditions, the jet would allow vertical propagation of waves into the stratosphere, which could lead to stratospheric warmings.

Frederiksen (1982) demonstrated, using a two-layer spherical quasi-geostrophic model, that the stability of the flow can affect the structure of the fastest growing modes. For his case 1, run with the most unstable flow, the fastest growing modes had a monopole structure and a rapid eastward propagation, which would correspond to the usual synoptic-type eddies. His case 3 run, which was less unstable, produced high-north-of-low dipole structures which were very slow moving, which would correspond to blocking episodes.

Feldstein and Held (1989) used a two-layer quasi-geostrophic model to examine the effect of meridional shear on baroclinic wave lifecycles. For weakly supercritical flow, the most influential factor in the resulting behaviour was whether the meridional flow had a strong enough shear to create an upper-layer critical latitude (where the zonal flow equals the wave's phase speed). For the case of no critical latitude, the lifecycle has symmetric baroclinic growth and decay, whereas with a critical latitude, the decay is barotropic. This latter behaviour is similar to that seen in modelled non-linear life-cycles, e.g. Simmons and Hoskins (1977).

Feldstein (1991) looked at non-linear instabilities of various eastward and west-

ward propagating jets, showing the resulting behaviour of superimposed waves to be dependent on both the jet width and its direction.

Lee (1995) showed how the background flow could deform the high-frequency transient eddies to produce localised storm tracks. However, if the background deformation field was too strong, the eddies would be irreversibly deformed, weakening the downstream stormtrack.

2.7.6.2 Effect On Larger-Scale Waves

Kaas and Branstator (1993) performed two GCM runs which were forced towards different zonal states, the first one was associated with statistically enhanced blocking activity in a control experiment, the second with reduced blocking activity, in order to investigate the control of the zonal flow on blocking occurrence. They found that the flow did affect the blocking levels, which were increased in the first run and decreased in the second run.

Ferranti *et al.* (1994) examined the effect of localised SST anomalies on blocking activity. In figure 2.13a, taken from their paper, the dotted line shows the blocking frequency with longitude from the ECMWF analyses, and the solid line shows the results from a simulation with climatological SSTs. This shows that the model under-predicts the frequency of blocking, and tends to have an eastward bias from the observed modal location. When an increased SST was used near Indonesia, this produced increased ridges over the north east sides of the major oceans, and lead to an increase in blocking activity in these regions. The solid line in figure 2.13b shows the result of this experiment, the other two lines being as in figure a. Now a much better representation of the observed blocking frequency is obtained. This was not just due to the fact that this SST increased the likelihood of satisfying the blocking criteria with its increased mean geopotential height. By calculating the average height response from the Indonesian anomaly and adding this to the climatological result, then calculating the blocking frequency based on this perturbed height field gave the solid line in figure 2.13c, which is slightly increased from climatology (dotted line), but a smaller increase than from the actual perturbed experiment. They also found that tropical anomalies had a greater effect on the extra-tropical circulation than extra-tropical SST anomalies did.

Yang and Hoskins (1996) showed that major jets act as waveguides for eastward and westward propagating waves as well as stationary waves, which can be thought of as a superposition of waves propagating in opposite directions. Eastward waves

a

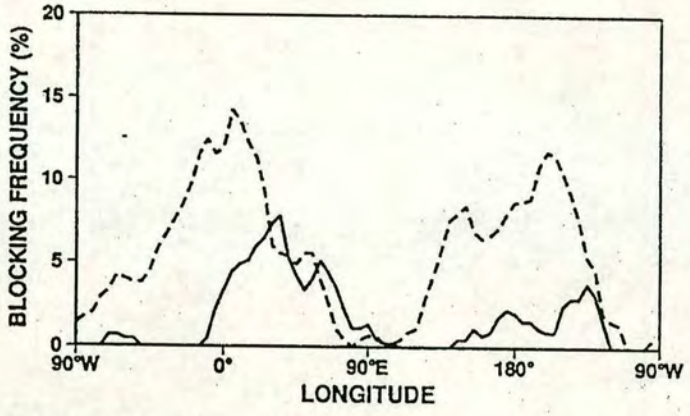

b

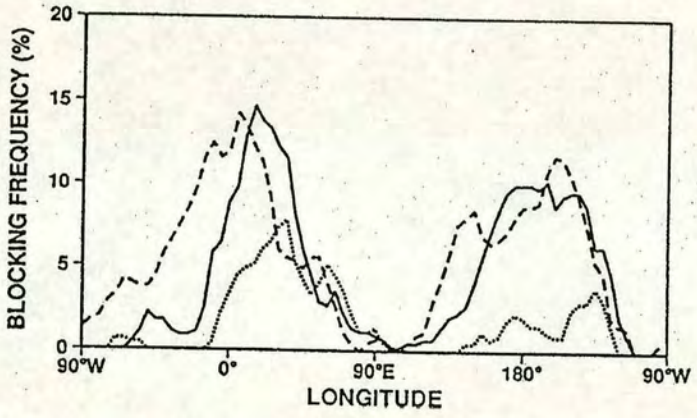

c

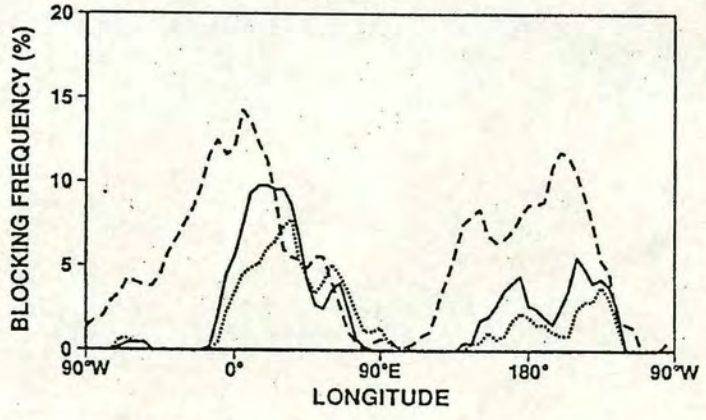

Figure 2.13: Figure a: DJF blocking frequency, dashed line from 5 winters of ECMWF analyses, solid line from ensemble with climatological SST. Figures b,c: dashed line as figure a, dotted line as figure a's solid line, solid line is blocking frequency from experiment with tropical SST in Indonesia (figure b) and from adding Indonesian time-average response in figure b to the height fields from the climatological experiment (figure a). From Ferranti *et al.* (1994).

would have a shorter wavelength and be more meridionally confined, whereas westward waves would have longer wavelengths, be less meridionally confined and have enhanced cross-equatorial propagation.

2.8 Non-linear models of blocking and low-frequency anomaly patterns

2.8.1 Rossby Waves

There have been many contributions in the literature concerned with the stability of baroclinic waves. Phillips (1954) grew unstable baroclinic waves in a two-layer model. Pedlosky (1964b) derived the classic condition for instability, namely that the gradient of the quasi-geostrophic potential vorticity must change sign at some point (Blumen (1968) extended this for non-parallel flows). He extended this work with a series of papers concerned with the finite-amplitude behaviour of unstable baroclinic waves. Pedlosky (1970) and Pedlosky (1971) showed that the amount of dissipation was important in determining the wave behaviour. For large dissipation values, the wave would approach a steady state, whereas with small dissipation values, the equilibrated state would undergo an oscillation of both the mean flow and the wave amplitude. For very small dissipation, an oscillation would persist which was independent of the initial conditions, termed a 'limit cycle'. Pedlosky (1972) showed that with small enough friction, two final asymptotic states may be reached by the wave, either a fixed amplitude stable state or a limit-cycle oscillation. Pedlosky and Frentzen (1980) investigated this dependence on the dissipation parameter further, and found that by increasing the dissipation slightly, families of oscillatory solutions with periods of even multiples of the originals were revealed. This period doubling eventually led to chaotic aperiodic solutions being formed.

Pedlosky (1981) performed an analytical study on the effect of resonant forcing by topography, showing the topography to have a stabilising effect on the waves. Pedlosky (1983) examined interactions between a wave event and a zonal flow. The lifecycle of the wave left the zonal flow with reduced potential energy, and he argued that with a weak dissipation to restore the flow back to the initial conditions, the process would repeat itself, setting up an oscillation cycle. Kalnay-Rivas and Merkine (1981), using a barotropic channel model, excited Rossby lee waves which were forced by the topography, and speculated that this would provide a simple mechanism for atmospheric blocking.

Boville (1982) extended the work of Pedlosky, but moving into a strongly, rather than a weakly, non-linear regime. Similar to the previous results, he found that a relatively narrow range of dissipation parameters would produce a vacillation phenomenon. He argued that these amplitude vacillations would be less likely to be seen in the atmosphere than structural vacillations, as they would require that wave-wave interactions would be small, which would not be the case. Plumb (1979) looked at forced waves in a baroclinic shear flow in a two-layer channel model. With the flow marginally stable and with a weak near-resonant forcing, a steady solution exists. If the forcing amplitude is sufficiently large and the forcing frequency satisfies certain conditions, then unstable vacillations are produced, with energy flowing between the wave and the mean flow. Plumb (1981) looked at a similar case but where the flow was baroclinically unstable. With no dissipation, a periodic solution as in Plumb (1979) was found, but including dissipation meant that multiple steady solutions were possible, like the multiple equilibria of Charney and DeVore (1979).

Jin and Ghil (1990) looked at the resonant response to topographical forcing of a zonal jet using weakly non-linear theory. They stated that for realistic mid-latitude flows, a dipole resonance seemed to be more important than a monopole resonance (or the type of Charney and DeVore (1979)). They discovered that the dynamical system solution, under certain parameter settings, would oscillate. By altering the parameters, a period doubling transition was also possible, leading to chaos. These oscillation were caused by either wave-wave or wave-zonal-flow interactions.

Nathan and Barcilon (1994) extended this work to include a steady, zonally varying vorticity source, which could interact with the wave perturbation field. They concluded that this interaction played an important role in the maintenance of atmospheric low-frequency oscillations.

Lorenz (1972) and Hoskins (1973) showed that all but the largest-scale Rossby waves would be unstable under atmospheric conditions.

Wu (1993) used a barotropic spherical-geometry model, and resonantly excited linearly unstable waves. He produced a cycle where a blocking-like split in one hemisphere with a zonal flow in the other hemisphere would be resonantly excited. This would then break down, and a similar pattern but in the opposite hemispheres would develop. He postulated that this could be a mechanism for generating low-frequency atmospheric variability.

Borges and Sardesmukh (1995) claimed that barotropic normal-mode instability was too weak to explain, by itself, the observed structures associated with extra-tropical low-frequency variability, which contradicts the proposal of Wu (1993).

2.8.2 Solitary Rossby Waves

It is possible to expand the linear solutions for Rossby waves to include a weak non-linearity. In the linear case, the streamlines and pv contours are concurrent, i.e. $q = F(\psi)$ for some function F. For the weakly non-linear case, we must consider deviations from this zonal state as a localised perturbation. If this deviation is weak, or the mean flow has a weak meridional shear, then the non-linear terms will appear at a higher order (Malguzzi and Malanotte-Rizzoli 1984). These non-linear terms are set to balance dissipation. By separating variables, splitting the function into separate x and y, z dependent components $X(x)\phi(y, z)$, the two components can be treated independently. The structure of $\phi(y, z)$ is shown to depend on the refractive index of the zonal background flow, which has already been discussed as affecting wave propagation characteristics (see section 2.7.4). In the case of a purely zonal flow with no shear, this reduces to be equal to the total stationary Rossby wavenumber. The structure of the refractive index with respect to y and z determines the form of the solution. As shown by Haines and Malanotte-Rizzoli (1991) in the barotropic case, if the refractive index has a central maximum/minimum, this means that the flow can support a weak splitting/intensification anomaly.

In the x direction, a long zonal wavescale is introduced in order that non-linear terms appear at the lowest order to balance dispersion. The zonal dispersion equation then gains a non-linear term, which allows a structure isolated in x to be produced. Figure 2.14 shows two such solitary wave solutions from Haines and Malanotte-Rizzoli (1991) for jets with different refractive index structures (one with a central maximum, the other having a central minimum). Although the amplitude of the anomalies for this theory by definition have to be small, it turns out that even at finite amplitude, they remain coherent structures. Haines and Malanotte-Rizzoli (1991) showed that when these solutions with larger finite amplitudes which invalidate the theory were integrated forward in time using a numerical channel model, they translated along the channel but remained of a similar coherent form as the initial conditions.

Haines *et al.* (1993) compared the theory of these solitary-wave intensifications with atmospheric data, and showed there to be some encouraging similarities, but

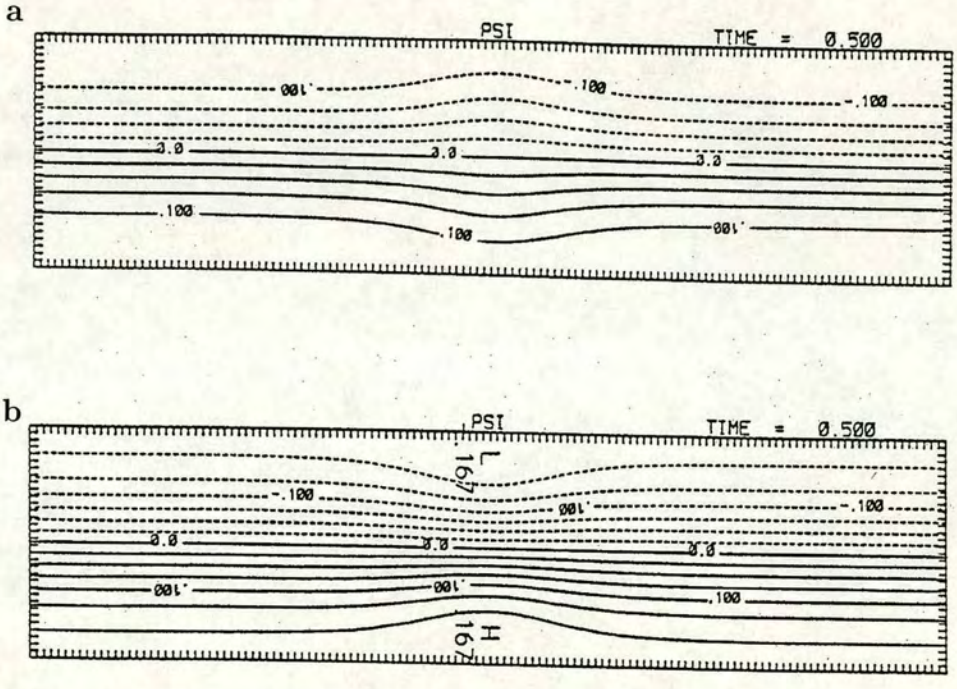

Figure 2.14: Solitary wave splitting (figure a) and intensification (figure b). From Haines and Malanotte-Rizzoli (1991).

they claimed that higher-resolution data was needed to draw any firm conclusions.

Helfrich and Pedlosky (1993), extended the stationary wave theory to allow for travelling waves, with the condition that the background state must be almost on the critical limit for instability. They show how instabilities of solitary waves can be of 2 forms; one where the solitary wave splits into 2, the other being an explosive fission instability which increases the wave amplitude beyond the limit of the weakly non-linear theory. Figure 2.15 shows a diagram from their paper showing these instability processes. Kubokawa (1989) also shows a splitting of a solitary wave similar to that of Helfrich and Pedlosky (1993) for a numerical model under oceanic conditions. They extend the work in this paper in Helfrich and Pedlosky (1995), whereby the fission instability case is integrated in a model to finite amplitude. Hickernell (1983) and Bona and Sachs (1988) were both cited by Helfrich and Pedlosky (1995) as developing a similar theory.

2.8.3 Modons

McWilliams (1980) first suggested the use of a modon as a model of blocking. Modons are analytic dipolar structures and are defined so that the quasi-geostrophic potential vorticity (q) and streamfunction possess a different functional relationship in the interior and exterior. Figure 2.16a shows a picture of an analytic modon, taken from Haines (1989). The similarity between the structure of this and that of a blocking dipole (e.g. figure 2.4) is apparent. If this is then plotted on a $q - \psi$ plot, then two lines of different gradient appear. Figure 2.16b shows the relationship between the quasi-geostrophic potential vorticity q and the streamfunction ψ for the modon, the two lines corresponding to the interior and exterior points, the different gradients revealing the different relationships.

Butchart *et al.* (1989) looked at atmospheric scatter diagrams (see Read *et al.* (1986)) of $q - \psi$ during an Atlantic blocking episode, and found similarities between the real data and that of the analytic modon, with this dual-gradient signature. Ek and Swaters (1994) have also found similar evidence in a block in the Pacific region.

Analytic modons have an existence condition which is precisely that which prevents stationary Rossby waves as free mode solutions. This is unlikely to be achieved for realistic atmospheric flow conditions.

Haines and Marshall (1987) examined eddy forcings of different barotropic flows either allowing or disallowing stationary Rossby waves as free modes. If stationary Rossby waves were not permitted, modon-like dipoles would be excited instead;

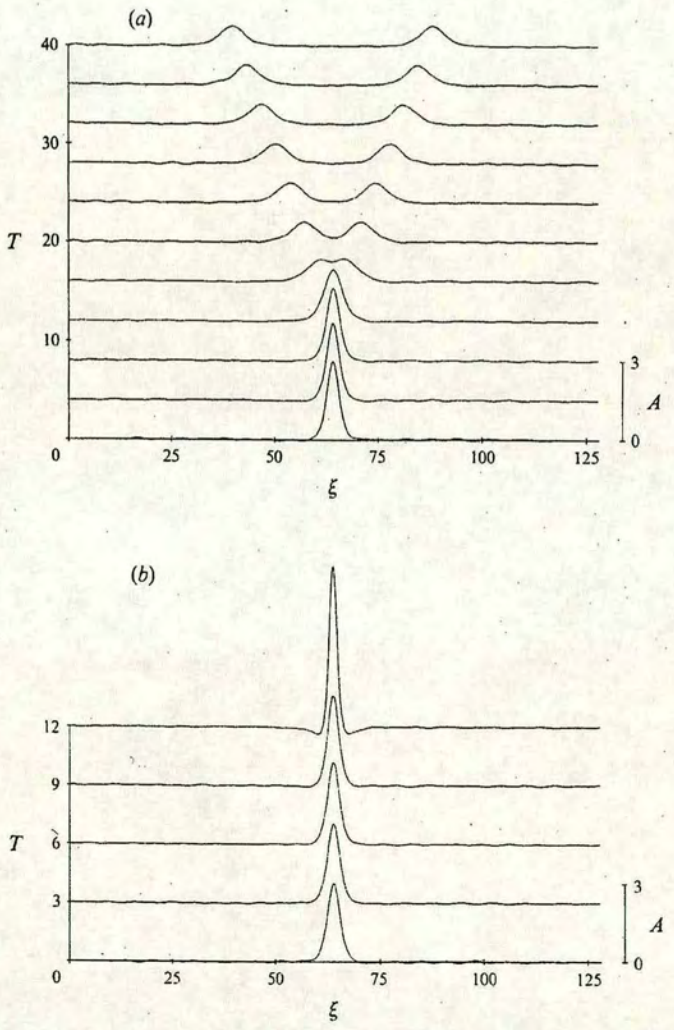

Figure 2.15: Solitary wave instabilities: splitting (figure a) and fission (figure b). From Helfrich and Pedlosky (1993).

otherwise the stationary Rossby wave would be resonantly excited, along with the possibility of an initial dipole excitation, which would propagate westwards and be dissipated, depending on the ratio between forcing and dissipation time-scales.

Haines (1989) used a 2-level quasi-geostrophic channel model and showed how it was possible to resonantly excite dipoles similar to modons using a steady dipolar forcing in westerly, vertically-sheared zonal wind conditions.

These demonstrated that providing the dissipation wasn't too strong, a coherent dipole structure could be maintained for a finite amount of time in a flow which did allow stationary Rossby waves as free modes.

Flierl and Haines (1994) developed a theory for this decay by Rossby wave radiation, showing that the decay timescale for the atmosphere may be shorter than the typical lifetime of blocks, but this would still be reasonable considering the effect of feedback from the high-frequency eddies acting to maintain the block against dissipation. Their numerical results showed that the dipoles shrink during decay but remain coherent structures, further adding to their suitability as descriptions of atmospheric blocking.

2.9 Summary

The results from these numerous studies seems to point to the fact that the background zonal jet structure plays a vital role in determining whether blocking will occur. This has come from observations, and from conditions necessary for many of the theories put forward as models to try and help to explain observed features of the atmospheric circulation in mid-latitudes.

Tibaldi *et al.* (1990) said that blocking prediction was underestimated in a medium-range forecast model, due to the inability to amplify stationary waves sufficiently (see figure 2.13a). G. J. Shutts (personal communication) has said that tuning of the gravity wave drag and orographic roughness parametrisation schemes in the Unified Model (the forecast model of the U.K. Met. Office) have lead to improvements to blocking forecasts, and that improvements to the zonal wind description have a big impact on blocking frequency. Any increase in understanding of these events, and likely conditions for their onset, would prove valuable in trying to improve weather prediction in the medium-range.

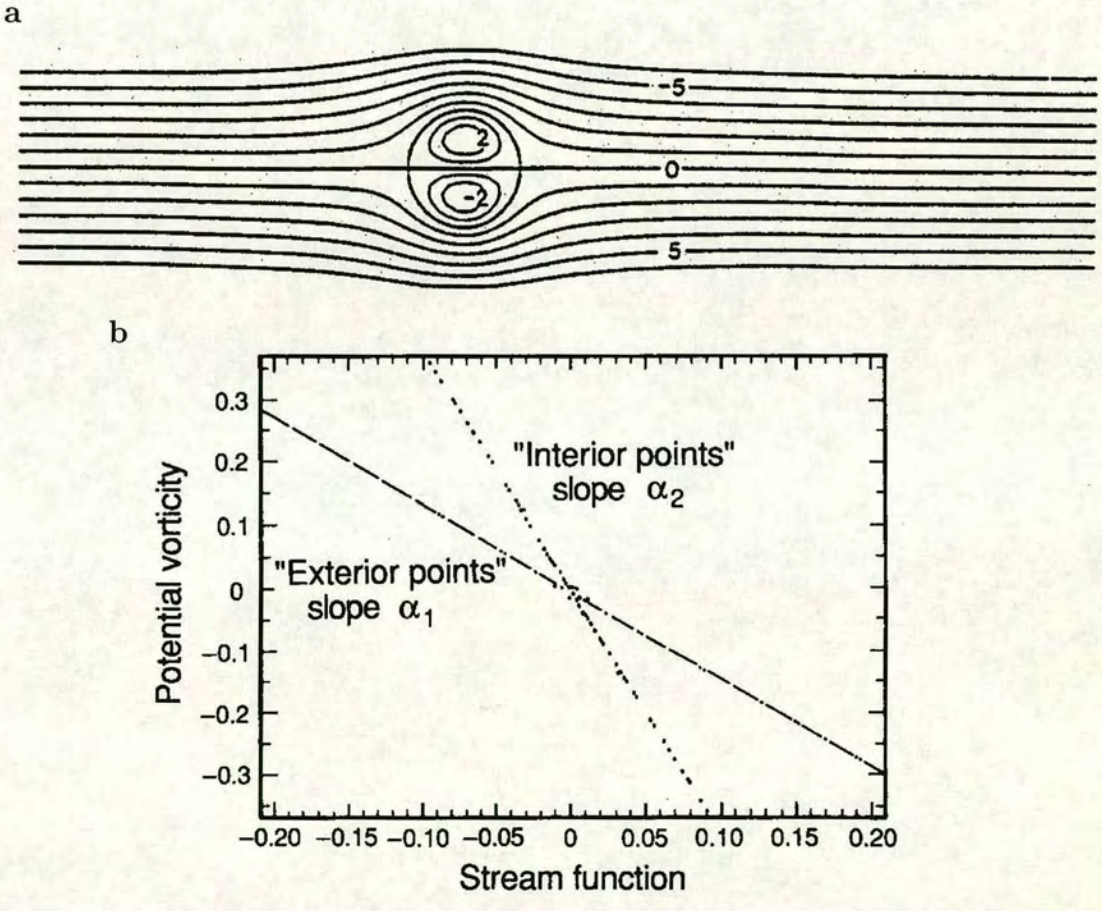

Figure 2.16: Streamfunction field (figure a) and its q-ψ relationship (figure b) of an analytic modon. From Haines (1989).

Chapter 3

The Model

3.1 Introduction

In this chapter we describe the model to be used in subsequent experiments in chapters 4 and 5. The model developed from trying to use as simple a model as possible which would capture the fundamentals of eddy growth in an initially zonal flow and allow as much control as possible over the choice of of this initial state. An equivalent-barotropic channel model, as used by Shutts (1983), is perhaps the simplest which could be used. In this work, a zonal flow in a channel was excited by eddy energy generated by a wavemaker. One limitation with such a model is that any external forcing term would appear on the right-hand side of the equations for the single layer. With a two-layer model, it is possible to have an external source of eddy energy in the lower-layer, simulating the low-level eddy generation through baroclinic instability. The wave energy can then propagate vertically into the upper-layer, which is free from an external forcing term. Vautard *et al.* (1988) and Vautard and Legras (1988) used a two-layer model such as described below, but generated the eddies by forcing a section of the flow to be baroclinically unstable. Although this approach may appear to provide a more realistic mechanism for eddy generation, a major drawback is the restriction placed on the initial flow state needing to be baroclinically unstable. Our formulation, which combines a wavemaker with a two-layer structure, allows much greater freedom in the selection of the initial conditions. The channel width and wavemaker function are the same as those used by Shutts (1983), and in much of Chapter 4, an average velocity over both layers of 7.5 ms^{-1} is used. We also include two scales of frictional damping which act to reduce the amplitude of the eddies and prevent numerical intability of the model equations. There is also a sponge layer of increased dissipation at the end of the channel designed to prevent

eddies from re-circulating.

Section 3.2 discusses the quasi-geostrophic approximation used by the model. Section 3.3 describes the equation set used by the model and section 3.4 provides a general description of the set-up. The dissipation and the wavemaker forcing details are given in sections 3.5 and 3.6 respectively. Section 3.7 gives details involving the computation used.

3.2 Quasi-Geostrophic Approximation

In the extra-tropics on the synoptic scale, the horizontal component of the velocity field can be approximated by its geostrophic value, since the Rossby Number:

$$Ro \equiv \frac{U}{f_0 L} = \frac{\text{Magnitude of Acceleration}}{\text{Magnitude of Coriolis Term}} = \frac{\frac{U^2}{L}}{f_0 U}. \tag{3.1}$$

is sufficiently small. This leads to the derivation of the quasi-geostrophic system of equations. For a derivation of the equations, the reader is referred to Chapter 6 of Holton (1992) for the isobaric co-ordinates case and Pedlosky (1986) for the derivation with height z as the vertical co-ordinate.

This gives us a time-tendency equation for the quasi-geostrophic potential vorticity q, which for adiabatic motion is:

$$\frac{Dq}{Dt} \equiv \frac{\partial q}{\partial t} + \mathbf{v}_g.\nabla q = 0, \tag{3.2}$$

where the quasi-geostrophic potential vorticity q is defined as:

$$q = \frac{1}{f_0}\nabla^2\phi + f + \frac{\partial}{\partial p}\left(\frac{f_0}{\rho_0}\frac{\partial \phi}{\partial p}\right), \tag{3.3}$$

where f is the planetary vorticity, f_0 is a constant, ρ_0 is the basic-state density, ϕ is geopotential.

Equation (3.3) is a partial differential equation with four independent variables, x, y, p and t. In order to remove p, we assume the fluid consist of two layers of uniform densities, and derive equations for the two layers separately.

See Pedlosky (1986) or Phillips (1956) for a full derivation.

3.3 Two-Layer Equations

Denoting upper layer with subscript 1, lower layer with subscript 3, and initial conditions with a superscript I, the equations of motion for the two layers are:

$$\frac{\partial q_1}{\partial t} + J(\psi_1, q_1) = -(\varepsilon + S(x))\nabla^2(\psi_1 - \psi_1^I) + \nu\nabla^4(\psi_1 - \psi_1^I), \quad (3.4)$$

$$\frac{\partial q_3}{\partial t} + J(\psi_3, q_3) = W - (\varepsilon + S(x))\nabla^2(\psi_3 - \psi_3^I) + \nu\nabla^4(\psi_3 - \psi_3^I), \quad (3.5)$$

with potential vorticity for the two layers given by:

$$q_1 = \nabla^2\psi_1 + \beta y - \lambda_1^2(\psi_1 - \psi_3), \quad (3.6)$$

$$q_3 = \nabla^2\psi_3 + \beta y + \lambda_3^2(\psi_1 - \psi_3), \quad (3.7)$$

where the Jacobian J is defined as:

$$J(\psi, q) = \frac{\partial\psi}{\partial x}\frac{\partial q}{\partial y} - \frac{\partial\psi}{\partial y}\frac{\partial q}{\partial x} \quad (3.8)$$

$$\equiv \mathbf{v}_g.\nabla q, \quad (3.9)$$

where ψ_j are the streamfunctions in the two layers, $\varepsilon, S(x), \nu$ are dissipation parameters, λ^2 is the parameter for the stretching term, equal to the reciprocal of the square of the Rossby radius of deformation $L_\lambda = 1130$km. W is the wavemaker eddy-forcing term. See later section for a fuller description of this. We have used a β plane approximation for the planetary vorticity, i.e.:

$$f = f_0 + \beta y, \quad (3.10)$$

where $f_0 = 10^{-4}\text{s}^{-1}$ and $\beta = 1.6 \times 10^{-11}\text{m}^{-1}\text{s}^{-1}$.

3.4 Model

We set up these equations for a two-layer channel with walls to the north and south boundaries, but with a re-circulation condition at the east-west ends. The channel is 6000 km wide and approximately 23000 km long, mapped by a 128×34 grid, equivalent to grid squares of approximately 200×200 km^2. Initially there is a jet stream in the upper layer and no flow in the lower layer. A 'wavemaker' is placed in the lower layer, providing a transient source of energy simulating the baroclinic eddies found in the atmospheric storm tracks. Dissipation terms relax the flow back to the initial conditions.

3.5 Dissipation

We have dissipation on two scales in the model: an Ekman friction with parameter $\varepsilon = 1.92 \times 10^{-7}$ s^{-1} and a sub-grid-scale dissipation with parameter $\nu = 4 \times$

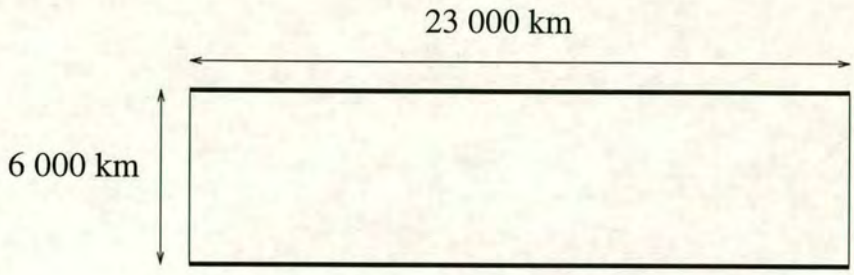

Figure 3.1: Showing scales of channel.

10^5 m^{2}s^{-1}. The $S(x)$ component of the Ekman friction term represents a sponge layer, a region of increased dissipation to prevent the eddies from recirculating around the channel. It is defined as:

$$S(x) = \begin{cases} S_{max} \sin^2\left(\frac{\pi}{2}\left(\frac{x-(1-\alpha)L_x}{\alpha L_x}\right)\right) & (1-\alpha)L_x \leq x \leq L_x, \\ 0 & \text{otherwise}, \end{cases} \tag{3.11}$$

where $S_{max} = 1.92 \times 10^{-4}$ s^{-1} and $\alpha = 0.2$. The sponge acts in the last $100\alpha\% = 20\%$ of the channel. All components of the dissipation relax the flow back to the initial conditions, rather than damping to zero flow everywhere.

3.6 Wavemaker

The W term represents a wavemaker providing a source of eddy enstrophy in the lower-layer only. It is based on the one used by Shutts (1983) and is defined as:

$$W(x,y,t) = \tilde{W}(x,y)\cos k(x-ct)), \tag{3.12}$$

$$\tilde{W}(x,y) = \begin{cases} A \sin\left(\pi\left(\frac{x-x_0}{\Delta x}\right)\right)\sin\left(\pi\left(\frac{y-y_0}{\Delta y}\right)\right) & x_0 \leq x \leq x_0+\Delta x, \\ & y_0 \leq y \leq y_0+\Delta y, \\ 0 & \text{otherwise}, \end{cases} \tag{3.13}$$

where the dimensions of the wavemaker are $\Delta x = 4200$ km , $\Delta y = 2500$ km, the wavenumber in the x direction is given by $k = \frac{3\pi}{\Delta x}$ km^{-1}, and the phase speed velocity $c = 7.5$ms^{-1}. These values were very similar to those used by Shutts (1983).

The wavemaker is defined in such a way that:

$$\int\int W dx dy \equiv 0, \tag{3.14}$$

$$\int W dt \equiv 0, \tag{3.15}$$

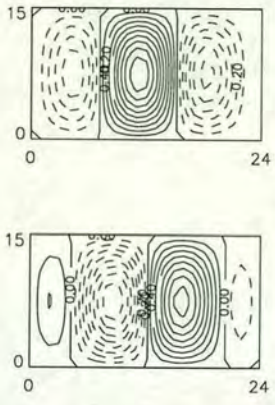

Figure 3.2: Wavemaker forcing function at two instants one-quarter phase apart.

to ensure that no net vorticity is added.

Using a wavemaker, rather than defining a baroclinically-unstable jet as in Vautard *et al.* (1988), allows a greater freedom of choice for the upper-layer jet. The zonal and meridional lengthscales of the eddies are 1400km and 2500km respectively, indicating that they are meridionally elongated, as Hoskins *et al.* (1983) showed was the case for high frequency eddies in the atmosphere.

Figure 3.2 shows a representation of the wavemaker at two times approximately one-quarter phase apart.

The eddies produced then propagate up into the upper-layer, interacting with the flow. This provides a more realistic situation than in a barotropic framework, as it is low-level wave energy caused by baroclinic instability which propagates upwards at the entrance to the storm tracks in the atmosphere. Figure 2.11 in Chapter 2, section 2.7.3, shows the EP fluxes for a growing baroclinically unstable wave at various phases during the cycle. The initial instability is at low levels. This disturbance reaches upper levels by propagation, rather than through a direct instability mechanism. Since the density of air is much less at upper-levels, the displacements caused by the eddies can be much greater and therefore more non-linear, resulting in wave-breaking. It is therefore speculated that the mechanism by which the disturbance is generated is less important in subsequent motions than the method of generation, which would justify us using a wavemaker to create eddies rather than through an instability mechanism.

Table 3.1 summarises the parameters used by the model. The β value is typical of atmopsheric mid-latitudes. The Rossby Deformation radius was chosen such that the gradient of potential vorticity in both layers remained positive for all initial flows used. This ensured that all initial flows were baroclinically and

barotropically stable. The dissipation parameters and wavemaker amplitude were eventually decided on by fine tuning through experimentation.

Parameter	Value
General	
Dimensions	23000 km × 6000 km
Grid points	128 × 34
Grid spacing	182 km
$\beta = \frac{df}{dy}$	1.6×10^{-11} m^{-1}s^{-1}
λ^2	7.844×10^{-13} m^{-2}
Rossby Deformation Radius	1130 km
Dissipation	
ε	1.92×10^{-7} s^{-1}
ν	4×10^{5} m^{2}s^{-1}
S_{max}	1.92×10^{-4} s^{-1}
α	0.2
Wavemaker	
Region Size $\Delta x \times \Delta y$	4200 km × 2500 km
Eddy Size $x \times y$	1400 km × 2500 km
Eddy Phase Velocity c	7.5 ms^{-1}
Eddy Period	2.25 days

Table 3.1: A summary of the parameters used in the model.

3.7 Computation

The model has a timestep of 3125 seconds (0.87 hours), with the data being dumped every 10 dumpsteps or 0.36 days. The scheme used to calculate the Jacobian is the scheme of Arakawa (1966), which conserves mean kinetic energy and vorticity, and prevents nonlinear computational instability. The vorticity is calculated from the streamfunction using a finite difference method.

We define the initial conditions in terms of the streamfunction and potential vorticity in each layer. The tendency from the Jacobian, wavemaker forcing and dissipation is then calculated for each layer. This is then transformed into a streamfunction tendency by rewriting the equations in terms of their barotropic and baroclinic modes, i.e.:

$$\frac{\partial}{\partial t}\left(\frac{\psi_1 + \psi_3}{2}\right) = \frac{\partial}{\partial t}\left(\nabla^{-2}\left(\frac{q_1 + q_3}{2} + \beta y\right)\right), \tag{3.16}$$

$$\frac{\partial}{\partial t}\left(\frac{\psi_1 - \psi_3}{2}\right) = \frac{\partial}{\partial t}\left((\nabla^2 - \lambda^2)^{-1}\left(\frac{q_1 - q_3}{2}\right)\right), \tag{3.17}$$

and using a numerical inverse Poisson solver. Equation 3.16 is integrated with boundary condition:

$$\frac{\partial}{\partial t}\left(\frac{\psi_1 + \psi_3}{2}\right)_{walls} = 0, \tag{3.18}$$

and equation 3.17 is integrated with boundary conditions:

$$\int \frac{\partial}{\partial t}\left(\frac{\psi_1 - \psi_3}{2}\right) = 0, \tag{3.19}$$

$$\frac{\partial}{\partial t}\left(\frac{\psi_1 - \psi_3}{2}\right)_{walls} = \text{constant}, \tag{3.20}$$

which ensure that the total channel momentum is conserved.

The streamfunction modes are then updated using a centred-difference method, so that at timestep t:

$$\frac{\psi_j(t + \Delta t) - \psi_j(t - \Delta t)}{2\Delta t} = \Delta\psi_j(t), \tag{3.21}$$

which then gives us an equation for the time integration:

$$\psi_j(t + \Delta t) = \psi_j(t - \Delta t) + 2\Delta t \Delta\psi_j(t). \tag{3.22}$$

In order to help prevent a splitting instability, every 100 timesteps or 10 dumpsteps, the fields are averaged as:

$$\psi_j^{New}(t) = \frac{\psi_j(t) + \psi_j(t-1)}{2}. \tag{3.23}$$

At the initial timestep, a forward difference is used to advance the model, since there is no previous field:

$$\psi_j(t = \Delta t) = \psi_j(t = 0) + \Delta t \Delta\psi_j(t). \tag{3.24}$$

We also assumed no flow vertically out from the top or bottom of the model, and continuity in the x direction i.e. flow in at one end must match the flow out at the other.

3.8 Discussion

Although obviously there are major differences between this channel model and the real atmosphere, the relative simplicity of such a model which exhibits similar behaviour to that seen in the real atmosphere can allow analysis that is not possible with a more complex model formulation.

EX BIBL. UNIV. EDINBURGH

Chapter 4

Transient Eddy Forcing of Large-Scale Disturbances

4.1 Introduction

In this chapter, we use the model described in chapter 3 to simulate mid-latitude atmospheric conditions in a storm track. We prescribe an upper-layer westerly flow, and examine the effects of a transient forcing, provided by the lower-layer wavemaker, on the large-scale flow patterns. Using a barotropic channel model with a wavemaker as a forcing, Shutts (1983) found that a blocking pattern could only be excited if the initial jet allowed a dipolar stationary Rossby-wave to be a steady solution of the channel. We extend this work into a model with two layers, by looking at the forced steady responses using different upper-layer jets, of which some satisfy the condition of Shutts (1983). Vautard (1990) found that certain atmospheric 2D streamfunction patterns were more likely than others to precede blocking, indicating that there could be information contained within the structure of the incoming jet to enable a better prediction of subsequent blocking activity to be made. The work of Thorncroft *et al.* (1993) showed how the jet structure could drastically alter the non-linear development of baroclinic wave lifecycles, providing further evidence of the importance of jet structure on wave behaviour. Section 4.2 describes linear Rossby wave theory, both with and without dissipation taken into account. We then perform some experiments to examine the similarities and differences between the theory and the model output. We select one of the flows (the case with upper-layer velocity 15ms^{-1}) which produces a pattern similar to that of atmospheric blocking, and examine this more fully in the remainder of the chapter. Section 4.5 looks at the momentum equations, with a view to explaining the quadrupolar forcing pattern observed from the wave-

maker. Section 4.6 examines the potential vorticity fields for both layers and their separate inversions showing associated circulation patterns. Section 4.7 looks at the time evolution of the model run and different measures of variance. Section 4.8 evaluates the potential vorticity budget, with the eddy potential enstrophy budget being examined in section 4.9. Section 4.10 shows the effects of increasing the wavemaker amplitude, exciting the anomalous component of the flow to larger amplitudes. Section 4.11 discusses the sensitivity of the model results to the parameter settings. Section 4.12 presents a summary and discussion of the chapter.

4.2 Linear Rossby Wave Theory

In this section, we look for wave-like solutions superimposed on various zonal flows in the two-layer channel, described in Chapter 3, of the form:

$$\psi'_j = A_j e^{i(kx+ly-\omega t)} \tag{4.1}$$

where k is the wavenumber in the x direction ($k = \frac{2\pi}{\lambda_x}$ where λ_x is the wavelength in the x direction), l is the wavenumber in the y direction, ω is the phase speed, A_j is the wave amplitude in layer j and $j = 1, 2$ refers to the two model layers. Note that the amplitude may be complex, which would indicate a vertical phase shift.

4.2.1 Frictionless case

We shall first examine the case without friction, for simplicity. Our channel equations, neglecting friction, are:

$$\frac{\partial q_j}{\partial t} + J(\psi_j, q_j) = 0. \tag{4.2}$$

We want to split the flow into steady background zonal $(\Psi_j(y), Q_j(y))$ and eddy $(\psi'_j(x,y,t), q'_j(x,y,t))$ components and linearise about the background flow. Equation 4.2 becomes:

$$\frac{\partial q'_j}{\partial t} + \frac{\partial \psi'_j}{\partial x}\frac{\mathrm{d}Q_j}{\mathrm{d}y} - \frac{\mathrm{d}\Psi_j}{\mathrm{d}y}\frac{\partial q'_j}{\partial x} = 0. \tag{4.3}$$

If we then substitute in equation 4.3 for the eddy components from equation 4.1, and replace the background flow by:

$$\Psi_1 = -U_1 y, \tag{4.4}$$

$$\Psi_2 = -U_2 y, \tag{4.5}$$

$$Q_1 = \beta y + \lambda^2(U_1 - U_2)y, \tag{4.6}$$

$$Q_2 = \beta y - \lambda^2(U_1 - U_2)y, \tag{4.7}$$

we get:

$$\begin{aligned} i\omega(-(k^2+l^2+\lambda^2)A_1 + \lambda^2 A_2) + ikA_1(\beta + \lambda^2(U_1 - U_2)) & \\ +U_1 ik(-(k^2+l^2+\lambda^2)A_1 + \lambda^2 A_2) &= 0, \end{aligned} \tag{4.8}$$

$$\begin{aligned} i\omega(-(k^2+l^2+\lambda^2)A_2 + \lambda^2 A_1) + ikA_2(\beta - \lambda^2(U_1 - U_2)) & \\ +U_2 ik(-(k^2+l^2+\lambda^2)A_2 + \lambda^2 A_1) &= 0. \end{aligned} \tag{4.9}$$

We now search for stationary solutions, setting $\omega = 0$. This is likely to be the form of a resonant response to local stationary forcing. For example, Hoskins and Ambrizzi (1993) demonstrated this with a spherical barotropic model, exciting Rossby wave patterns along waveguides using a localised forcing. Even though the forcing in our model is transient, the location of the wavemaker remains fixed. In our model, we shall also set the lower-layer flow U_2 to be zero. As we are attempting to model a jet stream in the atmosphere using two discrete layers, and the flow in the lower layer should be much weaker than in the upper layer. In reality, the flow will only be zero at the ground, but using this approximation means that the lower-layer background flow will not advect potential vorticity away from the wavemaker region.

Using these two approximations, the equation for the lower layer, equation 4.9, becomes:

$$ikA_2(\beta - \lambda^2 U_1) = ikA_2 \frac{\mathrm{d}Q_2}{\mathrm{d}y} = 0. \tag{4.10}$$

Providing that k and $\frac{\mathrm{d}Q_2}{\mathrm{d}y}$ are not zero, this means that the lower-layer must have a zero perturbation, $A_2 = 0$. This is due to the singularity condition of setting the phase speed and lower-layer velocity to be zero. Assuming this, equation 4.8 becomes:

$$ikA_1((\beta + \lambda^2 U_1) + U_1(-(k^2+l^2+\lambda^2))) = 0. \tag{4.11}$$

Cancelling terms gives:

$$ikA_1(\beta - U_1(k^2+l^2)) = 0. \tag{4.12}$$

For non-trivial solutions ($A_1 \neq 0$) with non-zero k, we get

$$K^2 \equiv k^2 + l^2 = \frac{\beta}{U_1}. \tag{4.13}$$

where K^2 is the total wavenumber. This is equivalent to the stationary Rossby wave equation for a barotropic atmosphere. Since β is real and positive, this states that we must have westerly flow (i.e. $U_1 > 0$) for Rossby wave solutions. If we are looking for a wave which is dipolar in the meridional direction, as in a blocking-type case, then we should set:

$$l = \frac{2\pi}{L_y} = \frac{2\pi}{6 \times 10^6} \text{ m}^{-1}, \tag{4.14}$$

where L_y is the channel width. There will be a maximum value for U_1, beyond which no stationary dipolar waves will be permissible solutions of the channel. This will occur when k has its minimum value, i.e. $k = 0$. This gives a maximum value for U_1 as:

$$U_1^{MAX} = \frac{\beta}{l^2} = 14.59 \text{ ms}^{-1}. \tag{4.15}$$

For U_1 values greater than this, k^2 will be negative, allowing imaginary solutions for k. These correspond to exponentially decaying solutions rather than wave-like ones. If, however, k was imaginary, this would give a solution which was exponential rather than wave-like in the x direction. This could be a valid solution in the presence of a wall or a source region to stand up against. If we force the lower layer, the wavemaker region can act as a source to permit these types of solution.

There will also be a constraint on the maximum size of U_1 regarding the stability of the jet. In order for the jet to remain stable, the potential vorticity gradients must not change sign anywhere in the channel (Pedlosky (1964a)). This would happen if:

$$\frac{\mathrm{d}Q_2}{\mathrm{d}y} = \beta - \lambda^2 U_1 < 0. \tag{4.16}$$

So, for the jet to remain stable, we have the condition that:

$$U_1 < \frac{\beta}{\lambda^2} = 20.40 \text{ ms}^{-1}. \tag{4.17}$$

With this analysis, the combination of neglecting dissipation and setting the lower-layer velocity to equal zero requires there to be no wave anomaly present in the lower layer. This is because we create a singular point for the equation set, with the phase speed and velocity both being zero. This tells us no information about what possible vertical structure of the wave is likely to be observed. We must consider the equations with the added complication of friction in order to gain any information regarding vertical structure.

4.2.2 Friction included

The following analysis is similar to that found in Pedlosky (1986), with the inclusion of two friction types (note that Pedlosky (1986) only inclued one type of friction, and ignored planetary vorticity). The linearised model equations with dissipation included are given by:

$$\frac{\partial q_j'}{\partial t} + \frac{\partial \psi_j'}{\partial x}\frac{\mathrm{d}Q_j}{\mathrm{d}y} - \frac{\mathrm{d}\Psi_j}{\mathrm{d}y}\frac{\partial q_j'}{\partial x} = -\varepsilon\nabla^2\psi_j' + \nu\nabla^4\psi_j', \tag{4.18}$$

for $j = 1, 2$. This means we are relaxing the flow back to zero ψ_j', q_j'. If we substitute in as before, we get two equations:

$$A_1((K^2+\lambda^2)(c-U_1) + (\beta + \lambda^2 U_1) + \frac{i}{k}(\varepsilon K^2 + \nu K^4)) - A_2\lambda^2(c-U_1) = 0, \tag{4.19}$$

$$A_1(-c\lambda^2) - A_2((K^2+\lambda^2)c + (\beta - \lambda^2 U_1) + \frac{i}{k}(\varepsilon K^2 + \nu K^4)) = 0, \tag{4.20}$$

where $c = \frac{\omega}{k}$ is the phase speed in the x direction. The condition that the determinant must be zero for there to be non-trivial solutions gives us an equation for the phase speed of the wave c , namely equation 4.21:

$$c = \frac{\omega}{k} = \frac{U_1}{2} - \frac{\beta(K^2+\lambda^2)}{K^2(K^2+2\lambda^2)} - \frac{i(\varepsilon K^2 + \nu K^4)(K^2+\lambda^2)}{kK^2(K^2+2\lambda^2)}$$
$$\pm\frac{i(\frac{4}{k^2}\lambda^4(\varepsilon K^2+\nu K^4)^2 + U_1^2K^4(4\lambda^4 - K^4) - 4\beta^2\lambda^4 - i\frac{8\beta\lambda^4}{k}(\varepsilon K^2+\nu K^4))^{\frac{1}{2}}}{2K^2(K^2+2\lambda^2)} \tag{4.21}$$

Once c has been calculated, we substitute back into either equation 4.19 or 4.20. This then gives us the ratio of the wave amplitudes between the two layers as a complex number. If it is entirely real and positive, the wave would be equivalent barotropic. If it is real and negative, the wave would be in vertical anti-phase. If the ratio $\frac{A_1}{A_2}$, denoted as $A_r + iA_i$, has an imaginary component, then there will be a phase tilt between the two layers. The amplitude and phase relationships between the layers are given by equations 4.22 and 4.23.

$$\text{Amplitude A} = (A_r^2 + A_i^2)^{\frac{1}{2}}, \tag{4.22}$$

$$\text{Phase Angle } \phi = \tan^{-1}\left(\frac{A_i}{A_r}\right). \tag{4.23}$$

The inverse tangent function is assumed to be in the range $0 < \phi < \pi$. From the phase angle, and whether A_r is positive or negative, we can calculate a value for the actual phase between 0 and 2 π, calculated by:

$$\text{Phase} = \begin{cases} \phi & \text{if } A_r > 0, \\ \phi + \pi & \text{otherwise.} \end{cases} \tag{4.24}$$

A phase of 0 (or 2 π) would indicating an equivalent barotropic mode, whereas a phase of $\frac{\pi}{2}$ would mean the upper layer leads the lower layer (in the positive x direction) by a quarter-cycle. Phase π would mean the wave was in vertical anti-phase. We have assumed k to be real, which gives a sinusoidal solution in the x direction.

To look for evanescent solutions with friction, we instead set the wave solution to be time-independent, i.e. $\omega = 0$. If we re-write $k = -ia$, where a is real, equation 4.1 gives us solutions of the form:

$$\psi_j' = A_j e^{i(-iax+ly)} = A_j e^{ax} e^{ily}. \tag{4.25}$$

Where a is positive/negative, this indicates a solution decaying exponentially upstream/downstream. Substituting into equation 4.18, we get:

$$A_1(-(K^2+\lambda^2)U_1 + (\beta + \lambda^2 U_1) - \frac{1}{a}(\varepsilon K^2 + \nu K^4)) + A_2\lambda^2 U_1 = 0, \tag{4.26}$$

$$-A_2((\beta - \lambda^2 U_1) - \frac{1}{a}(\varepsilon K^2 + \nu K^4)) = 0, \tag{4.27}$$

where $K^2 = -a^2 + l^2$. In the frictionless case, equation 4.27 gave the condition that $A_2 = 0$ since the lower-layer potential vorticity gradient was non-zero. The addition of friction permits us a solution with a non-zero A_2. To satisfy equation 4.27, we can either have $A_2 = 0$, in which case equation 4.26 can be solved to give a value for a, or $((\beta - \lambda^2 U_1) - \frac{1}{a}(\varepsilon K^2 + \nu K^4)) = 0$, which can then be solved to give a value for a, and in which case equation 4.26 reduces to:

$$A_1(-K^2 U_1 + \lambda^2 U_1) + A_2\lambda^2 U_1 = 0, \tag{4.28}$$

which can be re-written as:

$$\frac{A_2}{A_1} = \frac{K^2}{\lambda^2} - 1. \tag{4.29}$$

4.3 Solutions for specific jets

We shall examine the possible solutions for specific jets. We shall take five different examples, $U_1 = 5, 10, 12.5, 15, 20$ ms^{-1}, and then use these five examples with a model run, to compare the theory with the data.

Table 4.1 gives a summary of results for the five different jets using the previous equations. Note that these are all for a dipolar meridional wave, i.e. substituting from equation 4.14 for the value of l. The values for the dissipation are those used for model runs (see table 3.1).

Wave-like Solutions							
	No Friction $A_2 = 0$		Friction $A_2 \neq 0$				
U_1 (ms^{-1})	k (m^{-1})	c_g (ms^{-1})	k (m^{-1})	c_i (ms^{-1})	A_2/A_1	**Phase**	c_g
5	$\pm 1.45 \times 10^{-6}$	6.57	1.45×10^{-6}	-0.77	0.050	-0.25π	+ve
10	$\pm 7.09 \times 10^{-7}$	6.28	7.09×10^{-7}	-0.60	0.057	-0.26π	+ve
12.5	$\pm 4.28 \times 10^{-7}$	3.57	4.22×10^{-7}	-0.64	0.050	-0.27π	+ve
15	–	–	–	–	–	–	–
20	–	–	–	–	–	–	–

Evanescent Solutions				
	No Friction $A_2 = 0$	Friction		
		$A_2 \neq 0$		$A_2 = 0$
U_1 (ms^{-1})	$a = -\frac{k}{i}$ (m^{-1})	$a = -\frac{k}{i}$ (m^{-1})	A_2/A_1	$a = -\frac{k}{i}$ (m^{-1})
5	-	0.57×10^{-7}	0.39	0.65×10^{-7}
10	-	0.84×10^{-7}	0.39	1.30×10^{-7}
12.5	-	1.10×10^{-7}	0.38	2.21×10^{-7}
15	$\pm 1.73 \times 10^{-7}$	1.57×10^{-7}	0.37	3.64×10^{-7}
20	$\pm 5.45 \times 10^{-7}$	7.36×10^{-7}	-0.29	5.74×10^{-7}
				-1.20×10^{-7}
				-5.02×10^{-7}

Table 4.1: Values obtained for meridionally dipolar stationary waves and exponentially decaying solutions for 5 different initial upper-layer zonal flows.

4.3.1 Wave-like Solutions

The upper table is for wave-like solutions, calculated both with and without friction. As we can clearly see, the addition of friction has virtually no effect on determining the stationary zonal wavenumber for a particular upper-layer jet. We can see that as U_1 increases, k decreases, and so the zonal wavelength increases, until it becomes impossible to have a dipolar stationary wave as a solution (indicated by the dashed lines). For the frictionless case, it is implied that $c_i = 0$, $A_2/A_1 = 0$ (and so Phase has no meaning), whereas we obtain different values when friction is included. These show that c_i is always negative, implying a decaying wave. This is due to the presence of dissipation. If there was no dissipation, any stable waves would be neutral, i.e. neither growing or decaying. With friction present, a neutral wave must be extracting energy from the background flow in order to survive against the dissipation. Unstable waves must be converting energy at a faster rate than the friction is removing it. Any wave extracting less energy than the neutral wave will have a negative c_i value, such is the case with our waves. The table also shows that the upper-layer wave-amplitude is approximately 20 times that of the lower-layer, and that the wave is a quarter wavelength out of phase. As we approach the limit of no friction, the ratio of lower to upper-layer amplitude approaches zero.

4.3.1.1 Group Velocity c_g

The group velocity, c_g, is defined as:

$$\text{Group Velocity } c_g = \frac{\partial \omega}{\partial k} = \frac{\partial (c_r k)}{\partial k}. \tag{4.30}$$

For the frictionless case, the group velocity can be calculated directly, since:

$$\omega = ck = Uk - \frac{\beta k}{k^2 + l^2}. \tag{4.31}$$

Differentiate with respect to k, and get:

$$\text{Group Velocity } c_g = \frac{\partial \omega}{\partial k} = U - \frac{\beta(k^2 - l^2)}{(k^2 + l^2)^2}. \tag{4.32}$$

The table shows that for the frictionless case, the group velocity is positive i.e. downstream, and decreases in magnitude as the upper-layer flow increases. For the case with friction, the group velocity can also be shown to be positive for the three wave-like cases, decreasing in magnitude as U_1 increases. This is done by plotting ω against k for particular values of U_1.

4.3.2 Evanescent Solutions

The lower table gives the solution values for evanescent solutions, ones where the wavenumber is imaginary. For the case with no friction, exponential solutions are permitted only when the upper-layer velocity is larger enough to prevent wave-like solutions. The inclusion of friction allows both wave and exponential solutions to occur simultaneously. For all jets except 20ms^{-1}, there are two solutions, both upstream. One solution has zero amplitude in the lower layer, the other has ratio of approximately 2:5 between the lower- and upper-layer amplitudes. The value of a increases as U_1 is increased, indicating a shorter decay lengthscale. The case with $U_1 = 20\text{ms}^{-1}$ is little different. The solution with non-zero A_2 is now baroclinic, i.e. the ratio between the layers is negative. Also, there are now 3 solutions with $A_2 = 0$, the two extra solutions being downstream and decaying.

4.4 Modelling Experiments

In this section, we shall use the model described in Chapter 3 to perform numerical experiments with the values of the jet shown in table 4.1. The initial conditions are a zonal jet with velocity U_1 in the upper layer, and zero velocity in the lower layer. We run the model for 360 days (1000 dumpsteps).

Since, as discussed previously in section 2.7.3, the method of low-level wave activity generation is less important than the non-linear upper-level wave-breaking phase, in our experiments we shall replace the generation of low-level wave activity through baroclinic instability with a wavemaker in the lower layer (as described in Chapter 3). This gives us the freedom to choose a jet structure which is not baroclinically unstable, allowing a wider variety of initial condition. Note that none of the jets which could allow stationary Rossby waves are baroclinically unstable. The wavemaker can also act as a kind of localised forcing, as the waves are generated in a certain confined region, rather than the whole channel.

In the real atmosphere, during the development of cyclone waves, diabatic effects, absent from our model, will be evident from the conversion of water from liquid to vapour form and back again. Of course, this requires a liquid water source, the oceans, which are spatially fixed and so can provide a localisation for the storm track regions. Also the land-sea surface thermal contrasts must play a role in the positioning of the storm tracks, fixing the positions of maximum available potential energy for the instability to feed off.

For these model runs, the wavemaker had an amplitude $A = 1.2 \times 10^{-9}\text{s}^{-2}$. This

was linearly increased from zero over the first 18 days, after which it remained constant.

The other parameters are as described in Chapter 3.

4.4.1 $U_1 = 5$ ms^{-1}

Figure 4.1 shows the time-mean streamfunction for the upper and lower layers for the case with $U_1 = 5$ ms^{-1}, taken over the last 220 days. The contour intervals for the streamlines are indicated beneath each plot. In the upper layer, the anomaly from the initial condition has been superimposed (contour interval is a factor of 10 smaller than for the main contour lines). In this and subsequent diagrams, the dashed contours indicate negative values. The position of the wavemaker in the lower layer is indicated by the rectangular box. We shall take the x direction as zonally eastwards, and the y direction as meridionally northward.

Downstream from the wavemaker region, a dipolar standing wave is generated, evident in the upper layer only. The theory gave a value for the zonal wavenumber as $k = 1.45 \times 10^{-6}$m^{-1}. This gives a value for the zonal wavelength λ_x as:

$$\lambda_x = \frac{2\pi}{k} = 4330 \text{ km} = 24 \text{ gridpoints.} \tag{4.33}$$

This agrees with the spacing of the centres of the two largest-amplitude anomalies in the upper layer. The fact that the group velocity from theoretical calculations is in the downstream direction is also consistent with the wave location, downstream of the region of forcing. Theory also suggests that the upper-layer wave amplitude should be greater than the lower layer amplitude (for the frictionless case, the lower-layer wave had zero amplitude; with friction included, the upper-layer stream function amplitude was approximately 20 times larger). This also agrees with the model run. Note that there is no disturbance in the region $x > 100$ grid points. This is due to the sponge region with increased dissipation located at the end of the channel to prevent the eddies generated by the wavemaker from re-circulating.

In the lower layer, the main feature is the quadrupolar disturbance over the wavemaker region. An explanation for this structure will be given in a later section (section 4.5). Over the wavemaker region, the validity of the linear theory is questionable, due to the large anomalies and presence of strong forcing. The right-hand dipole is seen to have a NW-SE tilt in the north of the channel, and a NE-SW tilt in the south. This tilting is reminiscent of the radiation field for stationary barotropic Rossby waves from a local dipolar source (e.g. see figure

13 from Haines (1989)), which are prevented from extending further meridionally by the walls. It can be seen that there is a westward vertical phase tilt with height in this region. This implies that the wave is extracting available potential energy from the background flow, in addition to that provided from the wavemaker forcing. These would be balanced with the dissipation provided by the friction. Upstream of the wavemaker, a decaying baroclinic dipolar solution is observed. This upstream propagation fits with the picture of exponentially-decaying Rossby wave free modes from a quadrupolar source. Although neither of the two solutions given in table 4.1 are of this form, a superposition of the two solutions with appropriate amplitudes can produce a baroclinic anomaly of the type observed. See section 4.4.3 for an example of such a calculation.

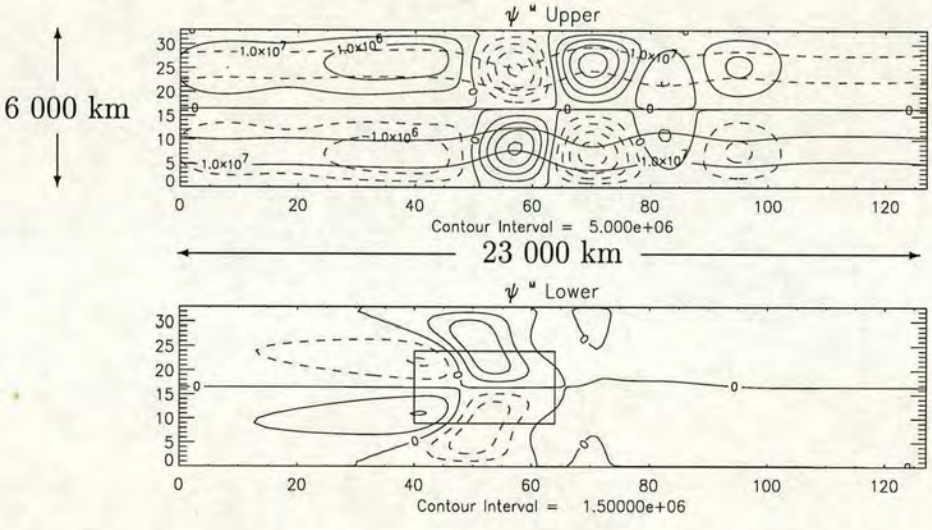

Figure 4.1: Time-mean streamfunction (units m^2s^{-1}) for the two layers for the run with upper-layer velocity 5 ms^{-1} and wavemaker amplitude $A = 1.2 \times 10^{-9}s^{-2}$. The position of the wavemaker in the lower layer is outlined. The contour values are shown beneath the plots (the upper-layer anomaly contours are $5 \times 10^5 m^2s^{-1}$). Scale arrows are included.

4.4.2 $U_1 = 10$ ms^{-1}

We now double the upper-layer velocity to $U_1 = 10$ ms^{-1} and run the model again, keeping everything else the same. Figure 4.2 shows the corresponding time-mean streamfunction fields for both layers from this run. The main contours are the same as in figure 4.1, but the contours for the anomaly are twice as large ($1 \times 10^6 m^2s^{-1}$). Immediately, we can see that in the upper-layer, there is a stationary wave excited which has a larger zonal wavelength than in the previous

case. The theory predicts a value for the zonal wavenumber of $k = 7.09 \times 10^{-7}\mathrm{m}^{-1}$ (see table 4.1). This gives a value for the zonal wavelength λ_x of:

$$\lambda_x = \frac{2\pi}{k} = 8860 \text{ km} = 49 \text{ gridpoints.} \tag{4.34}$$

The distance between the centres of the two positive anomalies in the northern half of the upper layer gives a similar result (9300 km, 51 gridpoints). Note that the amplitude of the anomaly in the upper layer is over three times larger than in figure 4.1 for the $U_1 = 5$ ms^{-1} case. Now, the first region of splitting encountered as we move downstream in the upper layer occurs at x=45, further downstream than in the previous case. In the lower layer, we again have the quadrupole structure over the wavemaker region, but there are differences from the previous case. The left-hand dipole pair now has its maxima further from the centre of the channel than in figure 4.1, and the right-hand pair has less of a meridional tilting than before and has increased in amplitude from the previous case. Again, upstream of the wavemaker, the anomaly is baroclinic. The superposition of the two exponential waves found by the unforced theory, as discussed in section 4.4.1, provide a means of explaining this observed pattern. See section 4.4.3 for an example.

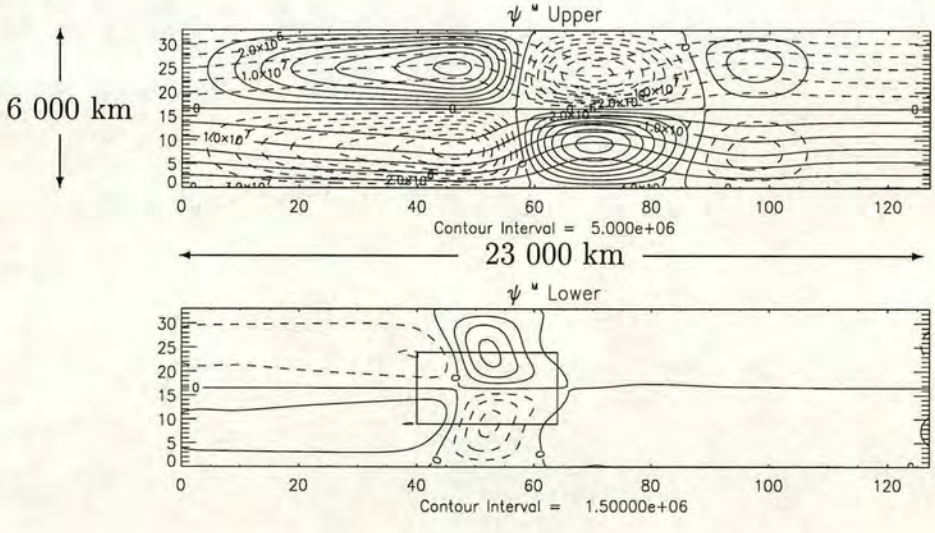

Figure 4.2: As figure 4.1 except for the run with upper-layer velocity 10 ms^{-1}. The upper-layer anomaly contours are $1 \times 10^6 \mathrm{m}^2\mathrm{s}^{-1}$.

4.4.3 $U_1 = 12.5$ ms^{-1}

Figure 4.3 shows the time-mean streamfunction for the case with $U_1 = 12.5$ ms^{-1}. The main contour intervals are again unchanged, but the upper-layer anomaly

streamlines are at 2.5×10^6 m^{2}s^{-1} intervals. In the upper layer, the wave-splitting region has again moved further downstream, producing a quadrupolar anomaly, the dominant component being a split at x=50, with a weaker intensification region further downstream. The value for the zonal wavenumber is given in table 4.1 as $k = 4.28 \times 10^{-7}$m^{-1}, giving a zonal wavelength of:

$$\lambda_x = \frac{2\pi}{k} = 14700 \text{ km} = 81 \text{ gridpoints.} \tag{4.35}$$

A rough approximation to this from the model run may be obtained by doubling the distance between the maxima and minima (this is the only reasonable estimate available). This gives a value of $\lambda_x = 12700$ km $= 70$ gridpoints which underestimates the theoretical result, but we must consider that the sponge layer will be affecting this result by terminating the wave prematurely. The upper-layer anomaly is again larger than with the weaker jets, and is starting to resemble a more blocking-like dipolar structure, with the upper- and lower-layer splitting dipoles approaching an equivalent-barotropic structure. We have a quadrupolar anomaly in the lower layer again. There is little evidence of meridional bowing or tilting, probably due to changes in Rossby-wave propagation characteristics, and now the right-hand dipole pair is of larger amplitude than the left-hand pairing. This resembles the experiment performed by Haines (1994) in a barotropic channel model, which was similar to the work of Shutts (1983), in which a jet split was caused through excitation by a wavemaker.

We now show how the linear solutions including friction, shown in table 4.1, can match up with the decaying model solutions in the region upstream from the forcing. For this case, table 4.1 shows we have two upstream exponential solutions, one equivalent barotropic and one with $A_2 = 0$. The lower-layer wave must therefore come wholly from the equivalent barotropic wave. Along a line of constant y, the wave solutions are of the form:

$$\psi_j(x) = \Psi_j e^{ax}, \tag{4.36}$$

where i indicates the layer (1 or 2 for upper and lower). If we take the streamfunction value at positions x_A and x_B in one layer and divide, we have the equation:

$$\frac{\psi(x_A)}{\psi(x_B)} = e^{a(x_A - x_B)}, \tag{4.37}$$

which, when rearranged, gives us a value for the decay parameter of:

$$a = \frac{1}{(x_A - x_B)} \ln\left(\frac{\psi(x_A)}{\psi(x_B)}\right). \tag{4.38}$$

We first of all consider the lower layer, since only one of the possible wave solutions has any contribution there. Using the stream function grid point values at (10,25) and (35,25) and substituting in equation 4.38 gives us:

$$a = \frac{1}{(10-35)\frac{6\times10^6}{33}} \ln\left(\frac{-1.76\times10^6}{-2.25\times10^6}\right) = 5.3\times10^{-8}\mathrm{m}^{-1}. \qquad (4.39)$$

Table 4.1, for the $A_2 \neq 0$ wave, has an a value of $1.10\times10^{-7}\mathrm{m}^{-1}$. These values disagree by a factor of two, although it is likely that the presence of the sponge layer may be having an effect. However, if we assume that this smaller value is correct, and proceed to get a value of Ψ_2 for the lower layer by substituting back for either of the streamfunction values into equation 4.36, we get a value of:

$$\Psi_2 = \frac{-1.76\times10^6}{e^{5.3\times10^{-8}(10\times\frac{6\times10^6}{33})}} = \frac{-2.25\times10^6}{e^{5.3\times10^{-8}(25\times\frac{6\times10^6}{33})}} = -1.60\times10^6\mathrm{m}^2\mathrm{s}^{-1}. \qquad (4.40)$$

To get the corresponding upper-layer Ψ_1 value, we divide Ψ_2 by the A_2/A_1 ratio from table 4.1, in this case 0.38:

$$\Psi_1 = \frac{\Psi_2}{\left(\frac{A_2}{A_1}\right)} = \frac{-1.60\times10^6}{0.38} = -4.21\times10^6\mathrm{m}^2\mathrm{s}^{-1}. \qquad (4.41)$$

We now have the necessary information to construct the $A_2 \neq 0$ wave. If we subtract this wave from the time-mean values of upper-layer streamfunction at our two chosen points, the residual values should match with the other wave from linear theory, which has $A_2 = 0$. We can then calculate an a value for the upper-layer wave in a similar way. When we do this, we get an a value or the second wave of $2\times10^{-7}\mathrm{m}^{-1}$, which agrees well with the linear theory value of $2.21\times10^{-7}\mathrm{m}^{-1}$, and a corresponding Ψ_1 value o .

4.4.4 $U_1 = 15$ ms^{-1}

We now increase the upper-layer velocity to $U_1 = 15$ ms^{-1}, the time-mean streamfunction is shown in figure 4.4. All the contour intervals are the same as the previous figure 4.3. From table 4.1, we see that there are now no stationary dipolar Rossby-wave solutions for this value of the upper-layer velocity (it is very close to the limit for the frictionless case). This is reflected in figure 4.4 by the fact that there is a single equivalent-barotropic dipolar split anomaly located at $x = 53$ (again further downstream than previous cases), with again an increase in magnitude over previous jets. The structure of this response to eddy forcing, with an equivalent-barotropic splitting, is very similar to a blocking dipole (see Rex (1950a)).

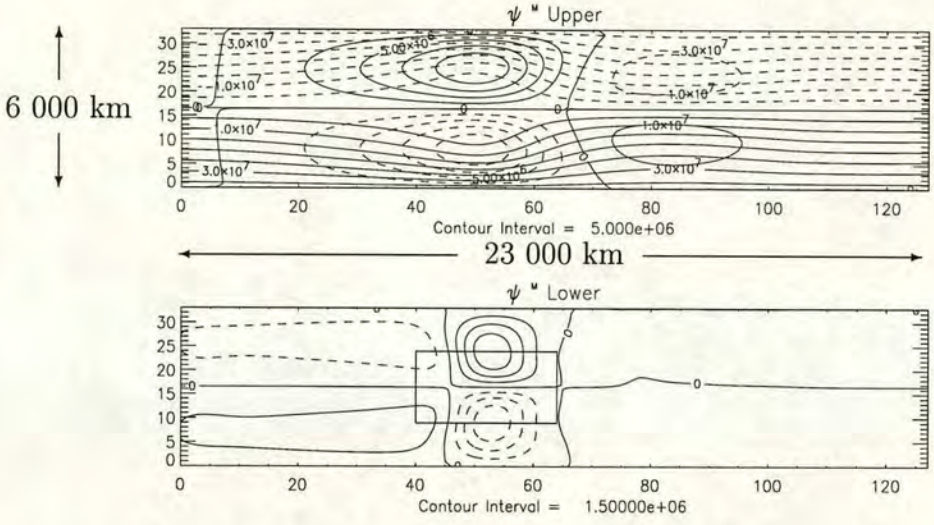

Figure 4.3: As figure 4.1 except for the run with upper-layer velocity 12.5 ms^{-1}. The upper-layer anomaly contours are $2.5 \times 10^6 \mathrm{m}^2\mathrm{s}^{-1}$.

There are also similarities between this and a splitting solitary Rossby wave at finite amplitude (see Haines and Malanotte-Rizzoli (1991)). Because of its similarity to atmospheric blocking, we shall examine this model run further in later sections.

The lack of vertical phase tilt for this value of U_1 indicates that the wave cannot be gaining energy through the conversion of available potential energy from the background flow. It must be gaining the energy required to maintain itself against dissipation effects solely from energy of the high-frequency wavemaker eddies. Again, there is another weaker dipolar anomaly in the lower layer, stretching upstream to the sponge region.

For this value of U_1, we obtain the largest amplitude of anomaly. Although the linear equations give us no information concerning the magnitude of anomaly expected (since we have not specified any forcing), only on possible ratios between the two layers, we can only speculate on the reason for this increase of stream-function anomaly with U_1. One reason will concern the stationary Rossby-wave solutions available. As U_1 is increased, these dipolar waves have a larger k value (shorter zonal wavelength) and have decreasing group velocity. Since we have a large ∇^4 frictional term, which is strongest for smaller wavelengths, this will have a smaller contribution for the waves with larger wavelengths. Also, since the group velocity, and hence energy propagation speed, is reduced as U_1 increases, the transport energy away from the wavemaker region becomes slower, and so there is the potential for an energy build-up in the region of the wavemaker, leading to

larger wave amplitudes there.

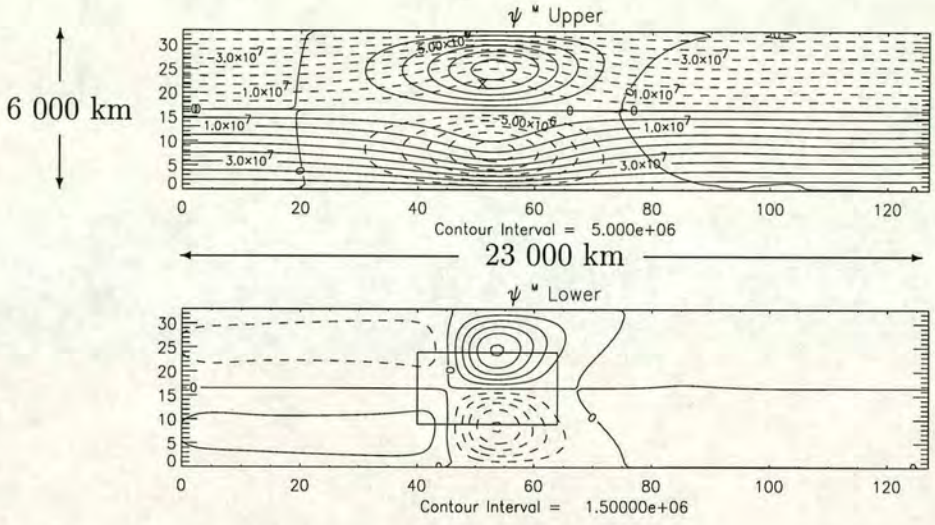

Figure 4.4: As figure 4.1 except for the run with upper-layer velocity 15 ms^{-1}. The upper-layer anomaly contours are $2.5 \times 10^6 m^2 s^{-1}$.

4.4.5 $U_1 = 20$ ms^{-1}

Finally, we look at the run with upper-layer velocity $U_1 = 20$ ms^{-1}, with the time-mean streamfunction shown in figure 4.5. Again, the contour intervals are as before except for the upper-layer anomaly, which are now double those in the previous figure 4.4 at $5 \times 10^6 m^2 s^{-1}$. In the upper-layer, we have a region of intensification upstream of the forcing region, and a splitting region downstream, with a decaying solution to the sponge region. The lower-layer flow is markedly different from previous cases, with a strong quadrupolar response extending in both directions toward the sponge region. Note that the response is equivalent barotropic at most longitudes, including upstream of the wavemaker, where it has been baroclinic for all previous values of U_1 used. From table 4.1, it can be seen that the possible wave solutions change as we increase U_1 to $20 ms^{-1}$. The exponential solution with non-zero A_2 value is now baroclinic, with a negative amplitude ratio between the two layers. Together with the other upstream solution with $A_2 = 0$, it is possible to construct both barotropic and baroclinic upstream decaying solutions. We now also have two 'extra' exponential solutions, which correspond to downstream decaying solutions, both with $A_2 = 0$. However, neither of these permit a non-zero wave-amplitude in the lower layer for a downstream decaying solution, which figure 4.5 seems to show. It would appear that linear

theory is unable to explain the wave produced in this case.

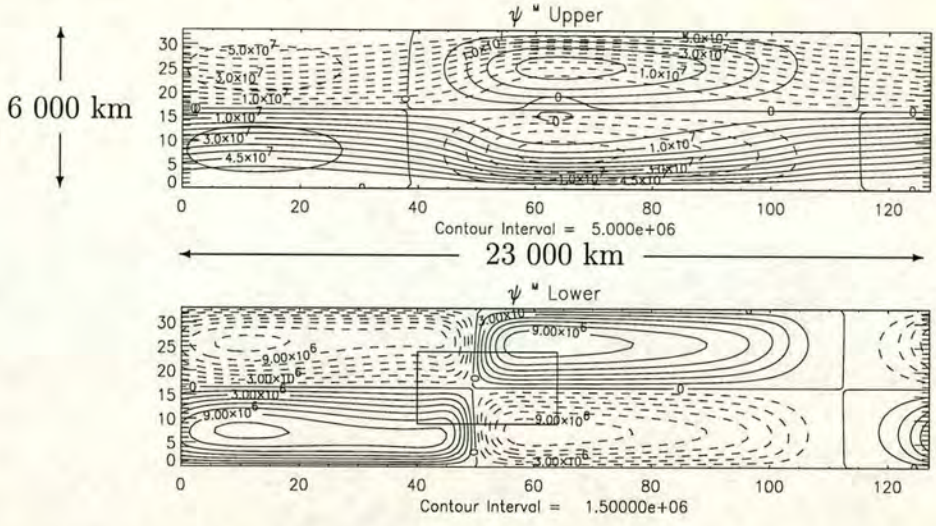

Figure 4.5: As figure 4.1 except for the run with upper-layer velocity 20 ms^{-1} The upper-layer anomaly contours are $5 \times 10^6 m^2 s^{-1}$).

4.4.6 Summary

Summarising the results from the previous experiments and theory, we find that as the upper-layer velocity is increased, the zonal wavelength of the stationary dipolar Rossby wave solution increases until a dipolar Rossby wave is no longer a solution. Then the flow maintains a blocking-like split, and as U_1 is increased further, this becomes a long downstream-evanescent solution. The solutions have their main splitting region further downstream and their amplitude larger as U_1 is increased. The lower-layer streamfunction field shows a quadrupolar response, with the amplitude ratios varying as U_1 is increased. They initially show a horizontal bowing/tilting pattern, but this disappears as U_1 gets sufficiently large. The case with $U_1 = 15$ ms^{-1} is particularly reminiscent of a blocking pattern, and so we shall study this in more detail in the following sections. We find that away from the region of forcing, the linear theory fits reasonably well with the observed fields to a certain extent, in particular the downstream wave-like solutions. Upstream, we find that a superposition of two linear solutions can usually explain the observed wave pattern, the case when $U_1 = 20 ms^{-1}$ seems an exception. However, it gives us no indication of the relative magnitudes of these we might expect, and so is rather limited as a predictive tool. Over the wavemaker region, the linear theory is unable to give any useful insights into the observed anomalies. This

is understandable, especially as there is a direct forcing in this region, and since the flow in the lower layer is zero, any perturbation, however small, cannot be regarded as 'small' in comparison to it.

4.5 Momentum Budgets

In this section we examine the momentum equations for the layers in the model. We decompose the flow into time-mean component (defined with a superscript M) and 'eddy' component, the deviation from this time-mean, defined with a prime $'$. The time-mean zonal and meridional momentum equations may then be written as follows:

$$\frac{\partial u^M}{\partial t} + \frac{\partial (u^M)^2}{\partial x} + \frac{\partial (u^M v^M)}{\partial y} + \frac{\partial (u'^2)^M}{\partial x} + \frac{\partial (u'v')^M}{\partial y} - \beta y v^M - f_0 v^M_{ag} = -(\varepsilon + S(x))(u^M - u^I) + \nu \nabla^2 (u^M - u^I), \quad (4.42)$$

$$\frac{\partial v^M}{\partial t} + \frac{\partial (v^M)^2}{\partial y} + \frac{\partial (u^M v^M)}{\partial x} + \frac{\partial (v'^2)^M}{\partial y} + \frac{\partial (u'v')^M}{\partial x} + \beta y u^M + f_0 u^M_{ag} = -(\varepsilon + S(x)) v^M + \nu \nabla^2 v^M, \quad (4.43)$$

where subscript ag indicates the ageostrophic component of the velocity (terms with subscripts are geostrophic values). For simplicity, we have not included the wavemaker terms in these equations.

We can use this version of the momentum equations (4.42 and 4.43) to derive an appropriate form of the vorticity equation:

$$\frac{\partial \zeta^M}{\partial t} + \mathbf{v}^M . \nabla (\zeta^M + f) + f_0 \nabla . \mathbf{v}^M_{ag} + \frac{\partial^2 (v'^2 - u'^2)^M}{\partial y \partial x} - \frac{\partial^2 (u'v')^M}{\partial y^2} + \frac{\partial^2 (u'v')^M}{\partial x^2} = -(\varepsilon + S(x))(\zeta^M - \zeta^I) + \nu \nabla^2 (\zeta^M - \zeta^I). \quad (4.44)$$

As discussed in Hoskins (1983b), and re-iterated in Hoskins *et al.* (1983), in the atmosphere the eddy flux convergence term $\frac{\partial (v'^2)^M}{\partial y}$ in the meridional momentum equation (4.43) is larger than the advection by the mean-flow term, and so must be balanced with the ageostrophic component $-f_0 u^M_{ag}$. In two dimensional motion this balancing ageostrophic circulation will be non-divergent. This implies a corresponding meridional component $v^M_{ag} = \frac{1}{f_0} \frac{\partial (v'^2)^M}{\partial x}$, which would become an eddy forcing term in the zonal momentum equation (4.42) as $\frac{\partial (v'^2)^M}{\partial x}$. If either the

x-lengthscale of the $(u'v')^M$ term is much larger than its y-lengthscale (implying that $\frac{\partial^2(u'v')^M}{\partial y^2} \gg \frac{\partial^2(u'v')^M}{\partial x^2}$), or if $\frac{\partial^2(v'^2-u'^2)^M}{\partial y \partial x}$ dominates the other two eddy terms in equation 4.44, then it would be an appropriate assumption to neglect $\frac{\partial^2(u'v')^M}{\partial x^2}$. We can then write the eddy terms in equation 4.44 in terms of the divergence of a "vector" $\mathbf{E}$:

$$\frac{\partial^2(v'^2-u'^2)^M}{\partial y \partial x} - \frac{\partial^2(u'v')^M}{\partial y^2} = \frac{\partial}{\partial y}(\nabla.((v'^2-u'^2)^M, -(u'v')^M)) = \frac{\partial}{\partial y}(\nabla.\mathbf{E}), \quad (4.45)$$

where:

$$\mathbf{E} = ((v'^2 - u'^2)^M, -(u'v')^M). \quad (4.46)$$

Since the mean vorticity is of the form $\zeta^M = -\frac{\partial u}{\partial y} + \frac{\partial v}{\partial x} + f$, $\mathbf{E}$ can be interpreted as a flux of zonal momentum, and would appear on the right hand side of equation 4.42 as $\nabla.\mathbf{E}$. This implies that regions of divergence of $\mathbf{E}$ correspond to a positive forcing on the time-mean zonal momentum by the eddies (with a convergence implying a negative forcing).

In the quasi-geostrophic framework of our model, the ageostrophic velocity is not explicitly defined, but can be determined from the term required to balance the momentum equations. We shall now look at the balances in the above equations for our model, using the run with $U_1 = 15$ ms^{-1}.

4.5.1 Zonal momentum budget

Figure 4.6a shows the time-mean zonal velocity u^M for both layers. In the upper-layer plot, there is a minimum over the region of jet splitting, and a maximum near the walls around this split. The lower-layer echoes these features, and has additional minima running along the walls upstream of the forcing region.

In the zonal-momentum equation (4.42), we find that the eddy terms (not shown) are much smaller than the comparable time-mean terms. This is consistent with the scale analysis performed by Hoskins (1983b) for typical atmospheric values. Figure 4.6b,c show the second and third terms on the left hand side of equation 4.42. In the upper-layer there is a degree of spatial cancellation between the terms, although figure 4.6b has a larger amplitude. Figure 4.6d shows the term involving the planetary vorticity, $-\beta y v^M$, which is of quadrupolar form in both layers. It is easy to see where this structure comes from by examining the v^M term in figure 4.6f, which is then multiplied by $-\beta y$.

We can sum over all the terms in equation 4.42, including the dissipation terms, to give us the mean ageostrophic meridional velocity $f_0 v_{ag}^M$, which is shown in

figure 4.6e. In each layer, the field is primarily composed of the sum of terms from figures 4.6b and 4.6d, with the region over the sponge layer coming from the dissipation terms. We shall return to this field later once we have examined the meridional momentum equation to find u^M_{ag}, and are able to plot the ageostrophic circulation as a vector field.

4.5.2 Meridional momentum budget

We now examine the relative budgets in the meridional momentum equation (4.43). First, we consider the mean meridional velocity field v^M in figure 4.6f. This consists of a quadrupolar structure either side of the split region, since the time-mean streamlines are perturbed outward from the channel centre upstream of the split region and return towards the centre of the channel downstream of the split. This time, considering the second, third, fourth and fifth terms of equation 4.43, we find that in the upper layer, it is the $\frac{\partial(u^M v^M)}{\partial x}$ term which is dominant (figure 4.6g). This is dominated by the $u^M \frac{\partial v^M}{\partial x}$, as we can see since the maxima and minima correspond to regions of strongest zonal gradient changes of v^M (figure 4.6f). However, in the lower layer, the $\frac{\partial(v'^2)^M}{\partial y}$ eddy term dominates the other three terms (figure 4.6h). Hoskins (1983b) found this term to be the dominant eddy term in the atmosphere at upper levels. This consists of a dipolar structure over the wavemaker region. Figure 4.6i shows the term involving the planetary vorticity, $\beta y u^M$ (note that the contour intervals are greater than those in plots g and h). This term is continually increasing in the northward direction, with local maxima and minima where u^M has its extreme values. Again, we sum all the terms to give us the ageostrophic term $-f_0 u^M_{ag}$, which is shown in figure 4.6j. This is dominated by the planetary vorticity term in 4.6i, except in the lower-layer over the wavemaker region, where the 4.6h contributes by increasing the amplitude of the dipole forcing pattern there.

4.5.3 Ageostrophic Circulation

From figures 4.6e and 4.6j, if we divide by f_0, we can obtain the time-mean ageostrophic circulation pattern $\mathbf{v}^M_{ag}$. This is shown in figure 4.7a, together with contours of its divergence. The upper-layer term is dominated by the zonal component, eastward in the northern half of the channel, westward in the southern half. The velocities increase towards the channel walls. This is due to the fact that they are primarily balanced by the $\beta y u^M$ term in equation 4.43, which is

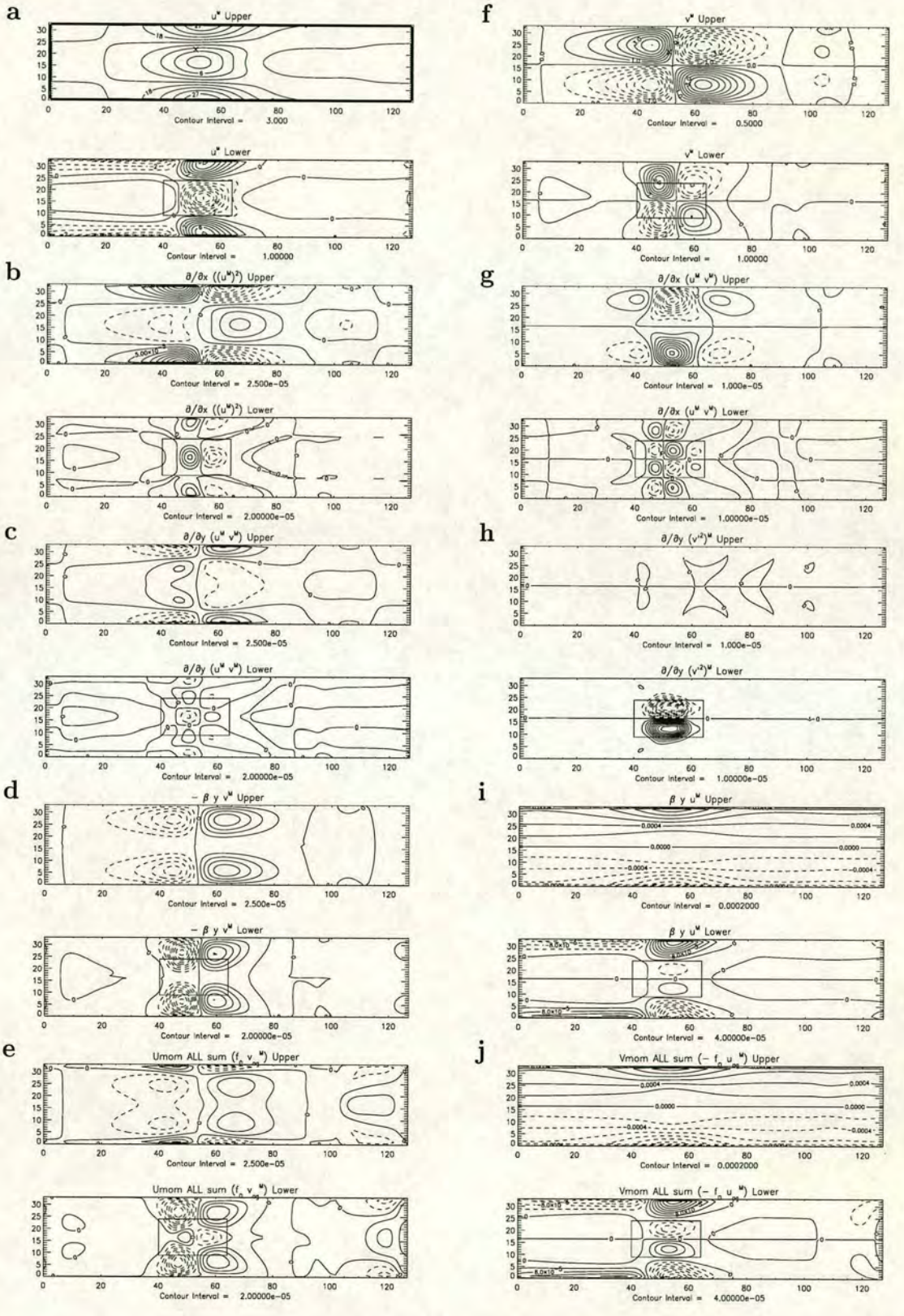

Figure 4.6: Time-mean zonal and meridional velocities (figure a and f respectively) and selected terms from the zonal (left column) and meridional (right column) momentum budgets.

maximum at the walls. As an estimation of their magnitude, we get:

$$u_{ag}^{M} = \frac{\beta y_{wall}}{f_0} u^{M} \simeq 0.5\ u^{M} \tag{4.47}$$

This makes the velocities quite large in comparison to the geostrophic values near the walls. In the lower layer, we have a similar zonal pattern near the walls in the region upstream of the wavemaker. The main region of interest is over the wavemaker region, where there is a dipolar anticyclonic circulation evident. Hoskins (1983b) stated that atmospheric datasets often show an anticyclonic ageostrophic circulation around storm track regions. This pattern would partly fit that description at the edges of the channel, but the circulation pattern is not completed.

The overlaid contours show the divergence of this velocity field, which represents the total divergence, since the geostrophic component of velocity is non-divergent by definition. Note that in regions apart from the sponge layer, the divergence in the lower layer is equal and opposite to that in the upper layer as you would expect by conservation of mass. A positive divergence in the lower layer indicates a downwards vertical motion, a convergence indicating an upward motion. The vertical motion is confined mainly to the region of forcing, with a quadrupolar structure.

4.5.4 E Vectors

Figure 4.7b shows the **E** vectors ($\mathbf{E} = ((v'^2 - u'^2)^M, (-u'v')^M)$) for this run. We have not filtered the fields for this, assuming any eddy activity to be of high-frequency, generated from the wavemaker (a time-series plot, figure 4.10, confirms this to be the case). In both layers, they are concentrated over the wavemaker region and are primarily zonal, pointing eastward. This is consistent with the findings of Hoskins *et al.* (1983) for high-pass meridionally elongated eddies, with their group velocity larger than the mean flow. This would appear to agree with the findings that the upper-layer disturbance is downstream of the forcing region. However, if we calculate the **E** vectors for the runs with smaller U_1 values, they also point downstream, despite the fact that the upper-layer disturbance appears to be further upstream from the wavemaker region. The divergence of $\mathbf{E} = \frac{\partial}{\partial x}((v'^2 - u'^2)^M) - \frac{\partial}{\partial y}((u'v')^M)$, the contours of which are overlaid on figure 4.7b, shows a dipolar structure in both layers, with positive values over the left-hand side of the wavemaker, indicating a decreasing of the mean westerlies by the eddies, and negative ones over the right, implying the eddies are forcing an increase in the mean westerly flow. This is the approximated forcing by the eddies on the time-

mean zonal velocity, which is dominated by the $\frac{\partial(v'^2)^M}{\partial x}$ component of $\nabla.\mathbf{E}$. Note that the contour intervals for the upper-layer divergence are much smaller than those for the lower layer, implying that the high-frequencies have much smaller effect in the upper layer.

4.5.5 Wavemaker response structure

Figure 4.7c shows the contribution to the vorticity equation from the dominant component of the $-\frac{\partial}{\partial y}\nabla.\mathbf{E}$ vector, which becomes $-\frac{\partial(v'^2)^M}{\partial x \partial y}$ when considered on the right-hand side of the vorticity tendency equation (4.44) after the differentiation with respect to y. In both layers, the term shows a quadrupole forcing structure over the wavemaker region. This term will form a component of the potential vorticity eddy-feedback term: $J(\psi', q')^M = (\mathbf{v}'.\nabla q')^M = \nabla.(\mathbf{v}'q')^M$ which is examined further in section 4.8.1. This quadrupolar structure is evident in the time-mean streamfunction fields of all the model experiments shown (figures 4.1, 4.2, 4.3, 4.4, 4.5).

4.5.6 Summary

In this section we have been looking at the balances in the momentum equations, and calculating the associated ageostrophic velocities. It is clear that the dominant contribution from the eddies is in the lower layer, associated with the $(v'^2)^M$ and its spatial derivatives, probably due to the meridionally-extended shape of the eddies excited by the wavemaker. The other eddy terms are comparatively weak when compared to the time-mean terms. A $(v'^2)^M$ maximum over the wavemaker region, when differentiated with respect to the x and y directions, produces a quadrupolar forcing function.

4.6 Blocking Split, $U_1 = 15$ ms^{-1}

Of the runs considered in the previous sections, setting the upper-layer jet to $U_1 = 15$ ms^{-1} produced the most realistic blocking-like split, with an equivalent-barotropic dipole structure as the main feature of the anomaly. It is close to the limit of dipolar stationary Rossby wave existence, and the split is directly over the region of forcing. It is for this reason that we choose this run to study more closely, considering other diagnostics to help our understanding of the processes involved in maintaining such a split against the effects of dissipation.

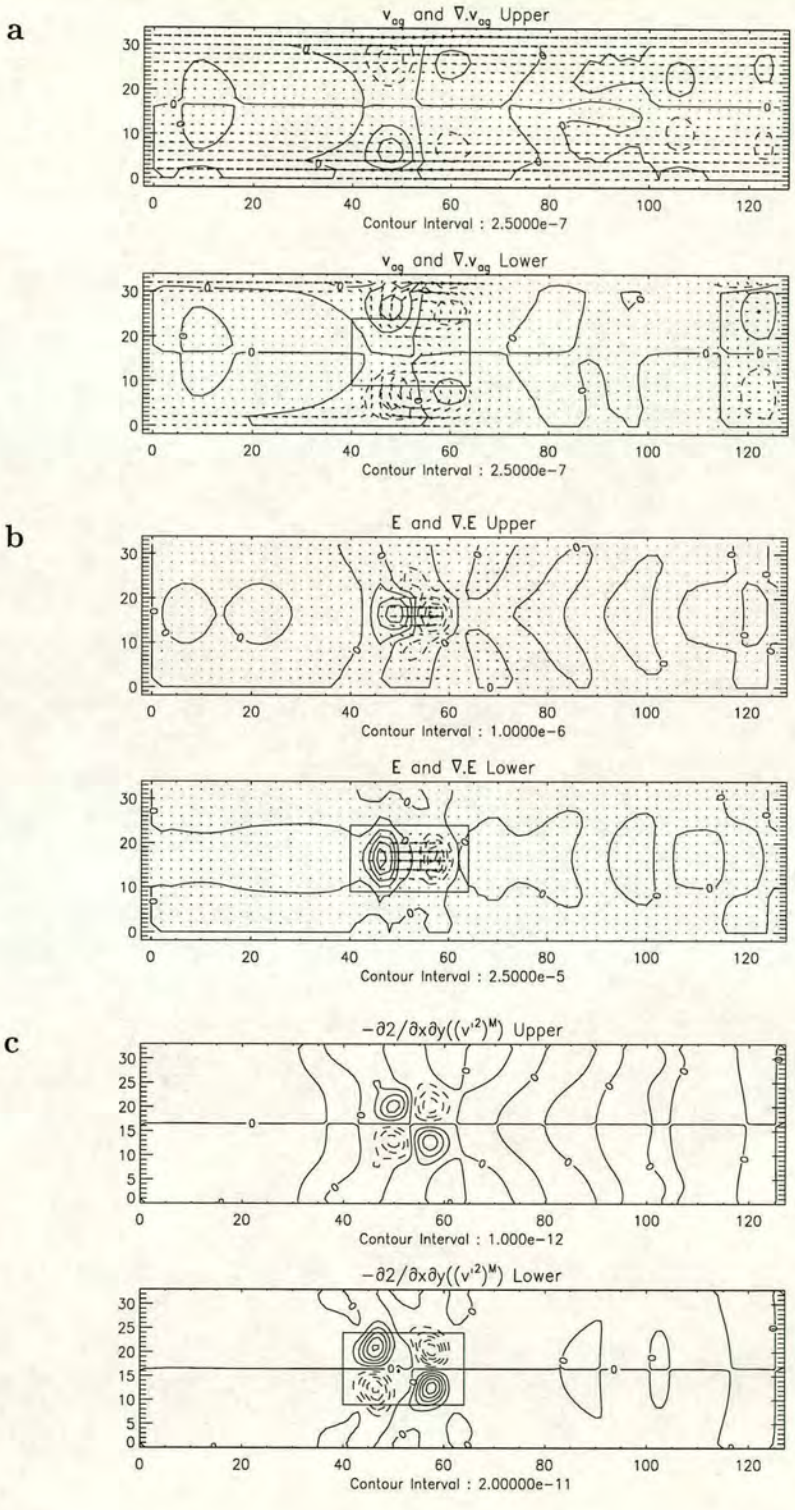

Figure 4.7: (a) Ageostrophic circulation $\mathbf{v}_{ag}$ (arrows) and its divergence $\nabla.\mathbf{v}_{ag}$ (contours, interval units s^{-1}). Maximum arrow length corresponds to a velocity of 13.1ms^{-1} (upper) and 3.1ms^{-1} (lower); (b) $\mathbf{E}$ vector (arrows) and its divergence $\nabla.\mathbf{E}$ (contours, interval units ms^{-2}). Maximum arrow length corresponds to a value of 3.5m^{2}s^{-2} (upper) and 117m^{2}s^{-2} (lower); (c) Dominant eddy term in the vorticity budget $-\frac{\partial^2 (v'^2)^M}{\partial x \partial y}$ (units s^{-2}).

4.6.1 Time-mean potential vorticity

The time-mean potential vorticity fields are shown in figure 4.8. The upper-layer shows a very similar structure to the streamfunction field of figure 4.4, with the splitting over the wavemaker region. The similarity of this to the streamfunction demonstrates the closeness of the time-mean solution to that of a free-mode, where:

$$q = G(\psi) \tag{4.48}$$

for some function G which ensures that the streamlines and PV contours are parallel. The lower-layer shows a somewhat different anomaly pattern. If we consider the northern half of the channel (the southern half being a reflection of opposing sign), we see there are three anomalies, two positive ones at the corners of the wavemaker region, and a negative anomaly in the centre of the wavemaker region. In both layers, as we move away from the wavemaker region, the contours converge to their initial values, except upstream of the wavemaker in the lower layer. If we compare this plot (figure 4.8) with that of the dominant eddy vorticity forcing term $-\frac{\partial^2(v'^2)^M}{\partial x \partial y}$ in figure 4.7c, we see that the forcing term appears to be out of phase by $\frac{\pi}{2}$. We shall look at these balances more closely in a later section (4.8), considering the PV budget equation.

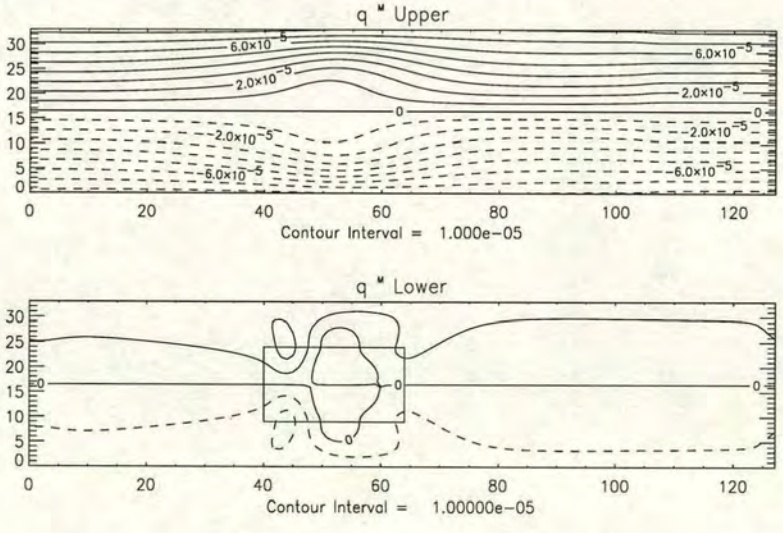

Figure 4.8: Time-mean potential vorticity (units s^{-1}) for the two layers for the run with upper-layer velocity 15ms^{-1} and wavemaker amplitude $A = 1.2 \times 10^{-9}$s^{-2}. The position of the wavemaker in the lower layer is outlined. The contour values are shown beneath the plots.

4.6.2 PV Inversion

Following the work of Bishop and Thorpe (1994), we can consider the potential vorticity distribution to be similar to that of an electrostatic potential. This means we can consider PV to be like point charges, where the effect of each can be summed to represent the total field. In our case with PV, we can consider the anomalies in each layer to each contribute to the final streamfunction state. This invertibility principle is one of the fundamentals of PV thinking in general, i.e. if you know the PV distribution and appropriate boundary conditions, you can invert to obtain the flow field (Hoskins *et al.* (1985)). With this in mind, we aim to determine the contribution to the streamfunction flow field from the PV anomalies in the upper and lower layers separately.

To do this, we take the upper-layer time-mean PV distribution together with the lower-layer initial zonal PV field. Using the inversion routine as the model does, described in Chapter 3, we obtain the streamfunction field. We repeat this, but with the initial distribution from the upper layer together with the lower-layer time-mean field. The results from performing these two experiments are shown in figures 4.9 a,b. From this we can see that the upper-layer PV anomaly produces an equivalent barotropic dipole structure, with an anti-cyclonic circulation to the north of a cyclonic one, typical of a blocking dipole. The lower-layer PV distribution, together with the initial zonal upper-layer PV, shows virtually no response in the upper layer, the lower-layer having a three dipole structure, the dominant one being a cyclonic north of anti-cyclonic forcing, which extends upstream towards the wavemaker region. The sum of these two anomalies will give us the time-mean streamfunction distribution. This experiment shows that the upper-layer time-mean streamfunction anomaly is caused by the upper-layer re-arrangement of PV and not simply from the effects of the lower-layer PV structure, which is consistent with that observed in the atmosphere, where the re-arrangement of air at upper levels is shown using potential vorticity diagnostics e.g. Shutts (1986). Also, modelling studies of simplified baroclinic wave lifecycles show that they cause the re-arrangement at upper-levels due to the fact that as density increases with height, so the wave amplitude increases until it wave breaking occurs, for example Thorncroft *et al.* (1993).

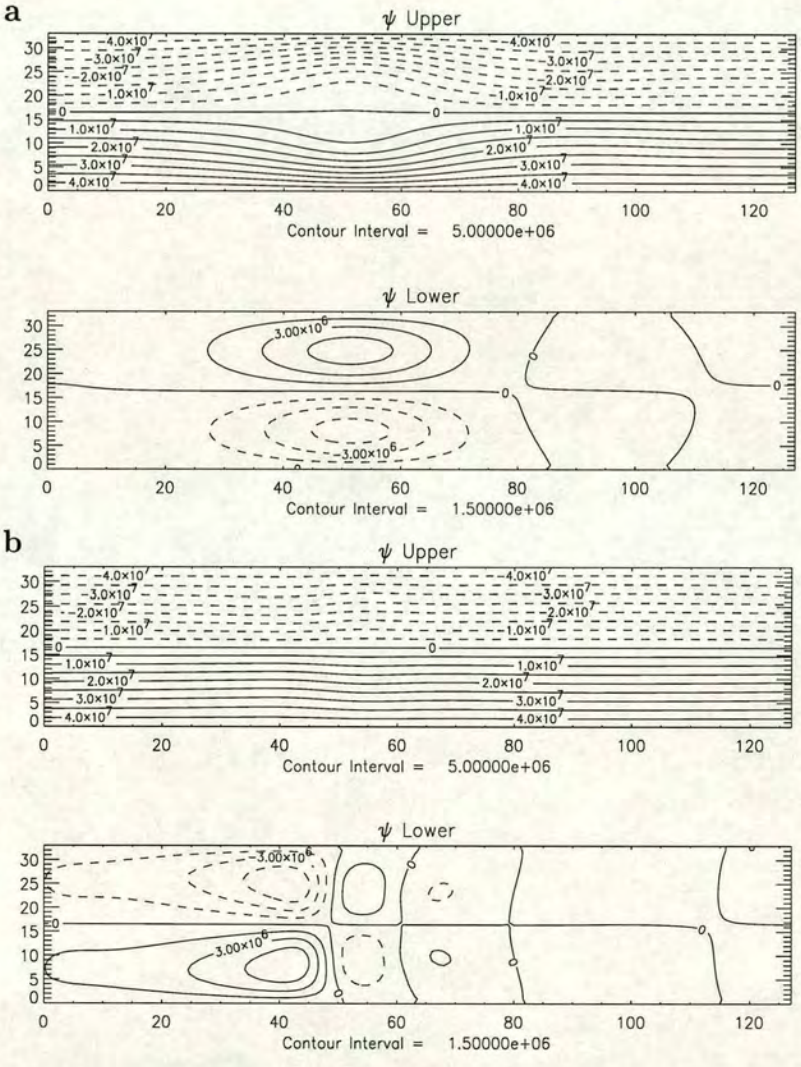

Figure 4.9: Streamfunction fields derived from combination of the time-mean and initial potential vorticity fields. Figure a is from using the upper-layer initial PV with the lower-layer time-mean distribution. Figure b is the opposite, with the upper-layer time-mean PV field together with the lower-layer initial field. The sum of the two anomalies should equate to the time-mean anomaly. Units s^{-1}.

4.7 Time evolution

So far, we have only been concerned with the time-mean response to the wavemaker forcing. We now look at the evolution with time of the model flow. The simplest way to do this is to select a point in the channel, and plot the evolution of a quantity with respect to time. For this purpose, we choose a point in the northern half of the upper-layer, located over the splitting region, point $(x, y) = (51, 22)$, and choose to plot the evolution of the streamfunction ψ_1. Figure 4.4 shows this point with a cross. Figure 4.10 shows the evolution of the streamfunction at this point, together with a fourier transform taken over the last 600 dumpsteps, to the right of the vertical dashed line shown on the time-series plot. We can see that after an initial settling down period, the timeseries reaches a quasi-steady solution with a streamfunction value higher than the initial state, indicating a splitting of the jet at that point. Superimposed on this steady state are small oscillations, caused by the eddies generated by the wavemaker. The fourier transform shows a large peak at 48. This value corresponds to 48 oscillations within the 600 dumpstep (217 day) period, which translates to a period of 4.5 days. This is for a complete wave-cycle, the period for each individual eddy being half of this value (2.25 days), similar to the atmospheric timescale for synoptic weather systems. We use the period to the right of the vertical line to calculate the diagnostics used in the following sections. The period to the left of this line, although not used for the budget analyses of this chapter, will be referred back to after considering the oscillatory motions of chapter 5.

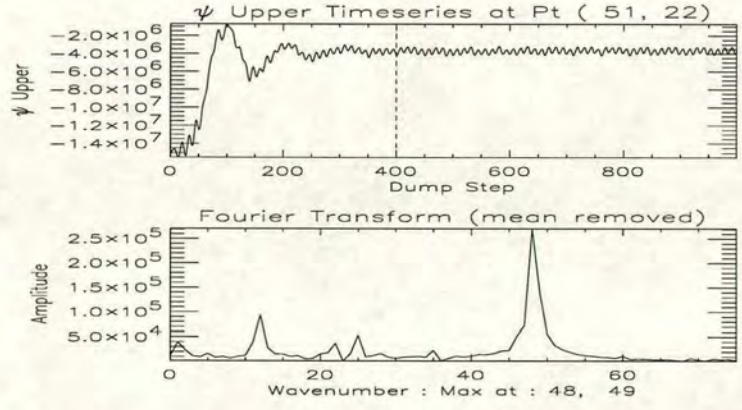

Figure 4.10: Streamfunction timeseries (upper plot, units m^2s^{-1}) and fourier transform (lower plot) at point (51,22) in the upper layer.

.

4.7.1 Variances

For any function $f(t)$, with a time-mean of $f^M(t)$, we can write the variance of f, $\mathrm{Var}(f)$, as:

$$\mathrm{Var}(f) = \frac{1}{N}\sum_{t=t_1}^{t_N}(f - f^M)^2 = (f'^2)^M, \tag{4.49}$$

where N is the number of time-steps used in the summation and $'$ indicates a deviation from the time-mean.

We perform this variance calculation on three fields in the following subsections: Streamfunction Variance, Eddy Kinetic Energy (E.K.E.) and Potential Vorticity Variance.

4.7.1.1 Streamfunction Variance

The streamfunction variance is obtained by substituting ψ for f in equation 4.49, giving $(\psi'^2)^M$. This field is shown in figure 4.11a for the two layers. This field is not conservative (i.e. $\frac{D}{Dt}(...) \neq 0$ in the absence of external forcing/dissipation). Therefore, as shown in Lee (1995), the modulation of eddies (i.e. altering their shape) will alter these values. The lower-layer component, which is more than a factor of 10 stronger than the upper-layer term, consists of an zonally-elongated monopole stretching over the wavemaker region, with a maximum at the centre of the forcing region. The wavemaker region is expected to be the region of greatest fluctuation, and this field reflects this. In the upper layer, we have two maxima in the channel, located along the centre of the channel. They occur at x values of 42 and 62, which if we look at time-mean streamfunction field (figure 4.4), we see that these points lie either side of the central split region. Because the streamfunction gradients are weakest over the centre of the split, the variance there is not particularly large, even though this is the region where the eddies propagating upwards will be largest. The maxima occur zonally upstream and downstream from this region, where the streamfunction gradients are stronger. This means that any perturbation of the mean streamlines will have a larger ψ change, and therefore have a large variance, whereas where weak gradients are perturbed, the streamfunction difference is less, so the variance is weaker.

4.7.1.2 Eddy Kinetic Energy

For the Eddy Kinetic Energy, we substitute f in equation 4.49 for $\frac{1}{2}\nabla\psi$, to give $\frac{1}{2}((\nabla\psi')^2)^M = \frac{1}{2}(\nabla\psi'.\nabla\psi')^M$. Since the velocity can be written in terms of the

streamfunction as follows:

$$\mathbf{v} = (u, v) = \left(-\frac{\partial \psi}{\partial y}, \frac{\partial \psi}{\partial x} \right) = \mathbf{k} \times \nabla \psi. \tag{4.50}$$

This gives an alternative form for the E.K.E. as $\frac{1}{2}(u'^2 + v'^2)^M$. This term is shown in figure 4.11b. Once again, this term is not conserved following the motion in the absence of external forcing/dissipation, which must be considered in its interpretation.

Because of the spatial derivative, this term shows the variances of a smaller spatial scale than that of the streamfunction variance. The lower-layer component has a maximum over the wavemaker region as the streamfunction variance did. However, in this case, the maximum is more circular, compared to the elongated structure of figure 4.11a. The upper-layer component has a central maximum directly overhead from the wavemaker region. There are also much weaker minima downstream and towards the wall where the time-mean velocities are larger due to the splitting of the jet.

4.7.1.3 Potential Vorticity Variance

The potential vorticity variance is obtained by replacing f with q in equation 4.49. This term is then equivalent to twice the eddy potential enstrophy term $\frac{1}{2}(q'^2)^M$. This term is shown in figure 4.11c. This is the only one of the three variances which is conservative in a Lagrangian sense in the absence of external forcing/dissipation. Since the potential vorticity has the vorticity component $\nabla^2 \psi$, we can see that these three variances represent increasingly smaller spatial scales of motion, from $\psi \rightarrow \nabla \psi \rightarrow q$, due to the increasing spatial derivative. The lower-layer component once more shows an elongated maximum over the wavemaker region, similar to the streamfunction variance of 4.11a. The upper-layer no longer has a maximum along the centre of the channel, as in the previous two cases. This time there is a double maxima which curves around the split of the upper-layer jet. It is only at the spatial scale of the potential vorticity that this appears as a feature of variance. There are also some weaker maxima downstream from the split-jet region. As the eddies emerge from the lower-layer, they are sheared by the large-scale split-jet flow. This meridional shearing enhances the energy cascade to larger scales (see the eddy straining hypothesis in Shutts (1983), Shutts (1986)). The split-maxima around the jet is similar to that found in Shutts (1983) for a barotropic channel model. In his non-linear case, there was a central maxima with a pair of streaks extending downstream, but as he used a barotropic model, the wavemaker and

split were at the same level. This would be similar to the pattern were we to superimpose our upper- and lower-layer contours on the same plot.

4.7.1.4 Variance Summary

The previous subsections have shown three different measures for the variance in the model which correspond to different horizontal scales. In the recent paper by Lee (1995), he showed that different measures of variance displayed different characteristics of storm tracks, depending on whether they were conserved quantities. In his case, he showed that the non-conserved diagnostics showed two storm-track regions when the eddies were deformed by a background flow, whereas the conserved enstrophy diagnostic showed one continuous maximum. This would suggest that the potential enstrophy would maybe be the best measure of the high-frequency eddy tracks. Figure 4.11c shows a double upper-layer maximum, with several secondary maxima downstream. This would suggest that most of the eddy activity is dissipated over the splitting region, with little reaching further downstream.

4.8 Potential vorticity budget

We now consider the potential vorticity budget for the time-mean flow. By doing this, we should gain an appreciation of the roles of the wavemaker eddies, the mean-flow forcing and the dissipation, and the relative balances between them. As we did for the momentum equations, we shall split the flow into time-mean and eddy components and then take the time-mean of the model equations (3.4 and 3.5) from chapter 3, which gives:

$$0 = \frac{\partial q_j}{\partial t} = -J(\psi_j', q_j')^M - J(\psi_j^M, q_j^M) - (\varepsilon + S(x))\nabla^2(\psi_j^M - \psi_j^I) + \nu\nabla^4(\psi_j^M - \psi_j^I) \tag{4.51}$$

where $j = 1, 2$ denote the two layers.

We now consider the terms on the right hand side of equation 4.51. The first term $-J(\psi', q')^M$ represents the forcing of the time-mean flow by the transient eddies, the eddy feedback. If there were no eddies, this term would be zero. The second term $-J(\psi^M, q^M)$ is the self-advection by the time-mean flow. The condition for a free-mode is that this term must be equal to zero. The last two terms are the two dissipation terms. Note that there is no contribution from the

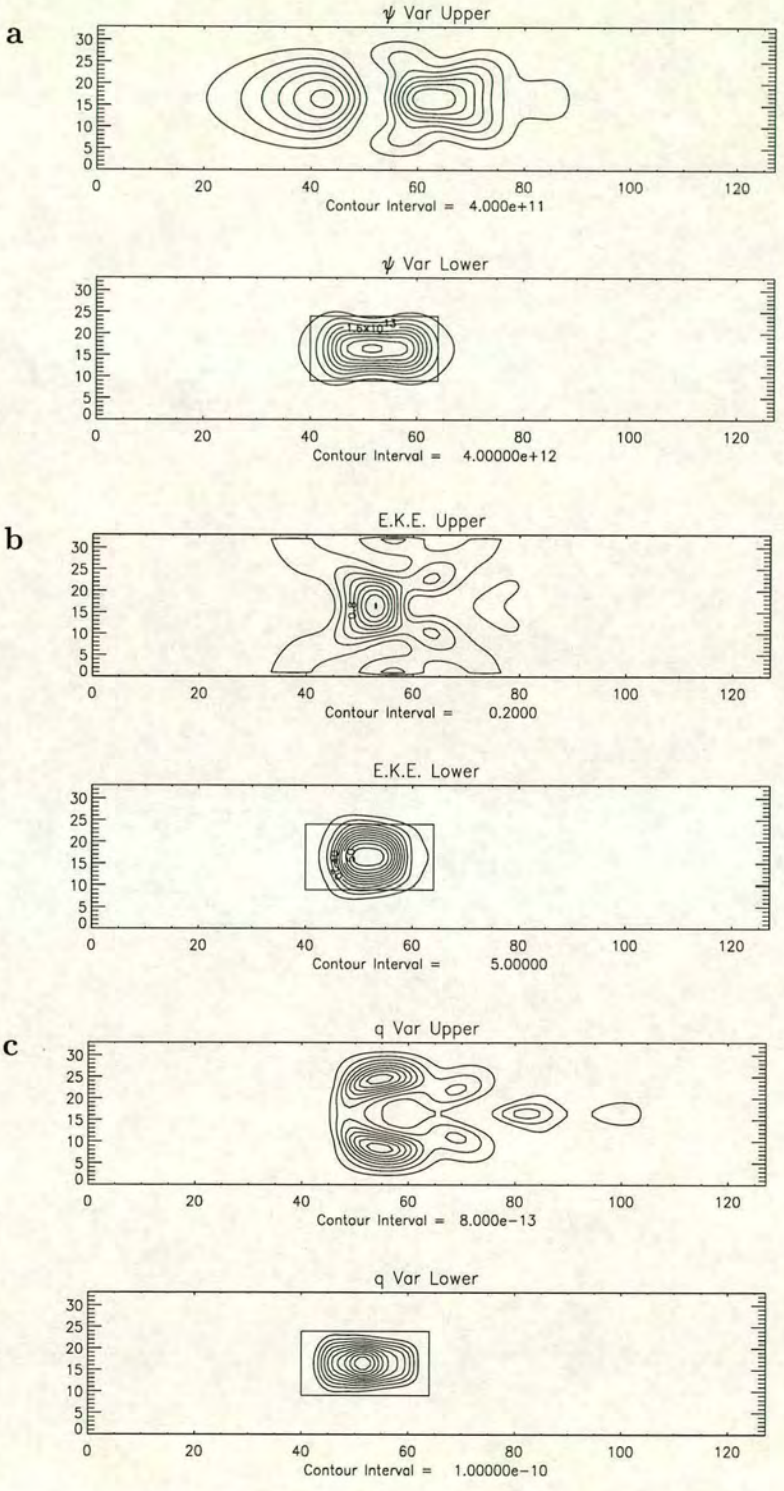

Figure 4.11: Streamfunction variance $(\psi'^2)^M$ (units $\mathrm{m^4 s^{-2}}$, figure a), eddy kinetic energy $\frac{1}{2}(u'^2+v'^2)^M$ (units $\mathrm{m^2 s^{-2}}$, figure b) and potential vorticity variance $(q'^2)^M$ (units $\mathrm{s^{-2}}$, figure c) for the two layers for the run with upper-layer velocity 15 $\mathrm{ms^{-1}}$ and wavemaker amplitude $A = 1.2 \times 10^{-9}\mathrm{s^{-2}}$. The position of the wavemaker in the lower layer is outlined. The contour values are shown beneath the plots.

wavemaker term, since it is defined to have a zero contribution in a time-mean sense.

4.8.1 Eddy forcing $-J(\psi', q')^M$

The eddy feedback term $-J(\psi', q')^M$ is shown in figure 4.12. It is dominated by the lower-layer component which has a quadrupole structure over the wavemaker region. Referring back to figure 4.7c, we see the dominant component of the vorticity forcing, $-\frac{\partial^2(v'^2)^M}{\partial x \partial y}$, shares this quadrupolar form. An explanation of this structure was provided earlier in section 4.5, due to the form of the forcing function and the eddies generated by this.

If we compare this lower-layer forcing structure to the time-mean potential vorticity field in figure 4.8, we see that there are similarities in that there is a quadrupolar shape in the lower layer. However, there are also differences, since the lower-layer q^M field actually has a third dipolar anomaly further downstream. The upper-layer term, with contour levels 20 times smaller than those of the lower layer, shows a bowing of the contours around the splitting of the upper-layer flow.

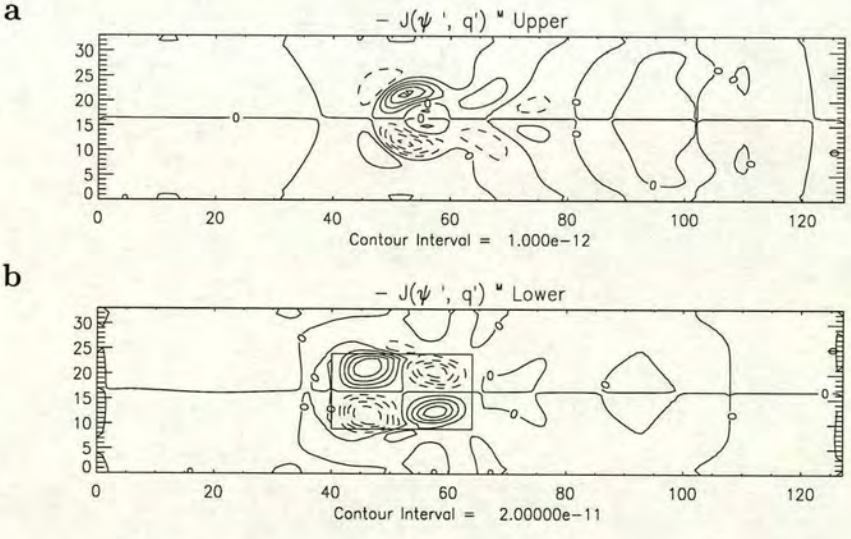

Figure 4.12: Eddy feedback $-J(\psi', q')^M$ on the potential vorticity tendency for the upper (Fig. a) and lower (Fig. b) layer. Note that the component in the upper layer is much weaker than that in the lower layer (different contour intervals). Units s^{-2}.

4.8.2 Applying eddy-feedback as a steady forcing

We can consider using this time-mean eddy-feedback term and applying it as a constant forcing to the model, rather than using the wavemaker, and integrating the model until a steady state is reached.

We do this with three experiments: one using the forcing from both layers, one with just the upper-layer forcing and one using only the lower-layer component. When using the forcing from both layers, a steady response virtually identical to that of the wavemaker run in figure 4.4 is produced. Similarly, when just the lower-layer forcing is applied, there is no discernible difference between this and the previous experiment with both layers included. Finally, when just the upper-layer forcing was applied, the conditions obtained were virtually identical to the initial conditions. From these experiments, we can conclude that the upper-layer eddy-feedback term is of little importance in determining the large-scale response; it is the lower-layer component which is influential. This is hardly surprising considering that the lower-layer forcing term was much larger in magnitude than the corresponding upper-layer term. The bowing of the trough lines in the upper-layer feedback are therefore relatively unimportant in maintaining the split, but are indicative of the shearing process occurring in the upper layer. This result is consistent with the idea, first conjectured by Green (1977), that the feedback of the high-frequency eddies is acting to maintain the split, although he only considered upper-levels. Diagnostic studies, such as Illari (1984) and Shutts (1986), have shown this to be true for atmospheric data at upper levels. In our simple model, it is the component of feedback in the lower-layer which is essential for maintaining the split. As pointed out by Shutts (1986), in atmospheric flows, the eddy feedback term is often small relative to other terms, making analysis difficult. This is probably one of the biggest disadvantages of using the wavemaker as an external forcing, rather than by generating transience through instability mechanisms (as Vautard *et al.* (1988) and Vautard and Legras (1988) did).

Using a model with more vertical resolution, i.e. a greater number of layers, might improve the situation, but also add further complications, as this model was chosen as the simplest which could represent baroclinic effects, which a single layer equivalent-barotropic model is unable to do. Also, the relative densities between the two layers could be altered, which would result in different λ values for each layer. Some experiments along these lines were performed, and managed to increase magnitudes of the upper-layer anomaly compared to that in the lower layer, but the lower-layer eddy feedback was still always found to be dominant

compared to that in the upper layer.

4.8.3 Mean forcing $-J(\psi^M, q^M)$

The time-mean flow feedback $-J(\psi^M, q^M)$ is shown in figure 4.13. In the lower-layer, there is a quadrupolar forcing structure but of the opposite sign to that of the eddy feedback shown in figure 4.12. These two terms provide a first-order balance for the budget in the lower-layer PV equation. However, the sum of these two terms is not identically zero, but provides a balance with the dissipation. In the upper-layer, there are several regions of interest. Over the split region there is a minimum to the north of a maximum region. This corresponds to a negative PV forcing in the north and a positive PV forcing in the south which acts to maintain the jet splitting. Down the centre of the channel further downstream is a zonally elongated region of positive north of negative forcing, which acts to intensify the jet. Also, there are regions of forcing located along the walls to the north and south of the split-jet. The other main region of interest lies towards the far end of the channel ($x = 105$). The upper-layer anomalies in this region are due to the increased dissipation of the sponge layer, which acts to quickly return the flow to its initial state. Thereby, the flow adopts a state which provides the necessary potential vorticity transports to achieve this. Note that there are no anomalies in this region in the lower-layer, since the flow is virtually identical to the initial conditions here.

4.8.4 Dissipation

We shall plot the two dissipation terms separately. Figure 4.14 shows the Ekman dissipation term. At the same contour levels as the mean feedback term, the only contribution which shows is over the sponge layer, where the dissipation coefficient is larger. This balances with the opposite anomalies in that region of the mean feedback term. Figure 4.15 shows the subgridscale dissipation term $\nu\nabla^4(\psi^M - \psi^I)$. The upper-layer component has a dipolar form which approximately balances the time-mean feedback term. The lower-layer has a quadrupolar form, but weaker than that of either of the feedback terms, and also the positions of the maxima do not correspond exactly with those of the feedback terms. Since the ∇^4 dissipation has a greater effect on the smaller-scale eddies, it would be more usual to have the ∇^2 dissipation most significant on larger scales. These figures would suggest that this is not the case, except over the sponge region, and that the ∇^2 friction is negligible. If we perform a model run identical to this, but without the $\varepsilon\nabla^2$

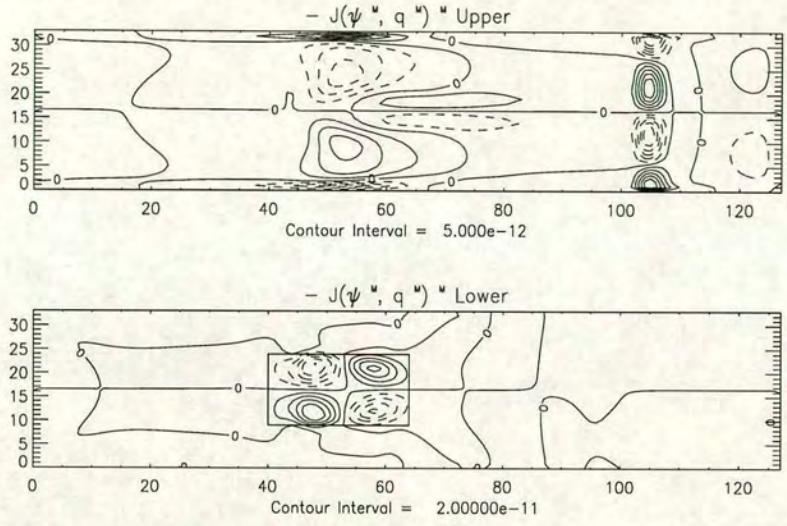

Figure 4.13: Time-mean jacobian $-J(\psi^M, q^M)$ (units s^{-2}) for the two layers for the run with upper-layer velocity 15 ms^{-1} and wavemaker amplitude $A = 1.2 \times 10^{-9}\mathrm{s}^{-2}$. The position of the wavemaker in the lower layer is outlined. The contour values are shown beneath the plots.

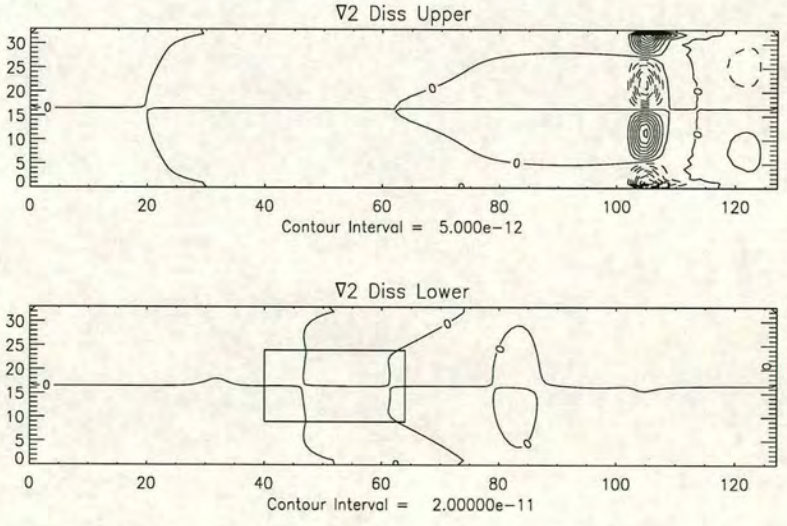

Figure 4.14: Ekman dissipation term $-(\varepsilon + S(x))\nabla^2(\psi^M - \psi^I)$ (units s^{-2}) for the two layers for the run with upper-layer velocity 15 ms^{-1} and wavemaker amplitude $A = 1.2 \times 10^{-9}\mathrm{s}^{-2}$. The position of the wavemaker in the lower layer is outlined. The contour values are shown beneath the plots.

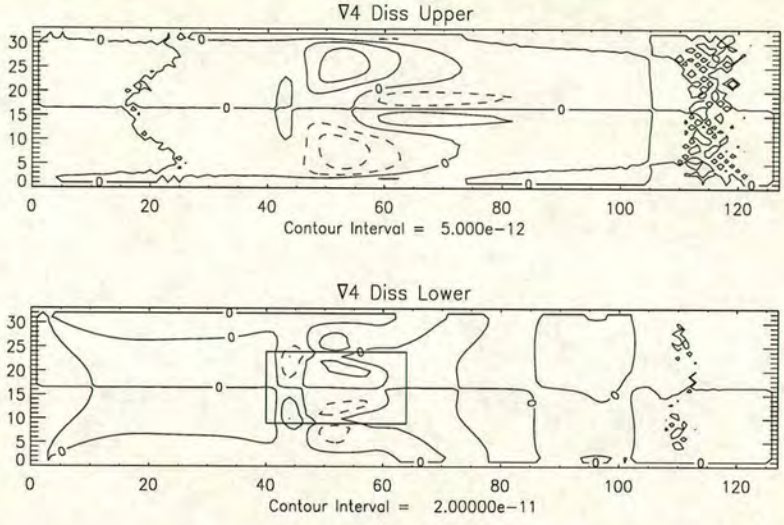

Figure 4.15: Sub-gridscale dissipation term $\nu\nabla^4(\psi^M - \psi^I)$ (units s^{-2}) for the two layers for the run with upper-layer velocity 15 ms^{-1} and wavemaker amplitude $A = 1.2 \times 10^{-9}s^{-2}$. The position of the wavemaker in the lower layer is outlined. The contour values are shown beneath the plots.

friction, the model evolution remains similar to the original experiment. However, in the next chapter, when using a different initial jet, removing this $\varepsilon\nabla^2$ friction component, despite its relatively small contribution, does affect the evolution of the model integration.

4.8.5 Summary

To summarise the results of the PV budget analysis, we find that in the lower layer, the principal balance is between the eddy and time-mean flow feedback terms. The sum of these two terms balances a weaker contribution by the ∇^4 diffusion. In the upper-layer budget, in the region of the split away from the wavemaker, the balance is between the mean-flow self-advection and the ∇^4 dissipation. In the upper-layer sponge region, the balance is between the mean-flow feedback and the Ekman (∇^2) friction. Studies of atmospheric data during blocking events have shown the principal balance to be between the eddy feedback term and the mean-flow advection term (e.g. Illari (1984)). This is the major balance in our lower layer. Mullen (1987) found the eddy forcing to be one-quarter wavelength upstream of the blocking region. In our lower layer, the eddy feedback term maxima are not coincident with the potential vorticity anomaly maxima, but located downstream. It must be remembered that atmospheric studies are usually performed at upper levels, and ideally, it is in the upper-layer of our model where

we would like to draw comparisons. A larger upper-layer response could possibly be acheived using more vertical levels, or using different densities for each layer. The latter was tried, and it was found to produce a larger upper-layer split in comparison to the lower-layer anomaly, but still the lower-layer eddy feedback was dominant. As will be shown in the next chapter, when we use a different upper-layer inital jet, altering these model characteristics can drastically affect the flow behaviour.

4.9 Enstrophy budget

We now look at the budget of eddy potential enstrophy, to establish the balances between the relative terms. If we take the model equations (3.4 and 3.5) from chapter 3, split the flow into time-mean and eddy components as for the PV budget in section 4.8. Multiply by the eddy potential vorticity q'_j and take the time-mean to get an equation for the tendency of the eddy potential enstrophy:

$$\frac{\partial}{\partial t}\left(\frac{q_j'^2}{2}\right)^M + \mathbf{v}_j^M.\nabla\left(\frac{q_j'^2}{2}\right)^M + (\mathbf{v}'_j q'_j)^M.\nabla q_j^M + (\mathbf{v}'_j q'_j.\nabla q'_j)^M = (F'_j q'_j)^M + (D'_j q'_j)^M \tag{4.52}$$

where $j = 1, 2$ denotes the two layers. The first term on the left hand side of the equation will be zero if the time-averaging period is of sufficient length. The remaining terms will then have to balance to zero everywhere. Note that the $(F'_j q'_j)^M$ term can only have a contribution in the lower layer, as the only external non-dissipative forcing is provided by the wavemaker.

4.9.1 Global enstrophy budget

Figure 4.16 shows the plots for the remaining three terms on the left hand side of equation 4.52. Figure 4.16a shows the second term, $\mathbf{v}^M.\nabla\left(\frac{q'^2}{2}\right)^M$, which is the advection of eddy enstrophy by the time-mean flow. First of all, notice that the contour levels are a factor of 100 larger in the lower layer. This is due to the wavemaker forcing being present in the lower layer only (the terms in the PV budget were similarly larger in the lower layer). In the upper-layer, as the flow is predominantly in the zonal direction, the dominant component will be $u^M\frac{\partial}{\partial x}\left(\frac{q_j'^2}{2}\right)^M$. The upper-layer plot shows a series of alternate maxima and minima which follow the path of the jet around the split, merging downstream of the block. If we compare this plot to that of the PV variance (twice the eddy potential enstrophy)

in figure 4.11c, we see that the maxima and minima of figure 4.16a coincide with the regions of increase and decrease of the variance term along the streamfunction path. The main features of the lower-layer field are a double minima to the left of the wavemaker region, with a maximum over the right hand side.

The next term in the eddy enstrophy equation (4.52), $(\mathbf{v}'q')^M.\nabla q^M$, is shown in figure 4.16b. This is the time-mean eddy flux of potential vorticity down the time-mean potential vorticity gradient. Comparing the upper-layer plot with the $\mathbf{v}^M.\nabla\left(\frac{q'^2}{2}\right)^M$ term shown in figure 4.16a , we see that these terms are approximately equal and opposite, sharing a very similar structure. However, the lower-layer plot does not show a balance with the advection term. Over the left of the wavemaker region, there is a double maxima which has a tendency to partially cancel with the advection term of figure 4.16a. Over the right of the wavemaker, there is a weak anomaly, with a central maximum flanked to the north and south by minimum regions. Figure 4.17a shows the eddy PV flux $(\mathbf{v}'q')^M$ superimposed on q^M contours. Note that the maximum values for $(\mathbf{v}'q')^M$ are 2.3×10^{-6} and $9.5 \times 10^{-5}\mathrm{ms}^{-2}$ for the upper- and lower-layer terms respectively, the lower-layer component being considerably larger. Where the arrows are up/down the q^M gradient, $(\mathbf{v}'q')^M.\nabla q^M$ will be positive/negative. In the lower layer, over the left-hand side of the wavemaker region, there are clear upgradient fluxes, corresponding to the maxima in $(\mathbf{v}'q')^M.\nabla q^M$ seen in figure 4.16b. The upper-layer plot, although considerably weaker, appears to show a northward eddy flux of PV over the split region, in contradiction to that required to maintain a blocking circulation with a low-PV anomaly to the north. However, it is the divergent component of this flux which is important in the PV budget. We shall look at integrated budgets of this term in the next section.

Figure 4.16c shows the triple eddy correlation term $(\mathbf{v}'q'.\nabla q')^M$. Note that the contour levels are 10 times weaker than in figures 4.16a,b. This plot shows how considerably weaker this term is compared to the previous two, and shows very little structure of note. The upper-layer component shows a central minimum over the split region with two zonally-elongated maxima to the north and south. The lower-layer consists of several small-scale anomalies. We can effectively neglect this term in comparison to the previous two.

The sum of these three terms $u^M.\frac{\partial}{\partial x}\left(\frac{q'^2}{2}\right)^M + (\mathbf{v}'q')^M.\nabla q^M + (\mathbf{v}'q'.\nabla q')^M$ is shown in figure 4.17b. Note that the contour intervals are half the value they were in figures 4.16a,b, because this is effectively the difference between two terms which are approximately equal and opposite, and therefore this term is smaller

in magnitude than the individual terms which comprise it. In the upper layer, this term is mostly negative, with contours following the time-mean streamlines, but over the central region of the split there is a positive region. The lower-layer term shows a dominant maximum over the central-right wavemaker region, with a weaker meridionally-extended minimum to its left, and a weaker maximum further upstream. These three terms, summed together, balance with the right-hand side of the equation.

The dissipation term from the right hand side of equation 4.52 $(D'q')^M$ is shown in figure 4.17c. Immediately we can see the similarity in the upper-layer plot to that of the previous plot of the sum of the left hand side (figure 4.17a), showing the good balance between the left and right hand sides of the enstrophy equation. The lower-layer plot has a minimum over the wavemaker region, the region of maximum mean eddy enstrophy. This differs from the plot in figure 4.17b, showing there is not as accurate a balance in the lower layer as in the upper. This must be due to the fact that we have neglected the explicit forcing term $(F'q')^M$, or for numerical errors such as from differentiation on a finite grid.

4.9.2 Integral enstrophy budget

As it is the divergent component of the PV flux which is important in the PV budget (equation 4.51), attempts have been made to use the potential enstrophy equation to give further insights into the effect of the eddies. Shutts (1983) defined a residual eddy PV flux as:

$$(\mathbf{v}'q')^M_* = (\mathbf{v}'q')^M - \mathbf{k} \times \nabla \left(\left(\frac{q'^2}{2} \right)^M \frac{\mathrm{d}\psi^M}{\mathrm{d}q^M} \right) \tag{4.53}$$

by assuming that the time-mean flow satisfied the steady, unforced PV equation and so was a free mode solution (equation 4.48) which would then make the left-hand side of the enstrophy equation (4.52), ignoring the triple prime term:

$$(\mathbf{v}'q')^M_* . \nabla q^M . \tag{4.54}$$

This tries to reduce the rotational component of the eddy flux, to isolate the divergent part which is the eddy feedback in the PV equation (equation 4.51). Haines (1994) showed in his experiments that this was unsatisfactory. He suggested an alternative view of the enstrophy equation, which will be repeated below. Let us consider the upper layer (i.e. no external forcing F). If we neglect the triple-prime term from equation 4.52, and then integrate over a region A bounded by a contour

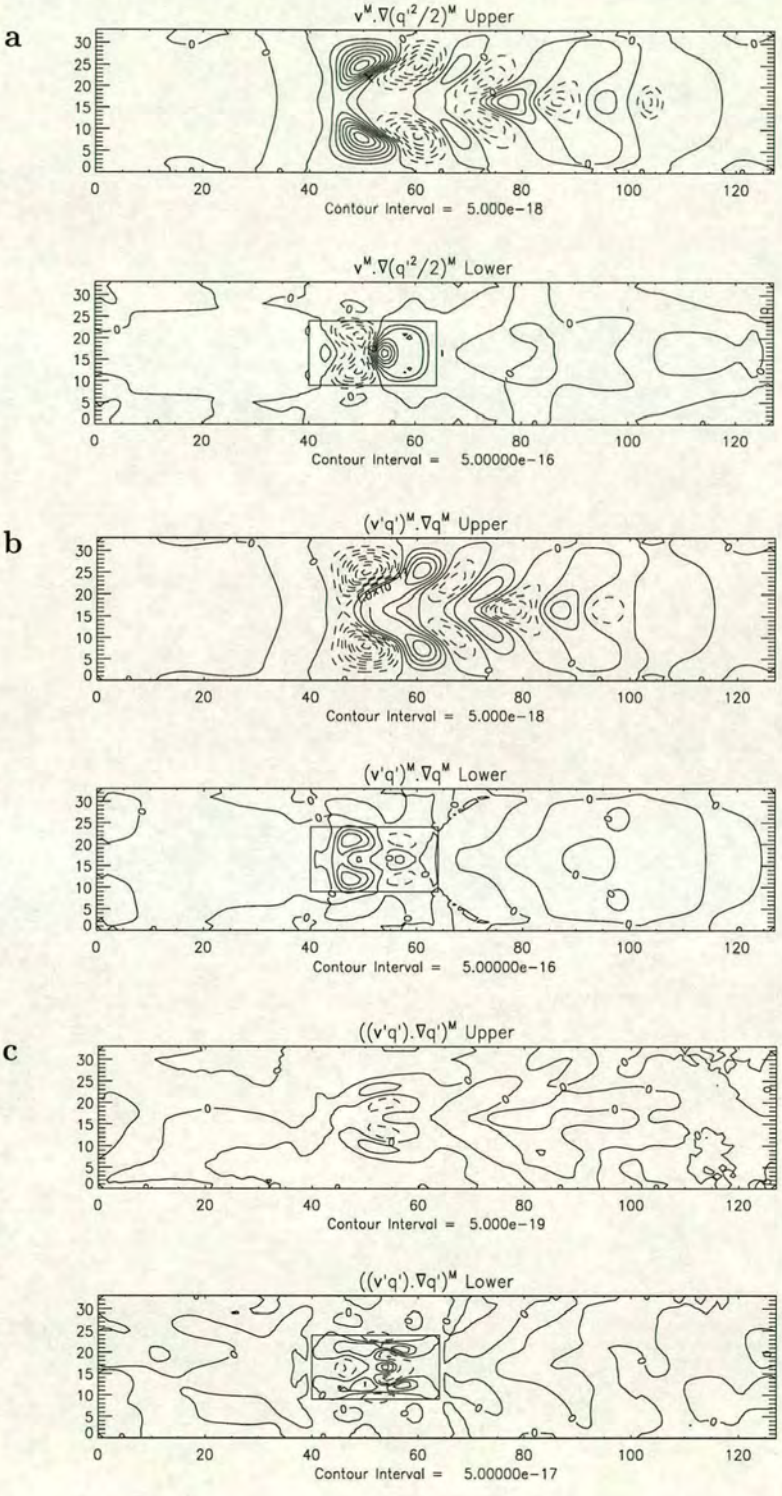

Figure 4.16: Terms in the enstrophy equation: $\mathbf{v}^M.\nabla\left(\frac{q'^2}{2}\right)^M$ (figure a), $(\mathbf{v}'q')^M.\nabla q^M$ (figure b) and $(\mathbf{v}'q'.\nabla q')^M$ (figure c) for the two layers for the run with upper-layer velocity 15 ms^{-1} and wavemaker amplitude $A = 1.2 \times 10^{-9}\mathrm{s}^{-2}$. Units s^{-3}. The position of the wavemaker in the lower layer is outlined. The contour values are shown beneath the plots.

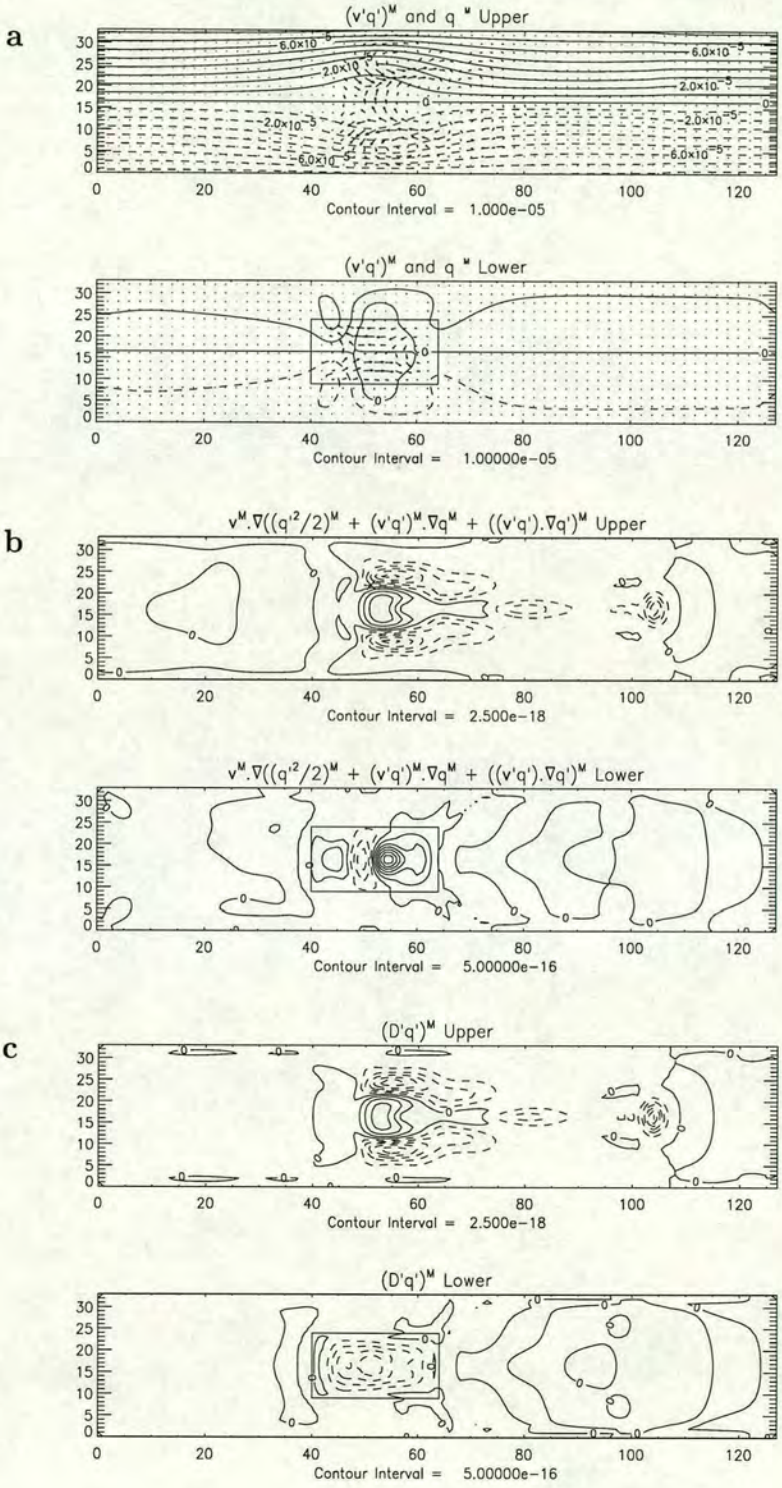

Figure 4.17: The eddy PV flux $(\mathbf{v}'q')^M$ superimposed on q^M contours (figure a), the sum of the three terms shown in figure 4.16 $\mathbf{v}^M.\nabla\left(\frac{q'^2}{2}\right)^M + (\mathbf{v}'q')^M.\nabla q^M + (\mathbf{v}'q'.\nabla q')^M$ (figure b) and the $(D'q')^M$ term (figure c) for the two layers for the run with upper-layer velocity 15 ms^{-1} and wavemaker amplitude $A = 1.2 \times 10^{-9}\mathrm{s}^{-2}$. Units s^{-3}. The position of the wavemaker in the lower layer is outlined. The contour values are shown beneath the plots.

of eddy enstrophy $\frac{(q'^2)^M}{2}$, the first term vanishes to give:

$$\int_A (\mathbf{v}'q')^M . \nabla q^M = \int_A (D'q')^M . \tag{4.55}$$

Imagine the stormtrack to be the region A, and that over this region, then if there is no external forcing, this should represent a region of net dissipation. Equation 4.55 would then imply that over this region, the eddies would provide a net flux of potential vorticity down the time-mean PV gradient.

We perform some calculations on our model run to test this theory. Figure 4.18 shows the results from applying this area integral over 8 contour values for the PV variance (or enstrophy) shown as contours in figure 4.11c. For each of the 8 contour values, at each upper-layer gridpoint, if the enstrophy is greater, we add the value of the $(\mathbf{v}'q')^M . \nabla q^M$ (see figure 4.16) at that point to a cumulative total. The number of gridpoints used for each enstrophy bound is shown in the left hand plot and the corresponding total obtained for the left hand side of equation 4.55 is shown in the right hand plot. As one would expect, as the enstrophy bound increases, so the number of gridpoints falling within this bound decreases. Also, the more points taken for the sample, the more negative the total summation becomes. For all enstrophy contour bounds, the total is shown to be negative, implying a net down-gradient eddy-flux of potential vorticity over the region. This would be consistent with the observed flux in the atmosphere during blocking events, in which the synoptic-scale eddies provide a southward flux of PV to maintain the low-PV (high-pressure) anomaly (Illari 1984).

4.10 Increasing wavemaker forcing

The split jet excited in figure 4.4 may be considered to be weaker than that of a real atmospheric block. With this in mind, we perform another experiment using the same value of $U_1 = 15\text{ms}^{-1}$, but constantly increasing the wavemaker amplitude A. An instantaneous low-pass filtered streamfunction field, is shown in figure 4.19. At this time, the wavemaker had an amplitude of $A = 2.6 \times 10^{-9}\text{s}^{-2}$, over twice the previous case. As we can see by comparing it with figure 4.4, the structure remains similar, an equivalent barotropic dipolar response, except this time the amplitude of the anomaly is much greater, showing how the eddies in the lower-layer can excite a large-amplitude stable blocking-like structure. The fact that it remains stable will be returned to in Chapter 5, when we consider adding a horizontal shear to the upper-layer flow.

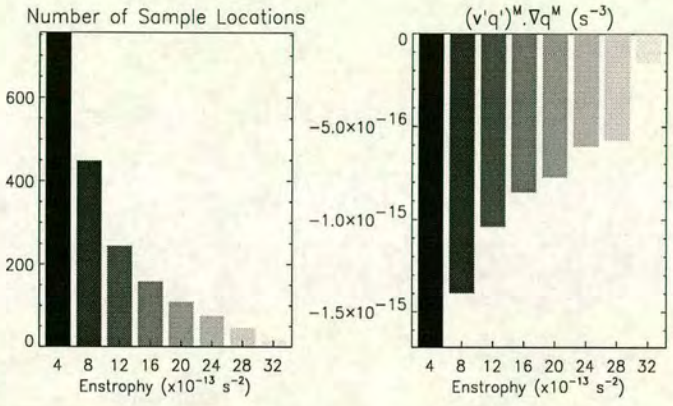

Figure 4.18: Upper-layer surface integral over regions bounded by eddy potential variance $\frac{1}{2}(q'^2)^M$ contours (units s^{-3}) for the run with upper-layer velocity 15 ms^{-1} and wavemaker amplitude $A = 1.2\times10^{-9}s^{-2}$. The left-hand plot shows the number of gridpoints used for each integral, the result of which is shown in the right-hand plot.

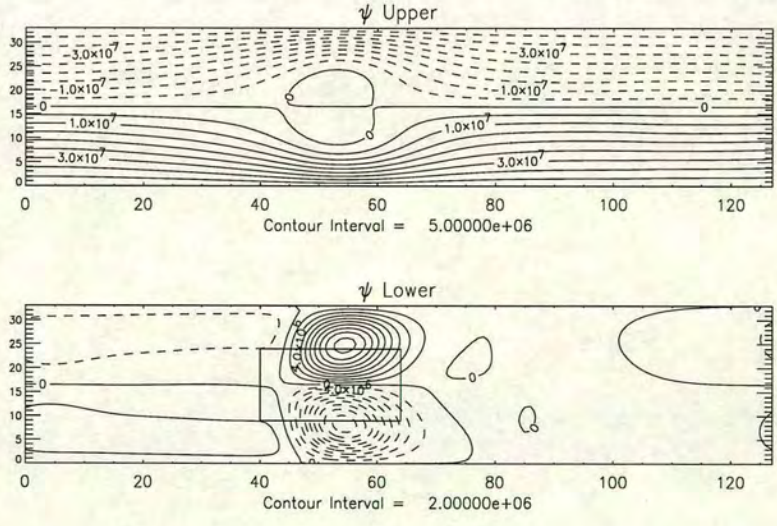

Figure 4.19: Instantaneous low-pass filtered streamfunction (units m^2s^{-1}) for the two layers for the run with upper-layer velocity 15 ms^{-1} and wavemaker amplitude constantly increasing (the wavemaker had amplitude $A = 2.6 \times 10^{-9}s^{-2}$ at this instant). The position of the wavemaker in the lower layer is outlined. The contour values are shown beneath the plots.

4.11 Sensitivity of results

Throughout all of these experiments, the parameter settings for the two dissipational friction terms, the sponge layer and the Rossby deformation radius term have remained unaltered. Likewise the dimensions of the channel and wavemaker forcing function have remained constant throughout. Many different combinations of various model parameters and configurations have been tried during the period of this study. Due to the differences between this idealised set-up and the real atmosphere, it is difficult to set parameters directly similar to atmospheric values. For the runs in this chapter, changing the dissipational parameters has an effect on the model response to the forcing. Providing the dissipation is large enough to prevent unlimited growth of an anomaly to numerically-unstable levels, the results for the different strength initial flows are quantitatively similar, albeit with larger amplitudes for lower dissipational parameters and vice versa. The balance between the amplitude of the wavemaker and the damping terms was crucial in determining the amplitude of the anomaly produced.

Attempts were made to move the channel walls further apart to examine the effects of the walls on the inteegrations. The position of the walls determined the scale of anomaly produced, and dipole solutions spanning the width of the channel would normally be produced in these cases. In devising the experiments, the aim was that the lower-layer would be of secondary importance to the dynamics contained in the upper-layer, it would allow eddy excitation without an external forcing term in the upper-layer equations. One concern was the relative sizes of the anomalies produced in each layer, with the lower-layer having a large amplitude response as might be expected as the forcing was located there. The relative magnitudes could be altered by setting the stretching terms to be different in each layer. However, as we will show in subsequent section 5.9.2, this has a great effect on the regular oscillatory behaviour when using an upper-layer jet with horizontal shear.

4.12 Summary and Discussion

In this chapter, we have used the two-layer channel model described in Chapter 3 to investigate the effects of altering the flow in the upper-layer (U_1) on the stationary large-scale response to forcing by transient eddies. With $U_1 < 15\text{ms}^{-1}$, the splitting in the upper-layer is upstream of the forcing region, with a downstream Rossby-wave pattern excited. In the lower-layer, a quadrupole solution is

present, the left-hand pair similar to an exponential Rossby-wave solution tailing off from a source. Both of these results are consistent with the theoretical analysis. As U_1 is increased, so the stationary zonal wavelength for dipolar Rossby waves increases, the splitting region in the upper-layer moves further downstream and the upper-layer response increases in amplitude. At $U_1 = 15\text{ms}^{-1}$, when there is no longer a stationary Rossby wave solution possible, the response is an equivalent-barotropic dipole structure, very similar to that found in blocking episodes (Rex (1950a)), with little upstream or downstream effects. At upper-level velocities $U_1 > 15\text{ms}^{-1}$, the upper-layer split moves downstream from the wavemaker, tailing off slowly downstream. The linear theory is limited, especially over the wavemaker region itself, and cannot really provide any predictive information, e.g. where the upper-layer split will be relative to the forcing.

Because of the similarity of the $U_1 = 15\text{ms}^{-1}$ run to atmospheric blocking, this run is chosen for further, more in-depth, analysis. The meridionally-elongated shape of the eddies generated by the wavemaker are shown to produce the typical quadrupolar vorticity forcing structure evident in the model runs (Shutts (1983) showed a similar result in his one-layer model). This forcing is balanced primarily by the advection by the time-mean flow in the lower layer, which is similar to the balance found at atmospheric upper-levels (Illari 1984). The upper-layer balance is mainly between the time-mean advection and the sub-grid-scale dissipation term, the eddy feedback term is largely negligible, although it shows the bowing structure characteristic of eddies being sheared around the large-scale split. The enstrophy budgets are then analysed, including an integral budget over areas bounded by contours of eddy potential enstrophy ($(q'^2)^M$), which show that in the upper-layer, the eddy PV fluxes are downgradient in an integral sense, consistent with those found in the atmosphere. The same cannot be said of the lower-layer terms because of the external forcing provided by the wavemaker. Finally, the forcing amplitude was increased, to show that a highly non-linear large-amplitude stable response, very similar to an atmospheric block, can be excited by the wavemaker, without becoming unstable. In the next chapter, as meridional shear is added to the upper-layer jet, this property is shown to be altered considerably.

Chapter 5

Low-Frequency Vacillations

5.1 Introduction

In the previous chapter, we only considered upper-layer jets with no meridional shear. This meant that analytic Rossby-wave solutions could be easily obtained, but allowed for no meridional variation of quantities such as the refractive index (or potential function), as explained in chapter 2. In section 5.2, we run the model with an upper-layer jet with added horizontal shear, again with no lower-layer flow.

The effects on the subsequent behaviour when subjected to a wavemaker forcing are examined in section 5.3. Rather than reaching a steady equilibrium balance, a vacillation cycle is induced. The effect of the high-frequency eddies through the different phases of the cycle will be shown in section 5.4. In section 5.5, we examine the flow at different times and longitudes using a local stability criteria, which suggest that instability is the cause of breakdown. Energy diagnostics in section 5.6 will also be used to confirm this. Section 5.7 will look at the effects of altering the amplitude of the wavemaker, leading to different types of behaviour. Section 5.9 will present experiments and discuss the sensitivity of the previous results to some of the parameters chosen. A summary and discussion of the results will be presented in section 5.10.

5.2 Adding shear

We shall use the 15ms^{-1} jet from the previous chapter as a starting point, as this produced a realistic blocking-like split. Obviously, we could add any amount of shear in any form to the upper layer. To try and conserve at least one property of the initial jet, it is decided to maintain the value of the refractive index for infinite wavelengths (i.e. zonal and meridional wavenumbers, k and l, are zero) $\frac{\frac{\partial q_1}{\partial y}}{U_1}$ in

the centre of the channel. This means that the stationary Rossby wavenumber is preserved there, which should mean that an anomaly excited by the eddies, presuming it was behaving according to linear theory, should be of a similar scale at the centre.

We define the upper-layer velocity as:

$$U_1 = U_{centre} - \Delta U \left(\frac{1 - \cos my}{1 - \cos(3 \times 10^6 m)} \right) \tag{5.1}$$

where:

$$m = 5.2 \times 10^{-8} \mathrm{m}^{-1} \tag{5.2}$$

$$U_{centre} = 19 \mathrm{ms}^{-1} \tag{5.3}$$

$$\Delta U = 18 \mathrm{ms}^{-1} \tag{5.4}$$

where y ranges from -3000 km to 3000 km.

Figure 5.1 shows the upper-layer velocity (figure a), upper layer potential vorticity gradient (to the right of thin vertical line which indicates the planetary vorticity value β, figure b) and lower-layer potential vorticity gradient (to left of thin vertical line, figure b) and upper layer refractive index (figure c) for this jet (jet 2), with zero k and l wavenumbers, with values for the constant $15\mathrm{ms}^{-1}$ jet also shown (jet 1).

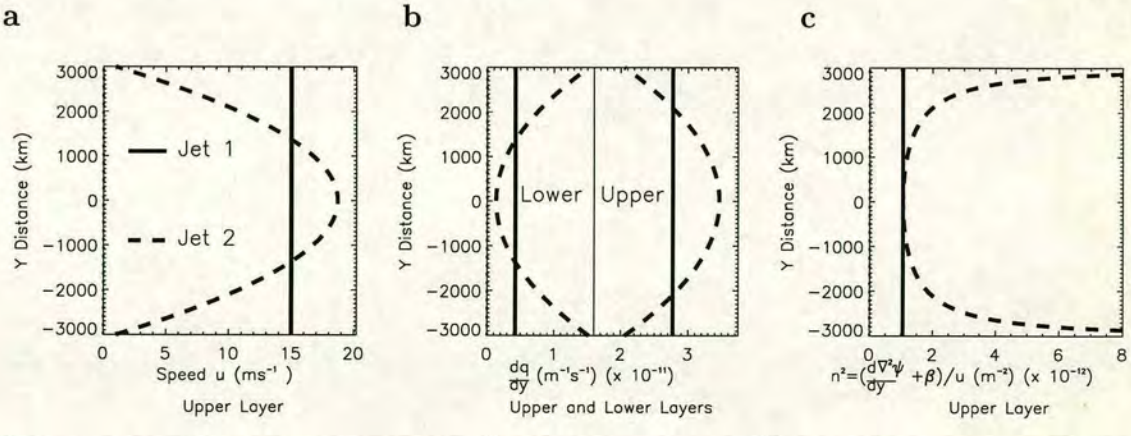

Figure 5.1: Upper-layer velocity (figure a, units ms^{-1}), upper-layer potential vorticity gradient (to right of thin vertical line (representing planetary vorticity value), figure b) and lower-layer potential vorticity gradient (to left of thin vertical line, figure b) with units $\mathrm{m}^{-1}\mathrm{s}^{-1}$ and upper layer refractive index for (figure c, units m^{-2}) shown for two jets. Jet 1 is the constant $15\mathrm{ms}^{-1}$ used previously, jet 2 is the case with horizontal shear.

With this choice of jet, we ensure that the flow is westerly everywhere. This avoids the complications of critical lines in the upper-layer, if the velocity is zero.

Also, the jet is defined such that the potential vorticity gradients are positive everywhere in both layers. This implies that the jet is baroclinically and barotropically stable to small perturbations in the classical sense (Pedlosky (1964a)).

5.2.1 Refractive Index considerations

The refractive index n^2 field for waves of infinite wavelength (k,l=0), in figure 5.1c, shows that this jet has a central minimum, which according to the soliton theory of Haines and Malanotte-Rizzoli (1991) would support a weakly non-linear jet intensification solution. The wave energy is focussed towards regions of high refractive index, which would be away from the channel centre in this case. Although jet 1 and jet 2 have the same value at the centre, if we consider the meridional average as a measure instead, this has a larger value for jet 2 than for jet 1. The average value is $2.53 \times 10^{-12}\mathrm{m}^{-2}$. If this value were obtained from an unsheared jet (i.e. as $\frac{\beta}{U_1}$), it would be the stationary wavenumber. The corresponding zonal U_1 value would be $6.3\mathrm{ms}^{-1}$, with a meridionally-dipolar wave having zonal wavenumber $1.2 \times 10^{-6}\mathrm{m}^{-1}$. This implies that for a dipolar disturbance, jet 2 will have a shorter x-wavelength stationary response than jet 1 (which was actually just over the limit for dipolar stationary waves).

5.3 Model behaviour

We keep everything the same as the previous wavemaker experiments except for altering the upper-layer flow field to the jet 2 form and relax back to this. The wavemaker amplitude used is $A = 9.2 \times 10^{-10}\mathrm{s}^{-2}$, which is less than that used for the run with constant upper-layer velocity of $15\mathrm{ms}^{-1}$ in the previous chapter. Again, the model is integrated for 360 days.

5.3.1 Time-mean response

Figure 5.2 shows the time-mean streamfunction and potential vorticity fields for the last 600 dumpsteps (approx. 200 days) of the run. The upper-layer streamfunction shows a splitting over the wavemaker region followed by a downstream intensification region. This is perhaps more reminiscent of the flows with upper-layer velocities weaker than $15\mathrm{ms}^{-1}$ (compare with figure 4.2, the case with $U_1 = 10\mathrm{ms}^{-1}$. The zonal lengthscale of the anomaly is shorter than that of the jet 1 case, as predicted due to the change in meridionally-averaged refractive

index, although the values do not match (the zonal wavenumber is estimated as $8.2 \times 10^{-7}\mathrm{m}^{-1}$, compared to the meridionally-averaged estimate of $1.2 \times 10^{-6}\mathrm{m}^{-1}$).

The lower-layer streamfunction shows the familiar quadrupole structure, similar to that of the jet 1 case. The potential vorticity fields (figure 5.2b) show a similar response, the main difference between this and the streamfunction is in the lower-layer, where the response is of smaller-scale and is situated more directly over the wavemaker region. There is also evidence of a lower-layer downstream response, not evident in the streamfunction field.

5.3.2 Time-series

As we did for the constant upper-layer velocity case, we now choose the same point as before, marked with a cross in figure 5.2, and plot a timeseries of upper-layer streamfunction ψ_1. This is shown in figure 5.3, and should be compared with figure 4.10 for the run with $U_1 = 15\mathrm{ms}^{-1}$.

This shows very different behaviour from the previous experiments with constant U_1 values. Instead of settling down to a steady value with only the weak high-frequencies of the wavemaker eddies superimposed, we get a large-amplitude low-frequency oscillation with period approximately 30 days. The Fourier transform of this field (taken from the last 600 dumpsteps with the mean removed) is also shown in figure 5.3. The small peak at 48 (relating to 48 oscillations in the 600 dumpstep period) corresponds to the wavemaker eddies, with period 4.5 days (2.25 days for each individual positive or negative anomaly to pass) and the larger peak at 7 corresponds the low frequency oscillation with a period of 31 days). A striking feature of the plot is the regularity with which the timeseries oscillates, certainly not characteristic of a chaotic process. Also, the two frequencies do not appear to be phase-locked, since at different peaks of the low-frequency cycle, the high-frequency component is at different phases.

The dots superimposed on the diagram indicate four times used in the next section to illustrate the different phases of the oscillation cycle.

5.3.3 Instantaneous plots

Perhaps the simplest way of showing the characteristics of the oscillation is to plot the model outputted fields at different instances throughout the cycle.

We can separate the flow into time-mean (denoted by a superscript M), low-frequency (superscript L) and high-frequency (superscript H) components, such

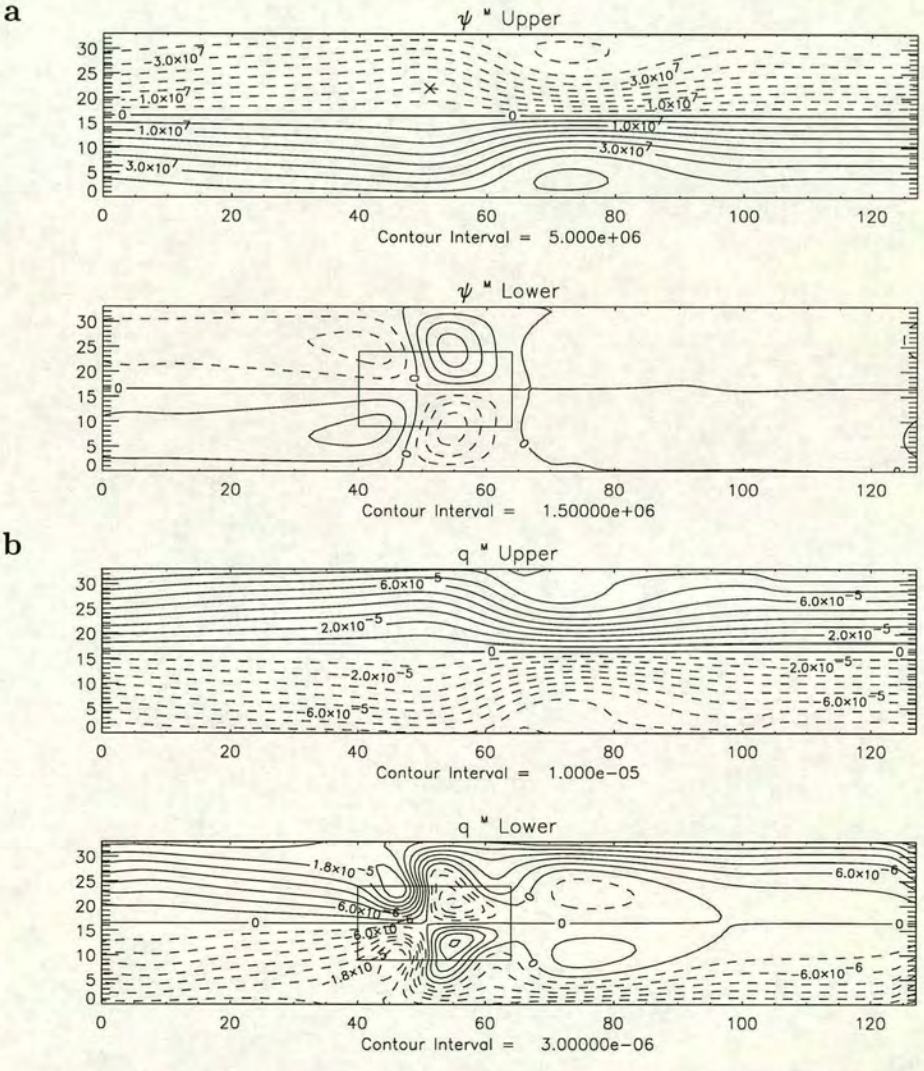

Figure 5.2: Time-mean streamfunction (figure a, units m^2s^{-1}) and potential vorticity (figure b, units s^{-1}) for the run with upper-layer velocity jet 2 (see figure 5.1) with wavemaker amplitude $A = 9.2 \times 10^{-10}s^{-2}$. Again, the position of the wavemaker in the lower-layer is outlined.

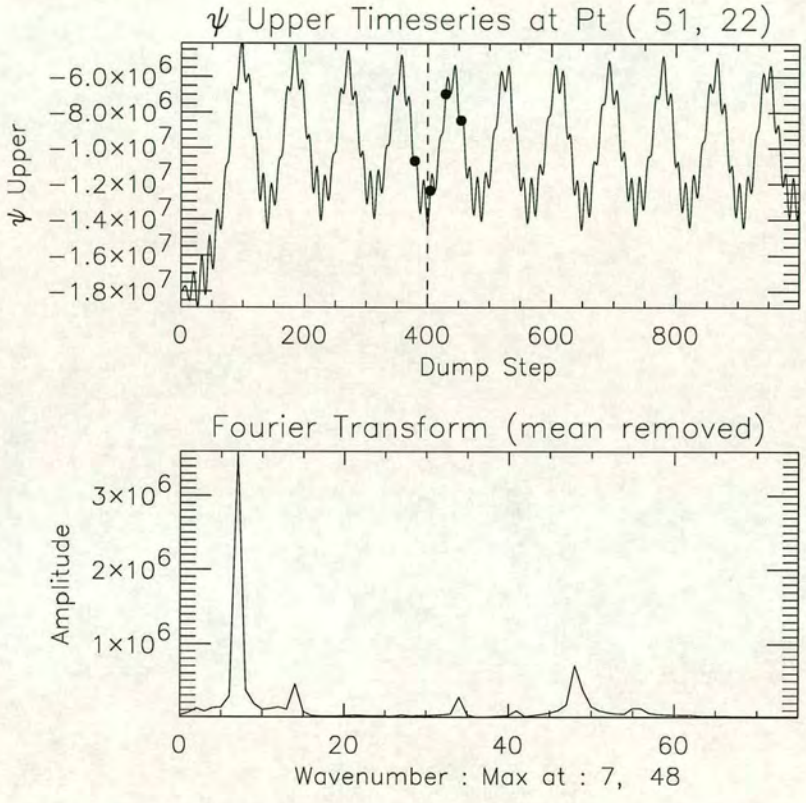

Figure 5.3: Streamfunction timeseries (upper plot) and Fourier transform (lower plot), at point (51,22) of the run with upper-layer velocity jet 2 (see figure 5.1) and wavemaker amplitude $A = 9.2 \times 10^{-10}\mathrm{s}^{-2}$. Units $\mathrm{m}^2\mathrm{s}^{-1}$. The dashed vertical line indicates the start position from where the time-mean and eddy diagnostics are taken. This time there is a low-frequency oscillation component evident as well as the high frequency of the wavemaker eddies. The four dots correspond to the four phases selected for further analysis, labelled (from left to right) Zonal, Grow, Block, Decay.

as:

$$\psi = \psi^M + \psi^L + \psi^H \tag{5.5}$$

using a filter technique. Because this model run has two very distinct frequencies, they are easily separable into the three components. We choose to separate into the time-mean plus low-frequency components, which we will denote with a superscript $M + L$, and the high-frequency component.

Figure 5.4 shows the filtered model fields (streamfunction ψ^{M+L} down the left column, potential vorticity q^{M+L} down the centre column) through the different phases of the oscillation. The fields have been low-pass filtered to remove the high frequency wavemaker eddies to allow the larger scales to be seen more clearly. The low-pass component of the high-frequency eddy feedback $-J(\psi^H, q^H)^{M+L}$ is shown down the right column. This gives an indication of the effect of the wavemaker eddies on the large-scale low-frequency flow.

The four low-pass filtered phases correspond to the model dumpsteps 380, 405, 430, 455 respectively, and are therefore 9 days (25 dumpsteps) apart. We shall label these phases Zonal, Growth, Blocked and Decay respectively. Since the oscillation has a 31 day period, this means that the time between the Decay phase and the Zonal phase of the next cycle is only 4 days. This is done to best show the different characteristics of each phase. The position of these four phases is shown on the time-series plot (figure 5.3). We shall now consider each phase separately.

5.3.3.1 Zonal : figures a,e,i

As can be seen from either the streamfunction ψ or potential vorticity q fields, this phase is not strictly zonal, although it has the weakest anomaly from the initial state. The upper-layer ψ contours show a weak widening over the wavemaker region, with an intensification downstream. In the lower-layer, there are the first signs of an anomaly forming over the wavemaker region, due to the lower-layer quadrupolar forcing of the high-frequency eddies (figure i). The upper-layer component is much weaker than the lower-layer, as would be expected as the wavemaker forcing is present in the lower-layer only.

5.3.3.2 Growth : figures b,f,j

The major noticeable difference between this phase and the previous zonal phase is the growth of the lower-layer quadrupole anomaly, evident in both the streamfunction and potential vorticity fields. Figure f shows tight q gradients forming

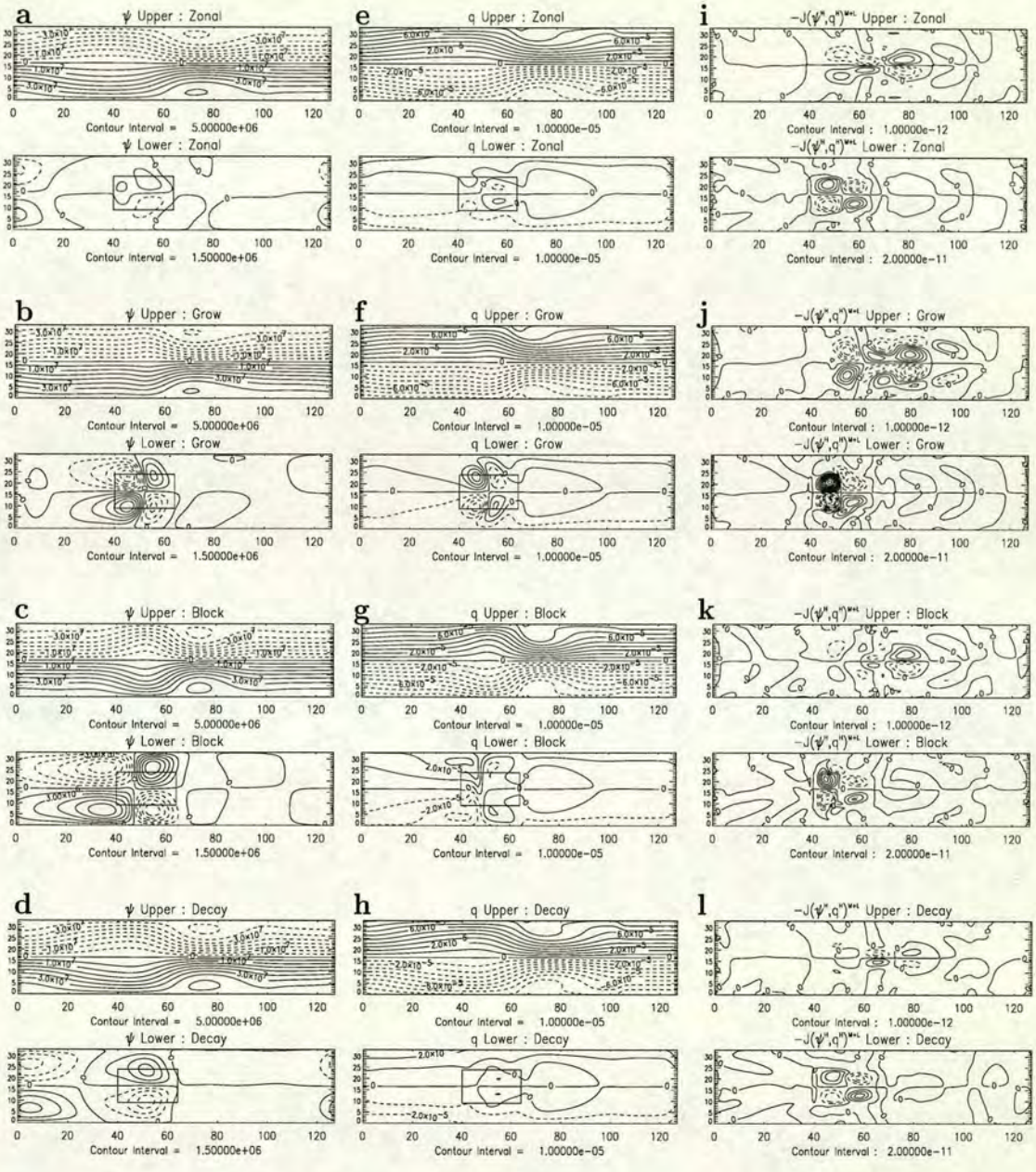

Figure 5.4: Instantaneous low-pass filtered streamfunction ψ^{M+L} (left column, Figs. a-d, units m^2s^{-1}) , potential vorticity q^{M+L} (middle column, Figs. e-h, units s^{-1}) and low-pass filtered high-frequency eddy feedback $-J(\psi^H, q^H)^{M+L}$ (right column, Figs. i-l, units s^{-2}) fields for phases of the low frequency oscillation (zonal (a,e,i), grow (b,f,j), block(c,g,k) and decay (d,h,l)). The time interval between each is 9 days (25 dumpsteps).

over the wavemaker region. In the upper-layer, the flow is more zonal upstream of the wavemaker, but a split is developing above the lower-layer anomaly. The high-frequency eddy forcing has increased in magnitude, attaining its largest amplitude during this phase.

5.3.3.3 Blocked : figures c,g,k

The upper-layer flow is now at its most split above the wavemaker region, with the downstream intensification also at maximum amplitude. The lower-layer streamfunction still shows a quadrupolar structure, but it has extended zonally upstream, and lost some of the tilting structure found in the growth phase. The potential vorticity field (figure g) shows that the tight quadrupole structure has dispersed outward toward the walls, there no longer being the tight gradients as in the previous phase. The eddy forcing (figure k) still retains the quadrupolar lower-layer forcing, the amplitude being reduced from the previous growth phase.

5.3.3.4 Decay : figures d,h,l

The lower-layer quadrupole streamfunction formation has now separated into two dipoles. The left-hand one is propagating upstream towards the sponge region, where it is dissipated. The right-hand one remains over the wavemaker region, having moved slightly upstream, and decays *in-situ*. The lower-layer q field (figure h) shows very little signature. The upper-layer streamfunction shows the split and intensification structure increasing in zonal wavelength. The high-frequency eddy forcing is now at its weakest of the four phases.

5.3.4 Höv Möller diagram

An alternative way of representing this cycle is to use a contour plot against time, a Hov Moller diagram. We need to reduce our space dimensions to 1, and so choose to plot the values at different times along the line $y = 25$, a strip running along the northern half of the channel. Figure 5.5 shows such a diagram, where the low-pass filtered fields are plotted with the initial flow subtracted. For the streamfunction fields, the light-coloured areas represent positive anomalies from initial zonal condition, which for the northern half of the channel represents a splitting of the jet stream. Associated with a positive streamfunction anomaly is a negative potential vorticity anomaly, and vice-versa. The four horizontal lines on each plot represent the four phases described in the previous section, reading (vertically upward) as Zonal, Growth, Blocked and Decay. For this diagram, the

upper-layer streamfunction anomaly (top-left) can be seen to increase in amplitude and then extend zonally and propagate upstream. The upper-level q (top-right) shows a similar picture, but with more small-scale definition, with negative values where the positive streamfunction values are. The lower-layer shows clearly the quadrupole build-up, shown as the small-scale intense dipole. The positive anomaly can be seen to propagate upstream, whilst the negative anomaly spreads zonally and decays.

5.3.5 Summary of vacillation

So, to summarise our observations of the vacillation cycle from just the streamfunction and potential vorticity fields, we have:

- The wavemaker provides a transient forcing which resonantly excites a large-scale flow pattern, as was the case with the U_1 constant cases.
- This pattern has a quadrupolar structure in the lower layer, and a split region with a downstream intensification in the upper layer.
- Unlike the case with a constant upper-layer jet, rather than reaching a steady equilibrium solution whereby the eddy-forcing balances the dissipation together with mean-flow advection, a vacillation cycle is induced.
- Through a combination of propagation and dissipation, the flow evolves back to a near zonal state, whereby the re-excitation of the large-scale stationary wave commences another cycle.

5.3.6 Time-mean eddy feedback

We can break down the potential vorticity tendency equation into mean, low-frequency and high-frequency components as follows:

$$\frac{\partial q^M}{\partial t} = -J(\psi^M, q^M) - J(\psi^L, q^L)^M - J(\psi^H, q^H)^M, \tag{5.6}$$

$$\frac{\partial q^L}{\partial t} = -J(\psi^{M+L}, q^{M+L})^L - J(\psi^H, q^H)^L, \tag{5.7}$$

$$\frac{\partial q^H}{\partial t} = \delta_{i,1} W - J(\psi^H, q^{M+L}) - J(\psi^{M+L}, q^H) - J(\psi^H, q^H)^H. \tag{5.8}$$

Adding equations 5.6 and 5.7 gives the $-J(\psi^H, q^H)^{M+L}$ terms plotted in figure 5.4(i-l). Equation 5.6 has three terms on the right hand side. The second and

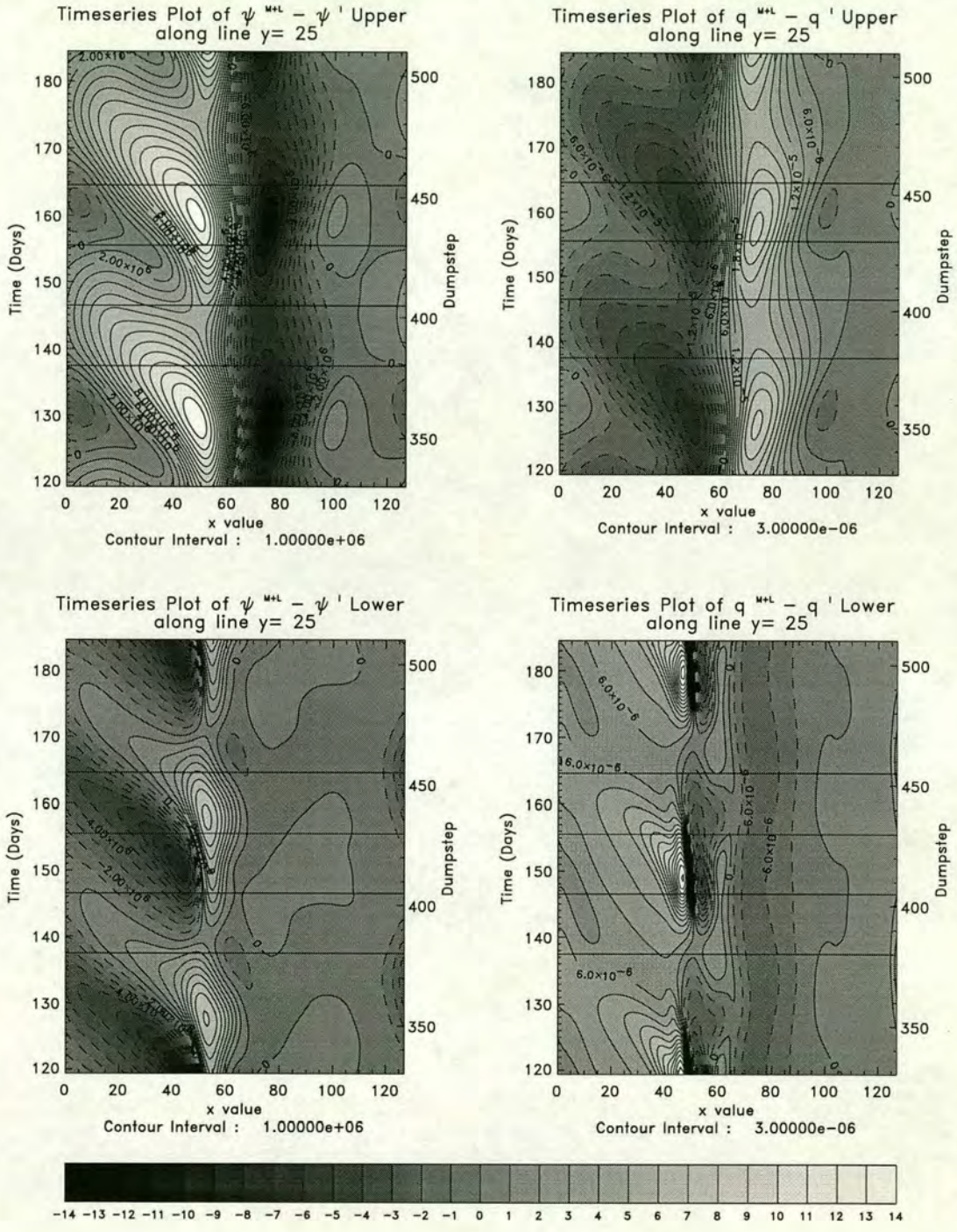

Figure 5.5: Höv Möller diagram of a slice at $y = 25$ with time increasing vertically upwards. The fields are difference from the initial conditions: upper streamfunction (top left), lower streamfunction (bottom left), upper potential vorticity (top right) and lower potential vorticity (bottom right). The time is now in units of days, with the period of the low frequency oscillation being approximately 31 days. The four horizontal lines on each plot indicate the four phase positions. Units are $m^2 s^{-1}$ for streamfunction, s^{-1} for potential vorticity.

third terms, the low and high frequency eddy feedback on the time-mean flow, are shown in figure 5.6. The lower-layer is dominated by the quadrupolar structure of the high-frequency term, the low-frequency term also being quadrupolar but with a smaller-scale and not centralised over the wavemaker region. In the upper-layer, the high-frequencies have a dipole with negative north of positive over the wavemaker region. This has the tendency to reduce the q gradients here. The low-frequency term has an opposite structure over this region. Also, the high-frequency term has a stronger reverse sign (positive north of negative) dipole downstream over the intensification region, which corresponds to a tightening of the q gradients and an intensification of the jet. The time-mean high-frequency eddy feedback $-J(\psi^H, q^H)^M$ of figure 5.6b can be compared to the low-pass filtered instantaneous terms $(-J(\psi^H, q^H)^{M+L})$ of figures 5.4(i-l). These show a similar structure to their time-mean term, but with varying amplitudes, reflecting how the high-frequency eddies appear to be constantly forcing the splitting pattern observed.

5.4 High-frequency eddy feedback changes through the cycle.

We have seen how the forcing by the high-frequency eddies on the low-frequency component of the flow alters during the cycle. The structure remains similar throughout the cycle, dominated by a quadrupolar structure in the lower-layer, though the magnitude can vary considerably. The maximum amplitude of the forcing occurs during the growth phase, whereas the maximum anomaly occurs in the blocked phase, implying that the response lags behind the forcing. It could perhaps be inferred that it is the oscillation in the forcing which forces the large-scale Rossby wave around the cycle. However, it is the changes in the large-scale circulation which also alter the high-frequency eddies in a continual feedback process, and so isolating either as a cause would be impossible. The oscillation in the forcing undoubtably has an effect in not producing a steady response, but can it explain the whole oscillation? This is doubtful, as the forcing retains a similar structure through the vacillation cycle, dominated by the lower-layer quadrupole structure. Simply varying its amplitude could not explain the separation of the streamfunction quadrupole response into two separate dipoles, nor the upstream propagation of the left pair. In a similar way as Shutts (1983) and that performed in section 4.8.2, to illustrate this fact, the high-frequency

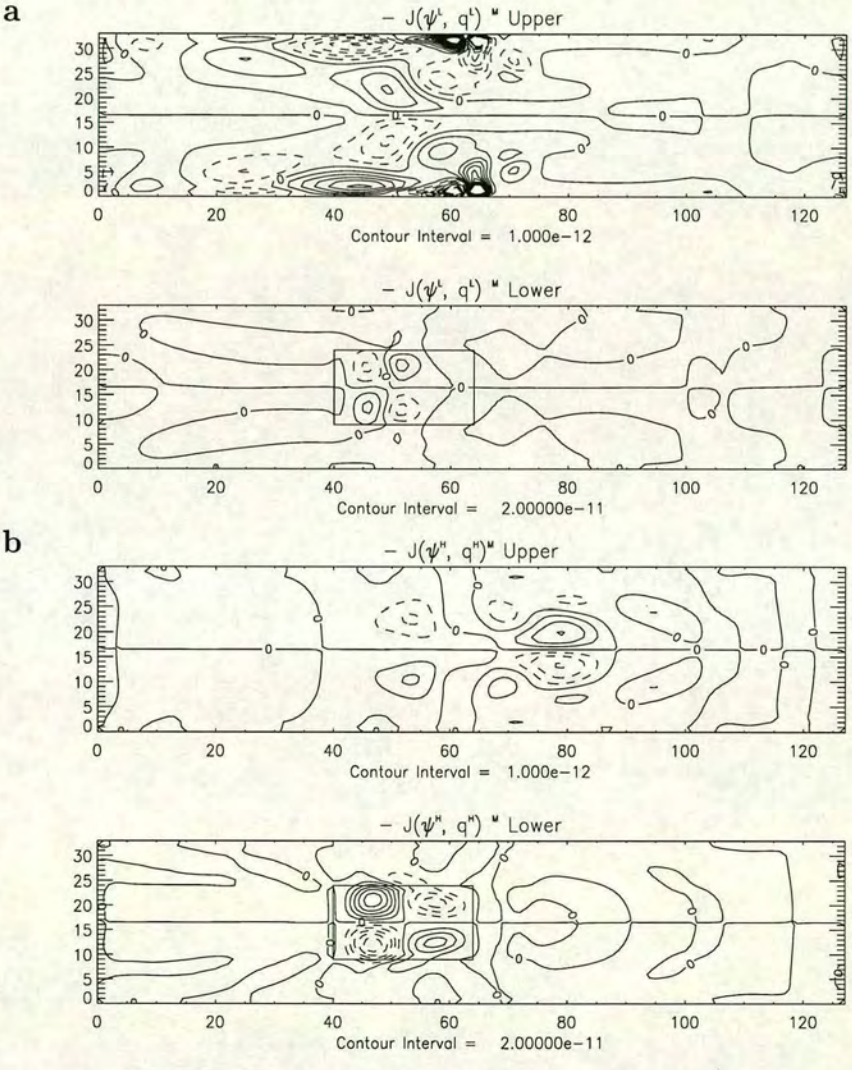

Figure 5.6: Time-mean eddy feedback on the potential vorticity tendency from the low frequency $-J(\psi^L, q^L)^M$ (figure a) and high frequency $-J(\psi^H, q^H)^M$ (figure b) eddies for the jet 2 wavemaker run. Units s^{-2}.

eddy forcing terms shown in figures 5.4(i-l) were used as a constant forcing in the model, replacing the wavemaker. The model was then integrated until a steady state was reached. Figure 5.7 shows the results for two of the phases, growth (figure a) and blocked (figure b). The growth phase forcing actually forced the

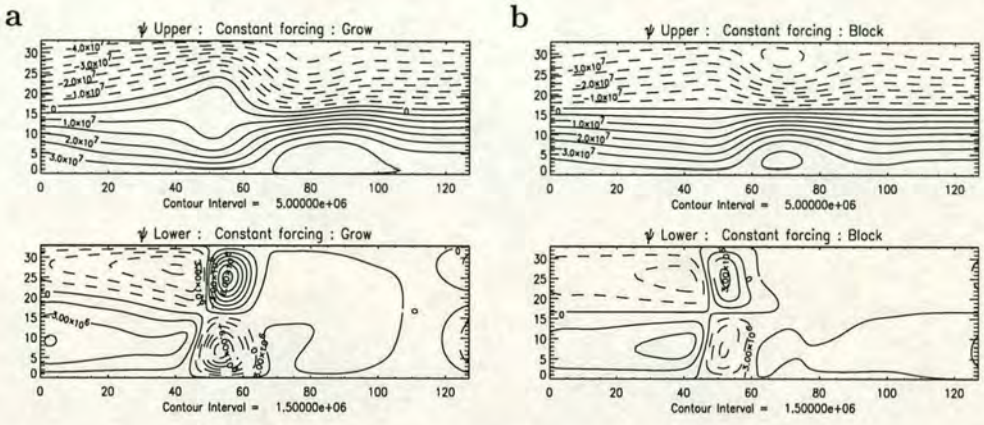

Figure 5.7: Upper and lower-layer streamfunction response to the instantaneous high frequency feedback -$J(\psi^H, q^H)^{M+L}$ as a steady forcing from the growth (figure a) and the blocked (figure b) phases. Units m^2s^{-1}.

flow to such a large amplitude that it goes unstable so a steady state wasn't reached. For this reason, the last 200 days of the run were averaged and displayed instead, which is why the flow is antisymmetric. As can be seen, the upper-layer has a large-amplitude split, which is much larger than at any time during the wavemaker-driven vacillation cycle. The blocked phase forcing, figure 5.7b, is much weaker, and the flow attains a steady state which has a weaker split than during the corresponding period in the wavemaker run. The results for the other two phases, zonal and decay, are rather similar to the blocked case, but with a smaller amplitude split. In all four cases, the size of anomaly produced by the steady forcing is larger than that during the zonal phase of the vacillation, when the anomaly is at its weakest. This implies that if there were no other mechanism involved in producing the oscillation, that once the anomaly had built up from initial conditions, it would not reduce below the minimum amplitude produced by the weakest high-frequency eddy forcing, which it clearly does. This suggests that another mechanism must be involved to reduce the amplitude of the anomaly closer to zero (especially in the lower layer).

It was speculated that a steady forcing could push an anomaly past a 'critical amplitude' which would be enough to cause instability leading to flow breakdown, and the steady re-excitation would cause a vacillation cycle. Attempts were made

using the growth-phase high-frequency eddy feedback (figure 5.4j) constant forcing at a reduced amplitude, to see whether a low-frequency vacillation cycle could be maintained using a constant forcing, rather than the wavemaker, but with little success. Using an amplitude of 80% of the original, a steady state was eventually maintained, but with a larger dipolar anomaly than the maximum in the vacillation cycle, which makes specifying a critical amplitude for instability to occur very difficult. The fact that this experiment failed to produce a regular cycle suggests that an amplitude reduction of the feedback term is also required to allow the flow anomaly to reduce sufficiently to allow a similar excitation as that from the zonal initial flow.

If we represent these responses by a single parameter value, using the value of streamfunction at the same point used for the previous time-series, we get figure 5.8. The solid circles show the values obtained by the wavemaker run (which were also shown on figure 5.3), the open triangles represent the values obtain by the steady forcing runs. This shows the model response lagging the high-frequency eddy forcing, which has its maximum at the growth phase, since the model response peaks at the blocked phase.

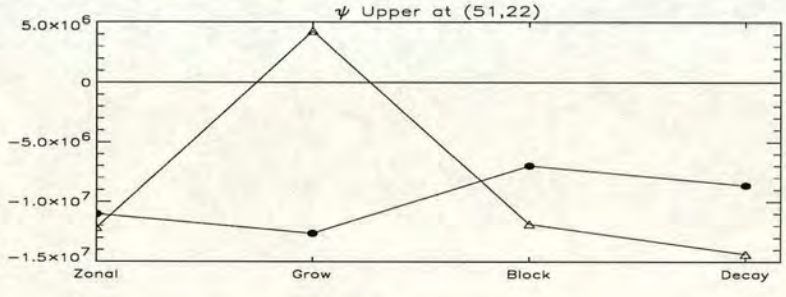

Figure 5.8: Plot showing the value of upper-layer streamfunction ψ at point (51,22) at the four phases of the oscillation during the wavemaker run (solid circles) and from the experiment using $-J(\psi^H, q^H)^{M+L}$ from the corresponding phases as a constant forcing (open triangles). Units m^2s^{-1}.

5.5 Instability theory

The previous section showed that although the high-frequency eddy forcing alters in magnitude through the cycle, it was not sufficient to explain the full vacillation behaviour. Helfrich and Pedlosky (1995) described how a finite-amplitude solitary wave in a marginally stable background flow could make the flow locally unstable, and so a similar approach is adopted here. The study of the full stability properties

of a transient, non-zonal flow is rather difficult, and so we elect to perform a simplified analysis in order to attempt to explain the behaviour.

We will examine the flow at various times and longitudes and examine the stability. We develop a simplified zonal assumption technique to approximate the flow at a particular x position as an equivalent zonal flow. Although this is not strictly correct, it should give an indication of the relative instability of the flow i.e. times and locations where the flow is more unstable than others.

Appendix A contains the full details of the derivation.

The following sequence of events leads us to a pair of eigenvalue equations.

- Take potential vorticity tendency equations for the channel.
- Assume frictionless and zero forcing function, i.e. right hand side zero.
- Linearise about a flow independent of x.
-
  - Move to a frame of reference translating at constant speed c.
  - Assume long timescale, so ignoring the time derivative term at this new frame of reference.
- Set zonal wavenumber to be a constant value (initially we will choose $k = 0$, but the sensitivity of this assumption is tested later).

These assumptions gives us an eigenvalue problem, with the phase speed c as the eigenvalue

$$\left(U_1(y)\left(\frac{\partial^2}{\partial y^2} - k^2 - \lambda^2\right) + \frac{dQ_1}{dy}\right)\psi_1' + U_1(y)\lambda^2\psi_3' = c\left(\left(\frac{\partial^2}{\partial y^2} - k^2 - \lambda^2\right)\psi_1' + \lambda^2\psi_3'\right) \tag{5.9}$$

$$\left(U_3(y)\left(\frac{\partial^2}{\partial y^2} - k^2 - \lambda^2\right) + \frac{dQ_3}{dy}\right)\psi_3' + U_3(y)\lambda^2\psi_1' = c\left(\left(\frac{\partial^2}{\partial y^2} - k^2 - \lambda^2\right)\psi_3' + \lambda^2\psi_1'\right) \tag{5.10}$$

where $U_i = -\frac{d\Psi_i}{dy}$ are the zonal velocity components of layer i of the low-pass filtered fields at a particular time and x position, with its corresponding potential vorticity gradient $\frac{dQ_i}{dy}$; ψ_i are the meridional eigenvectors and c are the zonal phase speed eigenvalues. We have assumed the zonal wavelength of the eigenmodes to be

infinite by setting $k = 0$ initially. The stability was analysed in a finite-difference representation at the same resolution as the channel.

In our case, our model outputs ψ_1 and ψ_3 as functions of x, y and t. If we loop through the variables x and t, then we end up with an equivalent $\Psi_1(y)$, $\Psi_3(y)$ for each x, t, which we then treat as if it were a zonal flow. Since this ignores extra curvature in the actual flow, it is likely to underestimate the stability of the flow. This means that if this zonal flow is found to be unstable, it is likely that the actual flow around that position is also unstable. We then calculate $Q_1(y)$ and $Q_3(y)$ from the $\Psi_1(y)$, $\Psi_3(y)$ fields using finite difference methods for the derivative term as described in the appendix. Note however that we do not take the model output q field at the same instant, as this will contain the extra term $\frac{\partial^2}{\partial y^2}\Psi(y)$. The problem was coded in matrix form and solved using a Numerical Algorithms Group (NAG) standard fortran library routine, which returns a set of eigenvalues, c, and corresponding eigenvectors (ψ_1, ψ_3). The presence of unstable eigenmodes is indicated by the existence of complex eigenvalues, $c = c_r + ic_i$, when the imaginary component, c_i, gives the growth rate and the real component, c_r, gives the propagation speed. Also, because the observed instability is dominated by a meridional wave number 2, we restrict our search to wave-2 eigenmodes, as these are the ones which will have most influence in exciting the blocking-type split. In the case where there are more than one unstable wave-2 eigenmode for a particular x and t, the one with the largest imaginary component of phase speed (and therefore largest growth rate) is selected.

Figure 5.9(a,b) show the real and imaginary components of the eigenvalue associated with the wave 2 eigenmode plotted as a function of zonal position and time. This method of display shows exactly at what zonal positions and at what times the flow becomes unstable. The times of the four phases shown in figure 5.4 are indicated.

We can see that in the zonal phase, the channel flow is stable for all values of x, whereas in the growth phase, at x values around 45, there are eigenmodes with an imaginary component of phase speed, indicating an unstable mode. These x values correspond to a position near the upstream end of the maximum split in the upper-layer jet stream. It appears to be the region of the westerly flow in the lower-layer upstream of the upper-layer split which is responsible for the instability. If the maximum growth rates of the unstable eigenmodes are calculated from $Im(c)$ by estimating a suitable k value ($k = 1.4 \times 10^{-6}$ m^{-1}), an e-folding timescale of a few days results. The real component of the eigenvalue for these unstable modes

is always negative indicating upstream propagation with a typical speed of around 10ms^{-1}. This is consistent with the observations of upstream propagation noted from the instantaneous snapshots of figure 5.4.

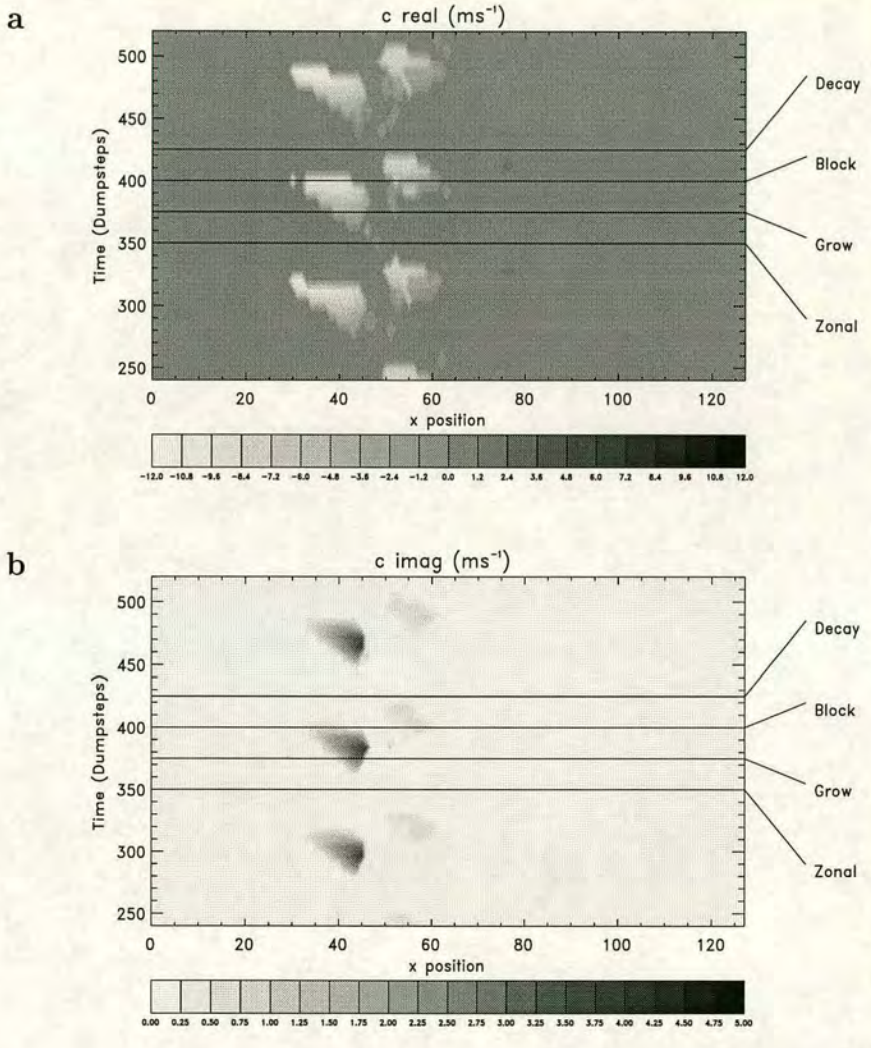

Figure 5.9: Real (figure a) and imaginary (figure b) components of the phase speed for the most unstable wave 2 eigenmode of the zonal problem with $k = 0$ as contours plotted against x position in channel (horizontal axis) and time (vertical axis). The four horizontal lines shown indicate the position of the four phases shown in figure 5.4 : reading vertically upwards, these are zonal, grow, block and decay. Units ms^{-1}.

If we then perform the above analysis using this value of k in the equations, rather than setting k=0 as we did initially, we get the results shown in figure 5.10. Comparing this with figure 5.9 with k=0, we see that although the pattern is over similar regions in the plot, the values are quite different with the $RE(c)$ now being

positive over most regions, and the $Im(c)$ component being more negative in value, indicating a faster growth rate. These differences arise due the assumptions made for a k value, and the fact that the flow examined is not the true flow. However, both these sets of results give a similar time and location for the instability, and both represent it as a localised and time-dependent phenomenon.

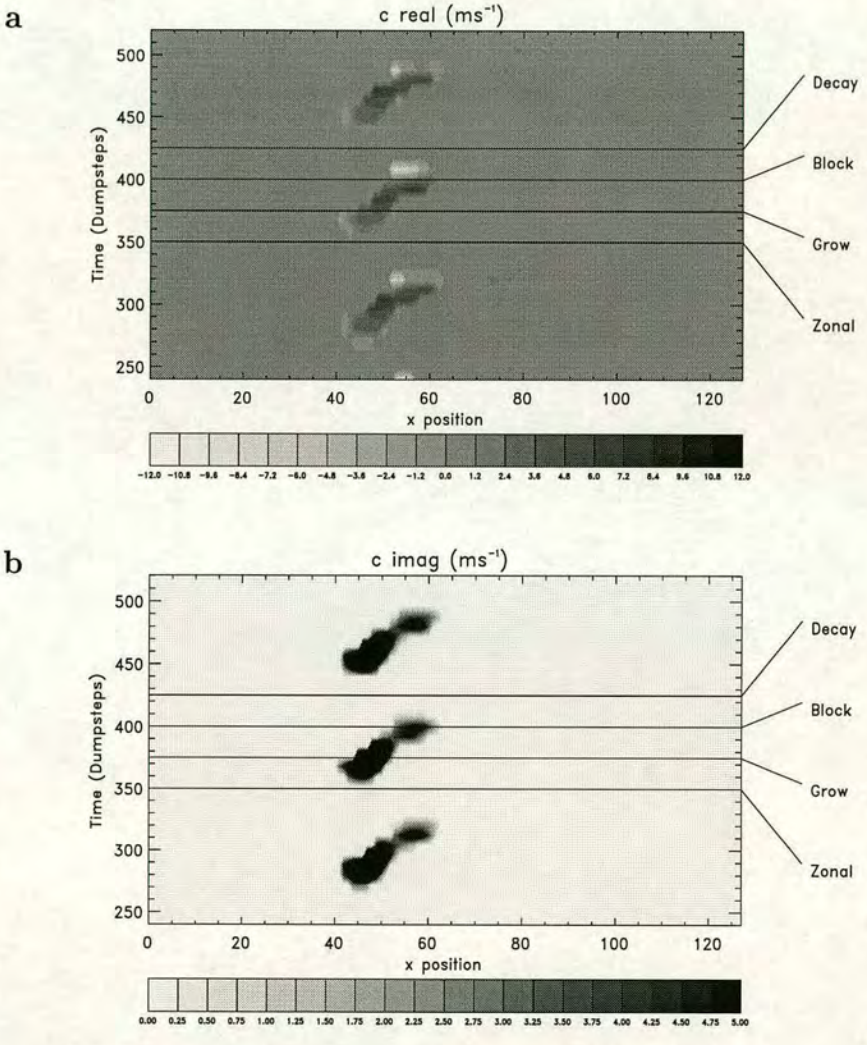

Figure 5.10: Real (figure a) and imaginary (figure b) components of the phase speed for the most unstable wave 2 eigenmode of the zonal problem with $k = 1.4 \times 10^{-6}$ m^{-1}. as contours plotted against x position in channel (horizontal axis) and time (vertical axis). The four horizontal lines shown indicate the position of the four phases shown in figure 5.4 : reading vertically upwards, these are zonal, grow, block and decay. Units ms^{-1}.

If we split the flows which are unstable into their barotropic and baroclinic components, such as

$$\psi_{bt} = \frac{\psi_1 + \psi_3}{2} \tag{5.11}$$

$$\psi_{bc} = \frac{\psi_1 - \psi_3}{2} \tag{5.12}$$

we find that neither of the components alone are unstable, which shows that the instability is of a mixed barotropic/baroclinic type, needing shears in both the horizontal and vertical in order to grow.

We can contrast this with the behaviour of zonal upper-layer jets, which only have a vertical component of shear. These remained stable even with a large amplitude anomaly.

5.6 Energy considerations

In this section we use an analysis of energy conversions as presented in the recent paper by Higgins and Schubert (1994). A fuller derivation of the equations can be found in Appendix B.

Following some mathematics, the following equation for the time tendency of the low-frequency kinetic energy $\frac{\partial}{\partial t}\left(\frac{\mathbf{v}^L.\mathbf{v}^L}{2}\right)$ is obtained,

$$\frac{\partial}{\partial t}(KE^L) = C(KE^M, KE^L) + C(KE^H, KE^L) + C(PE^L, KE^L) + R + F \tag{5.13}$$

where

$$C(KE^M, KE^L) = -\left\langle \zeta^L \mathbf{v}^L.\mathbf{k} \times \mathbf{v}^M \right\rangle$$

represents a barotropic energy conversion from the mean flow to the low-frequency kinetic energy,

$$C(KE^H, KE^L) = \left\langle \zeta^H \mathbf{v}^H.\mathbf{k} \times \mathbf{v}^L \right\rangle$$

represents a barotropic energy conversion from the high-frequency to the low-frequency kinetic energy,

$$C(PE^L, KE^L) = -\left\langle f_0 \psi^L \nabla.\mathbf{v}^L \right\rangle$$

represents a conversion from the low-frequency potential to low-frequency kinetic energy,

$$F = \mathbf{v}^L.(-(\varepsilon + S(x))\mathbf{v}^L + \nu\nabla^2\mathbf{v}^L)$$

is the component due to friction and R is the sum of all the remaining terms which are not included elsewhere. Note that $\langle\rangle$ indicates a sum over a layer and $\mathbf{v}$ is the geostrophic velocity in all terms except $\nabla.\mathbf{v}^L$.

We use a slightly different notation to Higgins and Schubert (1994), namely in the superscripts (our mean M is their seasonal mean S and our high-frequency H is their bandpass-frequency B), and we don't use a composite average over various events as they did. We simply look at the balances for one oscillation as the behaviour here is more regular than their GCM data. The divergence term $\nabla.\mathbf{v}^L$ is calculated using the vorticity tendency equation. Our R term has only been approximately calculated and, like Higgins and Schubert, we ignore any terms with the vertical velocity w in, but the balance appears to be good even neglecting these.

Figure 5.11 shows these terms as they vary through the vacillation cycle. The upper plots are for the upper-layer, the lower pair for the lower-layer. The left hand plots show the three conversion terms plus their sum, representing the total conversion term. The right hand plots show this total together with the R and F terms, the total sum of all the right hand side of equation 5.13, and finally a direct estimate of the left hand side tendency in KE^L, calculated from the model.

We first consider the balances in the lower-layer. The bottom-left plot shows that the dominant term is the barotropic conversion from high-frequencies. This involves a large peak during the growth phase period, indicating that the high-frequencies are responsible for the growth of the anomaly. In the blocked phase, the contribution from this term is approaching zero and it becomes negative in the decay phase. The bottom-right plot shows the contributions from the other terms to the total balance. The high-frequency conversion term is much larger in magnitude than the total conversion term, the difference coming from the friction, which is negative at all periods throughout the cycle, and the residual R terms, of which the dominant component is $\left\langle \mathbf{v}^L.(\zeta^H\mathbf{k} \times \mathbf{v}^H)^M \right\rangle$. Note that Higgins and Schubert found their R term to be dominated by the term $\left\langle \mathbf{v}^L.(\zeta^L\mathbf{k} \times \mathbf{v}^L)^M \right\rangle$. Now we shall consider the upper-layer. The conversion terms are different in this layer mainly due to the weaker effects of the high-frequencies. The upper-left plot shows that conversion from high-frequencies now has the smallest contribution. Instead, the conversion from low-frequency potential energy is the dominant term, which peaks just before the blocking peak. This is consistent with baroclinic instability setting in at that time, converting potential to kinetic energy. The conversion from the mean kinetic energy also supplements this term with a

peak just after the block peak, indicating a barotropic instability component. In the top-right plot, variations in total KE^L production is shown to mirror this conversion term, but with variation about zero due to the friction term which increases a little during the decay phase of the cycle. The R term in the upper-layer is negligible in the balance. Comparing the sum of the terms calculated with the energy tendency observed, we have a good shape, with a slight underestimation at all points, due to the terms neglected.

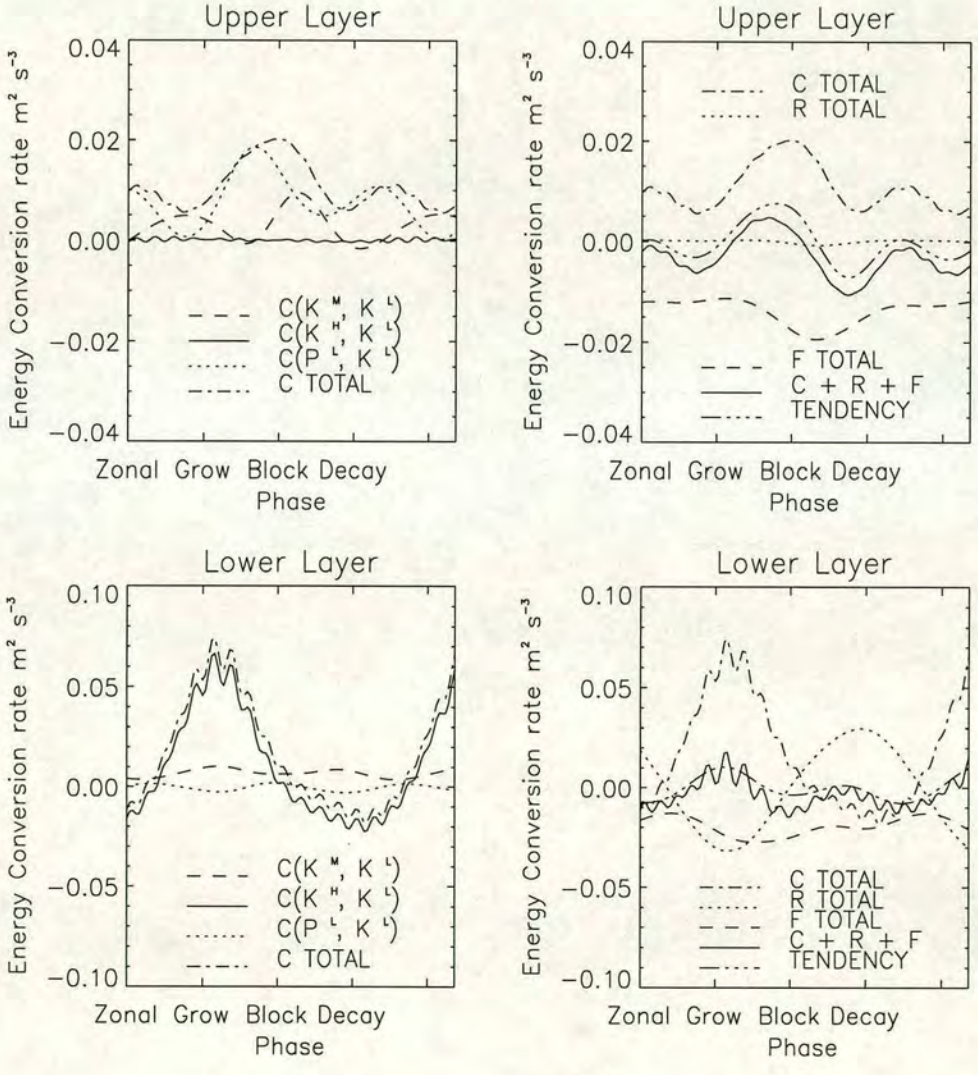

Figure 5.11: Left hand plots show the three conversion terms $C(K^M, K^L)$, $C(K^H, K^L)$ and $C(P^L, K^L)$ and the sum of all three (C) for the two layers separately. The right hand plots show this sum (C), the R term, the friction term (F), the sum of these three terms. Also, the tendency of the model flow for comparison, the last two should be equal except for remaining neglected terms. Units $m^2 s^{-3}$.

Run	Wavemaker Amplitude (s^{-2})	Proportion of Original
Original	9.2×10^{-10}	1.0
A	1.8×10^{-10}	0.2
B	1.4×10^{-9}	1.5
C	1.8×10^{-9}	2.0
D	2.8×10^{-9}	3.0

Table 5.1: Table of wavemaker amplitudes and ratios from the original for 3 further experiments.

5.7 Non-linear aspects

Having observed this low-frequency vacillation cycle, we can now examine the effects of altering the wavemaker amplitude on the behaviour of the large-scale flow, in particular with regard to the frequency characteristics of the excited flow.

We perform four runs with different values of the wavemaker, and display the time-series at the same point as before in figure 5.12.

Table 5.1 shows the amplitudes used for the four runs, compared with the original oscillating run.

In run A (figure 5.12a) with a reduced amplitude forcing, the wavemaker eddies are clearly visible but there is little sign of the low-frequency oscillation. In run B (figure 5.12b), where the amplitude of the wavemaker has been increased, the low-frequency oscillation period has decreased from 31 days to 24 days, but there are still only two frequencies evident. Run C increases the amplitude yet further. Extra peaks start to appear on the Fourier transform plot, indicating that more frequencies are beginning to appear. If the wavemaker amplitude is further increased the flow rapidly develops other oscillation frequencies and the response begins to be chaotic, as shown in figure 5.12c for run D. This transition to chaos is characteristic of other non-linear cases, see for example Pedlosky and Frentzen (1980), where period-doubling leads to a chaotic situation. This sensitivity to the wavemaker amplitude is consistent with an instability mechanism being responsible for the breakdown of blocking in the channel. If the amplitude of the split jet is insufficient (weak wavemaker), the low-frequency oscillation is absent. If the high-frequency eddies are stronger the split jet reaches the amplitude required for large-scale instability more rapidly and therefore block decay sets in leading to an increase in block-decay cycle frequency.

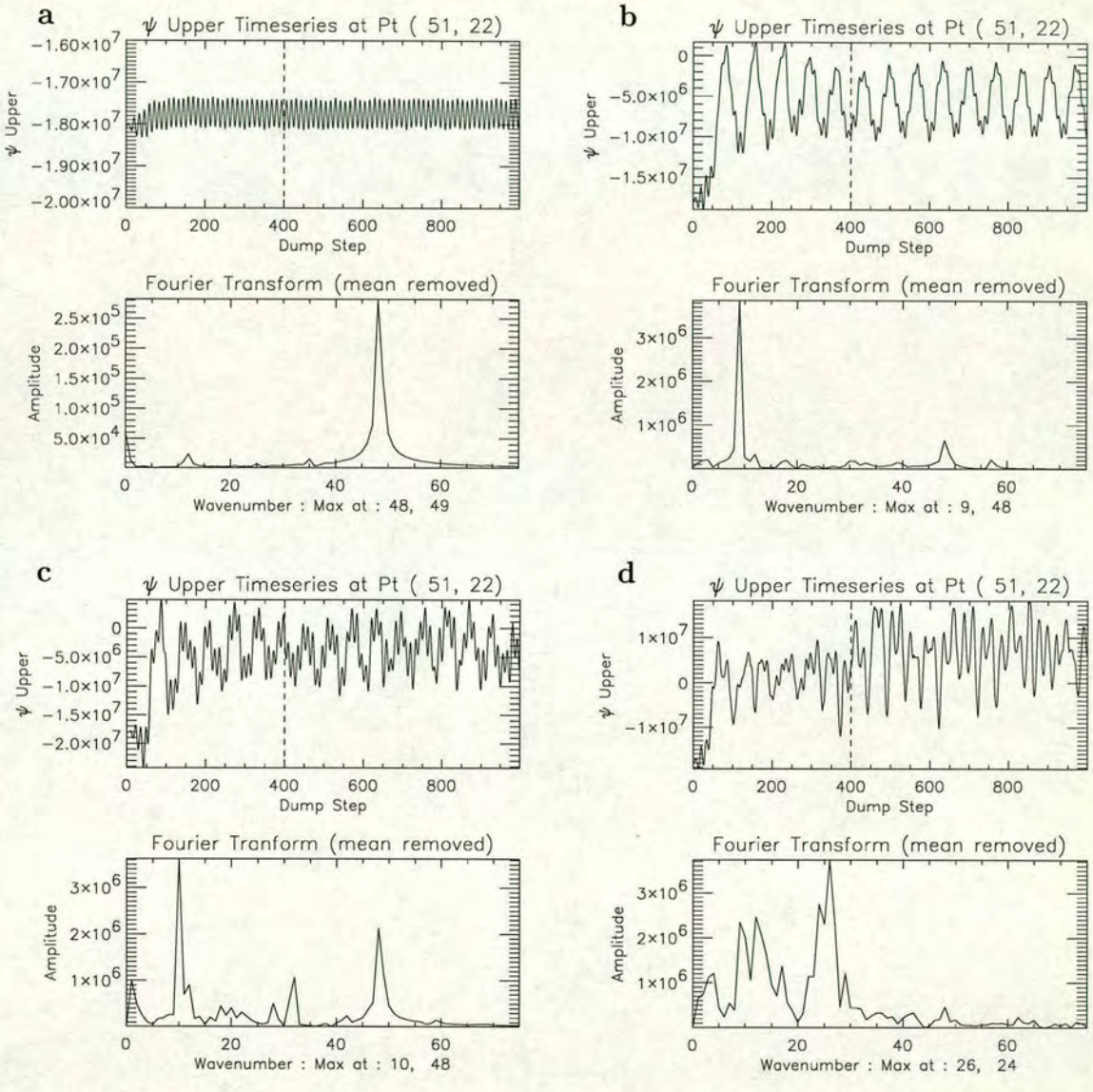

Figure 5.12: Streamfunction timeseries at point (51,22) in the upper-layer (units m^2s^{-1}) and corresponding Fourier transforms shown for jet 2 cases with wavemaker amplitudes $A = 1.8 \times 10^{-10}s^{-2}$ (figure a), $A = 1.4 \times 10^{-9}s^{-2}$ (figure b), $A = 1.8 \times 10^{-9}s^{-2}$ (figure c) and $A = 2.8 \times 10^{-9}s^{-2}$ (figure d) (compared with $A = 9.2 \times 10^{-10}s^{-2}$ for the standard case).

5.8 Oscillation transitions

We have now seen a cases in Chapter 4 where a stable dipolar standing wave is excited, and a case where a low-frequency vacillation cycle is generated by the same forcing but a different jet structure. However, it can be noted from the timeseries in figure 4.10, the case with upper-layer velocity 15 ms^{-1}, that even in such a case where the flow eventually attains a steady equilibrium solution, initially there appears to be an oscillation present, which eventually dies out.

We can look at a jet intermediate to this jet and the sheared jet of previous sections (Jet 2 from figure 5.1), namely Jet 3 in figure 5.13. This shares the common characteristic of conserving the effective refractive index value at the centre of the channel.

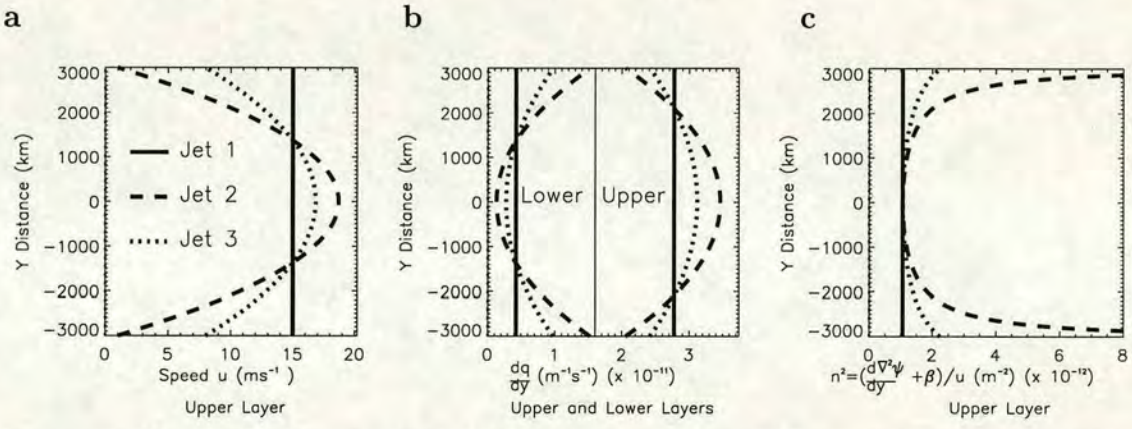

Figure 5.13: Upper-layer velocity (figure a, units ms^{-1}), upper-layer potential vorticity gradient (to right of thin vertical line (representing planetary vorticity value), figure b) and lower-layer potential vorticity gradient (to left of thin vertical line, figure b) with units $m^{-1}s^{-1}$ and upper layer refractive index for (figure c, units m^{-2}) shown for three jets. Jets 1 and 2 are as shown in figure 5.1, Jet 3 is an intermediate jet.

The timeseries for a model run using this jet 3 as an initial condition is shown in figure 5.14

The timeseries for the jet 3 shows more damped oscillations than the equivalent value for jet 1 (figure 4.10). Through examination of a movie of the individual low-pass filtered streamfunction and potential vorticity fields (not shown), we can see that the vacillations appear to be of a similar kind to those found in the continuous case (see figure fig:di:r5 for the jet 2 figures) As the shear of the jet increases far enough to Jet 2, the oscillations become continuous (see figure 5.3). It would appear that the large-scale flow evolves to a state which is more stable to perturbations generated by the wavemaker, but over a certain timescale. During

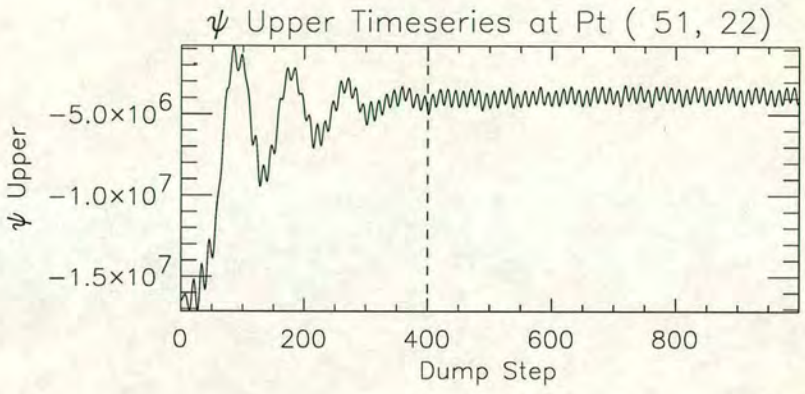

Figure 5.14: Streamfunction timeseries at point (51,22) of the run with upper-layer velocity jet 3 (see figure 5.13) and wavemaker amplitude $A = 9.2 \times 10^{-10}\mathrm{s}^{-2}$. Units $\mathrm{m}^2\mathrm{s}^{-1}$. This time there is a damped low-frequency oscillation component evident as well as the high frequency of the wavemaker eddies.

this transition period, the flow can become unstable and the anomaly decay due to the wavemaker perturbations, but not after this time. The timescale would seem to be longer for jet 3 than jet 1, and effectively infinite for jet 2, i.e. the flow does not evolve to a stable state. Further work is required to examine this behaviour more thoroughly.

5.9 Sensitivity Experiments

The following section will illustrate variations in the model output by altering the parameter set up by highlighting two main points, namely removing the ∇^2 friction and altering the densities in the model layers. A

5.9.1 Removing the ∇^2 friction

In section 4.8 we performed a potential vorticity budget for the a non-oscillating case, and found that the contribution from the ∇^2 friction was almost negligible. Removing this friction from the non-oscillatory case had little effect on the outcome. However, in the oscillatory case, removing this friction had a large effect on the model behaviour. Figure 5.15a shows a time series for a model run exactly

FFT Wavenumber	Prev FFT	Time Period (Days)
4	1	217
32	8	27
138	34/35	6.3
192	48	4.5

Table 5.2: Table of FFT wavenumber values and corresponding time periods.

as for the jet 2 case, except without the ∇^2 friction term present. Note that the model is run for 3 times longer than previous case, 3000 dumpsteps = 1080 days.

Over the first 600 model dumpsteps, a low-frequency vacillation can be seen as in the case with the friction included. However, after this time, the timeseries shows extra frequencies becoming present. The FFT for this is taken from 600-3000 dumpsteps, a period of 2400, which is 4 times the previous value of 600. Therefore, the numbers shown at the bottom will be 4 times larger than previous FFTs for the same wave frequency. Table 5.2 shows a conversion for the 4 main peaks shown in the figure to previous FFT values and a time period in days.

The peak at 192 corresponds to a period of 4.5 days, the wavemaker frequency, and the peak at 32 represents an oscillation with period of 27 days, which is approximately the value gained when the ∇^2 friction was included. The additional peaks at 4 and 138 represent ultra-low and high frequencies with periods of 217 days and 6.3 days respectively. It is speculated that the removal of the ∇^2 friction, which has more effect on the larger scales of motion, allows slowly generating large-scale instabilities to occur, where previously they would have been damped by the presence of this frictional term. The fact that it is not until over 200 days into the run that the presence of these additional frequencies is noticed.

To enable us to see whether these instabilities are symmetrical or anti-symmetrical about the channel centre, we can look at the timeseries of the sum and difference of two points at the same x position which are equally spaced about the channel centre. Retaining the same point as previously as one of the points, figures 5.15b and 5.15c show the timeseries and FFTs for the sum and difference respectively. The sum (figure 5.15b) shows oscillations which are symmetrical about the channel centre, which includes all except the 27 days period cycle (except for a small contribution which is probably due to lack of perfect symmetry about the channel centre). Figure 5.15c clearly shows that this 27 day cycle is anti-symmetric about the channel centre, as one would expect for the dipolar wave.

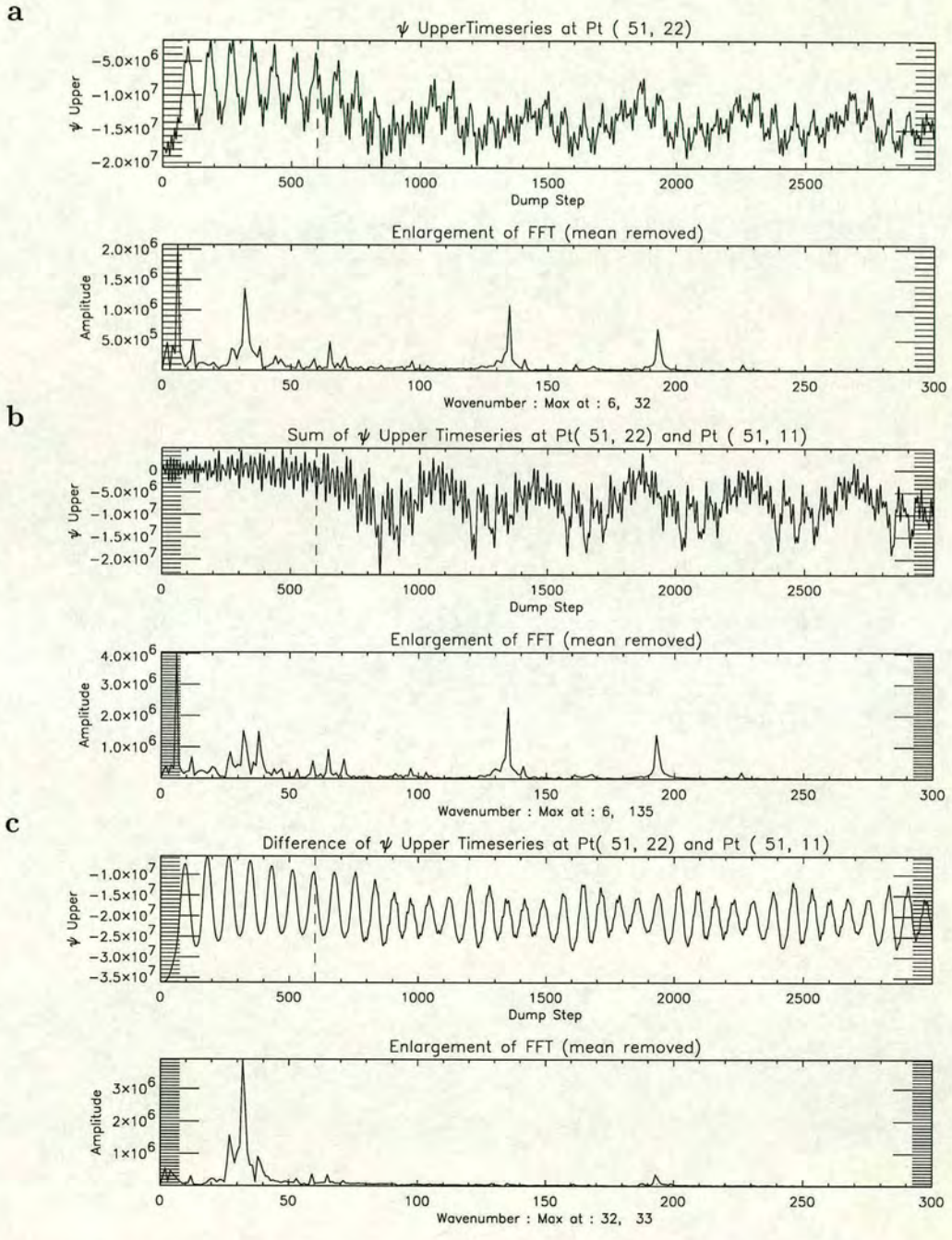

Figure 5.15: Streamfunction timeseries (upper plot) and Fourier transform (lower plot), at point (51,22) of the run with upper-layer velocity jet 2 (see figure 5.13), no ∇^2 friction and wavemaker amplitude $A = 9.2 \times 10^{-10}\mathrm{s}^{-2}$. Units $\mathrm{m}^2\mathrm{s}^{-1}$.

5.9.2 Altering the depths of each layer

One of the main concerns with the model response to the wavemaker forcing is that the amplitude in the lower layer is larger than would be desired. Although this is somewhat to be expected, since the wavemaker forcing is in the lower layer only, attempts were made to reduce this amplitude balance by altering the depths in the two layers, which had previously been set as equal. This can be done by having separate values for λ in the two potential vorticity definitions in equations 3.6 and 3.7.

If we make the depth of the lower layer one third that of the upper layer, making the total depth unaltered, this should encourage upper-layer potential vorticity anomalies for the same deviation of the interface. However, altering this affects the low-frequency variability, as can be seen in figure 5.16, which has the same set up as the original jet 2 vacillation case, but with different layers and run for three as long (1080 days). It is evident that a different low-frequency oscillation is present, with a time period of 85 days (the peak at 11). The peak at 210 is for the wavemaker frequency of 4.5 days. Instantaneous low-pass filtered fields (not shown) show that the upper-layer has a permanent split, with the oscillation being shown as increased variability about a blocked state, and cannot be described as previously. Further work could tackle trying to increase the upper-layer anomaly amplitude but retaining the low-frequency variability.

5.9.3 Sensitivity Summary

The last two subsections, plus discussion near the end of the previous chapter, have highlighted the sensitivity of these results, in particular the regular vacillation cycle, to the settings used for the model. Eliminating the larger-scale friction in the vacillating case allowed other cycles of lower-frequency to appear which had previously been damped by this frictional term. The experiments in Chapter 4 which produced a steady response were affected by changes in the frictional terms, but to a lesser extent. For example, the amplitudes of the anomalies would be altered, but the structure would remain similar providing the dissipation term did not become too small to produce continued growth. As the wavemaker is continually providing high-frequency eddy energy into a relatively confined channel, the dissipation must eliminate much of the energy to prevent the model becoming numerically unstable. It was found to be difficult to produce a regular vacillation cycle such as described in the majority of Chapter 5. Many experiments were

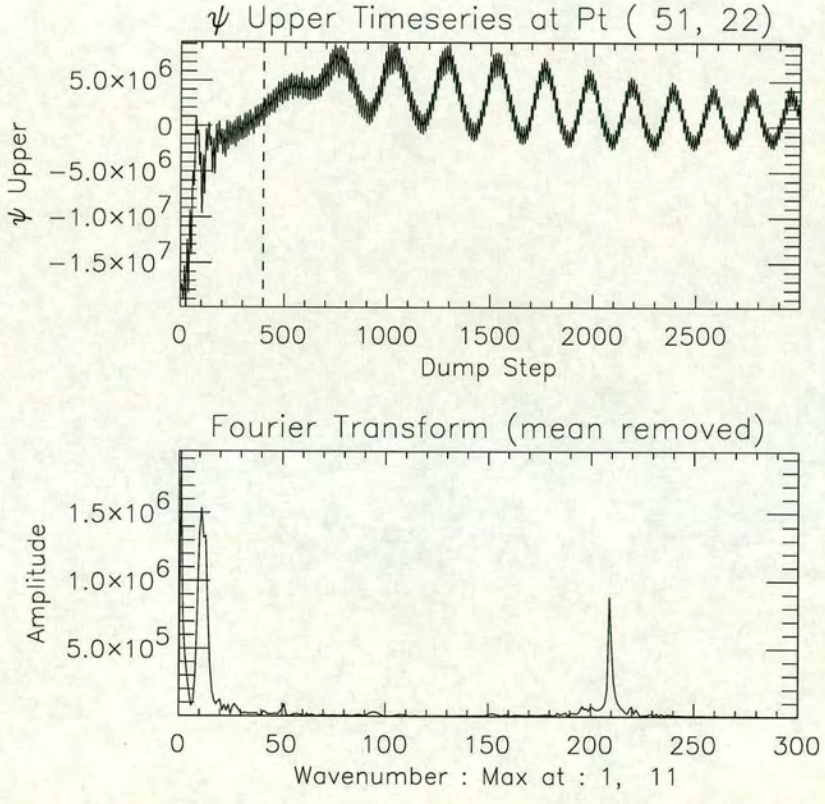

Figure 5.16: Streamfunction timeseries (upper plot) and Fourier transform (lower plot), at point (51,22) of the run with upper-layer velocity jet 1 (see figure 5.13) and wavemaker amplitude $A = 9.2 \times 10^{-10} \mathrm{s}^{-2}$. This run had varying λ parameters in the different layers. Units $\mathrm{m}^2\mathrm{s}^{-1}$.

carried out to try and maintain the regular cyclic behaviour and also increase the magnitude of the eddy-feedback term in the upper-layer, but none were successful. It would appear to be a narrow region of parameter space in which this behaviour occurs. This does not necessarily mean that there are no other settings which would produce similar results. However, we may have been fortunate in finding such a regime where this behaviour occurs.

5.10 Summary and Conclusions

5.10.1 Summary

In this chapter, we have noted very different behaviour from the previous chapter. By adding a component of horizontal shear to the upper-layer jet, we generated a vacillation cycle (not a stationary wave amplitude oscillation), whereby high-frequency eddies resonantly excite the large-scale flow, but this reaches an amplitude where it is rendered locally unstable, and this instability mechanism caused the destruction and ultimate breakdown of the split jet. As the forcing is continuous, when the jet resumes a more zonal state, re-excitation by the eddies continues the cycle. We have performed a simple local stability analysis which confirms that a mixed barotropic/baroclinic instability is the cause of the breakdown. This leads to propagation away from the source region, where it is dissipated, and the process repeats itself with the re-excitation of the split flow. An energy analysis also confirms this viewpoint, although care must be taken when using energy as a diagnostic, due to its non-conservative nature and the fact that filtering can lead to it being a rather non-physical quantity (see Plumb (1983)). The transition from a linear response to a non-linear response was demonstrated by increasing the wavemaker amplitude. The period of the oscillation decreased, indicating that the amplitude necessary for instability was reached more quickly because of faster growth times due to the increased forcing. By increasing the amplitude of the forcing further still, the flow becomes chaotic. We also demonstrate the sensitivity of the low-frequency vacillation to parameter changes in the model.

5.10.2 Discussion

These results indicate that the state of the upper-layer jet is critical in determining what sort of response will be produced from a transient source of high-frequency eddy energy, in this case the wavemaker. This would indicate that the atmospheric

jet will determine the sort of resonant response from high-frequency eddy-forcing from the transient cyclones of the storm tracks. Rex (1950a),Rex (1950b) showed that blocking was more prevalent in the Spring months, perhaps indicating that the conditions of the atmospheric jet were more similar to our jet 1 case, allowing a large amplitude anomaly to grow and be maintained by the eddy forcing. Vautard (1990) looked at atmospheric data to look for preferred changes between weather regimes, and found that a blocking state was most likely to be preceded by a state in which the atmospheric jet was of a zonal type. This could indicate this this sort of jet structure has features which are favourable to blocking development and persistence. Soliton theory would support this viewpoint, where the refractive index structure of the jet determines whether a weak split of intensification will be supported as a weakly non-linear perturbation solution. Even though these solutions are rather weaker, Haines and Malanotte-Rizzoli (1991) showed that in jets with the appropriate structure, a finite-amplitude solution would remain a coherent structure.

Further evidence to support the effect of jet structure on blocking activity was provided by Ferranti *et al.* (1994), as previously discussed in Chapter 2. They showed that the ECMWF forecast model produced a much more realistic reproduction of blocking frequency and location if they artificially increased tropical heating, which would affect the planetary wave structure, therefore having an effect on the jetstream over the Atlantic and Pacific. Thorncroft *et al.* (1993) showed two paradigms of baroclinic-wave lifecycle behaviour, which differed due to altering the basic state jet structure with the addition of a barotropic shear component. Their second lifecycle (LC2) had no cross-jet potential vorticity transport, which implied that this type of eddy (and, by implication, jetstream) would not be conducive to blocking.

The atmospheric flow will vary continuously between states which are more or less likely to produce favourable blocking conditions. The amplitude of the eddies is also likely to be of importance. Without them, there would be no cross-jet potential vorticity transport. It has been observed that before blocking events, there is often an explosive cyclogenesis (Colucci (1985)). It may be argued that the condition of the jet is ultimately responsible for this, the energy for baroclinic instability coming from the enhanced low-level thermal gradients on the eastern coasts of America and Asia. If the jet was particularly strong at this point, this may lead to increased eddy activity, and an increased likelihood of these rapidly-growing cyclones developing. Another implication for the state of the jetstream

concerns its stability. In our model run, by altering from jet 1 to jet 2, although both jets remain stable in the classical sense since the q-gradients remain positive everywhere, the jet 2 case has a lower-layer q gradient which approaches zero at the channel centre. It may therefore be argued that this jet is closer to being unstable that jet 1, it requiring a weaker large-scale anomaly, such as a block, superimposed on the jet stream to cause instability. Helfrich and Pedlosky (1993) examined solitary wave solutions for a background flow which was marginally stable. It was shown that a certain amplitude of anomaly could force the flow to be locally unstable, providing the "push" to an unstable environment. The behaviour in our model is likened to theirs. For a weak wavemaker forcing, there is little sign of an oscillation. It is only once the wave reaches a finite-amplitude that it is sufficient force the flow unstable, causing its breakdown. It is envisaged that this could also be the case for jet 1, but as it is further from instability than jet 2, it would require a larger amplitude anomaly to caused the instability to occur. Wu (1993) performed a similar type of experiment, resonantly exciting planetary waves to large amplitude whereby they became unstable. This was offered as a mechanism by which the transition between regimes, such as between blocking flow and a zonal flow, may be achieved. We appear to have a similar mechanism operating in our model runs.

In the recent paper by James *et al.* (1994), they find a low-frequency oscillation using a principal components analysis of an SGCM run. In the phase-space of the first two EOFs, the oscillation describes a circular orbit. They look at the effect on this trajectory of growing normal modes. They find that these can help push the flow around the trajectory cycle for approximately three-quarters of the flow, but fail to be able to move the flow out from one of the quadrants. This might imply that the missing mechanism is one of instability. If we consider our model to be similar to this, we find that the behaviour of our high-frequency eddies is to constantly force a split, albeit with a different magnitude forcing at different phases of the vacillation cycle. The fact that the eddy feedback can reduce in magnitude, but never reduce the flow back to the zonal phase of the cycle is likened to the fact of the quadrant in James *et al.* (1994) which cannot be escaped from by a normal-mode mechanism.

Chapter 6

Using a simplified global circulation model

6.1 Introduction

So far, in chapters 4 and 5, we have used a two-layer quasi-geostrophic model to perform our experiments. Although this has meant that analysing the flow should be more straight-forward than using a global model, it is restricting somewhat due its lack of vertical resolution and the nature of the walls, for which there is no real comparison in the real atmosphere. Although one might argue that the critical lines, regions of zero velocity where the flow changes from westerly to easterly, might act as walls to partially reflect wave activity (see Kilworth and McIntyre (1985) for an in-depth discussion on Rossby-wave critical layers), they also absorb it, unlike the walls of our channel. It is therefore advisable to use a more realistic model, to investigate whether similar behaviour can be found there, in order to strengthen any conclusion drawn from the two-layer channel model work.

For this purpose we shall use the UK Universities Global Atmospheric Modelling Programme (UGAMP) Simplified Global Circulation Model (SGCM). This model has been used by a number of researchers, for investigating baroclinic wave life cycles.

In this chapter we shall, first of all, briefly describe this model and its basic characteristics, and then describe the set-up we will use. In subsequent sections, we shall show results from integrations of the model, and compare these with the results of previous chapters, and also work by other authors. We shall end with a summary and conclusions.

6.2 The model

The UGAMP SGCM was first written in 1975, details can be found in Hoskins and Simmons (1975). It was later amended by Simmons and Burridge (1981) to include an energy and angular-momentum conserving finite-difference scheme, still retaining the basic sigma vertical co-ordinate (sigma is defined as the pressure divided by the surface pressure). It is an adiabatic multi-level spectral model, and the next section shall describe further the set up used.

6.3 The set up

We shall be running the model as a single-hemisphere case, where the flow is assumed equal and opposite in the opposing hemisphere. It is run with spectral triangular truncation 42 (T42), with 15 vertical levels (sigma co-ordinates), no zonal symmetry. There is no moisture included, therefore the only diabatic processes are therefore dissipation, which is a ∇^6, with a timescale of $\frac{1}{6}$ day acting on the shortest retained lengthscale (i.e. wavenumber 42), and a restoration of the initial state, with a 4 day restoration timescale. There are 48 half-hourly timesteps per day.

6.3.1 Zonal wind

The equations used in the model are for the tendencies of divergence, absolute vorticity, temperature and surface pressure. Assuming the initial flow to be non-divergent, the model can be initialised in two ways. Either the zonal surface pressure and zonal temperature field can be given, from which the zonal vorticity is obtained by an iterative approximation, or *vice versa*. In our case, we choose the first method. We want to have a zonal state which is close to baroclinic stability, total stability would be virtually impossible to acheive in practise due to very slowly-growing unstable waves. This is for a number of reasons, primarily in order to match up with our previous experiments, where it is the superposition of the anomaly on the background flow which causes the instability. For similar reasons as stated for that model, the atmosphere is said to be on the verge of instability, and certainly not unstable at all locations. We intend to use an unstable (to all intents and purposes) flow, and generate an instability through eddy interactions. We don't expect to get a similar regular low-frequency oscillation with this model, due to its increased complexity. However, it will be interesting to see what parallels

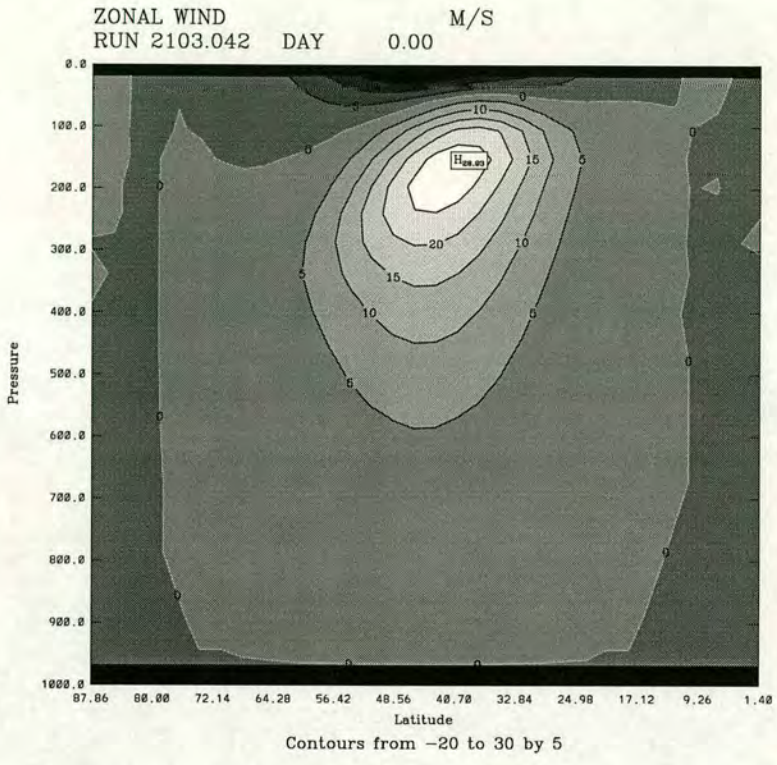

Figure 6.1: Initial zonal wind, units ms^{-1}.

can be drawn between the two model types.

We take the standard jet case initially used by Simmons and Hoskins (1977), and subsequently used in many other papers, and reduce the lower temperature gradients to increase the stability of the flows. The iteration technique is then applied to this new temperature (plus original surface pressure field, in this case zero), to give a vorticity field. The model is then ready to be integrated. Figure 6.1 shows the initial zonal wind. This shows a maximum at upper levels at the 200mb level.

Figure 6.2 shows the corresponding initial zonal potential temperature and temperature fields. The temperature gradients are very weak near the surface, reducing the amount of available potential energy for the eddies to extract energy from, and through thermal wind balance, provide a weak vertical shear.

A control run is performed where the model is integrated for 60 days with a weak white-noise surface pressure perturbation field. During this period, no significant anomaly to the zonal flow pattern was detected, showing that this jet structure was baroclinically stable to small perturbations near the surface.

Since we have reduced the baroclinicity of the flow, we shall need some way of generating eddy activity. As in the two-layer model, we shall use a low-level

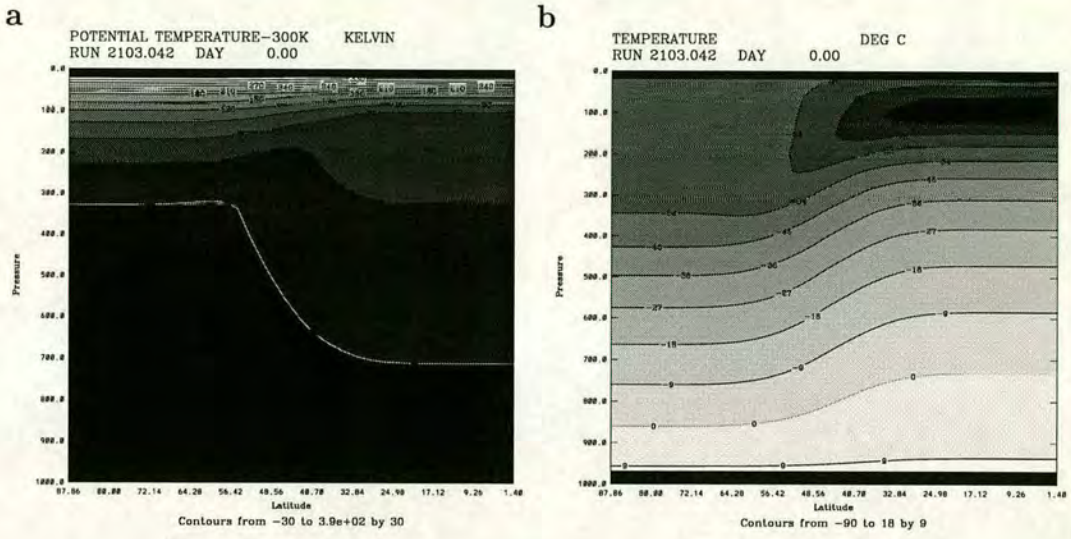

Figure 6.2: Potential Temperature (units degrees Kelvin) and Temperature (units degrees celsius) fields.

wavemaker, the description of which follows.

6.3.2 Wavemaker

The wavemaker we shall use is of a similar form to the one from our two-layer model, specifying a three-wave structure which moves in an eastward direction with constant velocity, again inside an amplitude envelope, ensuring no net vorticity is added. Figure 6.3 shows the representation of the forcing used at the initial state. It is defined over the region of longitude 0° and 40° and latitude 40°N and 60°N. This gives approximate individual eddy dimensions of 2140km in the north-south direction, and between 714km at 60°N and 1090km at 40°N, with a central value at 50° of 918km. Because the model is spectral, we create a gridpoint field for the wavemaker which is then converted into spectral coefficients, up to the spectral resolution used by the model, in our case, T42. This is the reason for the patterned effects over the whole hemisphere, where the spectral resolution cannot perfectly match the gridpoint field. This wave-3 pattern propagates eastward with a period of 2 days per individual eddy. As we have half hourly timesteps, 96 individual wavemaker fields were required to generate the wavemaker forcing. When the 96 steps were completed, the sign was reversed and the 96 stages repeated again. The wavemaker forcing is applied to the vorticity tendency field in the lower layers. It is arranged with a linear height dependent component, so that there is no contribution at levels 1 to 10, but a steady increase

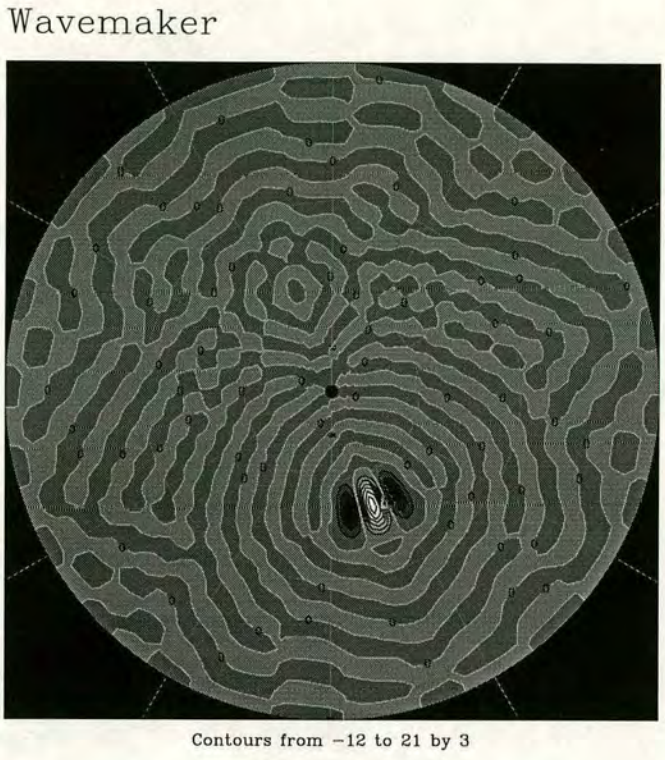

Figure 6.3: Wavemaker forcing.

until its maximum contribution is at level 15, the lowest model level.

This set-up of baroclinically stable jet with zero low-level velocities and a wavemaker to provide excitation is designed as an extension to the channel model work but in a spherical domain. By using a wavemaker rather than allowing the eddies to grow more naturally thorugh instability mechanisms allows a greater control for confining the area of their action. This can be thought of as mimicking the land-sea contrasts of the real atmosphere which would otherwise not be found in a model with no orography such as this, the region of the wavemaker being the storm-track region of eddy generation through instability processes.

As the waves propagate vertically upwards, most of the interaction between the more developed waves and the background flow occur at high levels around the jet maximum (as in Thorncroft *et al.* (1993)). For this reason, the fact that eddies are not generated through baroclinic instability is not too critical, providing they still propagate vertically into the jet core region.

6.4 Model run and diagnostics

We run the model for 120 days, outputting data daily. These data were then manipulated using a standard Reading University Program (bgflux).

The time-mean fields over the last 60 days of the run for the streamfunction at 400mb and surface pressure are shown in figures 6.4 and 6.5 respectively.

Figure 6.4 shows a ridge over the upstream end of the wavemaker region, indicating a time-mean slowing-down and splitting of the flow at that level. At other longitudes, the time-mean flow is not purely zonal, for example a weak trough at 50°W. The velocity of the flow varies too, with a stronger jet region, indicated by the more-tightly packed streamlines, between 90°W and 150°W.

Figure 6.5, showing the time-mean surface pressure, shows a splitting over the upstream edge of the wavemaker region, similar to figure 6.4 but stronger, indicating an equivalent barotropic structure, similar to that found in real blocking events. There is, as in figure 6.4, a region of increased velocity towards 90°W, and also a region of weaker velocity over the region 150°W to 120°E, more pronounced than for the streamfunction at 400mb field. These diagrams tend to show an equivalent barotropic nature to the main features of the flow. If we now look at a vertical cross-section showing the time-mean zonal wind over the same period, figure 6.6, this will show us how the vertical structure of the inital jet has altered with the inclusion of the wavemaker forcing. The time-mean zonal velocities at lower levels have increased over the model integration, similar to that found in the wave lifecycle experiments of Simmons and Hoskins (1977) and Thorncroft *et al.* (1993). This fact was evident in the surface pressure field of figure 6.5. However, these low-level velocities are still much weaker than those in the core of the upper-level jet.

6.5 Time-dependent behaviour

So far we have only looked at the time-mean response to the eddy forcing. This will tell us nothing about the time-dependent behaviour of the model during the integration. We shall therefore show a progression in time of the streamfunction at 400mb and the surface pressure, the two fields considered so far.

In order to reduce any high-frequency transience from the fields, to give a clearer picture of the major events, we shall use a 5-day running mean i.e. the plot for a particular day will be a time-average of the 5 days of data, centered on the required day. Figures 6.7, 6.8, 6.9 and 6.10, show these 5-day running means at

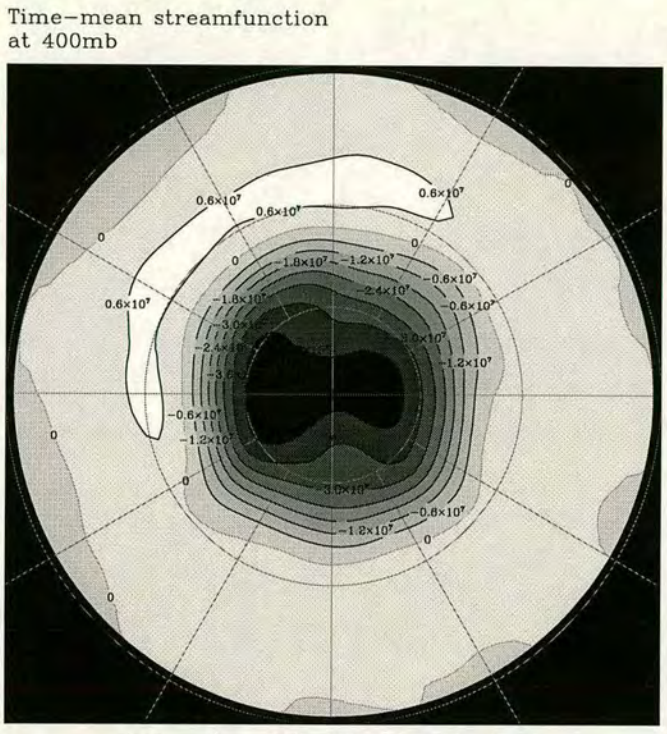

Figure 6.4: Time-mean stream function at 400mb level over the last 60 days of the model run. Units m^2s^{-1}.

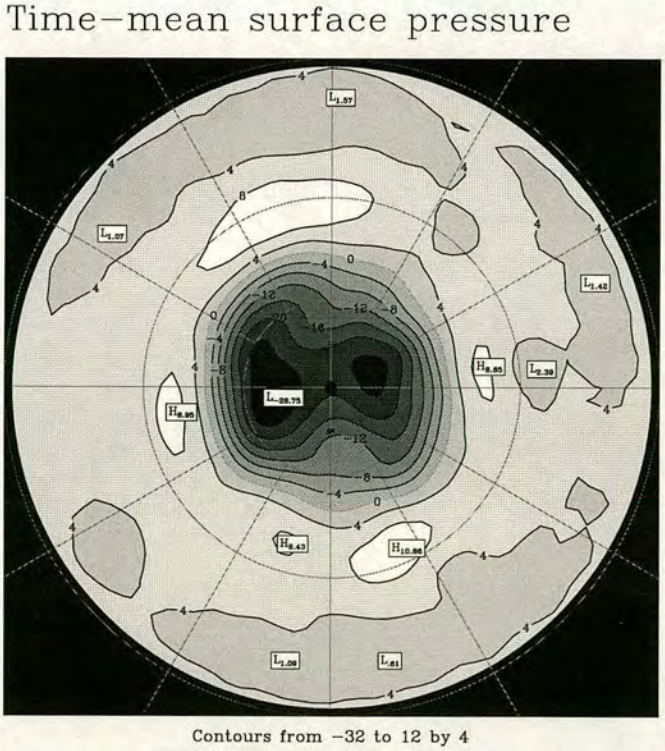

Figure 6.5: Time-mean surface pressure over the last 60 days of the model run. Units mb.

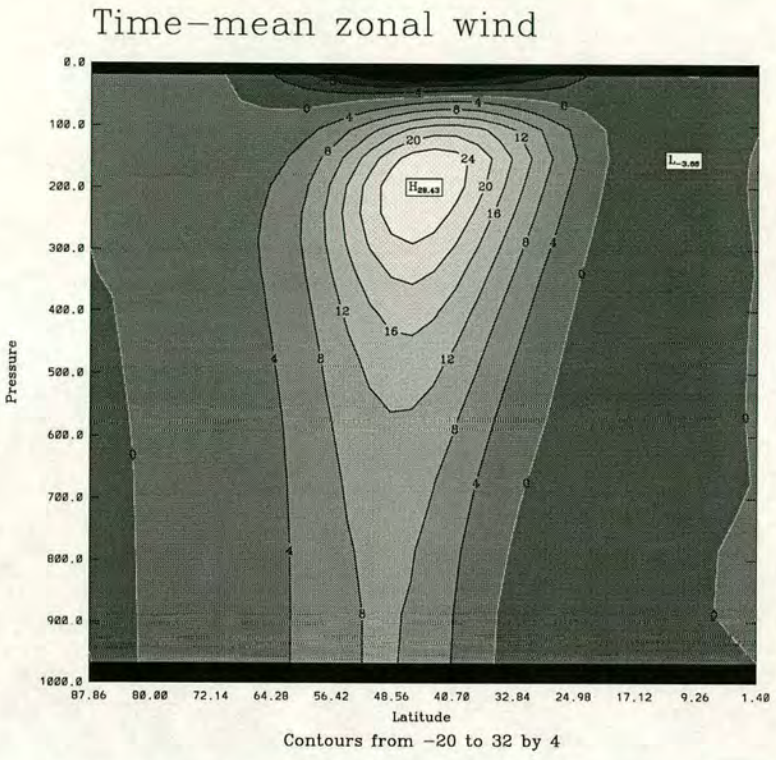

Figure 6.6: Time-mean zonal wind, units ms^{-1}.

five day intervals, starting with day 62 and ending on day 117, covering a 55 day period. In all these figures, for reference purposes, we take the 0° contour to be vertically downward from the centre of each plot (although, there is no orography in this model, the wavemaker is situated to the right of this line).

By first of all comparing the streamfunction at 400mb, in the left hand columns, with the surface pressure plot from the same day, it is apparent that there is a significant equivalent-barotropic component to the flow, with large similarities between the two fields.

At day 62, we see a blocking-type pattern evident to the right of the 0° line in the same position as the split in the time-mean plot (figure 6.6). By day 67, this split has broadened until it has almost disappeared by day 72, except for a weak upper-level trough (the signature in the surface pressure plot is not blocking-like). At day 77, it would seem that the block was starting to redevelop, but on day 82 we can see a ridge pattern, with a region of high pressure over the wavemaker region.

Day 92 shows a jet intensification over the position where the blocking pattern was 30 days previously. By day 102, this intense jet has weakened, and a splitting is beginning to form, which becomes more evident by day 107 and stronger still

by day 112. However, the flow by day 117 appears very different indeed. An equivalent barotropic anticyclone system appears to be retrogressing westward, but the dipole pattern is not evident, being more like an omega type block (shaped as Ω), more commonly found over the Pacific regions.

These figures show the variety of different patterns observed over a single 55 day period. Many of these have been observed in the atmosphere (refer to chapter 2 for descriptions of dipole and omega blocking, intense jet anomalies etc.)

6.6 Summary and Conclusions

It is probably too much to hope that a regular low-frequency vacillation cycle might be found, such as the one described in Chapter 5. After all, it is relatively difficult to obtain one in the two-layer channel model. However, this has shown that a similar set-up as the channel model, namely a zonal jet with a low-level 'artificial' wavemaker generator can produce features similar to those recognised in the atmosphere. The high-frequency eddies excite the flow through non-linear interactions.

There is obviously much more investigative work which may be performed using this model. Longer runs with different jets with varying characteristics may produce regime-like behaviour, and a link may be sought between the initial background jet structure and the preferred residence of the model in phase space.

Further analysis should be performed as we have done for the channel model. It would be useful if a state of permanent blocking could be induced, and then changes necessary in the mean flow to break this down could be investigated.

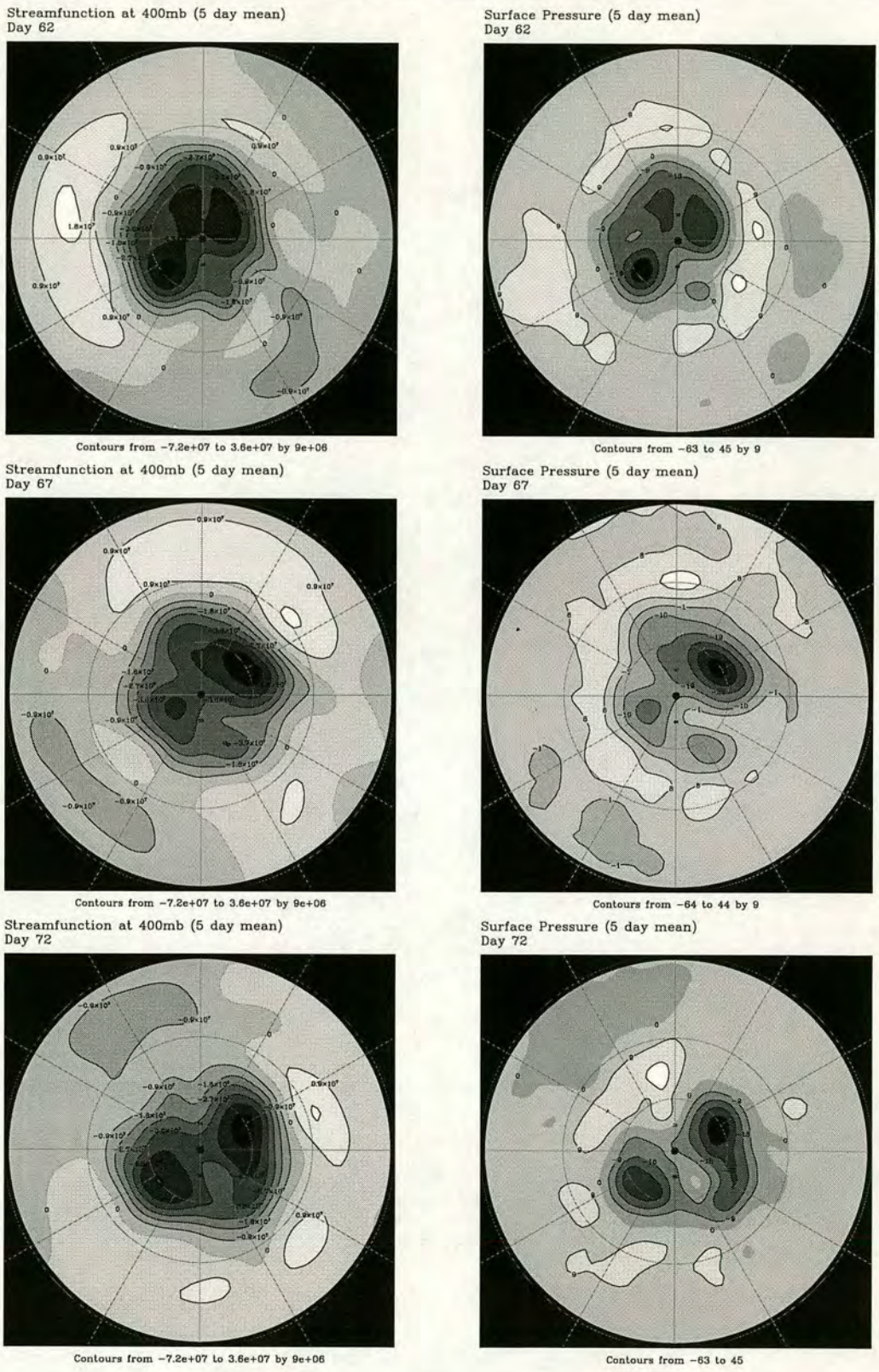

Figure 6.7: 5-day means of streamfunction at 400mb level (units m^2s^{-1}) and surface pressure (mb), intervals of 5 days for days 62, 67 and 72.

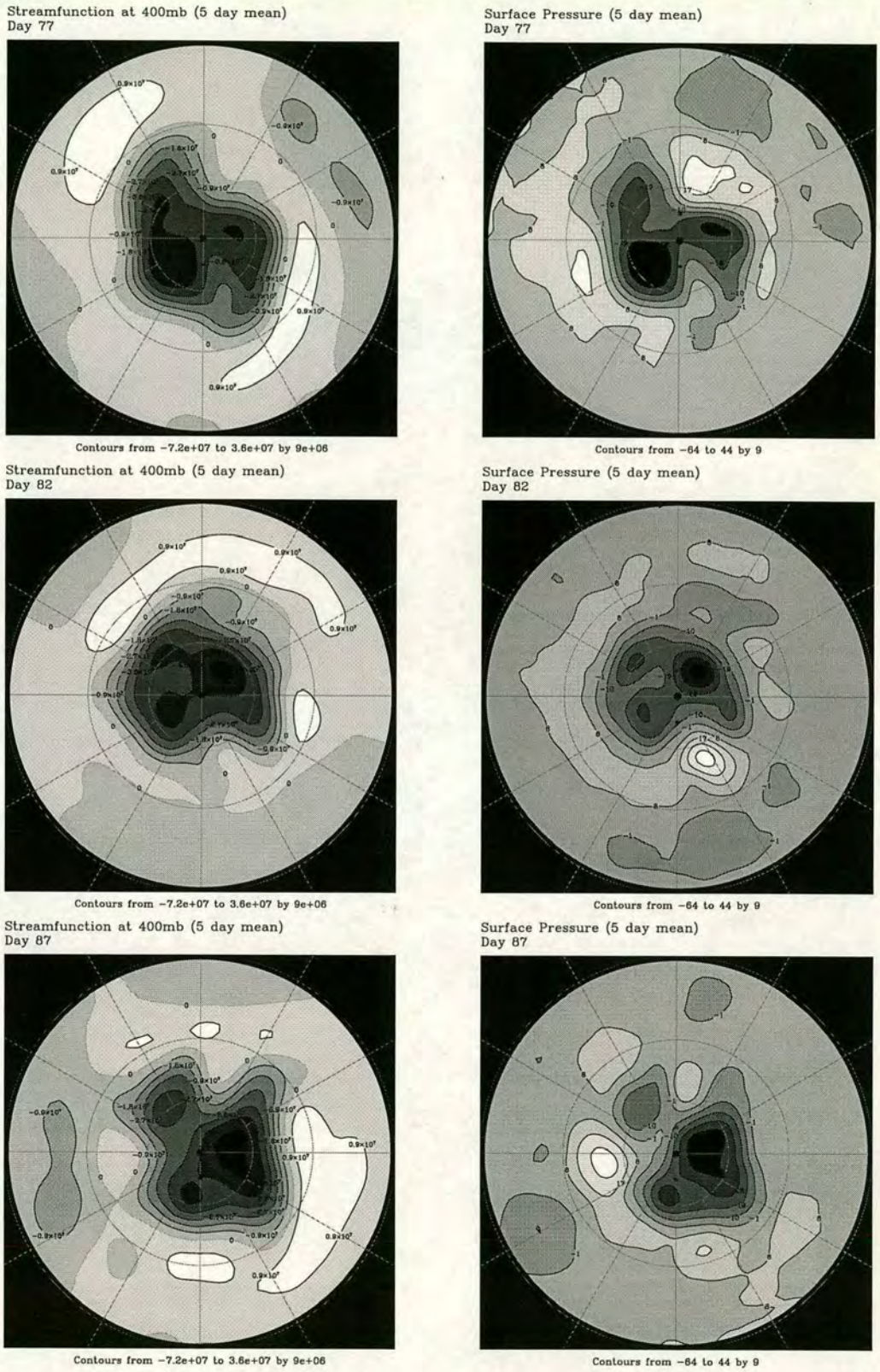

Figure 6.8: 5-day means of streamfunction at 400mb level (units m^2s^{-1}) and surface pressure (mb), intervals of 5 days for days 77, 82 and 87.

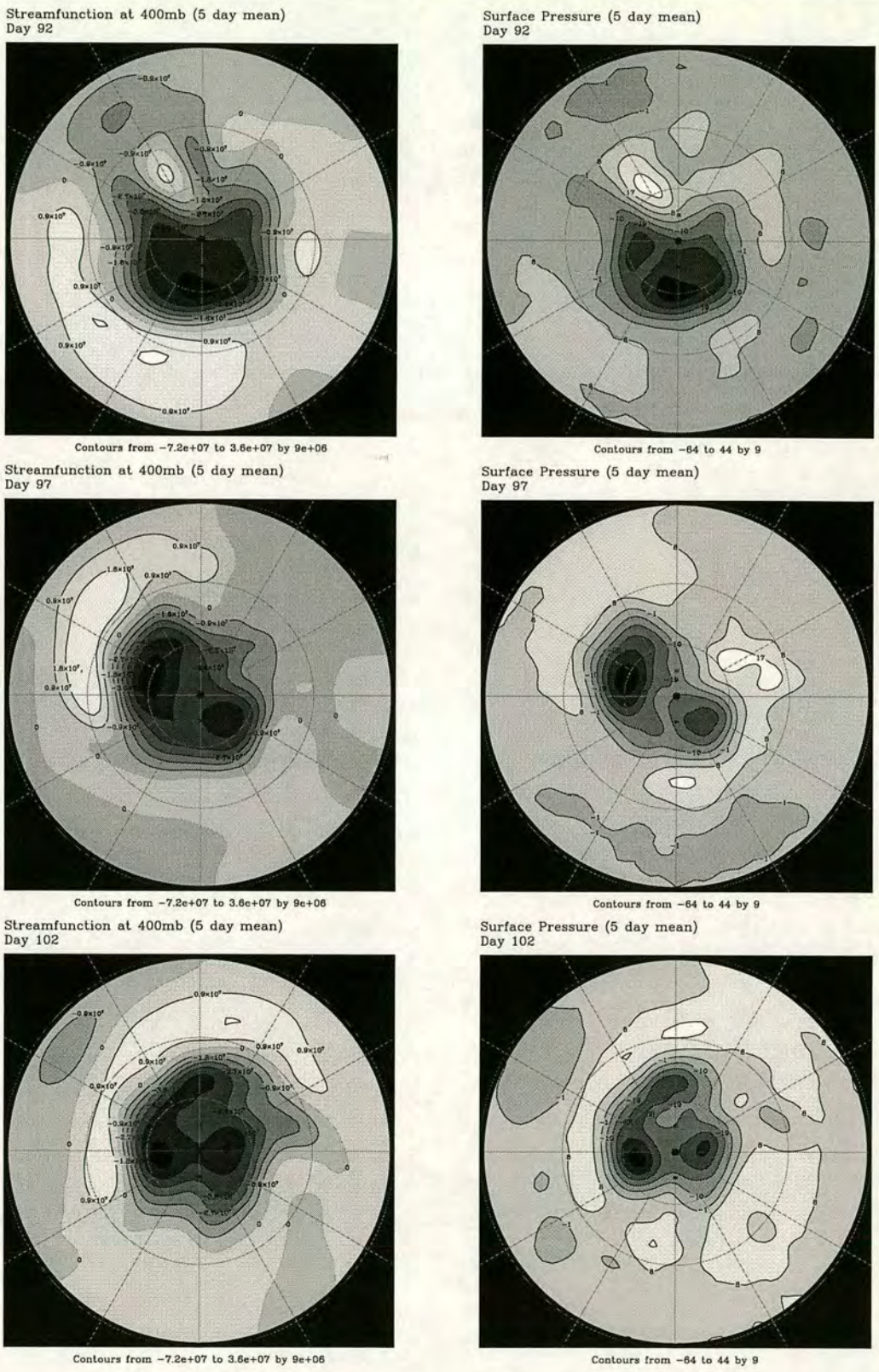

Figure 6.9: 5-day means of streamfunction at 400mb level (units m^2s^{-1}) and surface pressure (mb), intervals of 5 days for days 92, 97 and 102.

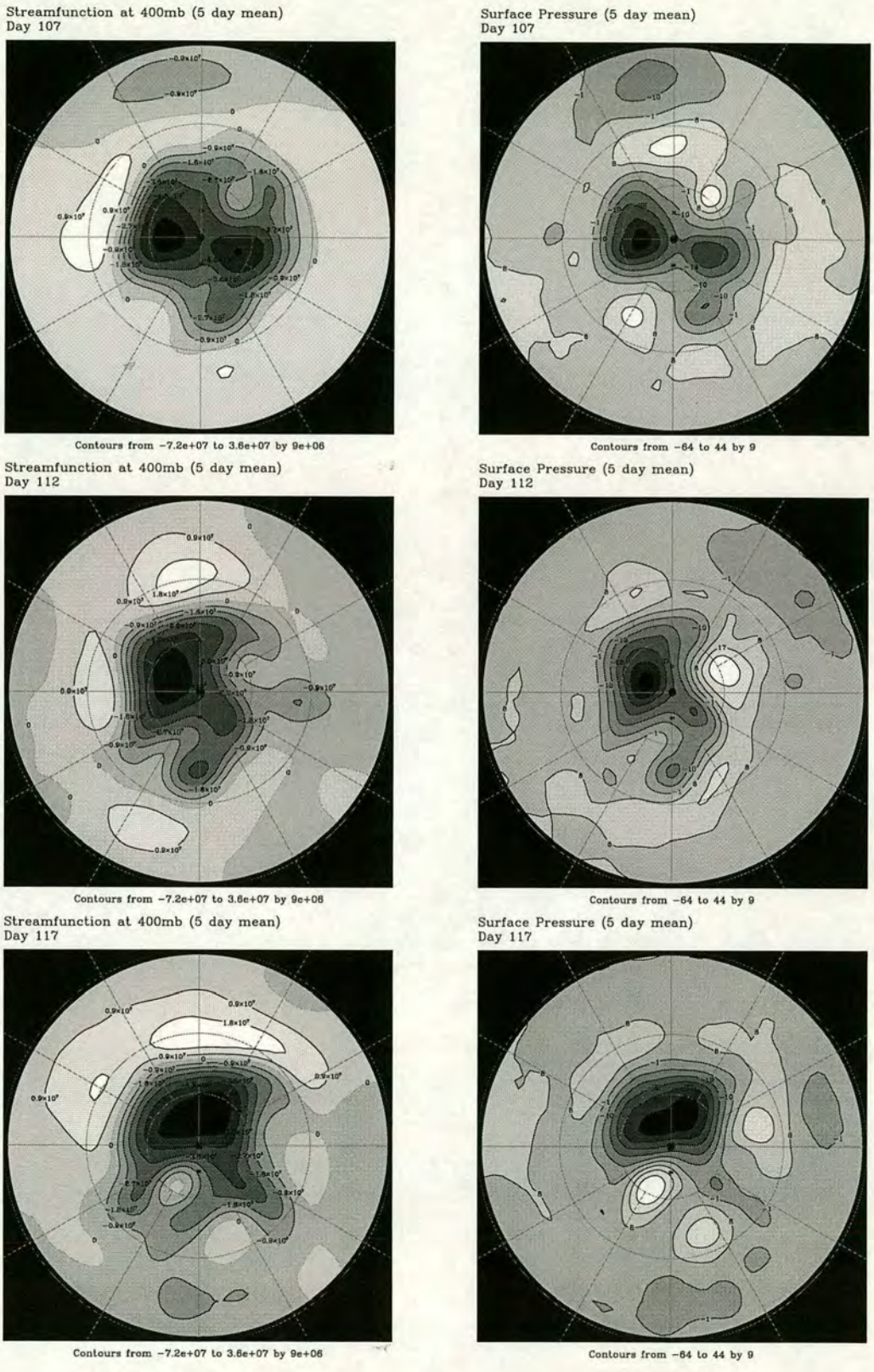

Figure 6.10: 5-day means of streamfunction at 400mb level (units m^2s^{-1}) and surface pressure (mb), intervals of 5 days for days 107, 112 and 117.

Chapter 7

Summary, Conclusions and Discussion

The work contained in this thesis has attempted to examine the possible link between low-frequency and quasi-stationary atmospheric circulation patterns and the structure of the incoming jet stream. The ideas of high-frequency eddy feedback providing a mechanism for the persistence of such anomalies has been around for twenty years or so, although the intermittent behaviour of blocking-type anomalies and the reasons for their eventual breakdown is much less understood. An insight into the interactions involved in these atmospheric flow patterns would prove enormously useful in aiding weather prediction and further understanding of these anomalous events.

For the majority of experiments, a 'back to basics' approach was taken. Despite the advances in numerical modelling, simple models can often provide a greater insight to a problem by eliminating or reducing the inevitable complexities associated with more sophisticated models.

Following from the pioneering work of Shutts (1983) using a barotropic channel model with a wavemaker, and that of Vautard *et al.* (1988) in a two-layer baroclinic model with an unstable jet region generating the eddy activity, which both showed results of a similar nature to atmospheric observations, we chose to combine the two approaches.

Using a two-layer model was the most simple way of allowing baroclinic effects, despite the limited vertical resolution. As we wanted full control over the initial jet structure, and since the atmosphere is certainly not stable at all longitudes, we chose to excite the flow with a wavemaker as Shutts did, but in the lower layer only, attempting to mimic the generation of baroclinic instability at low-levels in the atmosphere, allowing the wave energy to propagate vertically.

This model showed how stationary waves could be excited from a source of high-frequency eddies. Certain jet flows close to the limit for allowing dipolar stationary Rossby waves has a solution in the channel allowing large-amplitude blocking-like structures to persist. These were very similar to the results obtained by Shutts (1983) in a barotropic channel model, where he obtained a persistent split-jet flow pattern reminiscent of atmospheric blocking.

However, when a horizontal shear was added to the upper-layer velocity profile, we were able to obtain rather different behaviour. This time, rather than persistence, an intermittency developed with a low-frequency vacillation cycle in which the jet begins to split but was maintained, the flow reverting to a more zonal state, this process repeating itself.

The growth of the split was again due to excitation by the high-frequency eddies generated by the wavemaker, but the decay was shown to be caused by a local instability process, whereby the presence of the anomaly caused the flow to become unstable and breakdown.

Also shown using this model was a 'transition to chaos' by increasing the forcing amplitude. From a state with only the high-frequencies evident, increasing the forcing developed a low-frequency oscillation whose frequency increased with the wavemaker amplitude until the flow became chaotic in nature.

The work in chapter 6 showed an attempt to use a spherical model with much greater resolution to help bridge the gap between the idealised study of the channel model and the real atmosphere. Although the experiments were certainly not extensive, they show that a low frequency variability was generated using a similar set-up to the channel model, although the regularity is lost with this more complex model.

These experiments have demonstrated a possible growth and decay mechanism for low-frequency atmospheric events such as blocking through excitation and instability process, even in a highly-simplified framework.

Further work should build on these results, attempting to explore the possibilities that more predictive information for the ensuing behaviour can be found in the incoming jet stream. At present, we are unable to determine the subsequent-flow type given the initial set-up, and the regularly-repeating low-frequency cycle is seemingly fairly difficult to obtain. Expanding this area of work would prove most beneficial if this could be extended to real atmospheric flows.

With the two-layer model, even the flows which eventually attain a steady equilibrium solution initially appear to have a form of damped oscillation. This could

be worthy of investigation, in particular with relation to why the behaviour does not persist in all cases. It would appear the background flow evolves to a more stable state, so perhaps the trajectory of the background flow from the initial state should be the main focus.

The work in chapter 6 merely demonstrates that low frequency variability similar to atmospheric motions is evident in a simplified set-up using a spherical model with much greater resolution. There is obviously much more work to be performed here. The choice of incoming jet would appear to be crucial in determining the subsequent behaviour, in a similar way to that of Thorncroft *et al.* (1993), where the two lifecycle events were caused by the differences in the incoming jet stream. With longer model runs and suitable diagnostics, the preference for certain regimes depending on initial conditions may be sought.

This research has highlighted the rich and varied patterns of behaviour found in such simple models as these, as shown by Lorenz with his three equation model of chaos. There is still much to learn from studying models of this kind, rather than electing to only use the more complicated numerical models associated with the rapid increase of computer power over the last couple of decades.

Appendix A

Derivation of Zonal Instability Equations

The equations for the channel, if we neglect and forcing or dissipation terms, are:

$$\frac{\partial q_1}{\partial t} = -J(\psi_1, q_1), \tag{A.1}$$

$$\frac{\partial q_3}{\partial t} = -J(\psi_3, q_3), \tag{A.2}$$

We now want to linearise the channel equations about a background flow (not necessarily the initial conditions) which is independent of x, allowing small perturbations on it. If we define the streamfunction and potential vorticities (background (Ψ, Q), perturbation (ψ', q') conditions as:

$$\Psi_1(y) \equiv -\int U_1(y)dy, \tag{A.3}$$

$$\Psi_3(y) \equiv -\int U_3(y)dy, \tag{A.4}$$

$$Q_1(y) \equiv -\frac{\partial U_1}{\partial y} + \beta - \lambda^2(\Psi_1 - \Psi_3), \tag{A.5}$$

$$Q_3(y) \equiv -\frac{\partial U_3}{\partial y} + \beta + \lambda^2(\Psi_1 - \Psi_3), \tag{A.6}$$

$$q_1' \equiv \nabla^2\psi_1' - \lambda^2(\psi_1' - \psi_3'), \tag{A.7}$$

$$q_3' \equiv \nabla^2\psi_3' + \lambda^2(\psi_1' - \psi_3'), \tag{A.8}$$

then the linearised equations for the channel are:

$$\frac{\partial q_1'}{\partial t} = -J(\Psi_1, q_1') - J(\psi_1', Q_1), \tag{A.9}$$

$$\frac{\partial q_3'}{\partial t} = -J(\Psi_3, q_3') - J(\psi_3', Q_3). \tag{A.10}$$

Since the background and initial terms are functions of y alone, this simplifies to:

$$\frac{\partial q_1'}{\partial t} = +\frac{d\Psi_1}{dy}\frac{\partial q_1'}{\partial x} - \frac{\partial \psi_1'}{\partial x}\frac{dQ_1}{dy}, \tag{A.11}$$

$$\frac{\partial q_3'}{\partial t} = +\frac{d\Psi_3}{dy}\frac{\partial q_3'}{\partial x} - \frac{\partial \psi_3'}{\partial x}\frac{dQ_3}{dy}. \tag{A.12}$$

We move to a frame of reference travelling in the x direction with speed c, which gives:

$$\frac{\partial q_1'}{\partial t} = -(U_1(y) - c)\frac{\partial q_1'}{\partial x} - \frac{\partial \psi_1'}{\partial x}\frac{dQ_1}{dy}, \tag{A.13}$$

$$\frac{\partial q_3'}{\partial t} = -(U_3(y) - c)\frac{\partial q_3'}{\partial x} - \frac{\partial \psi_3'}{\partial x}\frac{dQ_3}{dy}. \tag{A.14}$$

We now assume that the timescale is long. This mean that the partial time derivatives on the left hand side become zero, and we get:

$$0 = -(U_1(y) - c)\frac{\partial q_1'}{\partial x} - \frac{\partial \psi_1'}{\partial x}\frac{dQ_1}{dy}, \tag{A.15}$$

$$0 = -(U_3(y) - c)\frac{\partial q_3'}{\partial x} - \frac{\partial \psi_3'}{\partial x}\frac{dQ_3}{dy}. \tag{A.16}$$

Since Ψ and Q are functions of y alone, we can write:

$$0 = \frac{\partial}{\partial x}\left((U_1(y) - c)q_1' + \psi_1'\frac{dQ_1}{dy}\right), \tag{A.17}$$

$$0 = \frac{\partial}{\partial x}\left((U_3(y) - c)q_3' + \psi_3'\frac{dQ_3}{dy}\right). \tag{A.18}$$

We assume that the terms inside the large brackets are zero, which gives:

$$(U_1(y) - c)q_1' + \psi_1'\frac{dQ_1}{dy} = 0, \tag{A.19}$$

$$(U_3(y) - c)q_3' + \psi_3'\frac{dQ_3}{dy} = 0. \tag{A.20}$$

Rearranging gives us an eigenvalue problem, with the phase speed as the eigenvalue:

$$U_1(y)q_1' + \psi_1'\frac{dQ_1}{dy} = cq_1', \tag{A.21}$$

$$U_3(y)q_3' + \psi_3'\frac{dQ_3}{dy} = cq_3'. \tag{A.22}$$

Substituting in for q_i' from:

$$q_i' = \nabla^2 \psi_i' + (-1)^i \lambda^2 (\psi_1' - \psi_3'), \tag{A.23}$$

gives:

$$U_1(y)\left(\left(\frac{\partial^2}{\partial x^2} + \frac{\partial^2}{\partial y^2}\right)\psi_1' - \lambda^2(\psi_1' - \psi_3')\right) + \psi_1' \frac{dQ_1}{dy} = c\left(\left(\frac{\partial^2}{\partial x^2} + \frac{\partial^2}{\partial y^2}\right)\psi_1' - \lambda^2(\psi_1' - \psi_3')\right), \tag{A.24}$$

$$U_3(y)\left(\left(\frac{\partial^2}{\partial x^2} + \frac{\partial^2}{\partial y^2}\right)\psi_3' + \lambda^2(\psi_1' - \psi_3')\right) + \psi_3' \frac{dQ_3}{dy} = c\left(\left(\frac{\partial^2}{\partial x^2} + \frac{\partial^2}{\partial y^2}\right)\psi_3' + \lambda^2(\psi_1' - \psi_3')\right). \tag{A.25}$$

If we assume that the horizontal wavenumber of the perturbation is constant, i.e.:

$$\frac{\partial^2 \psi_i'}{\partial x^2} = -k^2 \psi_i' \tag{A.26}$$

and rearrange equations A.24 and A.25 to separate the terms containing ψ_1' and ψ_3', we get:

$$\left(U_1(y)\left(\frac{\partial^2}{\partial y^2} - \lambda^2 - k^2\right) + \frac{dQ_1}{dy}\right)\psi_1' + U_1(y)\lambda^2\psi_3' = c\left(\left(\frac{\partial^2}{\partial y^2} - \lambda^2 - k^2\right)\psi_1' + \lambda^2\psi_3'\right), \tag{A.27}$$

$$\left(U_3(y)\left(\frac{\partial^2}{\partial y^2} - \lambda^2 - k^2\right) + \frac{dQ_3}{dy}\right)\psi_3' + U_3(y)\lambda^2\psi_1' = c\left(\left(\frac{\partial^2}{\partial y^2} - \lambda^2 - k^2\right)\psi_3' + \lambda^2\psi_1'\right). \tag{A.28}$$

By writing the differential term $\frac{\partial^2}{\partial y^2}$ in finite difference form, given as:

$$\frac{\partial^2 \phi}{\partial y^2} \equiv \frac{\phi_{n+1} + \phi_{n+1} - 2\phi_n}{(\Delta y)^2} \equiv N^2(\phi_{n+1} + \phi_{n+1} - 2\phi_n), \tag{A.29}$$

we can represent this in matrix notation:

$$A\underline{x} = cB\underline{x}, \tag{A.30}$$

where $\underline{x}$ represents (ψ_1', ψ_3'). If A, B have dimensions 2 $\times$ y-gridpoints N(34) squared, then the matrix coefficients should be as given in table A. Solving this will give us a series of eigenvalues $c = c_r + ic_i$ and corresponding eigenvectors

A	Entry (i from 2 to N-1)
(i-1,i)	$N^2 U_{1_i}$
(i,i)	$-(\lambda^2 + k^2 + 2N^2)U_{1_i} + \frac{dQ_1}{dy}$
(i+1,i)	$N^2 U_{1_i}$
(i+N,i)	$\lambda^2 U_{1_i}$
B	Entry (i from 2 to N-1)
(i-1,i)	N^2
(i,i)	$-(\lambda^2 + k^2 + 2N^2)$
(i+1,i)	N^2
(i+N,i)	λ^2
A	Entry (i from N+2 to 2N-1)
(i-1,i)	$N^2 U_{3_i}$
(i,i)	$-(\lambda^2 + k^2 + 2N^2)U_{3_i} + \frac{dQ_3}{dy}$
(i+1,i)	$N^2 U_{3_i}$
(i-N,i)	$\lambda^2 U_{3_i}$
B	Entry (i from N+2 to 2N-1)
(i-1,i)	N^2
(i,i)	$-(\lambda^2 + k^2 + 2N^2)$
(i+1,i)	N^2
(i-N,i)	λ^2
A	Entry (i = 0, N, N+1, 2N)
(i,i)	1
B	Entry (i = 0, N, N+1, 2N)
(i,i)	0
A,B	Any others zero by default

Table A.1: Matrix coefficients for the case where $k = 0$, solving for eigenvalue c.

(ψ_1', ϕ_3') (which can also be complex in nature). We then search for those modes which have a non-zero imaginary component of the eigenvalue c (i.e. $c_i \neq 0$), which implies a growing mode. These will come in pairs, as the c values occur in complex conjugate pairs. We then check for those which have a real eigenvector component of wave-2 form.

Appendix B

Derivation of KE Tendency Equations

These equations follow a similar derivation from that in Higgins and Schubert (1994). Using a filtering technique, we split the flow into three components: time-mean, low-frequency and high-frequency, e.g.:

$$\psi = \psi^M + \psi^L + \psi^H, \tag{B.1}$$

$$\mathbf{v} = \mathbf{v}^M + \mathbf{v}^L + \mathbf{v}^H. \tag{B.2}$$

The momentum equation for either channel layer is:

$$\frac{\partial \mathbf{v}}{\partial t} + \mathbf{v}.\nabla\mathbf{v} + f\mathbf{k} \times \mathbf{v} + \nabla f_0\psi = \mathbf{F}, \tag{B.3}$$

where

$$\mathbf{F} = -(\varepsilon + S(x))\mathbf{v} + \nu\nabla^2.\mathbf{v}, \tag{B.4}$$

which becomes:

$$\frac{\partial \mathbf{v}^{L+H}}{\partial t} + (\mathbf{v}^{M+L+H}.\nabla)\mathbf{v}^{M+L+H} + f\mathbf{k} \times \mathbf{v}^{M+L+H} + \nabla f_0\psi^{M+L+H} = \mathbf{F}. \tag{B.5}$$

Using the identity:

$$(\mathbf{v}.\nabla)\mathbf{v} = \nabla\left(\frac{\mathbf{v}.\mathbf{v}}{2}\right) + (\mathbf{k}.\nabla \times \mathbf{v})\mathbf{k} \times \mathbf{v}, \tag{B.6}$$

this becomes:

$$\frac{\partial \mathbf{v}^{L+H}}{\partial t} + \nabla(K + f_0\psi^{M+L+H}) + (\zeta^{M+L+H} + f)\mathbf{k} \times \mathbf{v}^{M+L+H} + \omega^{M+L+H}\frac{\partial \mathbf{v}^{M+L+H}}{\partial p} = \mathbf{F}. \tag{B.7}$$

The time-mean of this equation is then taken, which gives:

$$\frac{\partial \mathbf{v}^M}{\partial t} + \nabla(K^M + f_0\psi^M) + (\zeta^M + f)\mathbf{k} \times \mathbf{v}^M + \omega^M \frac{\partial \mathbf{v}^M}{\partial p} = \mathbf{M}, \tag{B.8}$$

where:

$$\begin{aligned} \mathbf{M} \equiv \; & - \; (\nabla K^L)^M - (\zeta^L \mathbf{k} \times \mathbf{v}^L)^M - \left(\omega^L \frac{\partial \mathbf{v}^L}{\partial p}\right)^M \\ & - \; (\nabla K^H)^M - (\zeta^H \mathbf{k} \times \mathbf{v}^H)^M - \left(\omega^H \frac{\partial \mathbf{v}^H}{\partial p}\right)^M + \mathbf{F}^M. \end{aligned} \tag{B.9}$$

To obtain an equation for the time-tendency of the low-frequency kinetic energy $\frac{\mathbf{v}^L.\mathbf{v}^L}{2}$, we subtract B.8 from B.7, then take the scalar product with $\mathbf{v}^L$, using the vector identities:

$$\mathbf{v}.\nabla g = \nabla.g\mathbf{v} - g\nabla.\mathbf{v}, \tag{B.10}$$

$$\mathbf{v}.g\mathbf{k} \times \mathbf{v} = g\mathbf{v}.\mathbf{k} \times \mathbf{v} = 0, \tag{B.11}$$

and assuming that co-variances between high and low frequencies are small i.e. terms of the following combinations are zero:

$$HL = HM = HLL = HMM = HLM = 0. \tag{B.12}$$

This gives:

$$\begin{aligned} & \frac{\partial K^L}{\partial t} + \nabla.(K^L\mathbf{v}^L) - K^L\nabla.\mathbf{v}^L + \nabla.f_0\psi^L\mathbf{v}^L - f_0\psi^L\nabla.\mathbf{v}^L + \nabla.(K^H\mathbf{v}^L) \\ & -K^H\nabla.\mathbf{v}^L + \nabla.(\mathbf{v}^L.\mathbf{v}^M)\mathbf{v}^L - (\mathbf{v}^L\mathbf{v}^M)\nabla.\mathbf{v}^L - \mathbf{v}^H.\zeta^H\mathbf{k} \times \mathbf{v}^L + \mathbf{v}^L.\zeta^L\mathbf{k} \times \mathbf{v}^M \\ & +\mathbf{v}^L.\omega^L\frac{\partial \mathbf{v}^L}{\partial p} + \mathbf{v}^L.\omega^H\frac{\partial \mathbf{v}^H}{\partial p} + \mathbf{v}^L.\omega^L\frac{\partial \mathbf{v}^M}{\partial p} + \mathbf{v}^L.\omega^M\frac{\partial \mathbf{v}^L}{\partial p} = \mathbf{v}^L.\mathbf{F} - \mathbf{v}^L.\mathbf{M}. \end{aligned} \tag{B.13}$$

This is slightly different from Higgins and Schubert (1994) as they use a composite averaging techinique. We then integrate this equation with respect to x and y over the layer, which gives:

$$\left\langle \frac{\partial}{\partial t}(KE^L) \right\rangle = C(KE^M, KE^L) + C(KE^H, KE^L) + C(PE^L, KE^L) + R + F, \tag{B.14}$$

where:

$$C(KE^M, KE^L) = -\left\langle \zeta^L\mathbf{v}^L.\mathbf{k} \times \mathbf{v}^M \right\rangle,$$

represents a barotropic energy conversion from the mean flow to the low-frequency kinetic energy,

$$C(KE^H, KE^L) = \left\langle \zeta^H\mathbf{v}^H.\mathbf{k} \times \mathbf{v}^L \right\rangle,$$

represents a barotropic energy conversion from the high-frequency to the low-frequency kinetic energy,

$$C(PE^L, KE^L) = -\left\langle f_0 \psi^L \nabla . \mathbf{v}^L \right\rangle,$$

represents a conversion from the low-frequency potential to low-frequency kinetic energy,

$$F = \mathbf{v}^L . (-(\varepsilon + S(x))\mathbf{v}^L + \nu \nabla^2 \mathbf{v}^L),$$

is the component due to friction and R is the sum of all the remaining terms which are not included elsewhere,

$$R = -\left\langle \mathbf{v}^L . \mathbf{M} \right\rangle + \left\langle \mathbf{v}^L . \mathbf{F} \right\rangle + \left\langle K^L \nabla . \mathbf{v}^L \right\rangle - \left\langle K^L \nabla . \mathbf{v}^M \right\rangle + \left\langle \mathbf{v}^L . \mathbf{v}^H (\nabla . \mathbf{v}^H) \right\rangle + \left\langle \frac{\partial \mathbf{v}^L}{\partial p} . (\omega^L \mathbf{v}^M + \omega^H \mathbf{v}^H) \right\rangle - \left\langle \frac{\partial}{\partial p} [\omega^L (K^L + \mathbf{v}^L . \mathbf{v}^M) + \omega^H (\mathbf{v}^L . \mathbf{v}^H) + \omega^M K^L] \right\rangle . \tag{B.15}$$

Only the top line of equation B.15 is used to calculate R. Note that $\langle\rangle$ indicates a sum over a layer and $\mathbf{v}$ is approximated by the geostrophic velocity in all terms except $\nabla . \mathbf{v}^L$. To calculate $\nabla . \mathbf{v}^L$, we first take the geostropic continuity equation:

$$\nabla . \mathbf{v}^L + \frac{\partial \omega^L}{\partial p} = 0, \tag{B.16}$$

then use the vorticity equation (filtered for the low-frequency) rearranged, which gives:

$$f_0 \frac{\partial \omega^L}{\partial p} = \frac{\partial \zeta^L}{\partial t} + \mathbf{v}^L . \nabla (\zeta^L + f), \tag{B.17}$$

$$\nabla . \mathbf{v}^L = -\frac{1}{f_0} \left(\frac{\partial \zeta^L}{\partial t} + \mathbf{v}^L . \nabla (\zeta^L + \beta y) \right). \tag{B.18}$$

The time tendency term is estimated from the difference between the previous and subsequent dumpsteps.

Bibliography

Anderson, J. L.: 1995, A simulation of atmospheric blocking with a forced barotropic model., *Journal of the Atmospheric Sciences* **52**, 2593–2608.

Andrews, D. G. and McIntyre, M. E.: 1976, Planetary waves in horizontal and vertical shear : The generalised Eliassen-Palm relation and the mean zonal acceleration., *Journal of the Atmospheric Sciences* **33**, 2031–2048.

Arakawa, A.: 1966, Computational design for the long-term numerical integration of the equations of fluid motion: Two-dimensional incompressible flow. Part 1., *Journal of Computational Physics* **1**, 119–143.

Berggren, R., Bolin, B. and Rossby, C.-G.: 1949, An aerological study of zonal motion, its perturbations and break-down., *Tellus* **1**, 14–37.

Bishop, C. H. and Thorpe, A. J.: 1994, Potential vorticity and the electrostatics analogy - quasi-geostrophic theory., *Quart. Journal of Royal Met. Soc.* **120**, 713–731.

Blumen, W.: 1968, On the stability of quasi-geostrophic flow., *Journal of the Atmospheric Sciences* **25**, 929–931.

Bona, J. and Sachs, R. L.: 1988, Global existence of smooth solutions and stability of solitary waves for a generalized Boussinesq equation., *Communications in Mathematical Physics* **118**, 15–29.

Borges, M. D. and Sardesmukh, P. D.: 1995, Barotropic Rossby wave dynamics of zonally varying upper-level flows during northern winter., *Journal of the Atmospheric Sciences* **52**, 3779–3796.

Boville, B. A.: 1982, Strongly nonlinear vacillation in baroclinic waves., *Journal of the Atmospheric Sciences* **39**, 1227–1240.

Branstator, G.: 1983, Horizontal energy propagation in a barotropic atmosphere with meridional and zonal structure., *Journal of the Atmospheric Sciences* **40**, 1689–1708.

Branstator, G.: 1995, Orgaization of storm track anomalies by recurring low-frequency circulation anomalies., *Journal of the Atmospheric Sciences* **52**, 207–226.

Butchart, N., Clough, T. A., Palmer, T. N. and Trevelyan, P. J.: 1982, Simulations of an observed stratospheric warming with quasigeostrophic refractive index as a model diagnostic., *Quart. Journal of Royal Met. Soc.* **108**, 475–502.

Butchart, N., Haines, K. and Marshall, J. C.: 1989, A theoretical and diagnostic study of solitary waves and atmospheric blocking., *Journal of the Atmospheric Sciences* **46**, 2063–2078.

Cai, M. and Mak, M.: 1990, Symbiotic relation between planetary and synoptic-scale waves., *Journal of the Atmospheric Sciences* **47**, 2953–2968.

Carlson, T. N.: 1992, *Mid-Latitude Weather Systems.*, Routledge.

Cehelsky, P. and Tung, K. K.: 1987, Theories of multiple equilibria and weather regimes - a critical reexamination. 2. Baroclinic 2-layer models.., *Journal of the Atmospheric Sciences* **44**, 3282–3303.

Charney, J. G. and DeVore, J. G.: 1979, Multiple flow equilibria in the atmosphere and blocking., *Journal of the Atmospheric Sciences* **36**, 1205–1216.

Colucci, S. J.: 1985, Explosive cyclogenesis and large-scale circulation changes: Implications for atmospheric blocking., *Journal of the Atmospheric Sciences* **42**, 2701–2717.

Colucci, S. J., Loesch, A. Z. and Bosart, L. F.: 1981, Spectral evolution of a blocking episode and comparison with wave interaction theory., *Journal of the Atmospheric Sciences* **38**, 2092–2111.

Dole, R. M.: 1986, Persistent anomalies of the extratropical northern hemisphere winter time circulation : Structure., *Mon. Weather Review* **114**, 178–207.

Dole, R. M.: 1989, Life cycles of persistent anomalies. Part I: Evolution of 500mb height fields., *Mon. Weather Review* **117**, 177–211.

Dole, R. M. and Gordon, N. D.: 1983, Persistent anomalies of the extratropical nothern hemisphere wintertime circulation : Geographical distribution and regional persistence characteristics., *Mon. Weather Review* **111**, 1567–1586.

Edmon, H. J., Hoskins, B. J. and McIntyre, M. E.: 1980, Eliassen-Palm cross sections for the troposphere., *Journal of the Atmospheric Sciences* **37**, 2600–2616.

Egger, J.: 1978, Dynamics of blocking highs., *Journal of the Atmospheric Sciences* **35**, 1788–1801.

Ek, N. P. and Swaters, G. E.: 1994, Geostrophic scatter diagrams and the application of quasi-geostrophic free-mode theory to a northeast Pacific blocking episode., *Journal of the Atmospheric Sciences* **51**, 563–581.

Feldstein, S. B.: 1991, A comparison of the weakly nonlinear instability of westerly and easterly jets in a two-layer beta plane model., *Journal of the Atmospheric Sciences* **48**, 1701–1717.

Feldstein, S. B. and Held, I. M.: 1989, Barotropic decay or baroclinic waves in a two-layer beta plane model., *Journal of the Atmospheric Sciences* **46**, 3416–3430.

Ferranti, L., Molteni, F. and Palmer, T. N.: 1994, Impact of localized tropical and extratropical SST anomalies in ensembles of seasonal GCM integrations., *Quart. Journal of Royal Met. Soc.* **120**, 1613–1645.

Fjortoft, R.: 1953, On the changes in spectral distribution of kinetic energy for twodimensional, nondivergent flow., *Tellus* **5**, 225–230.

Flierl, G. R. and Haines, K.: 1994, The decay of modons due to Rossby wave radiation., *Physics of Fluids* **6**, 3487–3497.

Frederiksen, J. S.: 1982, A unified three-dimensional instability theory on the onset of blocking and cyclogenesis., *Journal of the Atmospheric Sciences* **39**, 969–982.

Früh, W.-G.: 1996, Low-order models of wave interactions in the transition to baroclinic chaos., *Nonlinear Processes in Geophysics* **3**, 150–165.

Früh, W.-G. and Read, P. L.: 1997, Wave interactions and the transition to chaos of baroclinic waves in a thermally driven rotating annulus., *Philosophical Transactions of the Royal Society of London Series A* **355**, 101–153.

Green, J. S. A.: 1977, The weather during July 1976 : Some dynamical considerations of the drought., *Weather* **32**, 120–128.

Haines, K.: 1989, Baroclinic modons as prototypes for atmospheric blocking., *Journal of the Atmospheric Sciences* **46**, 3202–3218.

Haines, K.: 1994, Low-frequency variability in atmospheric middle latitudes., *Surveys in Geophysics* **15**, 1–61.

Haines, K. and Hannachi, A.: 1995, Weather regimes in the Pacific from a GCM., *Journal of the Atmospheric Sciences* **48**, 510–526.

Haines, K. and Malanotte-Rizzoli, P.: 1991, Isolated anomalies in westerly jet streams : A unified approach., *Journal of the Atmospheric Sciences* **48**, 510–526.

Haines, K. and Marshall, J.: 1987, Eddy-forced coherent structures as a prototype of atmospheric blocking., *Quart. Journal of Royal Met. Soc.* **113**, 681–704.

Haines, K., Malanotte-Rizzoli, P. and Morgan, M.: 1993, Persistent jetstream intensifications : A comparison between theory and data., *Journal of the Atmospheric Sciences* **50**, 145–154.

Hansen, A. R.: 1986, Observational characteristics of atmospheric planetary waves with bimodal amplitude distributions., *Advances in Geophysics* **29**, 135–162.

Hansen, A. R. and Chen, T.-C.: 1982, A spectral energetics anaylis of atmospheric blocking.., *Journal of the Atmospheric Sciences* **110**, 1146–1165.

Hansen, A. R. and Sutera, A.: 1986, On the probability density distribution of planetary-scale atmospheric wave amplitude., *Journal of the Atmospheric Sciences* **43**, 3250–3265.

Hansen, A. R. and Sutera, A.: 1995, Large amplitude flow anomalies in northern hemisphere midlatitudes., *Journal of the Atmospheric Sciences* **52**, 2133–2151.

Helfrich, K. R. and Pedlosky, J.: 1993, Time-independent isolated anomalies in zonal flows., *Journal of Fluid Mechanics* **251**, 377–409.

Helfrich, K. R. and Pedlosky, J.: 1995, Large-amplitude coherent anomalies in baroclinic zonal flows., *Journal of the Atmospheric Sciences* **52**, 1615–1629.

Hickernell, F. J.: 1983, The evolution of large-horizontal-scale disturbances in marginally stable, inviscid, shear flows. II. Solutions of the Boussinesq equation, *Studies in Applied Mathematics* **69**, 23–49.

Hide, R.: 1966, Review article on the dynamics of rotating fluids and related topics in geophysical fluid dynamics., *Bulletin of the American Meteorological Society* **47**, 873–885.

Higgins, R. W. and Schubert, S. D.: 1994, Simulated life cycles of persistent anticyclonic anomalies over the North Pacific : Role of synoptic-scale eddies., *Journal of the Atmospheric Sciences* **51**, 3238–3260.

Holton, J. R.: 1992, *An Introduction to Dynamic Meteorology.*, 3rd edn, Academic Press.

Hoskins, B. J.: 1973, Stability of the Rossby-Haurwitz wave., *Quart. Journal of Royal Met. Soc.* **99**, 723–745.

Hoskins, B. J.: 1983a, Dynamical processes in the atmosphere and the use of models., *Quart. Journal of Royal Met. Soc.* **109**, 1–21.

Hoskins, B. J.: 1983b, Modelling of transient eddies and their feedback on the mean flow., *in* B. J. Hoskins and R. P. Pearce (eds), *Large-Scale Dynamical Processes in the Atmosphere*, Academic Press.

Hoskins, B. J. and Ambrizzi, T.: 1993, Rossby wave progpagation on a realistically longitudinally varying flow., *Journal of the Atmospheric Sciences* **50**, 1661–1671.

Hoskins, B. J. and Karoly, D. J.: 1981, The steady, linear response of a spherical atmosphere to thermal and orographic forcing., *Journal of the Atmospheric Sciences* **38**, 1179–1196.

Hoskins, B. J. and Sardesmukh, P. D.: 1975, A diagnostic study of the dynamics of the northern hemisphere winter of 1985-86., *Quart. Journal of Royal Met. Soc.* **113**, 759–778.

Hoskins, B. J. and Simmons, A. J.: 1975, A multi-layer spectral model and the semi-implicit method., *Quart. Journal of Royal Met. Soc.* **101**, 637–655.

Hoskins, B. J. and Valdes, P. J.: 1990, On the existence of storm-tracks., *Journal of the Atmospheric Sciences* **47**, 1854–1864.

Hoskins, B. J., James, I. N. and White, G. H.: 1983, The shape, propagation and mean-flow interaction of large-scale weather systems., *Journal of the Atmospheric Sciences* **40**, 1595–1612.

Hoskins, B. J., McIntyre, M. E. and Robertson, A. W.: 1985, On the use and significance of isentropic potential vorticity maps., *Quart. Journal of Royal Met. Soc.* **111**, 877–946.

Illari, L.: 1984, A diagnostic study of potential vorticity in a warm blocking anticyclone., *Journal of the Atmospheric Sciences* **41**, 3518–3526.

Illari, L. and Marshall, J. C.: 1983, On the interpretation of eddy fluxes during a blocking episode., *Journal of the Atmospheric Sciences* **40**, 2232–2242.

James, I. N.: 1994, *Introduction to Circulating Atmospheres.*, Cambridge University Press.

James, P. M., Fraedrich, K. and James, I. N.: 1994, Wave-zonal-flow interaction and ultra-low-frequency variability in a simplified global circulation model., *Quart. Journal of Royal Met. Soc.* **120**, 1045–1067.

Jin, F.-F. and Ghil, M.: 1990, Intraseasonal oscillations in the Extratropics: Hopf bifurcation and topographic instabilities., *Journal of the Atmospheric Sciences* **47**, 3007–3022.

Kaas, E. and Branstator, G.: 1993, The relationship between a zonal index and blocking activity., *Journal of the Atmospheric Sciences* **50**, 3061–3077.

Kalnay-Rivas, E. and Merkine, L.-O.: 1981, A simple mechanism for blocking., *Journal of the Atmospheric Sciences* **38**, 2077–2091.

Karoly, D. J. and Hoskins, B. J.: 1982, Three dimensional propagation of planetary waves., *Journal of the Met. Soc. of Japan* **60**, 109–123.

Kilworth, P. D. and McIntyre, M. E.: 1985, Do Rossby-wave critical layers absorb, reflect, or overreflect?, *Journal of Fluid Mechanics* **161**, 449–492.

Kubokawa, A.: 1989, Growing solitary disturbance in a baroclinic boundary current., *Journal of Physical Oceanography* **19**, 182–192.

Lee, S.: 1995, Localized storm tracks in the absence of local instability., *Journal of the Atmospheric Sciences* **52**, 977–989.

Liu, Q.: 1994, On the definition and persistence of blocking., *Tellus* **46A**, 286–298.

Lorenz, E. N.: 1963, Deterministic nonperiodic flow., *Journal of the Atmospheric Sciences* **20**, 130–141.

Lorenz, E. N.: 1972, Barotropic instability of Rossby wave motion., *Journal of the Atmospheric Sciences* **29**, 258–264.

Malguzzi, P.: 1993, An analytical study on the feedback between large- and small-scale eddies., *Journal of the Atmospheric Sciences* **50**, 1429–1436.

Malguzzi, P. and Malanotte-Rizzoli, P.: 1984, Nonlinear stationary Rossby waves on non-uniform zonal winds and atmospheric blocking. Part I : The analytical theory, *Journal of the Atmospheric Sciences* **41**, 2620–2628.

Marcus, P. S.: 1990, Vortex dynamics in a shearing zonal flow., *Journal of Fluid Mechanics* **215**, 393–430.

Marshall, J. and Shutts, G.: 1981, A note on rotational and divergent eddy fluxes., *Journal of Physical Oceanography* **11**, 1677–1680.

Matsuno, T.: 1970, Vertical propagation of stationary planetary waves in the winter Northern hemisphere., *Journal of the Atmospheric Sciences* **27**, 871–883.

McIlveen, R.: 1992, *Fundamentals of Weather and Climate.*, Chapman and Hall.

McWilliams, J. C.: 1980, An application of equivalent modons to atmospheric blocking., *Dyn. Atmos. Oceans.* **5**, 43–66.

Molteni, F.: 1996a, On the dynamics of planetary flow regimes. Part I: The role of high-frequency transients., *Journal of the Atmospheric Sciences* **53**, 1950–1971.

Molteni, F.: 1996b, On the dynamics of planetary flow regimes. Part II: Results from a hierarchy of orographically forced models., *Journal of the Atmospheric Sciences* **53**, 1972–1992.

Mullen, S. L.: 1987, Transient eddy forcing of blocking flows., *Journal of the Atmospheric Sciences* **44**, 3–22.

Nathan, T. R. and Barcilon, A.: 1994, Low-frequency oscillations of forced barotropic flow., *Journal of the Atmospheric Sciences* **51**, 582–588.

Nitsche, G., Wallace, J. M. and Kooperberg, C.: 1994, Is there evidence of multiple equilibria in planetary wave amplitude statistics?, *Journal of the Atmospheric Sciences* **51**, 314–322.

Palmén, E. and Newton, C. W.: 1969, *Atmospheric Circulation Systems.*, Academic Press.

Palmer, T. N.: 1980, Diagnostic study of a wavenumber-2 stratospheric sudden warming in a transformed Eulerian-mean formalism., *Journal of the Atmospheric Sciences* **38**, 844–855.

Palmer, T. N.: 1981, Aspects of stratospheric sudden warmings studied from a transformed Eulerian-mean viewpoint., *Journal of Geophysical Research* **86**, 9679–9687.

Palmer, T. N.: 1993, Extended-range atmospheric prediction and the Lorenz model., *Bulletin of the American Met. Soc.* **74**, 49–65.

Pedlosky, J.: 1964a, The stability of currents in the atmosphere and the ocean : Part I., *Journal of the Atmospheric Sciences* **21**, 201–219.

Pedlosky, J.: 1964b, The stability of currents in the atmosphere and the ocean : Part II., *Journal of the Atmospheric Sciences* **21**, 342–353.

Pedlosky, J.: 1970, Finite-amplitude baroclinic waves., *Journal of the Atmospheric Sciences* **27**, 15–30.

Pedlosky, J.: 1971, Finite-amplitude baroclinic waves with small dissipation., *Journal of the Atmospheric Sciences* **28**, 587–597.

Pedlosky, J.: 1972, Limit cycles and unstable baroclinic waves., *Journal of the Atmospheric Sciences* **29**, 53–63.

Pedlosky, J.: 1981, Resonant topographic waves in barotropic and baroclinic flows., *Journal of the Atmospheric Sciences* **38**, 2626–2641.

Pedlosky, J.: 1983, The growth and decay of finite-amplitude baroclinic waves., *Journal of the Atmospheric Sciences* **40**, 1863–1876.

Pedlosky, J.: 1986, *Geophysical Fluid Dynamics.*, 2nd edn, Springer-Verlag.

Pedlosky, J. and Frentzen, C.: 1980, Chaotic and periodic behaviour of finite-amplitude baroclinic waves., *Journal of the Atmospheric Sciences* **37**, 1177–1196.

Pfeffer, R. L.: 1992, A study of eddy-induced fluctuations of the zonal-mean wind using conventional and transformed Eulerian diagnostics., *Journal of the Atmospheric Sciences* **49**, 1036–1050.

Phillips, N. A.: 1954, Energy transformations and meridional circulations associated with simple baroclinic waves in a two-level, quasi-geostrophic model., *Tellus* **6**, 273–286.

Phillips, N. A.: 1956, The general circulation of the atmosphere : a numerical experiment., *Quart. Journal of Royal Met. Soc.* **82**, 123–164.

Plaut, G. and Vautard, R.: 1994, Spells of low-frequency oscillations and weather regimes in the Northern hemisphere., *Journal of the Atmospheric Sciences* **51**, 210–236.

Plumb, R. A.: 1979, Forced waves in a baroclinic shear flow. Part 1 : Undamped evolution near the baroclinic instability threshold., *Journal of the Atmospheric Sciences* **36**, 205–216.

Plumb, R. A.: 1981, Forced waves in a baroclinic shear flow. Part 2 : Damped and undamped response to weak near-resonant forcing., *Journal of the Atmospheric Sciences* **38**, 1856–1869.

Plumb, R. A.: 1983, A new look at the energy cycle., *Journal of the Atmospheric Sciences* **40**, 1669–1688.

Plumb, R. A.: 1986, Three-dimensional propagation of transient quasi-geostrophic eddies and its relationship with the eddy forcing of the time-mean flow., *Journal of the Atmospheric Sciences* **43**, 1657–1678.

Read, P. L., Rhines, P. B. and White, A. A.: 1986, Geostrophic scatter diagrams and potential vorticity dynamics., *Journal of the Atmospheric Sciences* **43**, 3226–3240.

Reinhold, B. B. and Pierrehumbert, R. T.: 1982, Dynamics of weather regimes - quasi-stationary waves and blocking., *Monthly Weather Review* **110**, 1105–1145.

Rex, D. F.: 1950a, Blocking action in the middle troposphere and its effect upon regional climate. I. An aerological study of blocking action., *Tellus* **2**, 196–211.

Rex, D. F.: 1950b, Blocking action in the middle troposphere and its effect upon regional climate. II. The climatology of blocking action., *Tellus* **2**, 275–301.

Robinson, W. A.: 1994, Eddy feedbacks on the zonal index and eddy-zonal flow interactions induced by zonal flow transience., *Journal of the Atmospheric Sciences* **51**, 2553–2562.

Schilling, H.-D.: 1986, On atmospheric blocking types and blocking numbers., *Advances in Geophysics* **29**, 71–99.

Shutts, G. J.: 1983, The propagation of eddies in diffluent jetstreams : Eddy vorticity of 'blocking' flow fields., *Quart. Journal of Royal Met. Soc.* **109**, 737–761.

Shutts, G. J.: 1986, A case study of eddy forcing during an Atlantic blocking episode., *Advances in Geophysics* **29**, 135–162.

Simmons, A. J. and Burridge, D. M.: 1981, An energy and angular-momentum conserving vertical finite-difference scheme and hybrid vertical coordinates., *Monthly Weather Review* **109**, 758–766.

Simmons, A. J. and Hoskins, B. J.: 1977, The life cycles of some nonlinear baroclinic waves., *Journal of the Atmospheric Sciences* **35**, 414–432.

Simmons, A. J. and Hoskins, B. J.: 1980, Barotropic influences on the growth and decay of nonlinear baroclinic waves., *Journal of the Atmospheric Sciences* **37**, 1679–1684.

Thorncroft, C. D., Hoskins, B. J. and McIntyre, M. E.: 1993, Two paradigms of baroclinic-wave life-cycle behaviour., *Quart. Journal of Royal Met. Soc.* **119**, 17–56.

Tibaldi, S., Palmer, T. N., Brankovic, U. and Cubasch, U.: 1990, Extended-range predictions with ECMWF models - influence of horizontal resolution on systematic-error and forecast skill., *Quart. Journal of Royal Met. Soc.* **116**, 835–866.

Tung, K. K.: 1979, A theory of stationary long waves. Part III : Quasi-normal modes in a singular waveguide., *Monthly Weather Review* **107**, 751–774.

Tung, K. K. and Lindzen, R. S.: 1979a, A theory of stationary long waves. Part I : A simple theory of blocking., *Monthly Weather Review* **107**, 714–734.

Tung, K. K. and Lindzen, R. S.: 1979b, A theory of stationary long waves. Part II : Resonant Rossby waves in the presence of realistic vertical shears., *Monthly Weather Review* **107**, 735–750.

Tung, K. K. and Rosenthal, A. J.: 1985, Theories of multiple equilibria - A critical reexamination, Part I: Barotropic models., *Journal of the Atmospheric Sciences* **42**, 2804–2819.

Vautard, R.: 1990, Multiple weather regimes over the North Atlantic : Analysis of precursors and successors., *Monthly Weather Review* **118**, 2056–2081.

Vautard, R. and Legras, B.: 1988, On the source of low-frequency variability. Part II : Nonlinear equilibration of weather regimes., *Journal of the Atmospheric Sciences* **45**, 2845–2867.

Vautard, R., Legras, B. and Deque, M.: 1988, On the source of low-frequency variability. Part I : A statistical approach to persistence., *Journal of the Atmospheric Sciences* **45**, 2811–2843.

Wallace, J. M. and Blackmon, M. L.: 1983, Observations of low-frequency atmospheric variability., *in* B. J. Hoskins and R. P. Pearce (eds), *Large-Scale Dynamical Processes in the Atmosphere*, Academic Press.

Wallace, J. M. and Cheng, X.: 1991, Does low-frequency variability exhibit regime-like behaviour?, *Tellus A-B* **43**, 16–26.

Wallace, J. M. and Gutzler, D. S.: 1981, Teleconnections in the geopotential height field during the Northern hemisphere winter., *Monthly Weather Review* **109**, 784–812.

Wu, P.: 1993, Nonlinear resonance and instability of planetary waves and low-frequency variability in the atmosphere., *Journal of the Atmospheric Sciences* **50**, 3590–3607.

Yang, G.-Y. and Hoskins, B. J.: 1996, Propagation of Rossby waves of nonzero frequency., *Journal of the Atmospheric Sciences* **53**, 2365–2378.

Q. J. R. Meteorol. Soc. (1998), **124**, pp. 873–895

Vacillation cycles and blocking in a channel.

By K. HAINES* and A. J. HOLLAND

Department of Meteorology, University of Edinburgh, UK

(Received 16 December 1996; revised 5 August 1997)

SUMMARY

The response to a low-level high-frequency wavemaker forcing in a two-layer, β−plane, quasi-geostrophic channel model is examined. The wavemaker simulates regular baroclinic instability which then propagates to upper atmospheric levels to excite blocking. By altering the meridional shear in the upper-layer, the large-scale response can vary from a steady, large-amplitude split jet very similar to observed blocks, to a weaker split with a low-frequency vacillation cycle. The eddies will always resonantly excite the split flow, but a mixed instability process is responsible for the breakdown in cases which oscillate, as demonstrated using a simplified zonal stability analysis and energy tendency diagnostics. The re-excitement by the eddies continues the cycle. This model provides a theory of how the meridional structure of the upper level winds may determine whether a large amplitude block can be excited or persist in the presence of similar high-frequency eddy activity propagating up from below.

KEYWORDS: Blocking Low-frequency variability Eddy/Mean-flow interaction

1. INTRODUCTION

Atmospheric blocking has been studied intensively for the last decade because of its important influence on weather and regional climate and the difficulty of predicting blocking events or reproducing them within General Circulation Models (GCMs). An important influence on blocking studies was the proposal by Green (1977), that high-frequency transient eddies within the atmospheric storm tracks might play a role in maintaining the anomalous vorticity budget during blocking events. Numerous diagnostic studies using data eg. Illari (1984), Shutts (1986), Hoskins *et al.* (1985), Dole (1986,1989), and GCMs, eg. Mullen (1986), Branstator (1992), appear to confirm the importance of interactions between the smaller-scale, high-frequency, eddies and larger-scale blocking waves. Unfortunately none of these studies give direct indication that improved predictability may be possible, because transient cyclones are generated continuously in the storm tracks and the vast majority of them do not go on to initiate blocking. Studies by Dole (1986,1989), Mo and Ghil (1988), Vautard (1990) and Plaut and Vautard (1994) found consistent large scale blocking pre-cursor flow patterns and Vautard *et al.* (1996) attempted to use these precursors to investigate predictive skill. However this work remains mostly descriptive unless some theoretical foundations can be found. To have a chance of understanding any necessary pre-cursors for blocking, a simpler modelling approach is needed.

Perhaps the most convincing, and the simplest, model of eddies exciting a block can be found in Shutts (1983) where an equivalent barotropic channel is used with a wavemaker to artificially produce high-frequency eddies. This model produced a continuous state of blocking downstream of the region of eddy generation which Shutts showed to be due to eddy vorticity fluxes. The scale of the excited block is the stationary Rossby wave scale within the channel. Shutts also showed that blocking does not occur for more rapid flows in which a stationary wave cannot be excited. This suggests that an accessible quasi-steady free-mode state may be a necessary pre-condition for blocking. The atmosphere may always have blocking-like free states available if one considers the modon or soliton waves, eg. McWilliams (1980), Haines and Marshall (1987), Haines and Malanotte-Rizzoli (1991), Flierl and Haines (1994), which can persist in a wide variety

* Corresponding author: Department of Meteorology, University of Edinburgh, JCMB, Kings Buildings, Mayfield Road, Edinburgh, EH9 3JZ, UK. Email: K.Haines@ed.ac.uk

of zonal flows. However modons were not found in the Shutts (1983) study and we need to understand more clearly what factors control the resonant response of a jetstream to the presence of transient eddies in order to make further progress.

Vautard and Legras (1988) extended the Shutts model to 2-layers and dispensed with the wavemaker, maintaining instead a short region of baroclinity using thermal forcing. They showed convincingly that sometimes blocking did occur downstream, when a large amplitude stationary wave develops, and sometimes the downstream flow is more zonal. This result, while more realistic than the continuous blocking of Shutts, does not explore other influences on the frequency or persistence of blocking. In particular, variations in the mean flow which may be influenced by larger scale events, eg. teleconnections and variations in planetary wave amplitudes such as the Pacific North American (PNA) and North Atlantic Oscillation (NAO) patterns, might have an influence on blocking frequency and hence make blocking more predictable. Recent results in 2 areas suggest that this may be so.

Thorncroft *et al.* (1993) showed that changes in horizontal shear can influence the late-stage non-linear lifecycles of baroclinic waves. They hinted that different lifecycles may then have different probabilities of exciting a block. Secondly, Ferranti *et al.* (1994) have shown that tropical SSTs may influence blocking frequency in middle latitudes, presumably by modifying transient cyclone behaviour although this is not demonstrated. For a more detailed review see Haines (1994). These results have inspired us to return to simple models of blocking, forced by eddies, to try to address mean flow influences on blocking.

Section 2 describes the basic model framework consisting of a 2-layer quasi-geostrophic channel, like Vautard and Legras (1988), but with a wavemaker to produce eddies within the lower layer. The forcing/dissipation balances in the 2 layers are discussed. Section 3 presents results for a vertically sheared flow without horizontal shear. Section 4 describes the changes upon introducing a meridional shear to the jetstream in the upper layer. Section 5 presents a stability and energy analysis for the growth and decay of the observed jet-splitting events. Section 6 provides discussion and conclusions.

2. The Model

A 2-layer, zonally periodic, β-plane, quasi-geostrophic channel is used, satisfying the following equation;

$$\frac{\partial q_i}{\partial t} + J(\psi_i, q_i) = \delta_{i,1} W - (\epsilon + S(x))\nabla^2(\psi_i - \psi_i^I) + \kappa\nabla^4(\psi_i - \psi_i^I) \tag{1}$$

for $i = 1,2$, where

$$q_1 = \nabla^2\psi_1 + \beta y - \gamma^2(\psi_1 - \psi_2) \tag{2}$$

$$q_2 = \nabla^2\psi_2 + \beta y - \gamma^2(\psi_2 - \psi_1). \tag{3}$$

q is the quasi-geostrophic potential vorticity, ψ is the streamfunction, where the subscripts are 1 for the lower layer and 2 for the upper layer. The Jacobian may be rewritten as $J(\psi, q) \equiv \mathbf{v}.\nabla q \equiv \nabla.(\mathbf{v}q)$. W is a wavemaker forcing, $\delta_{i,1}$ is the Kronecker function, and ψ_i^I is a specified initial zonal flow towards which relaxation occurs. ϵ and κ are dissipation parameters and $S(x)$ is a sponge layer. The planetary vorticity gradient $\beta = 1.6 \times 10^{-11}\mathrm{m}^{-1}\mathrm{s}^{-1}$ and the deformation radius parameter $\gamma^2 = 7.844 \times 10^{-13}\mathrm{m}^{-2}$. The width of the channel is 6000km and the length is 20000km with a resolution $dx = dy$ =200km. Other parameter values are described below.

(*a*) *The Wavemaker*

In the atmosphere, transient eddies grow strongly by conversion of low-level available potential energy. The wave activity produced then propagates to upper-levels where meridional air parcel displacements may become very large due to the decrease in air density, and the waves become non-linear. Eliassen-Palm fluxes, eg. Edmon *et al.* (1980) can be used to follow the vertical and meridional propagation of the wave activity in a zonal mean framework. The physical distinction between the region of wave generation (near the surface) and the region of non-linear wave breaking and blocking initiation (at upper-levels) suggests that a wavemaker could reasonably be substituted as an eddy source at low-levels.

The use of a wavemaker is not a retrograde step from the Vautard and Legras (1988) work. Its use recognizes that baroclinic growth is a low-level phenomenon and it is therefore to some extent independent of the initiation of any blocking at upper levels, during the mature stage of storm lifecycles, as in Thorncroft *et al.* (1993). With a wavemaker at lower levels the wave activity at upper levels increases due to vertical propagation from below in a mostly conservative fashion, as it would with a truely unstable low level source. This aspect cannot be captured in a barotropic model in which the wavemaker and jetstream are in the same layer. The upward propagation phase still provides an opportunity for feedback where the presence of the block affects the transient eddy behaviour. Diabatic processes must also play a part in cyclone development. At low levels the availability of surface moisture from a warm ocean help to fix the baroclinic zones, again independently of the upper level jetstream structure. Although diabatic processes also affect upper levels they mostly play a dissipative role so that wave growth and breaking is essentially a function of the low level source and the upward propagation path of the eddies. The wavemaker framework simplifies the possible feedbacks considerably, allowing more freedom in choosing the upper-layer flow conditions which in turn feedback on high-frequency wave propagation.

In this model the wavemaker, W, is placed in the lower layer with the form,

$$W(x,y,t) = \tilde{W}(x,y)\mathrm{Cos}(kx - \omega t) \qquad x_0 < x < x_0 + L_x \tag{4}$$

$$\tilde{W} = A\ \mathrm{Sin}\pi\frac{(x-x_0)}{L_x}\mathrm{Sin}\pi\frac{(y-y_0)}{L_y} \qquad y_0 < y < y_0 + L_y$$

where $L_x = 4360\mathrm{km}$, $L_y = 2730\mathrm{km}$ and $k = 2\pi/(2900\mathrm{km})$. This wavemaker is based on that of Shutts (1983) and gives zero forcing in a spatial or temporal average sense. The period of the wavemaker corresponds to 4.5 days, i.e. a 2.25 day timescale for each synoptic system. Although the upper-layer flow is altered immediately by introduction of vorticity into the lower layer, the upper-layer potential vorticity is not directly modified and so irreversible changes in upper-layer time-mean flow can only occur through wave breaking and dissipation. However local reversible changes may still occur whose nature becomes clear if the flow returns to its previous configuration downstream of the region of eddy activity, Plumb (1990).

(*b*) *The Dissipation*

Values of the dissipation parameters are $\epsilon = 1.92 \times 10^{-7}\mathrm{s}^{-1}$, $\kappa = 4 \times 10^5\mathrm{m}^2\mathrm{s}^{-1}$. The Laplacian dissipation term $\nabla^2(\psi - \psi^I)$ has a vorticity dissipation coefficient $S(x)$ which increases ϵ by a factor of 1000 in the last fifth of the channel to provide a sponge to prevent the re-circulation of the wavemaker eddies. All dissipation terms relax the upper-layer flow back to a zonal flow $\psi_2^I(y)$, which may include a meridional wind shear. The lower-layer flow is kept small by the vorticity dissipation because $\psi_1^I = 0$ in all of the runs

reported here. This choice is made because the mean surface winds are much weaker than those at upper atmospheric levels. This also means that the vorticity introduced by the wavemaker in the lower layer is not immediately advected downstream.

(c) *Stationary Rossby Waves and Stability Criterion*

To interpret the results it is useful to first review the stationary wave properties of the zonal flows used. If the zonal flow in the channel is defined by;

$$\psi_1^I = 0; \qquad \psi_2^I(y) = -Uy, \tag{5}$$

$$q_1^I = (\beta - U\gamma^2)y; \qquad q_2^I = (\beta + U\gamma^2)y$$

where U is the constant upper-layer wind, then if $U > 14.6\text{ms}^{-1}$ no antisymmetric stationary waves can exist in the channel. If $U = 7.3\text{ms}^{-1}$, an antisymmetric stationary wave has the same zonal length scale as the channel width, i.e. 6000km. In any case stationary waves are confined to the upper layer and remain solutions at any amplitude, always with zero amplitude in the lower layer. This is true provided $U < \frac{\beta}{\gamma^2} = 20.4\text{ms}^{-1}$, otherwise the zonal flow becomes baroclinically unstable with $\frac{\partial q_1^I}{\partial y}$ negative. For any more general upper-layer flow with nonlinear $\psi_2^I(y)$, the linear stationary wavelength changes with latitude and exact solutions cannot be found at finite amplitude. All of the zonal flows studied here will be initially stable although the most interesting cases are those close enough to the stability limit that the presence of a superimposed block can make the flow locally supercritical. Two factors might support the study of such jets; (i) Stone (1972) suggested that the baroclinic waves are efficient at maintaining the atmospheric jet close to the critical stability limit, at least in a zonally averaged sense; (ii) most intense baroclinic activity occurs near the surface while the middle and upper troposphere, considered in isolation, may be less unstable.

(d) *Eddy-mean flow interaction*

In order to understand the dominant features of the eddy-mean flow interaction we can consider the unforced/undamped momentum equations at upper levels. By separating the flow into time-mean and eddy components (e.g. $\psi = \psi^M + \psi'$), the mean zonal and meridional momentum equations may be written

$$\frac{\partial u^M}{\partial t} + \frac{\partial (u^M)^2}{\partial x} + \frac{\partial (u^M v^M)}{\partial y} + \frac{\partial (u'^2)^M}{\partial x} + \frac{\partial (u'v')^M}{\partial y} - \beta y v^M - f_0 v_{ag}^M = 0, \tag{6}$$

$$\frac{\partial v^M}{\partial t} + \frac{\partial (v^M)^2}{\partial y} + \frac{\partial (u^M v^M)}{\partial x} + \frac{\partial (v'^2)^M}{\partial y} + \frac{\partial (u'v')^M}{\partial x} + \beta y u^M + f_0 u_{ag}^M = 0. \tag{7}$$

Velocity terms without subscripts are geostrophic components. The largest eddy terms in the model arise in the region over the wavemaker, which is defined to produce eddies which are meridionally elongated, consistent with the findings of Hoskins *et al.* (1983) for high-pass eddies. This means that $(v'^2)^M \gg (u'^2)^M$ or $(u'v')^M$ and the dominant eddy term is $\frac{\partial (v'^2)^M}{\partial y}$ in (7), as discussed in Hoskins (1983).

The mean vorticity ζ^M equation can then be written as

$$\frac{\partial \zeta^M}{\partial t} + \mathbf{v}^M.\nabla(\zeta^M + f) + f_0 \nabla.\mathbf{v}_{ag}^M$$
$$+ \frac{\partial^2 (v'^2 - u'^2)^M}{\partial y \partial x} - \frac{\partial^2 (u'v')^M}{\partial y^2} + \frac{\partial^2 (u'v')^M}{\partial x^2} = 0. \tag{8}$$

The $\frac{\partial (v'^2)^M}{\partial y}$ term becomes $\frac{\partial^2 (v'^2)^M}{\partial x \partial y}$ in the vorticity equation. Because of the amplitude envelope $\tilde{W}$ over the wavemaker, $(v'^2)^M$ will be a maximum at the centre of the region. The double derivative acting on this dominant term in (8) then gives rise to a quadrupole component in the eddy forcing. If only the last eddy term in (8) can be neglected then the Hoskins (1983) E-vector can be derived. Otherwise, when written out in full, the eddy feedback is $J(\psi', \zeta')^M \equiv \nabla.(\mathbf{v}'\zeta')^M$, which forms a component of the potential vorticity eddy feedback.

3. Uniform Upper-Layer Flow

For uniform upper-layer flow, $\psi_2^I(y) = -Uy$. The wavemaker was switched on with amplitude $A = 1.2 \times 10^{-9} \mathrm{s}^{-2}$ and the model was integrated for 360 days with the final 200 days being used for diagnostics. We show first results with $U = 15 \mathrm{ms}^{-1}$, close to the limit for stationary wave activity. Although this flow is baroclinically stable the potential vorticity gradient in the lower layer is considerably reduced so that the presence of any large scale waves may affect the flow stability. Figure 1 shows the upper and lower-layer mean, ψ^M and q^M, over the 200 day period. A large amplitude dipole block develops which is equivalent barotropic with strong easterly flow in the lower layer and almost no flow in the upper layer between the dipole vortices. The wavemaker position is marked. The split jetstream in the upper-layer is close to a free state with ψ^M and q^M contours nearly parallel, however a neutral stationary Rossby wave would have no flow in the lower layer . The strong low-layer circulation is therefore directly spun up by the wavemaker. There is little sign of stationary wave activity downstream of the block and the mean flow returns to its zonal state without oscillations.

If the balance of terms in the mean upper-layer potential vorticity budget is analysed, the main balance is between mean flow advection and dissipation in the region of the block. The transient eddy forcing term is an order of magnitude smaller, however when it is displayed in Fig. 2a, the characteristic bowed structure can be seen as eddies are deformed in the split jet entrance region.

It is the forcing by eddies in the lower-layer and the consequent existence of the large lower-layer dipole which is vital to maintaining the upper-layer split. The small size of the eddy forcing at upper-levels has always been a problem in studying eddy forcing from atmospheric diagnostics, as pointed out by Shutts (1986). To test the nature of the excitation of the mean response we took the eddy feedback terms from both layers, as shown in Fig. 2, and used them as steady forcing terms instead of the wavemaker. The steady response in both layers was indistinguishable from that shown in Fig. 1. Figure 3 shows a time-series of ψ_2 at the position marked with a cross in the upper model layer on Fig. 1a for the wavemaker run. After the initial build up period, the time-series of ψ shows a few low frequency oscillations before settling down with weak, regular high-frequency eddies passing through the block and little sign of any other frequencies. The initial low frequency oscillations should be noted because although they are transient in this run, which makes them difficult to analyse, they are much more dominant in the sheared jet study in section 4.

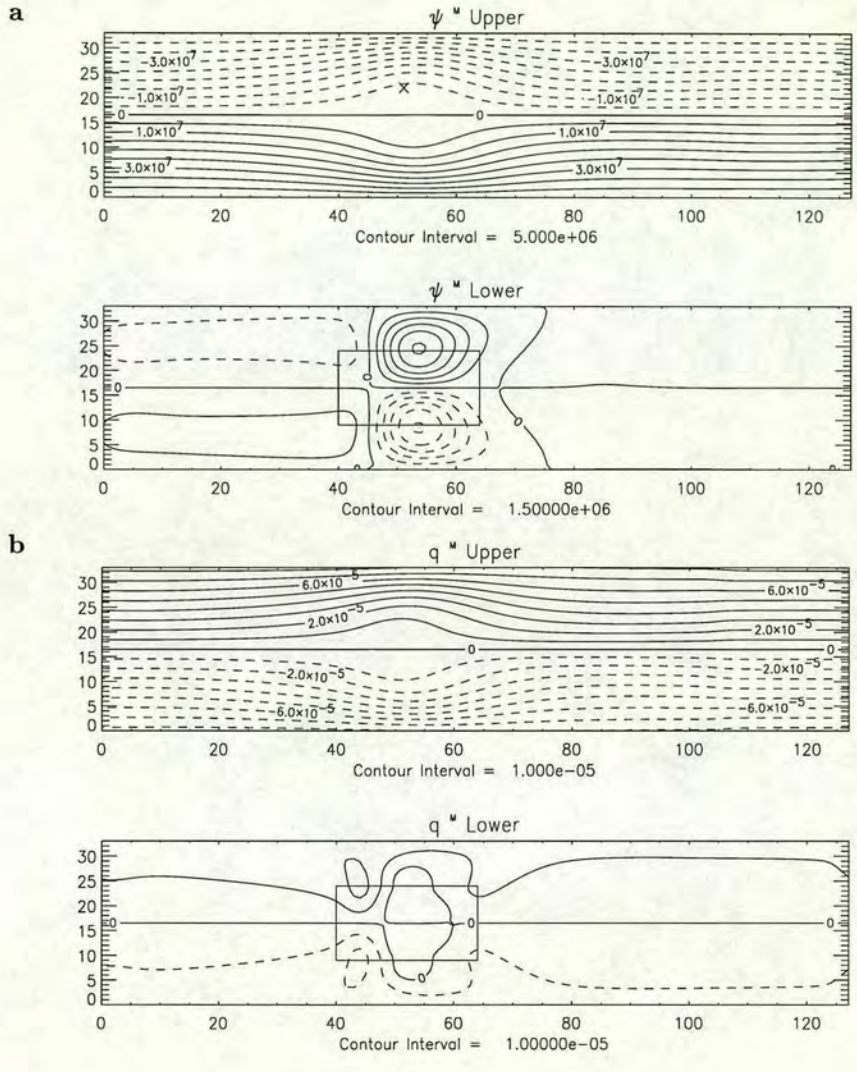

Figure 1. Time-mean streamfunction (Fig. a, units m^2s^{-1}) and potential vorticity (Fig. b, units s^{-1}) for the two layers for the run with upper layer velocity $15ms^{-1}$ and wavemaker amplitude $A = 1.2 \times 10^{-9}s^{-2}$. The position of the wavemaker in the lower layer is outlined. The contour values are shown beneath the plots for these and subsequent figures.

If this same experiment is performed with $U = 20ms^{-1}$, the split jet still appears but it is further downstream relative to the wavemaker, Fig. 4a. The wave activity in the upper-layer is advected rapidly away from the wavemaker region. If the experiment is performed with a smaller $U = 10ms^{-1}$, the response is a rather extended split upstream of the wavemaker with a pronounced jet intensification downstream followed by further oscillations as the excited stationary wave decays, Fig. 4b.

On the basis of these results we can make some speculations about the response of the atmospheric jetstream to upward propagating wave activity in the storm tracks. If the flow is too strong the jet splitting effect will be zonally elongated as the transient wave activity passes rapidly downstream. This is different to the result of Shutts (1983), where

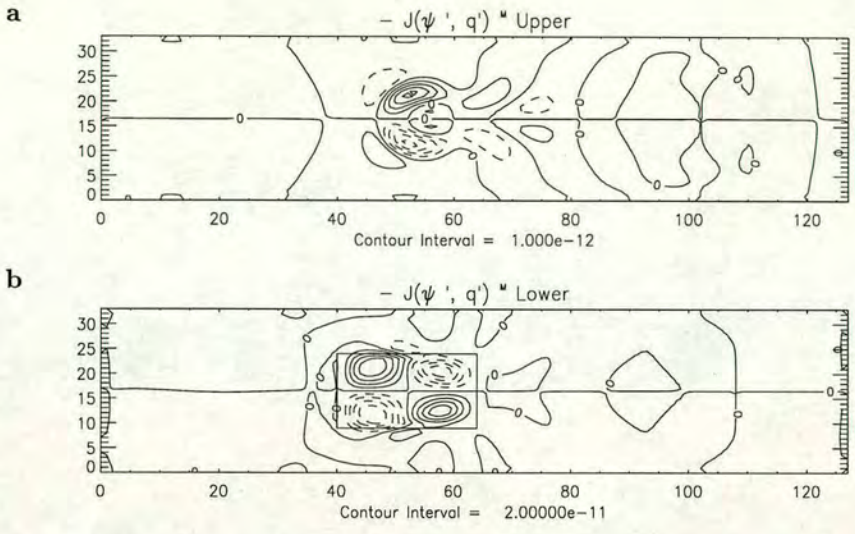

Figure 2. Eddy feedback $-J(\psi', q')^M$ on the potential vorticity tendency for the upper (Fig. a) and lower (Fig. b) layer. Note that the upper layer is much weaker than the lower layer (different contour intervals). Units s^{-2}.

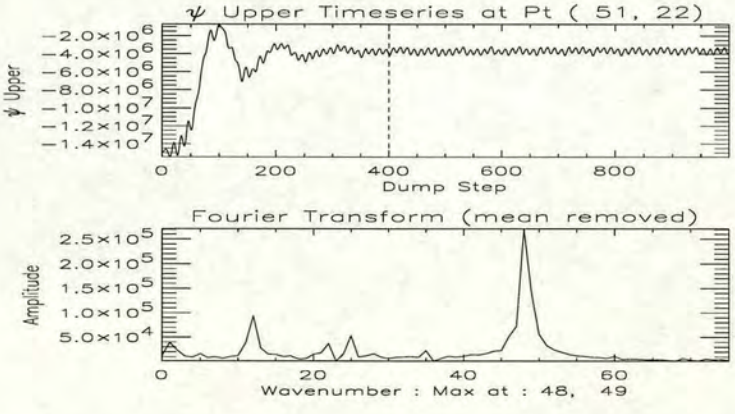

Figure 3. Streamfunction timeseries (upper plot, units m^2s^{-1}) and fourier transform (lower plot) at point (51,22) in the upper layer of the run with upper layer velocity $15ms^{-1}$ and wavemaker amplitude $A = 1.2 \times 10^{-9}s^{-2}$. After an initial settling down period, the flow retains a steady state, superimposed on which are the high frequency oscillations of waves generated by the wavemaker. The dashed vertical line indicates the start position from where the time-mean and eddy diagnostics are taken.

a strong jet lead to jet intensification, but this was due to the non-conservative wavemaker forcing in a barotropic model. The strong jet case might reflect the 'normal' jetstream situation in which only a weak split is normally observed at upper-levels towards the end of the atmospheric storm tracks. If the jet is very weak the split extends upstream. If we identify the wavemaker with, for example, the central Atlantic, then an upstream split would correspond to weak flow over N. America with a more intense jetstream region downstream over the east Atlantic.

So far the jets we have identified have a well defined time-mean response to the

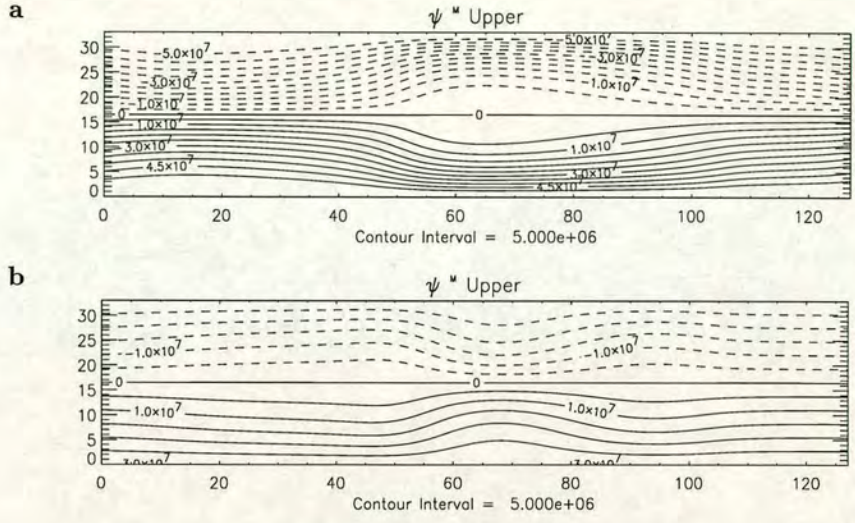

Figure 4. Upper layer time-mean streamfunction fields for the runs with constant upper layer velocity 20ms^{-1} (Fig. a) and 10ms^{-1} (Fig. b), both with wavemaker amplitude $A = 9.2 \times 10^{-10}\text{s}^{-2}$. Units m^2s^{-1}.

wavemaker. Changes in the upper-layer jet speed alter this response in a fairly continuous fashion between the weak and strong jet scenarios. The switch over from an upstream to a downstream split occurs around the stationary wave scale for the jet. In practice the finite-time required for upward wave propagation when more vertical resolution is present means that realistic responses to baroclinic wave growth are always likely to be shifted downstream of the region of maximum surface baroclinity. In the following section, we look at upper-layer jets containing horizontal shear.

4. Meridionally Sheared Jets

In this section we begin with the mean upper layer jet which produced the best blocking response in section 3, with $U = 15\text{ms}^{-1}$ and with no flow in the lower layer. We introduced meridional shear in the upper layer in such a way as to have little impact on the zonal Rossby wave propagation characteristics in the channel. An analytic form for the upper layer jet was chosen;

$$\psi_2 = -U_c y + \Delta U \left(\frac{y - \frac{1}{m} \sin my}{1 - \cos(3 \times 10^6 m)} \right)$$

$$U_2 = U_c - \Delta U \left(\frac{1 - \cos my}{1 - \cos(3 \times 10^6 m)} \right)$$

where $U_c, \Delta U, m$ are parameters of the jet. The Rossby wave propagation properties are determined by the refractive index of the flow which is defined as;

$$n^2 = \frac{1}{u} \frac{\partial q}{\partial y}.$$

We chose the parameters such that n^2 in the centre of the upper layer remained the same as for the uniform jetstream with $U = 15\text{ms}^{-1}$. For the main experiment we used $U_c = 19\text{ms}^{-1}$, $\Delta U = 18\text{ms}^{-1}$, $m = 5.2 \times 10^{-8}\text{m}^{-1}$, with meridional profiles shown in Fig. 5. The jet shear has the effect of bringing the initial flow even closer to the critical limit for stability. In this case the presence of a blocking wave will be shown to have a more profound influence on the stability of the jet than was seen in section 3.

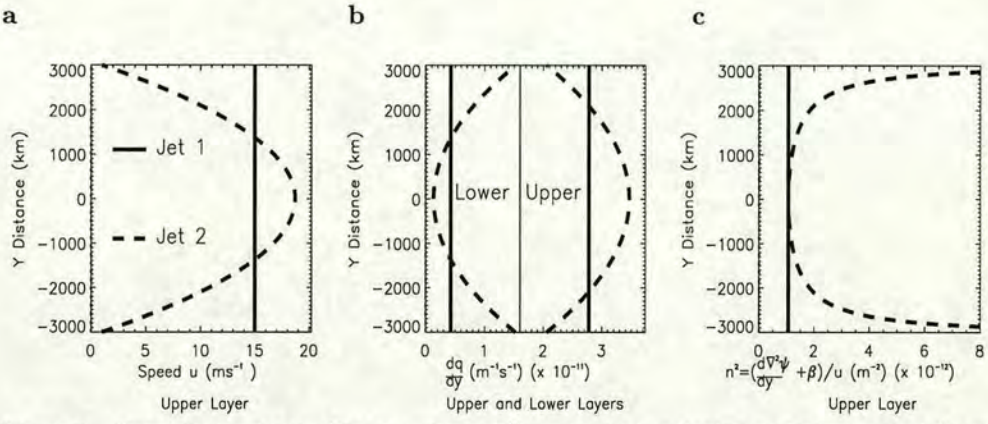

Figure 5. Upper layer velocity (Fig. a, units ms^{-1}), upper layer potential vorticity gradient (to right of thin vertical line (representing planetary vorticity value), Fig. b) and lower layer potential vorticity gradient (to left of thin vertical line, Fig. b) with units $\text{m}^{-1}\text{s}^{-1}$, and upper layer refractive index (Fig. c, units m^{-2}) shown for two jets. Jet 1 is the constant 15ms^{-1} used previously, jet 2 is the case with horizontal shear.

With a reduced wavemaker amplitude ($A = 9.2 \times 10^{-10}\text{s}^{-2}$) the model was run for 400 days with the final 300 days used for diagnostics. Figure 6 shows the time-mean streamfunction ψ^M in each layer. The position of the upper layer split is similar to that in Fig. 1. The mean flow splits over the wavemaker although with some stationary wave activity downstream, similar to the weak jet response in Fig. 4b.

Figure 7 shows the time series and fourier transform of ψ in the upper layer at the position marked in Fig. 6a. Clearly a radical change has taken place. As well as the high-frequency eddy activity which can still be seen, the flow now exhibits a low-frequency oscillation between higher amplitude, split-jet states which we will refer to as blocked, although they are weaker than in Fig. 1, and more zonal flow states. From the figure it can be seen that the low-frequency oscillation is quite regular with a period of 31 days. Note that the high and low-frequency oscillations are not phase locked, as can be seen, for example, from the distribution of high-frequency eddy signatures around the peaks of the low-frequency oscillation.

As the low-frequency oscillation is very regular we performed a fourier analysis on the streamfunction field which allows a separation of the instantaneous flow as follows;

$$\psi = \psi^M + \psi^L + \psi^H$$

where $\psi^{L,H}$ are the low and high-frequency eddy components respectively. The low-frequency component of the flow can be studied at different phases of the oscillation cycle. Figures 8(a-h) shows ψ^{M+L} and q^{M+L} in both layers for the four phases we have labelled zonal, growth, blocked and decaying and these phases are marked, in that order, on Fig. 7. Figures 8(i-l) show the feedback of the high-frequency eddies onto the mean and low-frequency flow at the different oscillation phases. These figures contain clues about

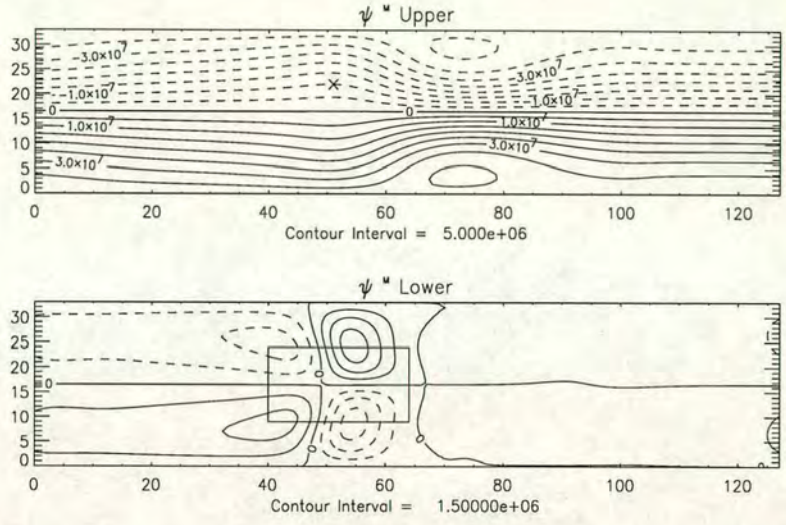

Figure 6. Time-mean streamfunction (units m^2s^{-1}) for the run with upper layer velocity as in jet 2 of Fig. 5, with wavemaker amplitude $A = 9.2 \times 10^{-10}s^{-2}$. Again, the position of the wavemaker in the lower layer is outlined.

the processes responsible for the low-frequency oscillation and we will look at them in more detail.

(*a*) *Low-Frequency Vacillation and Eddy Forcing*

The first thing to note is that in all phases the low-frequency signature, ψ^L, has an antisymmetric wave-2 structure about the channel centre.

(1) *Zonal phase (Figs. a,e,i):* Although not strictly zonal, this phase has the smallest anomaly from the initial conditions. In the upper-layer, there is a weak widening of the ψ contours over the wavemaker region, with an intensification further downstream. The lower-layer shows only a very weak anomaly forming over the wavemaker region. The high-frequency eddy forcing is developing in the upper-layer with an anti-cyclonic over cyclonic dipole above the wavemaker. In the lower-layer the quadrupole is weaker than in Fig. 2b.

(2) *Growth phase (Figs. b,f,j):* In this phase 9 days later, there is an obvious difference in the lower-layer, where a quadrupole in both circulation and potential vorticity has developed. In the upper-layer, upstream of the wavemaker, the flow is more zonal, but a split is developing over the wavemaker. At this phase the high-frequency eddy forcing is very strong in both upper and lower-layers.

(3) *Blocked phase (Figs. c,g,k):* The upper-layer flow is now at its most split over the wavemaker region, with the downstream intensification also strong. The lower-layer circulation anomaly has extended a little upstream and the lower potential vorticity quadrupole has weakened and separated meridionally. The high-frequency eddy forcing has weakened considerably in both layers from the growth phase.

(4) *Decay phase (Figs. d,h,l):* The upper-layer split now extends well upstream of the wavemaker. In the lower-layer the anti-cyclone over cyclone wave-2 anomaly is still near

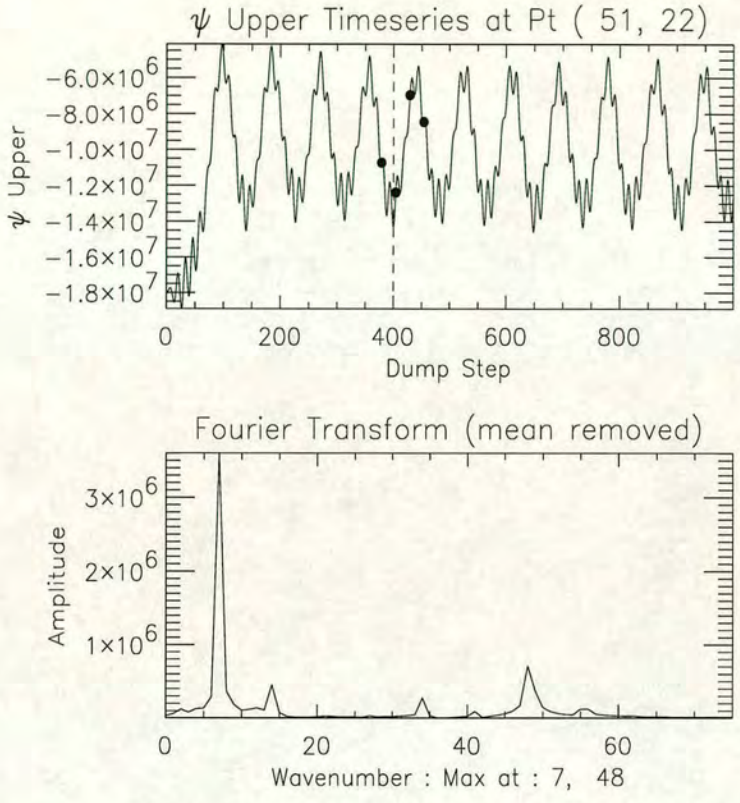

Figure 7. Streamfunction timeseries (upper plot, units m^2s^{-1}) and fourier transform (lower plot) at point (51,22) of the run with upper layer velocity jet 2 (see Fig. 5) and wavemaker amplitude $A = 9.2 \times 10^{-10}s^{-2}$. The dashed vertical line indicates the start position from where the time-mean and eddy diagnostics are taken. This time there is a low-frequency oscillation component evident as well as the high frequency of the wavemaker eddies.

the wavemaker but weak and with some upstream extension. The lower-layer potential vorticity anomalies are very weak. The high-frequency forcing is also at its weakest in both layers.

It is interesting to note that the structure of the high-frequency eddy forcing does not alter much through the low-frequency cycle, suggesting that the eddies are probably always tending to excite a split in the jetstream. The amplitude of the eddy feedbacks do change however and they seem to lead the amplitude of the low-frequency flow anomaly by $\frac{\pi}{2}$, being largest in the anomaly growth phase and weaker at the blocked phase, for example. These changes in eddy forcing clearly show some feedback of the large scale wave on the eddy behaviour.

We now consider the potential vorticity equation, with friction omitted, broken down as follows;

$$\frac{\partial q^M}{\partial t} = -J(\psi^M, q^M) - J(\psi^L, q^L)^M - J(\psi^H, q^H)^M, \tag{9}$$

$$\frac{\partial q^L}{\partial t} = -J(\psi^{M+L}, q^{M+L})^L - J(\psi^H, q^H)^L, \tag{10}$$

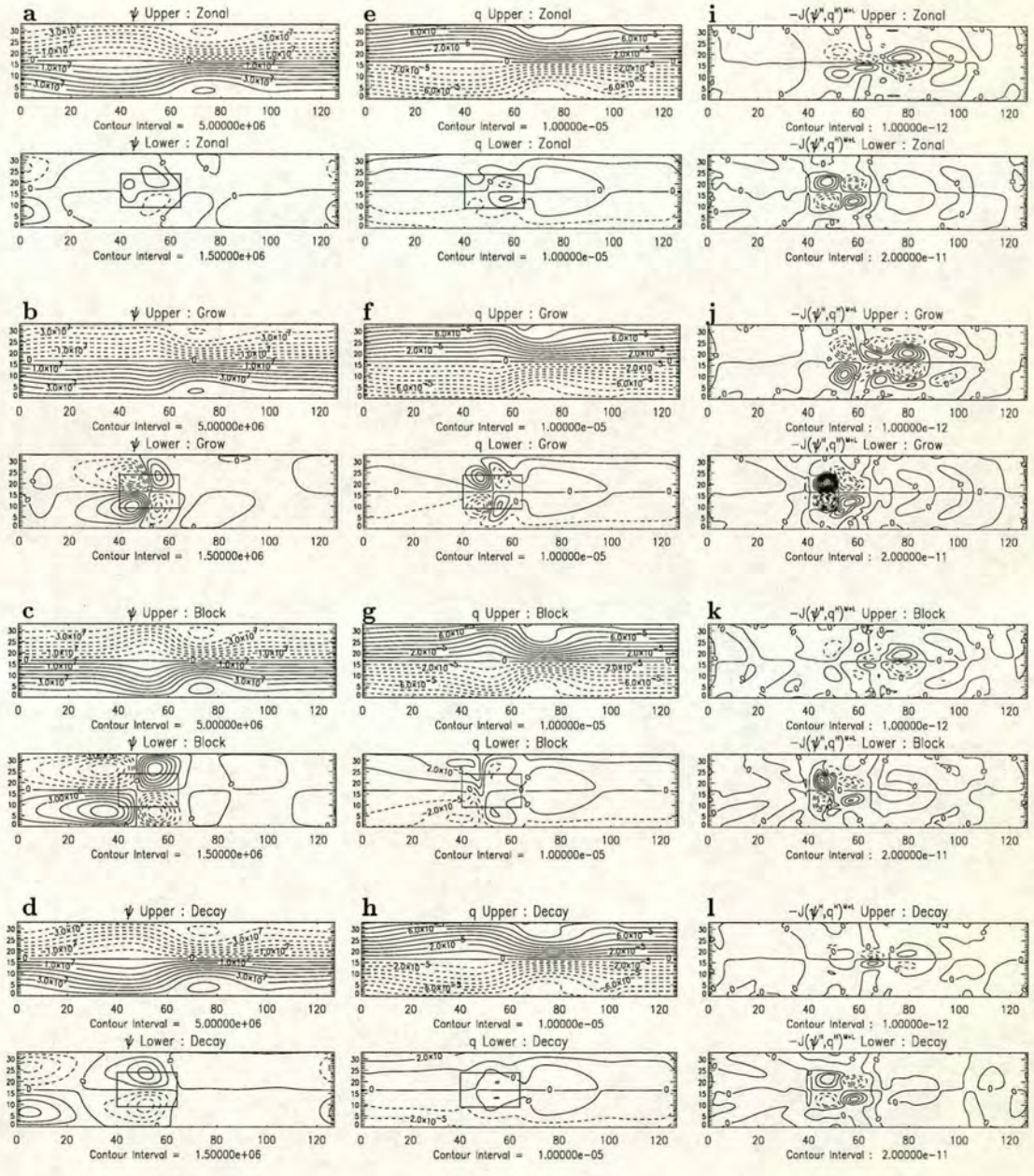

Figure 8. Instantaneous low-pass filtered streamfunction ψ^{M+L} (left column, Figs. a-d, units m^2s^{-1}) , potential vorticity q^{M+L} (middle column, Figs. e-h, units s^{-1}) and low-pass filtered high-frequency eddy feedback $-J(\psi^H, q^H)^{M+L}$ (right column, Figs. i-l, , units s^{-2}) fields for phases of the low frequency oscillation (zonal (a,e,i), grow (b,f,j), block(c,g,k) and decay (d,h,l)). The time interval between each is 9 days.

$$\frac{\partial q^H}{\partial t} = \delta_{i,1} F - J(\psi^H, q^{M+L}) - J(\psi^{M+L}, q^H) - J(\psi^H, q^H)^H. \tag{11}$$

Superscript $M + L$ corresponds to the low-frequencies plus the mean value. The second two terms on the rhs of Eq. (9) are shown in Figs. 9(a,b), which are the feedbacks by the low and high-frequency eddies respectively onto the mean flow. The high-frequency forcing in the lower-layer is dominant. The low-frequency forcing in the lower-layer also shows a weaker quadrupole of reversed sign and smaller zonal scale. In the upper-layer the low-frequency eddy feedback also opposes the high-frequency feedback over the wavemaker. The two terms on the right of Eq. (10) vary at each phase of the cycle. The high-frequency forcing terms from Eqs. (9, 10) are shown combined in Figs. 8(i-l). The persistent struc-

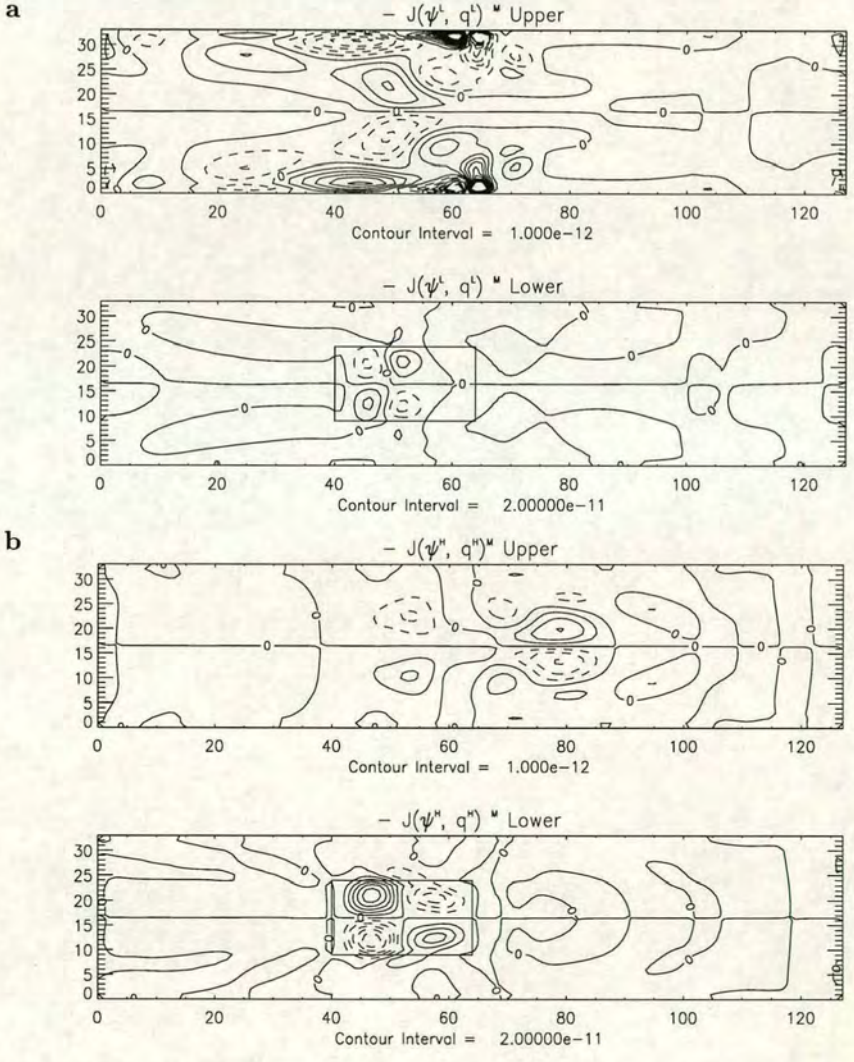

Figure 9. Time-mean eddy feedback on the potential vorticity tendency from the low frequency $-J(\psi^L, q^L)^M$ (Fig. a) and high frequency $-J(\psi^H, q^H)^M$ (Fig. b) eddies for the jet 2 wavemaker run. Units s^{-2}.

ture of the high-frequency eddy terms and the opposite sign (and equal magnitude in the

upper-layer) of the low-frequency forcing, suggests that the high-frequency eddies do not drive the flow through the entire low-frequency oscillation cycle as suggested by James *et al.* (1994). The oscillations in this model are in any case much more local than those of James *et al.* (1994) and the breakdown clearly involves propagation away from the region of active high-frequency eddies.

In order to reveal the role of the high-frequency eddies at different phases of the vacillation cycle, we took the term $-J(\psi^H, q^H)^{M+L}$ at the four chosen phases, Figs. 8i-l, and used it as a stationary forcing, substituting for the wavemaker, until a steady state was reached. This should show the steady response which would develop if this eddy forcing were imposed indefinitely, although in the vacillation the feedback is varying continuously. Figure 10 shows the streamfunction response in both layers using forcing only from the the growth (Fig. 8j) and blocked (Fig. 8k) phases. For the growth phase (Fig. 10a), the constant forcing forms a very large amplitude split, much larger than the observed split even in the blocked phase (Fig. 8c). The flow is anti-symmetric because it became unstable, so the time-mean over the last 200 days is shown. The result using eddy forcing from the block phase (Fig. 10b) is much weaker, and a stable steady state is reached with a weaker upper-layer split than is observed in the vacillating model. Figure 11 shows the value of upper-layer streamfunction at point (51,22) from Fig. 8 at

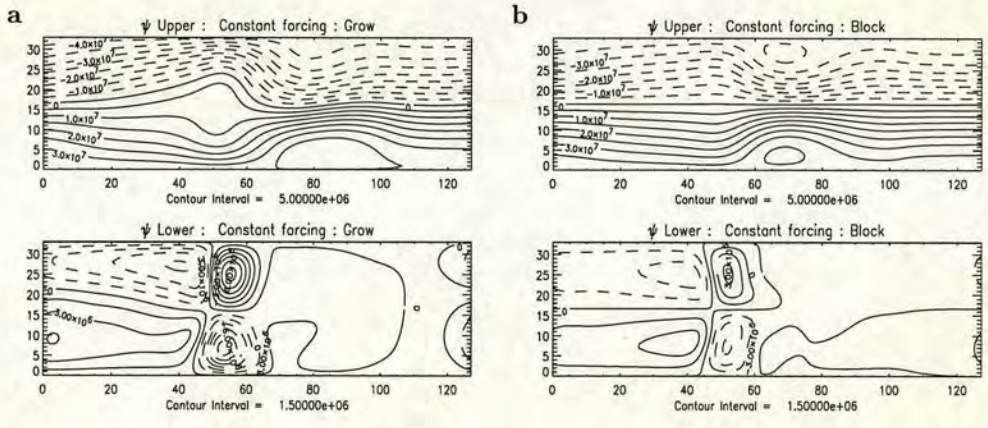

Figure 10. Upper and lower layer streamfunction response to the instantaneous high frequency feedback $-J(\psi^H, q^H)^{M+L}$ as a steady forcing from the growth (Fig. a) and the blocked (Fig. b) phases. Units m^2s^{-1}.

the four phases of the oscillation during the wavemaker run (solid circles) and from the experiment using $-J(\psi^H, q^H)^{M+L}$ from the corresponding phases as a constant forcing to steady state (open triangles). This clearly shows the model response, which peaks during the blocked phase, lagging the eddy forcing function, which has its maximum at the growth phase. As the forcing in the growth phase produces an anomaly much larger than the observed flow at that instant, there is a clear tendency for further jet splitting and the high-frequency eddies are crucial to the resonant growth towards the blocking flow phase. When the blocking phase is reached, the high-frequency forcing has decreased and is now insufficient to support the anomaly of the magnitude found. Unless other factors were to maintain the split, there will be a tendency for the split flow to weaken. However this analysis does not explain why the high-frequency eddy forcing decreases as the blocking phase is reached, nor what mechanism causes the decay of the block once the high-frequency feedback is reduced. These issues are addressed in section 5.

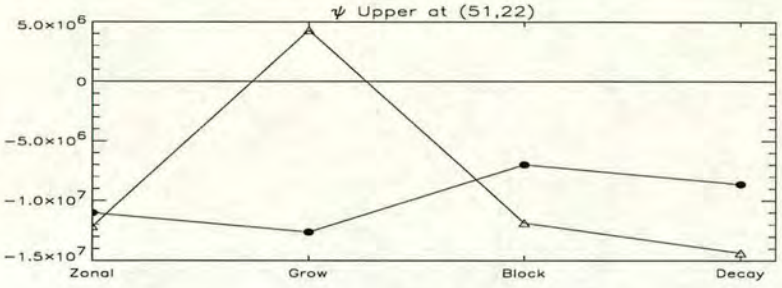

Figure 11. Plot showing the value of upper layer streamfunction ψ at point (51,22) at the four phases of the oscillation during the wavemaker run (solid circles) and from the experiment using $-J(\psi^H, q^H)^{M+L}$ from the corresponding phases as a constant forcing (open triangles). Units m^2s^{-1}.

(*b*) *Non-linear Aspects*

A further facet of the low-frequency oscillation is revealed by varying the amplitude of the wavemaker. Figure 12 shows three time-series of ψ at the same position as in Fig. 7. Figure 12a is for a wavemaker with amplitude reduced by a factor of 5. The wavemaker eddies are clearly visible but there is little sign of the low-frequency oscillation. Figure 12b is for a wavemaker with amplitude increased by a factor of 1.5 over that shown in Fig. 7 . In this case the low-frequency oscillation period has decreased from 31 days to 24 days. If the wavemaker amplitude is further increased the flow rapidly develops other oscillation frequencies and the response begins to be chaotic, as shown in Fig. 12c for the amplitude increased by a factor of 3 from the original ($A = 2.8 \times 10^{-9}s^{-2}$).

This sensitivity to the wavemaker amplitude is consistent with an instability mechanism being responsible for the breakdown of blocking in the channel. If the amplitude of the split jet is insufficient (weak wavemaker), the low-frequency oscillation is absent. If the high-frequency eddies are stronger the split jet reaches the amplitude required for instability more rapidly and therefore block decay sets in leading to an increase in block-decay cycle frequency. These results lead us to perform the stability analyses reported in the next section.

5. Low-Frequency Oscillations and Stability

The full stability properties of non-zonal flows such as those formed here are difficult to study and there are few general principles which can be used for guidance. During the low-frequency oscillation cycles the flow is never steady making a conventional stability analyses ambiguous, see Andrews (1984). The proper analysis method for such situations is error growth theory which can be studied through the development of singular vectors, e.g.. Farrell (1985). We chose to avoid these difficulties and opted instead for a greatly simplified analysis of the zonal flow stability of the different flow phases and, as will be seen, this appears to be sufficient to explain the low-frequency oscillation behaviour.

(*a*) *Stability Analysis*

To assess the stability of the low-frequency component of the channel flows in Fig. 8, the meridional streamfunction profile at each x position and at each time, t, was analysed in the following eigenvalue problem;

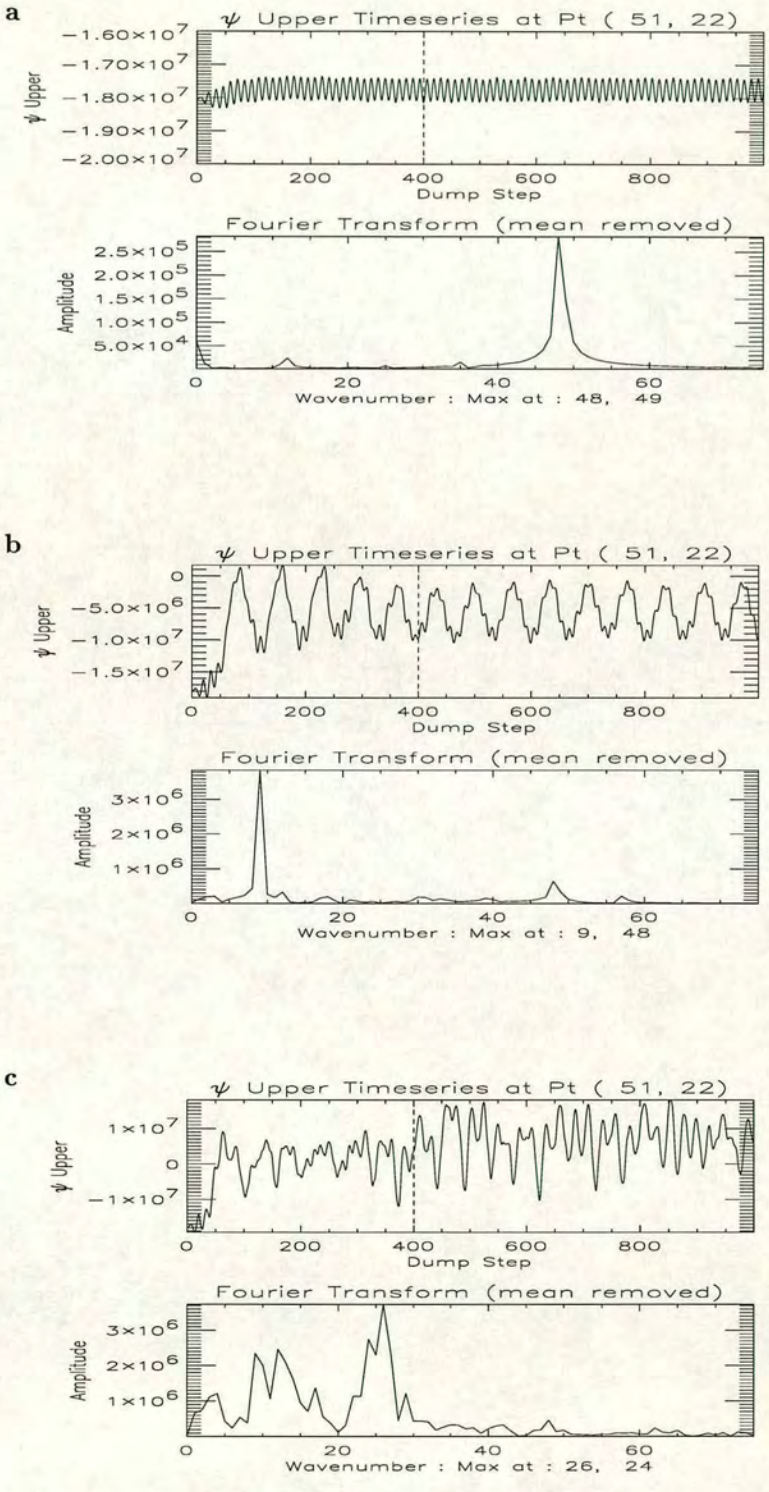

Figure 12. Streamfunction timeseries at point (51,22) in the upper layer (units m^2s^{-1}) and corresponding fourier transforms shown for jet 2 cases with wavemaker amplitudes $A = 1.8 \times 10^{-10}s^{-2}$ (Fig. a), $A = 1.4 \times 10^{-9}s^{-2}$ (Fig. b) and $A = 2.8 \times 10^{-9}s^{-2}$ (Fig. c) (compared with $A = 9.2 \times 10^{-10}s^{-2}$ for the standard case).

$$\left(U_2\left(\frac{\partial^2}{\partial y^2}-\gamma^2\right)+\frac{dQ_2}{dy}\right)\phi_2+\gamma^2U_2\phi_1 = c\left(\left(\frac{\partial^2}{\partial y^2}-\gamma^2\right)\phi_2+\gamma^2\phi_1\right) \quad (12)$$

$$\left(U_1\left(\frac{\partial^2}{\partial y^2}-\gamma^2\right)+\frac{dQ_1}{dy}\right)\phi_1+\gamma^2U_1\phi_2 = c\left(\left(\frac{\partial^2}{\partial y^2}-\gamma^2\right)\phi_1+\gamma^2\phi_2\right) \quad (13)$$

where U_i are the zonal velocity components of layer i of the low-pass filtered fields at a particular time and x position, with corresponding potential vorticity gradients $\frac{dQ_i}{dy}$; ϕ_i are the meridional eigenvectors and c are the zonal phase speed eigenvalues. These equations come from linearizing (1) about a zonal flow and seeking solutions of the form, $\psi_i' = \phi_i(y)e^{ik(x-ct)}$.

Several simplifications have been made for this analysis. The wavemaker, friction and all the zonal derivative terms have been neglected so that each meridional cross section in the channel is analysed as if it were a zonal flow. Such an analysis will not of course give the exact stability modes or growth rates but, to the extent that north-south gradients dominate the stability, this analysis should give a good indication of the source of unstable modes as a function of longitude and time for the flows in Fig 8. In deriving (12,13) we have also assumed the zonal wavelength of the eigenmodes to be infinite ($k = 0$) although the sensitivity to this assumption is tested.

The stability was analysed in a finite-difference representation at the same resolution as the channel. Equations (12,13) were put in matrix form, and a Numerical Algorithms Group (NAG) routine used to solve them. The presence of unstable eigenmodes is indicated by the existence of complex eigenvalues, c, when the imaginary component gives the growth rate and the real component gives the propagation speed.

Since the observed instability is dominated by a meridional wave number 2, we restrict our search to wave 2 eigenmodes. Figures 13(a,b) show the real and imaginary components of the eigenvalue associated with the wave 2 eigenmode plotted as a function of zonal position and time. This method of display shows exactly at what zonal positions and at what times the flow becomes unstable. The times of the four phases shown in Fig. 8 are indicated. The first thing to note is that there is a genuine change during the oscillation from periods when the flow is stable at all longitudes, to periods when instability is quite marked. Instability first appears during the growth stage of the oscillation with the unstable longitudes located around and upstream of the maximum split in the upper-layer jet stream. It appears to be the region of the westerly flow in the lower-layer, upstream of the upper-layer split which is responsible for the instability. If the maximum growth rates of the unstable eigenmodes are calculated from $Im(c)$ by estimating a suitable k value, an e-folding timescale of a few days results. The real component of the eigenvalue for these unstable modes is always negative indicating upstream propagation with a typical speed of around 10ms^{-1}. This is consistent with the description of the breakdown of blocking in section 4, in which a large-scale wave travels upstream from the blocking region.

If any of the steady blocking responses in section 3 are analysed, it is found that the zonal flow component at all longitudes remains stable, i.e. no complex eigenvalues exist. This is good evidence that the breakdown of the blocking phase in the channel is initiated by large scale instability. The instabilities shown in Fig. 13 are of mixed barotropic/baroclinic type as can be shown by separating the appropriate zonal flows into their barotropic and baroclinic components. Neither component is unstable in its own right and the instability relies on both vertical and horizontal shears in order to develop. This is consistent with the fact that in section 3 many high amplitude blocks

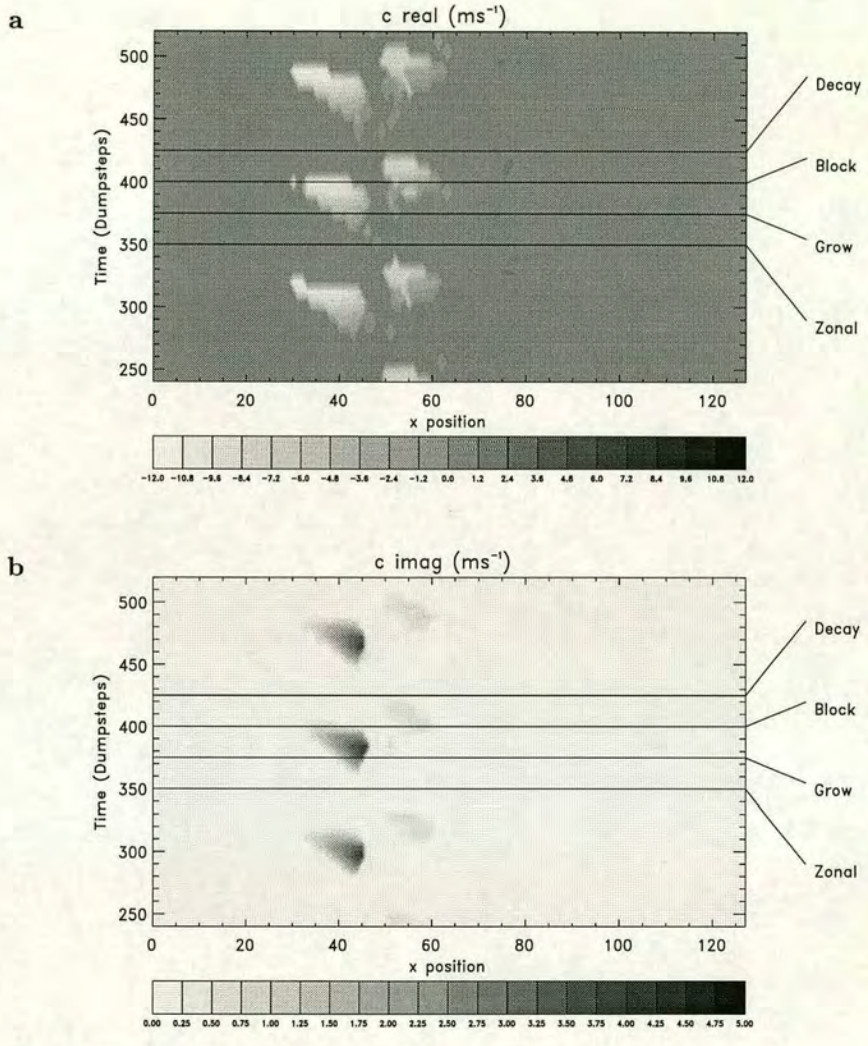

Figure 13. Real (Fig. a) and imaginary (Fig. b) components of the phase speed for the most unstable wave 2 eigenmode of the zonal problem as contours plotted against x position in channel (horizontal axis) and time (vertical axis). The four horizontal lines shown indicate the position of the four phases shown in Fig. 8 : reading vertically upwards, these are zonal, grow, block and decay. Units ms^{-1}.

were formed which were perfectly stable. The introduction of meridional shear into the original jet causes the flow to become locally unstable whenever a large amplitude block is superimposed.

(*b*) *Energy Diagnostics*

In this section we use an analysis of energy conversions similar to that presented in the recent paper by Higgins and Schubert (1994). Following some mathematics, to which reference to their appendix is made, the following equation for the time tendency of the

low-frequency kinetic energy $\frac{\partial}{\partial t}\left(\frac{\mathbf{v}^L.\mathbf{v}^L}{2}\right)$ is obtained,

$$\frac{\partial}{\partial t}(KE^L) = C(KE^M, KE^L) + C(KE^H, KE^L) + C(PE^L, KE^L) + R + F \qquad (14)$$

where

$$C(KE^M, KE^L) = - < \zeta^L \mathbf{v}^L.\mathbf{k} \times \mathbf{v}^M >$$

represents a barotropic energy conversion from the mean flow to the low-frequency kinetic energy,

$$C(KE^H, KE^L) = < \zeta^H \mathbf{v}^H.\mathbf{k} \times \mathbf{v}^L >$$

represents a barotropic energy conversion from the high-frequency to the low-frequency kinetic energy,

$$C(PE^L, KE^L) = - < f_0 \psi^L \nabla.\mathbf{v}^L >$$

represents a conversion from the low-frequency potential to low-frequency kinetic energy,

$$F = \mathbf{v}^L.(-(\varepsilon + S(x))\mathbf{v}^L + \nu\nabla^2.\mathbf{v}^L)$$

is the component due to friction and R is the sum of all the remaining terms which are not included elsewhere. Note that $<>$ indicates a sum over a layer and $\mathbf{v}$ is the geostrophic velocity in all terms except $\nabla.\mathbf{v}^L$.

We use a slightly different notation to Higgins and Schubert (1994), namely in the superscripts (our mean M is their seasonal mean S and our high-frequency H is their bandpass-frequency B), and we don't use a composite average over various events as they did. We simply look at the balances for one oscillation as the behaviour here is more regular than their GCM data. The divergence term $\nabla.\mathbf{v}^L$ is calculated using the vorticity tendency equation. Our R term has only been approximately calculated and, like Higgins and Schubert, we ignore any terms containing vertical velocity w, but the balance appears to be good even neglecting these.

Figure 14 shows these terms as they vary through the vacillation cycle. The upper plots are for the upper-layer, the lower plots for the lower-layer. The left hand plots show the three conversion terms plus their sum, representing the total conversion term. The right hand plots show this total together with the R and F terms, the total sum of all the right hand side of Eq. (14), and finally a direct estimate of the left hand side tendency in KE^L, calculated from the model.

We first consider the balances in the lower-layer. The bottom-left plot shows that the dominant term is the barotropic conversion from high-frequencies. This involves a large peak during the growth phase period, indicating that the high-frequencies are responsible for the growth of the anomaly. In the blocked phase, the contribution from this term is approaching zero and it becomes weakly negative in the decay phase. The bottom-right plot shows the contributions from the other terms to the total balance. The high-frequency conversion term is much larger in magnitude than the total conversion term, the difference coming from the friction, which is negative at all periods throughout the cycle, and the residual R terms, of which the dominant component is $< \mathbf{v}^L.(\zeta^H \mathbf{k} \times \mathbf{v}^H)^M >$. Note that Higgins and Schubert found their R term to be dominated by the term $< \mathbf{v}^L.(\zeta^L \mathbf{k} \times \mathbf{v}^L)^M >$.

Now we shall consider the upper-layer. The conversion terms are different in this layer mainly due to the weaker effects of the high-frequencies. The upper-left plot shows that conversion from high-frequencies now has the smallest contribution. Instead, the

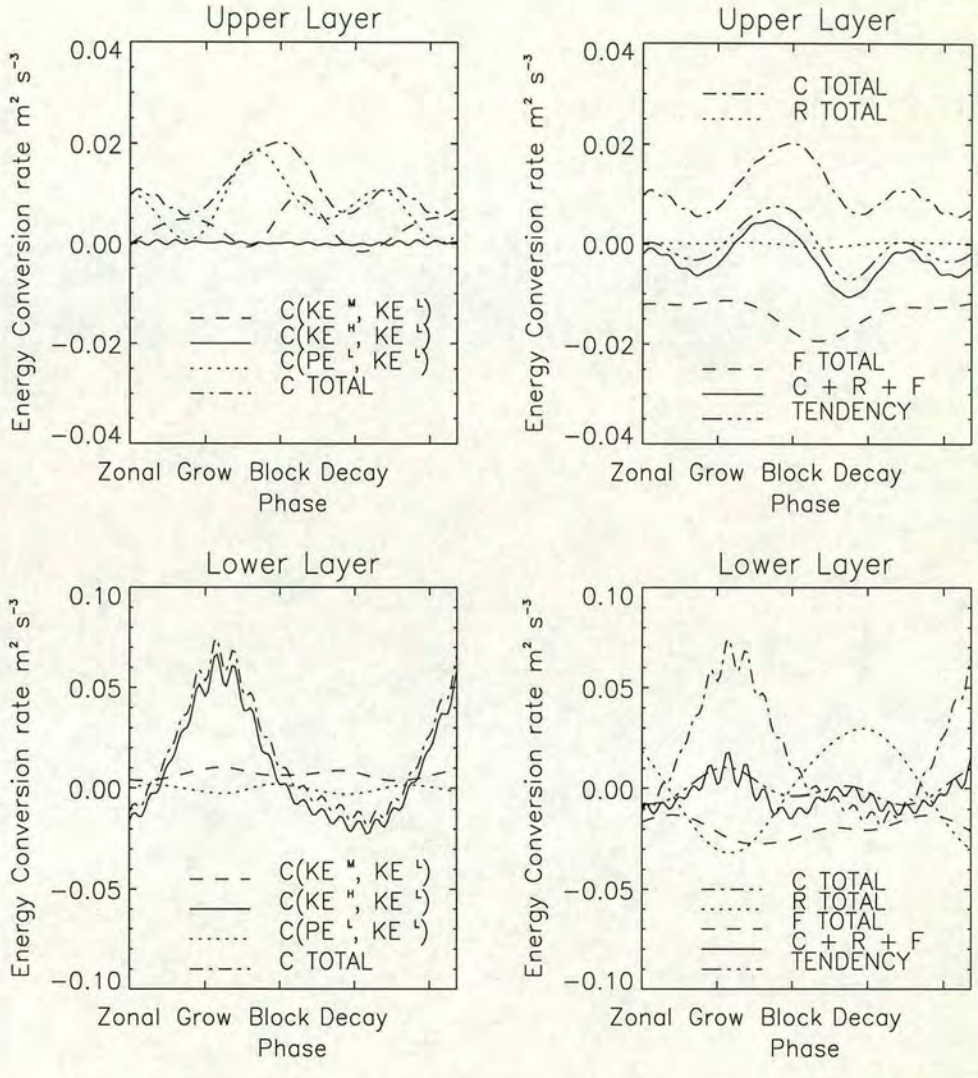

Figure 14. Left hand plots show the three conversion terms $C(KE^M, KE^L)$, $C(KE^H, KE^L)$ and $C(PE^L, KE^L)$ and the sum of all three (C) for the two layers separately. The right plots show C, the R term, the friction term (F), and the sum of all three. Also, the tendency of the model flow for comparison, the last two should be equal except for remaining neglected terms. Units $m^2 s^{-3}$.

conversion from low-frequency potential energy is the dominant term, which peaks just before the blocking peak. This is consistent with baroclinic instability setting in at that time, converting potential to kinetic energy. The conversion from the mean kinetic energy also supplements this term with a peak just after the block peak, indicating a barotropic instability component. In the top-right plot, variations in total KE^L production is shown to mirror this conversion term, but with variation about zero due to the friction which increases a little during the decay phase of the cycle. The R term in the upper-layer is negligible in the balance. Comparing the sum of the terms calculated with the energy tendency observed, we have captured the shape well, with a slight underestimation at all

points, due to the terms neglected.

(c) *Summary*

We are now in the position to describe schematically the stages and the physical mechanisms leading to the low-frequency blocking vacillations observed. **(1)** Resonant excitation of anticyclone/cyclone dipole by feedback from high-frequency eddies.
(2) This dipole anomaly becomes superimposed on the upper level jet approaching from upstream.
(3) If sufficient meridional shear is already present in the upper level jetstream the presence of the local dipole anomaly can induce local instability after the split reaches a certain amplitude.
(4) The split jet starts to break down by large-scale baroclinic-barotropic instability which transfers energy to a large-scale, westward-propagating wave.
(5) When the local split has gone, the high-frequency eddies begin to resonantly excite another split in the jetstream leading to another cycle.

Stage 3 is critical. The onset of local instability depends on the initial meridional structure of the upper level jet. If instability does not develop the split can go on to reach very large amplitude leading to persistent blocking, as in section 3. During the growth phase of the dipole the eddy forcing of the mean flow is at a maximum. Once the split becomes large and instability sets in, the eddy forcing weakens greatly as the split jet propagates upstream and gets out of phase with the wavemaker. These results suggest that although high-frequency eddies are vital for the development of blocking, as many other authors have shown, it may be the meridional structure of the upper level jet which determines the persistence and strength of the block.

6. Discussion

This paper reports results of experiments with a baroclinic channel model in which a low-frequency, blocking-like vacillation is produced. The excitation, splitting-jet phase of the vacillation is caused by vorticity fluxes from high-frequency transient eddies, but the response is largely a neutral stationary Rossby wave. As the split jet flow evolves, it enables the high-frequencies to increase their influence on the large-scale flow with a positive feedback effect. The breakdown phase is caused by large scale mixed barotropic-baroclinic instability which sets in when the split amplitude becomes large enough, but only if there is sufficient meridional shear in the upper-layer zonal jetstream. Without meridional shear, a large amplitude stable block is excited by the high-frequency eddies.

The development of local instability, such as that reported here, has been found by other investigators studying blocking-like flows. The recent work of Helfrich and Pedlosky (1993,1995) is an example in which local instability in a dipole soliton develops if the zonal flow on which the soliton grows is close to being baroclinically unstable. James *et al.* (1994) performed Empirical Orthogonal Function (EOF) analyses on the zonal wind of two 100-year integrations of a simplified GCM. They identified a low-frequency circulation in the phase space of the Principal Components (PCs) with a period of 150 days. By calculating the feedback of normal-mode lifecycles at various phases of the cycle, they showed a tendency to partially drive the zonal state along an anti-clockwise trajectory in the phase-space. All baroclinic lifecycles increased the PC1 value, but some other mechanism is needed to reduce the PC1 amplitude and complete the circuit.

Our case is similar, with the feedback from the high-frequency eddies pushing the flow towards the block stage, and the extra mechanism required to complete the cycle

is instability, evidence of which is provided by a local zonal-flow stability analysis and energy diagnostics. This instability also provides a mechanism for the propagation of wave information away from the region of splitting, which could contribute to the ultra-low frequency variability of James *et al.* (1994), Run A.

Future work will involve searching for evidence of this behaviour in more sophisticated models and in observed data. It has been known for some time that high-frequency eddies can reinforce atmospheric blocks, but little is known of why this behaviour doesn't always occur or continue indefinitely. The evolution of the large scale flow to become unstable, or affect the feedback mechanism in some way, may possibly provide further insights into the behaviour of low-frequency variance in the atmosphere. It could be that the jet stream evolves between different states which support different types and amplitudes of local anomaly. For instance, if the atmospheric jet was in a state similar to our jet 1 case, then a persistent blocked flow could be excited. The jet could then slowly shift towards a regime where the anomaly would become unstable and breakdown. If this transition was slow, then the flow could remain marginally stable for a period of time, which may result in an upstream propagation as seen in our model, consistent with findings from case studies. An improved predictability and understanding of blocking events would undoubtedly help reduce weather forecasting errors, especially in the medium-range.

Acknowledgements

The authors would like to thank the UK Universities' Global Atmospheric Modelling Programme (UGAMP) and NERC (Grant : GST/02/804) for providing the funding for this work, and the computing personnel at the University of Edinburgh for maintaining the facilities to make this research possible. Useful discussions with Chris Thorncroft of Reading University are also acknowledged.

References

Andrews, D. G. 1984 On the stability of forced non-zonal flows., *Quart. Journal of Royal Met. Soc.*, **110,** 657–662

Branstator, G. 1992 The maintenance of low-frequency atmospheric anomalies., *Journal of the Atmospheric Sciences*, **49,** 1924–1945

Dole, R. M. 1986 Persistent anomalies of the extratropical northern hemisphere winter time circulation : Structure., *Mon. Weather Review*, **114,** 178–207

Dole, R. M. 1989 Life cycles of persistent anomalies. Part I: Evolution of 500mb height fields., *Mon. Weather Review*, **117,** 177–211

Edmon, H. J., Hoskins, B. J. and McIntyre, M. E. 1980 Eliassen-Palm cross sections for the troposphere., *Journal of the Atmospheric Sciences*, **37,** 2600–2616

Ferranti, L., Molteni, F. and Palmer, T. N. 1994 Impact of localized tropical and extratropical SST anomalies in ensembles of seasonal GCM integrations., *Quart. Journal of Royal Met. Soc.*, **120,** 1613–1645

Farrell, B. F. 1985 Transient growth of damped baroclinic waves., *Journal if the Atmospheric Sciences*, **42,** 2718–2727

Flierl, G. R., and K. Haines 1994 The decay of modons due to Rossby wave radiation, *Phys. Fluids*, **6 (10),** 3489–3497

Green, J. S. A. 1977 The weather during July 1976 : Some dynamical considerations of the drought., *Weather*, **32,** 120–128

Haines, K. 1994 Low-frequency variability in atmospheric middle latitudes., *Surveys in Geophysics*, **15,** 1–61

Haines, K. and Marshall, J. 1987 Eddy-forced coherent structures as a prototype of atmospheric blocking., *Quart. Journal of Royal Met. Soc.*, **113,** 681–704

Haines, K. and Malanotte-Rizzoli, P. 1991 Isolated anomalies in westerly jet streams : A unified approach., *Journal of the Atmospheric Sciences*, **48,** 510–526

Helfrich, K. R. and Pedlosky, J. 1993 Time-independent isolated anomalies in zonal flows., *Journal of Fluid Mechanics*, **251,** 377–409

Helfrich, K. R. and Pedlosky, J. 1995 Large-amplitude coherent anomalies in baroclinic zonal flows., *Journal of the Atmospheric Sciences*, **52,** 1615–1629

Higgins, R. W. and Schubert, S. D. 1994 Simulated life cycles of persistent anticyclonic anomalies over the North Pacific : Role of synoptic-scale eddies., *Journal of the Atmospheric Sciences*, **51,** 3238–3260

Hoskins, B. J. 1983 Modelling of transient eddies and their feedback on the mean flow., *Large-Scale Dynamical Processes in the Atmosphere*, B. J. Hoskins and R. P. Pearce, Eds., Academic Press, London, UK.

Hoskins, B. J., James, I. N. and White, G. H. 1983 The shape, propagation and mean-flow interaction of large-scale weather systems., *Journal of the Atmospheric Sciences*, **40,** 1595–1612

Hoskins, B. J., McIntyre, M. E. and Robertson, A. W. 1985 On the use and significance of isentropic potential vorticity maps., *Quart. Journal of Royal Met. Soc.*, **111,** 877–946

Illari, L. 1984 A diagnostic study of potential vorticity in a warm blocking anti-cyclone., *Journal of the Atmospheric Sciences*, **41,** 3518–3526

James, P. M., Fraedrich, K. and James, I. N. 1994 Wave-zonal-flow interaction and ultra-low-frequency variability in a simplified global circulation model., *Quart. Journal of Royal Met. Soc.*, **120,** 1045–1067

McWilliams, J. C. 1980 An application of equivalent modons to atmospheric blocking., *Dyn. Atmos. Oceans.* **5,** 43–66

Mo, K. C., and Ghil, M. 1988 Cluster analysis of multiple planetary flow regimes., *Journal of Geophysical Research*, **93,** 10927–10951

Mullen, S. L. 1986 The local balances of vorticity and heat for blocking anticyclones in a spectral general-circulation model., *Journal of the Atmospheric Sciences*, **43,** 1406–1441

Plaut, G and R. Vautard 1994 Spells of low-frequency oscillations and weather regimes in the Northern Hemisphere., *Journal of the Atmospheric Sciences*, **51,** 210–236

Plumb, R. A. 1990 A nonacceleration theorem for transient quasi-geostrophic eddies on a three-dimensional time-mean flow., *Journal of the Atmospheric Sciences*, **47,** 1825–1836

Shutts, G. J. 1983 The propagation of eddies in diffluent jetstreams : Eddy vorticity of 'blocking' flow fields., *Quart. Journal of Royal Met. Soc.*, **109,** 737–761

Shutts, G. J. 1986 A case study of eddy forcing during an Atlantic blocking episode., *Advances in Geophysics*, **29,** 135–162

Stone, P. 1972 A simplified radiative-dynamical model of the static stability of rotating atmospheres., *Journal of the Atmospheric Sciences*, **29,** 405–418

Thorncroft, C. D., Hoskins, B. J. and McIntyre, M. E. 1993 Two paradigms of baroclinic-wave life-cycle behaviour., *Quart. Journal of Royal Met. Soc.*, **119,** 17–56

Vautard, R. 1990 Multiple weather regimes over the North Atlantic: Analysis of precursors and successors., *Monthly Weather Review*, **118,** 2056–2081

Vautard, R. and Legras, B. 1988 On the source of low-frequency variability. Part II : Nonlinear equilibration of weather regimes., *Journal of the Atmospheric Sciences*, **45,** 2845–2867

Vautard, R., C. Pires and G. Plaut 1996 Longe-Range atmospheric predictibility using space-time principal components., *Monthly Weather Review*, **124**, 288–307